

# Modeling and Simulation of Austenitic Welds and Coarse-grained Specimens

May 2020

Richard E Jacob  
Matthew S Prowant  
Chris A Hutchinson  
Nikhil Deshmukh  
Aaron A Diaz



## DISCLAIMER

This report was prepared as an account of work sponsored by an agency of the United States Government. Neither the United States Government nor any agency thereof, nor Battelle Memorial Institute, nor any of their employees, makes **any warranty, express or implied, or assumes any legal liability or responsibility for the accuracy, completeness, or usefulness of any information, apparatus, product, or process disclosed, or represents that its use would not infringe privately owned rights.** Reference herein to any specific commercial product, process, or service by trade name, trademark, manufacturer, or otherwise does not necessarily constitute or imply its endorsement, recommendation, or favoring by the United States Government or any agency thereof, or Battelle Memorial Institute. The views and opinions of authors expressed herein do not necessarily state or reflect those of the United States Government or any agency thereof.

PACIFIC NORTHWEST NATIONAL LABORATORY

*operated by*

BATTELLE

*for the*

UNITED STATES DEPARTMENT OF ENERGY

*under Contract DE-AC05-76RL01830*

# **Modeling and Simulation of Austenitic Welds and Coarse-grained Specimens**

May 2020

Richard E Jacob  
Matthew S Prowant  
Chris A Hutchinson  
Nikhil Deshmukh  
Aaron A Diaz

Prepared for  
the U.S. Nuclear Regulatory Commission  
under a Related Services Agreement with the U.S. Department of Energy  
Contract DE-AC05-76RL01830

Carol A. Nove, Contracting Officer Representative

Pacific Northwest National Laboratory  
Richland, Washington 99354

## Summary

The Pacific Northwest National Laboratory (PNNL) is conducting confirmatory research for the U.S. Nuclear Regulatory Commission to evaluate commercially available nondestructive examination (NDE) modeling and simulation software packages used in the nuclear industry. Ultrasonic (UT) simulation models were developed to aid in the design and qualification of inspection techniques and in the analysis of inspection results. CIVA, a modeling and simulation package developed by CEA, was selected for this study because it is readily available and has been used for NDE in the nuclear power plant (NPP) industry. To improve the effectiveness and reliability of ultrasonic inspections, CIVA can model variables such as noise and attenuation, beam propagation and flaw response, and probability of detection. The assessment in this report is focused on identifying UT modeling and simulation performance, reliability, and accuracy in relation to inservice inspection (ISI) scenarios commonly encountered in NPPs. In addition, the work reported here is intended to help provide guidance to establish standard methods to perform and evaluate simulations for more effective model implementation, simulation analysis, and interpretation of results.

This work is part of an ongoing effort to define best practices required for using computational models (in this case CIVA) to simulate ultrasonic testing scenarios being conducted on NPP components. In addition to model validation (i.e., the ability of a model to accurately reproduce all relevant conditions for a particular application), a number of other factors are considered, including operational and functional inputs to the models, computational complexity and model run-times, material microstructures, flaw morphology, uncertainty in model predictions, and the ability to extrapolate findings from model predictions to realistic scenarios. In this report, PNNL focused on the use of CIVA for evaluating models of the ultrasound beam and the use of both beam models and flaw response models for simulating coarse-grained materials in austenitic welds, dissimilar metal welds (DMW), and cast austenitic stainless steel (CASS) materials.

A common saying in simulation and modeling is, “All models are wrong, but some are useful.” PNNL’s research on modeling and simulation is striving to answer the question, “under what conditions do simulations provide useful predictions of flaw detection?” More specifically, can modeling currently be used to predict flaw responses

- in ferritic steel,
- in wrought austenitic steel,
- through austenitic steel welds, and
- in cast austenitic steel?

With respect to simulations of ultrasonic beams and flaw responses in homogeneous materials, such as ferritic and wrought austenitic steels, previous work has been conducted by multiple research groups (EPRI 2015; Dib et al. 2017; EPRI 2017; Holmer et al. 2017; Foucher et al. 2018). Accordingly in this report, PNNL has focused on austenitic and dissimilar metal weld (DMW) examinations and CASS materials.

Two keys are necessary to answer the latter two questions. (1) Robust models are required that are built on sound mathematical framework and use appropriate approximations, including the user-supplied input parameters and specimen descriptions. (2) Empirical studies are required in order to validate the models by testing simulated scenarios. In this regard, it is vital to obtain

and use laboratory-based true-state information to verify and validate the predictive qualities of models.

This report outlines the process of developing the building blocks needed for the aforementioned keys. For the first key (using a sound mathematical framework and acceptable approximations), one of the most critical user-supplied model inputs is the specimen information, including the geometry and granular structure. This report explores the process of developing models of austenitic welds and explores the practical and predictive limits of using such models in beam and flaw-response simulations. This report also describes the development of CASS models. The level of necessary realism in specimen models is examined, and the limitations of the modeling software are probed. For the second key (empirical studies), empirical beam mapping and flaw response activities are undertaken to provide validation for the simulations and to guide follow-on simulation studies. By developing the keys, the goal is to lay the critical groundwork necessary in the ongoing effort to define best practices required for using computational models to simulate ultrasonic testing scenarios being conducted on NPP components.

Quantitative metrics are important for comparing simulation results to one another and to empirical results. Such metrics facilitate objective decision-making by allowing analysts to avoid judgment calls. Several potentially useful metrics are described in this technical letter report (TLR), including a method for comparing flaw response signals when a calibration signal is not available and a method for comparing beam simulations using image similarity metrics.

Results from modeling and simulation tools such as CIVA are used to support NPP licensee requests for relief that are submitted to the Office of Nuclear Reactor Regulation (NRR) for review. This project is intended to provide NRR with a technical basis to more uniformly and effectively evaluate the adequacy of licensee submittals that use modeling and simulation results. In addition, industry representatives have indicated the desire to determine if simulations can be used in lieu of physical mock-ups to reduce the time and cost associated with inspection qualification.

After testing many of the features of the CIVA UT module and running multiple varied simulations, PNNL has demonstrated that CIVA is a powerful and versatile tool for ultrasonic modeling, but it should be used with care. The user should not automatically assume that simulation results are accurate reflections of reality; indeed, this is true when using any modeling software. The user should test CIVA parameters and settings and consult CIVA technical support through EXTENDE (EXTENDE Inc.,<sup>(a)</sup> Norfolk, VA) when needed, in order to become familiar with CIVA before relying on the results for decision-making. Before attempting to use beam simulations as a surrogate for flaw response simulations or for coverage calculations, it is important to understand the limitations imposed by parameters such as grain structures, sound attenuation, or probe position.

This TLR shows that the simulated flaw response through an austenitic weld model can be significantly and unpredictably affected by the flaw position because of beam scatter and redirection through the weld. Additionally, this TLR shows that realistic austenitic weld specimen models with many grain interfaces may provide a good representation of beam scatter if the grains are small enough. However, realistic weld models are difficult to produce and are computationally demanding to use in routine simulations. As an alternative to realistic weld

---

(a) EXTENDE Inc. is a subsidiary of EXTENDE S.A., Massey, France, the company that distributes CIVA.

models, the Ogilvy weld model is frequently used for simulations of austenitic welds because it provides an idealized and simplified weld microstructure. However, the Ogilvy model assumes a gradual change in crystalline orientation. This report shows that the Ogilvy model does not produce scatter in beam simulations and therefore may not provide the needed level of realism for modeling through austenitic welds.

This TLR demonstrates that realistic CASS models can be run in CIVA, but difficulties can arise due to the large number of regions and interfaces required to represent the microstructure. Results suggest that the coarse-grained equiaxed CASS structure that PNNL tested appears to be well approximated by Voronoi regions in beam simulations. Voronoi regions are advantageous because they are easy to define, and simulation run-times are much shorter. PNNL has not yet tested other CASS microstructures besides coarse-grained equiaxed, although a columnar model has been developed and will be reported on in the next report.

For any modeling strategy, results show that running multiple simulations with different model settings and/or specimen designs can help establish best-case, worst-case, and nominal scenarios. Various specimen geometries should be tested, such as different grain structures (e.g., different sizes, shapes, or arrangements) and assignments of Euler angles or material properties. Ultimately, a balance of model complexity with simulation time is needed; overly complex models are subject to user error, often take too long to execute, and consequently do not meet deadlines or accuracy expectations. Therefore, careful forethought should be given to what the desired outcomes are, what aspects of a scenario must be included, and what aspects can be ignored or eliminated. Furthermore, given the difficulties of developing coarse-grained models, confirming data from empirical measurements should be used to adjust model parameters in a careful and informed manner. It is important to remember that without empirical data there is no way of evaluating the realism or accuracy of simulations.

With respect to CIVA, it should be noted that its developers (CEA-LIST & EXTENDE) continue to conduct validation studies and incorporate software improvements. As discussed in the conclusions section of Dib et al. 2017, CIVA already has an extensive validation database published; however, there is no publication of any verification benchmarks of the software. Therefore, it is essential for the modeling software to be verified to demonstrate that it has correct numerical implementations of the underlying computational models. Thus, PNNL has been tasked by the NRC to assess NDE model/simulation performance, reliability, and accuracy.

## Acronyms and Abbreviations

CAD	computer-aided design
CASS	cast austenitic stainless steel
CEA	Commissariat à l'Énergie Atomique
COM	center of mass
CS	carbon steel
CT	computerized tomography
dB	decibels
DMW	dissimilar metal weld
EBSD	electron backscatter diffraction
EDM	electro-discharge machined
EPRI	Electric Power Research Institute
FSH	full screen height
GTAW	gas tungsten arc weld
GTD	geometric theory of diffraction
ID	inner diameter
IPF	inverse pole figures
MHz	megahertz
MSE	mean square error
NDE	nondestructive examination/evaluation
NPP	nuclear power plant
NRC	U.S. Nuclear Regulatory Commission
NRR	Office of Nuclear Reactor Regulation
NUREG/CR	Nuclear Regulatory Contractor Report
OD	outer diameter
p	Pearson correlation coefficient
PA	phased array
PNNL	Pacific Northwest National Laboratory
RES	Office of Research
SD	standard deviation
SMAW	shielded metal arc weld
SS	stainless steel
SSIM	structural similarity index metric
TLR	technical letter report
TRL	transmit-receive longitudinal
UT	ultrasonic testing
UV	UltraVision
WCL	weld centerline
WSS	wrought stainless steel

# Contents

Summary..... ii

Acronyms and Abbreviations ..... v

1.0 Confirmatory Research in NDE Modeling and Simulation ..... 1.1

    1.1 Introduction..... 1.1

    1.2 Motivation for the Current Work..... 1.2

    1.3 Scope and Objectives ..... 1.3

    1.4 Brief Summary of Previous Work ..... 1.3

    1.5 Report Organization ..... 1.6

2.0 Quantitative Metrics ..... 2.1

    2.1 Introduction..... 2.1

    2.2 Quantitative Metric for A-scan Comparisons ..... 2.2

    2.3 Quantitative Metric for B-scan Comparisons ..... 2.5

    2.4 Image Similarity Metrics ..... 2.7

3.0 CIVA Usability ..... 3.1

    3.1 Introduction..... 3.1

    3.2 Specimen Interaction Model ..... 3.1

    3.3 Adapted Focal Laws for Phased-Array Probes ..... 3.2

    3.4 CIVA Metamodels ..... 3.4

    3.5 Attenuation and Noise ..... 3.13

    3.6 Ogilvy Weld Model Parameters ..... 3.14

    3.7 Stiffness Matrix Parameters and Euler Angles ..... 3.17

    3.8 Flaw Definitions ..... 3.21

4.0 Experimental ..... 4.1

    4.1 Introduction..... 4.1

    4.2 Specimens..... 4.1

    4.3 Equipment ..... 4.4

        4.3.1 Probes ..... 4.4

        4.3.2 Data Acquisition System..... 4.5

    4.4 Experimental Setup ..... 4.6

    4.5 Results ..... 4.7

        4.5.1 WSS-WSS Welds ..... 4.7

        4.5.2 CS-CASS DMW Weld..... 4.12

5.0 Beam and Flaw Response Simulations with an Austenitic Model..... 5.1

    5.1 Introduction..... 5.1

    5.2 Ogilvy Weld Model ..... 5.2

    5.3 Austenitic Weld Model ..... 5.9

        5.3.1 Model Development..... 5.9

        5.3.2 Beam Simulations..... 5.17

5.3.3	Comparison with Experimental Beam Maps.....	5.31
5.3.4	Summary .....	5.39
5.4	Other Influential Parameters and Considerations.....	5.40
5.4.1	Probe Position and Implications for Flaw Detection .....	5.40
5.4.2	Crack Detection Simulations.....	5.48
5.4.3	Limited Coverage Scenarios.....	5.51
5.4.4	Probe Frequency .....	5.54
5.4.5	Simulation Complexity .....	5.55
5.5	Summary .....	5.57
6.0	Dissimilar Metal Weld.....	6.1
6.1	Introduction.....	6.1
6.2	Specimen Description .....	6.1
6.3	Beam Simulations .....	6.3
6.4	Flaw Response Simulations .....	6.9
6.5	Comparison with Experiment .....	6.10
6.6	Summary .....	6.13
7.0	CASS Model.....	7.1
7.1	Introduction.....	7.1
7.2	Realistic Model of Vintage CASS Microstructure .....	7.2
7.2.1	Specimen Model Preparation .....	7.2
7.2.2	CIVA Simulations.....	7.8
7.2.3	Voronoi Model Simulations .....	7.14
7.2.4	Accuracy Factor.....	7.26
7.2.5	Comparison with Experiment.....	7.29
7.3	Summary .....	7.30
8.0	Summary of Findings .....	8.1
8.1	Metrics.....	8.2
8.2	CIVA Usability .....	8.2
8.3	Coarse-grained Models .....	8.3
8.4	Evaluating Simulations – A Potential Thought Process.....	8.6
9.0	References.....	8.1
	Appendix A – Workflows .....	A.1
	Appendix B – B-scan Similarity Metric .....	B.1
	Appendix C – CIVA Tips .....	C.1
	Appendix D – Transformation of Bunge Euler Angles to CIVA Rotation Angles.....	D.1
	Appendix E – Grain Modeling .....	E.1
	Appendix F – Modeling Computer Specifications .....	F.1

## Figures

Figure 2.1.	The process of comparing simulation and experimental outputs should involve quantitative comparison and informed feedback so that justifiable conclusions can be drawn. ....	2.1
Figure 2.2.	Simulated A-scan (left) and rectified A-scan (right) with envelope (orange line).....	2.2
Figure 2.3.	An example of a rectified A-scan envelope with two main peaks. The 50% of maximum peak height ( <i>left</i> ) and 10% of maximum peak height ( <i>right</i> ) are identified. The 10% peak height of the right peak (green x's) encompass smaller, neighboring peaks. ....	2.3
Figure 2.4.	Gaussian curve fits (blue and yellow lines) to the two main peaks of the A-scan envelope (dotted line).....	2.3
Figure 2.5.	<i>Left</i> : A-scan (blue line) and envelope (orange line) with three peaks identified (green dots). <i>Right</i> : A-scan envelope (dashed line) with Gaussian fits to the three peaks (solid lines). The rightmost peak is highest, but the leftmost peak has the largest integral. ....	2.4
Figure 2.6.	<i>Left</i> : A-scan (blue line) and envelope (orange line) with two prominent overlapping peaks (green dots). <i>Right</i> : Gaussian fits of each peak. The individual fits to the peaks allow for the peaks to be integrated independently. ....	2.5
Figure 2.7.	Example of isolating a peak in a B-scan for analysis. A: Original B-scan with weld overlay. B: Surface plot of the B-scan with all peaks shown. C: Surface plot of the B-scan with a mask applied to all peaks except for the peak of interest. ....	2.6
Figure 2.8.	Example of two clearly different flaw response simulation results with nearly identical model input parameters. The only difference was the specimen interaction approximation (Specular [ <i>left</i> ] and Kirchoff [ <i>right</i> ]). ....	2.7
Figure 2.9.	Example of two subtly different beam simulation results with nearly identical model input parameters. The only difference between simulation settings was the accuracy factor (accuracy = 4 [ <i>left</i> ], accuracy = 64 [ <i>right</i> ]). ....	2.8
Figure 2.10.	The correlation of the pixel intensities from the figures shown in Figure 2.9 on a pixel-by-pixel basis. The red line shows the linear least squares fit. ....	2.9
Figure 3.1.	Weld geometry used for tests of Specular and Kirchhoff interaction models. <i>Left</i> : side view. The flaw position is indicated by the red arrow. <i>Right</i> : front view. The red region indicates a circumferential flaw. ....	3.2
Figure 3.2.	Simulation results using the Specular ( <i>top</i> ) and Kirchhoff ( <i>bottom</i> ) specimen interaction approximations. Red arrows indicate the flaw responses of the two simulations. The blue and black arrows indicate the counterbore and weld root responses, respectively. The red circle indicates unidentified echoes in the Specular approximation. ....	3.2
Figure 3.3.	Phased-array beam simulations through an Ogilvy weld model. <i>Top</i> : Non-adapted focal laws. <i>Bottom</i> : Adapted focal laws. ....	3.3

Figure 3.4. Probe and specimen weld profile configuration for metamodel tests. The green lines indicate the L-wave path, including the reflected beam from the flaw (red arrow) and the reflected and refracted beams from the weld interface..... 3.4

Figure 3.5. Parameters used to define the ranges of the four variables in the metamodel..... 3.5

Figure 3.6. Parallel plot showing the relationships between the different variation parameters. Top: Unfiltered plot. Bottom: Plot with a filter applied to the output values such that the highest output values are highlighted (yellow bracket). The filter reveals that the lowest values of probe center frequency (red bracket) combined with the highest values of probe diameter (blue bracket) generally resulted in the highest output values. .... 3.6

Figure 3.7. Metamodel Analysis screen showing the accuracy of the metamodel. The top two plots illustrate the uncertainty in the metamodel results (red is higher error, yellow is intermediate, and green is low). The lines in the parallel plot are color-coded according to the uncertainty ranges. The red bracket highlights that most of the high uncertainty results originated from the lower end of the range of center frequencies. .... 3.8

Figure 3.8. 1D Analysis screen. This plot illustrates how the simulation results depend on a selected parameter (bandwidth in this case), with the other parameters held constant. .... 3.9

Figure 3.9. 2D Analysis screen. This plot illustrates how the simulation results (represented by the color spectrum) are affected by two variables (diameter and center frequency in this case) while the others are held constant..... 3.10

Figure 3.10. Sensitivity Analysis screen. The lower plots illustrate how sensitive the metamodel results are to changes in the individual parameters. .... 3.11

Figure 3.11. Metamodel results from examining wedge parameters. A small change in the front length range between runs 2 and 3 resulted in a dramatic change in the parameter sensitivities. .... 3.12

Figure 3.12. Metamodel results from examining flaw parameters. The sensitivity to the flaw tilt depends strongly on the range of the tilt parameter. .... 3.12

Figure 3.13. CIVA screenshot showing attenuation options..... 3.14

Figure 3.14. Definition of the Ogilvy geometrical weld model. Free parameters  $T$ ,  $D$ ,  $\alpha$ , and  $\eta$  can be defined in CIVA by the user..... 3.14

Figure 3.15. Different weld morphologies controlled by the value  $T$ . From left to right:  $T=0.1, 0.5, 1, \text{ and } 2$ . The blue arrows indicate the origin, or center position, from which the Ogilvy model was calculated. .... 3.15

Figure 3.16. Ogilvy grain morphologies tested. The red arrows indicate the origin of the beam path. Note that only the front section of the probe (yellow) is shown. The blue arrows indicate the origins of the Ogilvy models..... 3.15

Figure 3.17. Rectified A-scans from simulations with the value of  $T$  varied. The A-scan envelopes (dashed lines) and Gaussian fits to main peaks (solid lines) are shown. In cases where two peaks are identified, the blue peak is from the weld root and the orange peak is from the flaw..... 3.16

Figure 3.18. Example of the B-scan reconstruction bug..... 3.17

Figure 3.19.	Stiffness matrix elements that can be edited for orthotropic symmetry. Stiffness matrix elements are labeled as C11, C22, etc. Euler angles in the specimen reference frame may also be defined on this screen. ....	3.18
Figure 3.20.	Ray-tracing images of the sound path through the weld with default stiffness matrix values and $\pm 10\%$ of the default values. A circumferential planar flaw is shown on the right side of the weld root. ....	3.19
Figure 3.21.	Metamodel sensitivity results of varying the stiffness matrix elements. For the ranges of elements used, results were most sensitive to C33 and insensitive to C66. ....	3.20
Figure 3.22.	Euler angle rotations according to the standard Bunge convention. These rotations are in the crystal's frame of reference and not in the specimen's frame of reference. ....	3.21
Figure 4.1.	Photo of 3C-022 with removed specimens. ....	4.2
Figure 4.2.	Photo of DMW pipe segment 14C-146. ....	4.2
Figure 4.3.	Photographs of the weld profiles of Specimen 1 ( <i>left</i> ) and Specimen 2 ( <i>right</i> ). The dashed line denotes the weld centerline. ....	4.3
Figure 4.4.	Photograph of the weld profile of Specimen 3. The dashed line denotes the weld centerline. ....	4.3
Figure 4.5.	2.0 MHz PAUT transducer. <i>Left</i> : Standard TRL configuration. <i>Right</i> : The transmit half of the pair, as used for sound field mapping. ....	4.4
Figure 4.6.	The pencil probe used in this study. The probe is housed within a sleeve, which is mounted inside a holder that can be attached to the scanning arm. ....	4.5
Figure 4.7.	Pencil probe frequency response from a 2.25 MHz transducer (dashed black line) driven at 2.0 MHz (solid black line). The signal response was self-normalized. ....	4.5
Figure 4.8.	Photograph of the locations of the probes during data acquisition. ....	4.6
Figure 4.9.	Photograph of the experimental setup for side-beam mapping data acquisition. ....	4.7
Figure 4.10.	Beam maps through WSS parent material. Clockwise from top left: 30°, 45°, 60°. ....	4.8
Figure 4.11.	Beam maps with the probe exit point near the WCL. <i>Left column</i> : Specimen 1. <i>Right column</i> : Specimen 2. Rows from top to bottom: 30°, 45°, 60°. Probe positions are shown for illustrative purposes and are not to scale. ....	4.9
Figure 4.12.	Beam maps with the probe exit point to the left of the WCL. <i>Left column</i> : Specimen 1. <i>Right column</i> : Specimen 2. Rows from top to bottom: 30°, 45°, 60°. Probe positions are shown for illustrative purposes and are not to scale. ....	4.10
Figure 4.13.	Beam maps with the probe exit point to the left of the weld toe. <i>Left column</i> : Specimen 1. <i>Right column</i> : Specimen 2. Rows from top to bottom: 30°, 45°, 60°. Probe positions are shown for illustrative purposes and are not to scale. ....	4.11
Figure 4.14.	Baseline beam maps with focal depths of 24 mm ( <i>left</i> ) and 84 mm ( <i>right</i> ) at 45°. ....	4.13

Figure 4.15.	Baseline beam maps with a focal depth of 84 mm at 30° ( <i>left</i> ), 45° ( <i>center</i> ), and 60° ( <i>right</i> ). .....	4.13
Figure 4.16.	Through-weld beam scans with the DMW specimen at a focal depth of 84 mm. <i>Top row</i> : 30°. <i>Middle</i> : 45°. <i>Bottom</i> : 60°. <i>Left column</i> : 0 mm from WCL. <i>Center</i> : 10 mm from WCL. <i>Right</i> : 20 mm from WCL. The approximate probe positions are illustrated at the top of each column; probes are not to scale. ....	4.14
Figure 5.1.	The weld region with the Ogilvy-model grains shown. The blue arrows indicate the origin, or center position, from which the Ogilvy model was calculated. ....	5.2
Figure 5.2.	Beam simulation from a PA probe at 45° through isotropic weld material.....	5.3
Figure 5.3.	Beam simulation results for a simple isotropic weld and Ogilvy-model welds using stiffness matrix elements reported in the literature. ....	5.4
Figure 5.4.	Average of the seven Ogilvy simulation results.....	5.6
Figure 5.5.	Total sound energy incident on the specimen backwall on the far side of the weld. ....	5.7
Figure 5.6.	A-scans and Gaussian fits for the isotropic case (top row) and the Gardahaut case (bottom row). For the Gardahaut case, the peaks were too close together to obtain accurate area measurements. ....	5.8
Figure 5.7.	Ratio of the flaw response to the root response. ....	5.8
Figure 5.8.	Cross section of the austenitic weld used for EBSD data acquisition. ....	5.10
Figure 5.9.	EBSD inverse pole figures for the X, Y, and Z axes. Each color represents a different crystalline direction, each of which can be defined by a set of Euler angles. The black line on the inset is an artefact from a subtle scratch on the specimen surface. ....	5.11
Figure 5.10.	An illustration of the quadtree decomposition process. Large quads are decomposed into smaller quads depending on if a homogeneity metric has been reached.....	5.12
Figure 5.11.	Example of a quadtree decomposition. This image is the result of a quadtree decomposition of a photograph of Times Square. Source: <a href="https://imgur.com/gallery/7qtKl">https://imgur.com/gallery/7qtKl</a> by “AndrewVetovitz”. ....	5.12
Figure 5.12.	Examples of decomposed and binned IPF image data. Top row: 3 Euler angle bins. Bottom row: 7 Euler angle bins. ....	5.14
Figure 5.13.	The 256-pixel, 7-bin geometry with columnar regions used for simulations. Different colors indicate different bin regions. ....	5.15
Figure 5.14.	Illustration of how quadpoint intersections were treated so that CIVA would process the geometry. Left: Dots indicate line segment termini, and the red dot indicates a quadpoint intersection. Right: The red line segment and red dot indicate new elements that were added to the geometry. The size of the red segment was exaggerated to illustrate the concept.....	5.16
Figure 5.15.	Beam simulation through isotropic material with a 2 MHz TRL probe at 45°. ....	5.17
Figure 5.16.	The 256-pixel, 3-bin geometry with columnar regions used for simulations. Different colors indicate different bin regions. ....	5.18

Figure 5.17. Beam simulation results of the ten 3-bin, 256-pixel scenarios with the 2 MHz TRL probe at 45°. Data were normalized to the peak signal of the image set. The X-axis is in mm from the beam exit point, and the Y-axis is in mm from the ID surface. ....5.19

Figure 5.18. Average image of the 256-pixel, 3-bin simulations.....5.21

Figure 5.19. Beam simulation results of the ten 7-bin, 256-pixel scenarios with the 2 MHz TRL probe at 45°. Data were normalized to the peak signal of the image set. The X-axis is in mm from the beam exit point, and the Y-axis is in mm from the ID surface. ....5.22

Figure 5.20. Average image of the 256-pixel, 7-bin scenarios. ....5.24

Figure 5.21. Sound intensity incident on the backwall versus position. The average 256-pixel, 3-bin case (blue), 7-bin case (orange), and the isotropic case (green) are shown. ....5.25

Figure 5.22. Beam simulation results of the ten 3-bin, 128-pixel scenarios with the 2 MHz TRL probe at 45°. Data were normalized to the peak signal of the image set. The X-axis is in mm from the beam exit point, and the Y-axis is in mm from the ID surface. ....5.27

Figure 5.23. Average image of the 128-pixel, 3-bin scenarios. ....5.28

Figure 5.24. CIVA screen capture illustrating the results of the 0.455 mm resolution simulation. ....5.30

Figure 5.25. Transmit (light green) and receive (dark green) rays at different TRL probe positions at 45°. *Left*: Probe position = 95.0 mm. *Right*: Probe position = 94.9 mm. All previous simulations were done with the probe at 95.0 mm. ....5.31

Figure 5.26. Beam simulation results through the 256-pixel, 7-bin austenitic weld model with a 2 MHz PA probe at 45° with a focal depth of 24 mm (0.95 in.). ....5.32

Figure 5.27. Average of the 10 PA beam simulations, normalized to Figure 5.26.....5.33

Figure 5.28. PA beam simulation through isotropic material, normalized to Figure 5.26. ....5.33

Figure 5.29. Empirical sound field through isotropic wrought stainless steel with the PA probe at 45° and a focal depth of 24 mm (0.95 in.). ....5.34

Figure 5.30. PA beam simulation through isotropic material with the PA probe at 45° and a focal depth of 24 mm (0.95 in.), normalized to itself.....5.34

Figure 5.31. Sound field through the weld of Specimen 1 with the 2 MHz PA probe at 45°. The probe position is shown for illustrative purposes and is not to scale. ....5.35

Figure 5.32. Sound field through the weld of Specimen 2 with the 2 MHz PA probe at 45°. The probe position is shown for illustrative purposes and is not to scale. ....5.35

Figure 5.33. PA beam simulation through isotropic material at 45° with 0.2 dB/mm attenuation.....5.36

Figure 5.34. Beam simulation results through the 256-pixel, 7-bin austenitic weld model with a PA probe at 45° with 0.2 dB/mm attenuation. ....5.38

Figure 5.35. Average of the ten PA beam simulations with 0.2 dB/mm attenuation.....5.39

Figure 5.36.	Beam models through the weld at different positions with a right-facing, 2 MHz TRL probe at 45°. The approximate weld boundaries are shown in grey. ....	5.41
Figure 5.37.	Example of three beam models showing the weld geometry and probe positions with the right-facing probe. ....	5.42
Figure 5.38.	Beam models through the weld at different positions with a left-facing, 2 MHz TRL probe at 45°. The approximate weld boundaries are shown in grey. ....	5.43
Figure 5.39.	Example of three beam models showing the weld geometry and probe positions with the right-facing probe. ....	5.44
Figure 5.40.	Integrated sound energy incident on the specimen backwall for the right-facing probe as a function of position. For comparison, the orange line illustrates the static isotropic beam.....	5.45
Figure 5.41.	Integrated sound energy incident on the specimen backwall for the left-facing probe as a function of position. For comparison, the orange line illustrates the static isotropic beam.....	5.46
Figure 5.42.	Total integrated signal for the right-facing probe ( <i>top</i> ) and the left-facing probe ( <i>bottom</i> ). The maximum (red arrow) and local minimum (purple arrow) of the right-facing probe are only 3.5 mm (0.14 in.) apart. ....	5.47
Figure 5.43.	Flaw response simulations with the right-facing probe. A 3 mm (0.12 in.) deep flaw was located at 127 mm (5 in.) ( <i>top</i> ) and 130.5 mm (5.14 in.) ( <i>center</i> ). A control simulation was performed away from the weld ( <i>bottom</i> ). ....	5.48
Figure 5.44.	EDM “crack” in a stainless steel test block (specimen on loan to PNNL courtesy of the EPRI NDE Center). ....	5.49
Figure 5.45.	CAD rendering of the EDM “crack.” Dashed lines are the outline of the crack, and solid lines show the simplified outline for CIVA import.....	5.49
Figure 5.46.	The austenitic weld model with the EDM crack added. ....	5.50
Figure 5.47.	Qualitative comparison of a flaw response simulation and empirical data of the EDM “crack.” The 2 MHz TRL probe at 45° was used. The red arrow indicates the target flaw and the green arrow indicates a second, smaller flaw that is about 17 mm (0.65 in.) away. The smaller flaw is visible in Figure 5.44. ....	5.51
Figure 5.48.	TRL-probe beam simulations through isotropic material ( <i>left</i> ) and the austenitic weld model ( <i>right</i> ) with the EDM crack. ....	5.52
Figure 5.49.	TRL-probe flaw response simulations through the austenitic weld with the EDM crack. ....	5.53
Figure 5.50.	Flaw response simulation with the 45°, 2 MHz TRL probe through the austenitic weld model and no coverage limitations. ....	5.53
Figure 5.51.	Flaw response simulations using the 2 MHz TRL probe through the austenitic weld model with a 6 mm (0.24 in.) deep notch on the far side. ....	5.54
Figure 5.52.	Beam simulations in an austenitic weld with different probe frequencies. Clockwise from top left: 1 MHz, 1.5 MHz, 4 MHz, and 2 MHz. Results are normalized to the peak signal intensity of the 1 MHz simulation. ....	5.55

Figure 5.53.	Flaw response simulation through the austenitic weld model using the 2 MHz TRL probe at 45° with no interface interactions. The green line is the transmitted and reflected beam. ....	5.56
Figure 5.54.	Flaw response simulation through the austenitic weld model using the 2 MHz TRL probe at 45° with interface interactions. The green lines indicate the beams reflected from the interactions with the weld model grains. ....	5.57
Figure 6.1.	Photograph of a polished and etched DMW weld section under ambient light. The CASS side is to the left. ....	6.2
Figure 6.2.	Photograph of the polished and etched DMW weld section with the light source to the left. ....	6.2
Figure 6.3.	DMW CAD drawing with weld regions labeled. ....	6.3
Figure 6.4.	DMW model with a crack in the butter region. ....	6.3
Figure 6.5.	Probe placement with respect to the DMW model for beam simulations. ....	6.4
Figure 6.6.	Beam simulation results using a 2 MHz TRL probe at 45° through the DMW with 10 different Euler angles. ....	6.5
Figure 6.7.	Normalized beam simulation through isotropic material. ....	6.6
Figure 6.8.	Average of the ten DMW beam simulations. ....	6.6
Figure 6.9.	Beam simulation results using a 2 MHz TRL probe at 45° through the DMW with a crack in the butter region. ....	6.8
Figure 6.10.	Mean of the beam simulations of the DMW with the crack. ....	6.9
Figure 6.11.	Flaw response simulation without ( <i>top</i> ) and with ( <i>bottom</i> ) interface interactions using a 2 MHz TRL probe at 45°. The L-wave transmit trajectory and reflections are shown by the green lines. ....	6.10
Figure 6.12.	Beam simulations through isotropic material without ( <i>top</i> ) and with ( <i>bottom</i> ) 0.1 dB/mm (2.5 dB/in.) attenuation. A 2 MHz PA probe at 45° with a 84 mm (3.3 in.) focal depth was used. ....	6.11
Figure 6.13.	Simulation results with the 2 MHz PA probe at 45° on the CS side of the DMW model. An attenuation of 0.1 dB/mm (2.5 dB/in) was added to the simulation. ....	6.12
Figure 6.14.	Average of the images in Figure 6.13. ....	6.13
Figure 7.1.	Coarse-grained CASS specimen AAD-3 photographed with ambient light. ....	7.2
Figure 7.2.	The section shown in Figure 7.1 with illumination from the left ( <i>top</i> ) and the right ( <i>bottom</i> ). ....	7.3
Figure 7.3.	Illustration of the steps used to extract the grain boundaries from photographs. A: Example photograph with lighting from the left. B: The red channel of the RGB image. C: Image from Panel B with the mask applied. D: Image from Panel C with image filtering applied. E: Binary image of highlighted grains. F: Boundaries from the grains in Panel E. ....	7.4
Figure 7.4.	Final grain outline image of AAD-3. ....	7.5
Figure 7.5.	Results of applying the line reduction algorithm with different threshold values to a section of the AAD-3 skeleton. ....	7.6
Figure 7.6.	Specimen model of AAD-3 used for simulations. ....	7.7
Figure 7.7.	Ambient-light photograph of B-519C, a columnar-grained CASS sample. ....	7.7

Figure 7.8.	Grain skeleton of Specimen B-519C. ....	7.8
Figure 7.9.	Skeleton of B-519C with the line reduction algorithm applied. ....	7.8
Figure 7.10.	Simulation results with a simple isotropic specimen. A 1 MHz PA probe at 45° was used. ....	7.9
Figure 7.11.	Color-coded image illustrating the distribution of Euler angles in one of the AAD-3 models. Each of the ten colors represents a different crystalline orientation. ....	7.10
Figure 7.12.	AAD-3 beam simulations. A 1 MHz PA probe at 45° was used with the focal spot in the plane of the simulation. ....	7.11
Figure 7.13.	Empirical beam maps from AAD-3, reproduced from PNNL-23393 (Crawford et al. 2014). A 1 MHz PA probe at 45° was used with the focal spot in the plane of the beam map. ....	7.12
Figure 7.14.	Average of the ten AAD-3 simulations. ....	7.13
Figure 7.15.	Example of Voronoi regions. <i>Left</i> : Seed points. <i>Right</i> : Voronoi regions drawn from the seed points. ....	7.14
Figure 7.16.	Testing beam redirection in a two-layer specimen. <i>Left</i> : Isotropic material. <i>Center</i> : Different sound speeds. <i>Right</i> : Different Euler angles. ....	7.15
Figure 7.17.	Simulation volume with 1000 volumetric Voronoi regions. Shown are the Voronoi regions that intersect the simulation plane. ....	7.16
Figure 7.18.	Beam simulation with 1000 volumetric Voronoi regions. This image is normalized to Figure 7.10. A 1 MHz PA probe at 45° was used with the focal spot in the plane of the simulation. ....	7.16
Figure 7.19.	Simulation volume with 5000 volumetric Voronoi regions. Shown are the Voronoi regions that intersect the simulation plane. ....	7.17
Figure 7.20.	Beam simulation with 5000 volumetric Voronoi regions. This figure is normalized to Figure 7.10. A 1 MHz PA probe at 45° was used with the focal spot in the plane of the simulation. ....	7.17
Figure 7.21.	Coarse-grained specimen models. <i>Left</i> : CIVA-generated Voronoi. <i>Right</i> : AAD-3. Both models are the same size and have the same number of regions in the 2D plane. ....	7.18
Figure 7.22.	Voronoi simulation results for $\Delta V = 4\%$ . A 1 MHz PA probe at 45° was used with the focal spot in the plane of the simulation. ....	7.19
Figure 7.23.	Voronoi simulation results for $\Delta V = 6\%$ . This figure is normalized to simulation 06 in Figure 7.22. A 1 MHz PA probe at 45° was used with the focal spot in the plane of the simulation. ....	7.20
Figure 7.24.	Voronoi simulation Results for $\Delta V = 8\%$ . This figure is normalized to simulation 06 in Figure 7.22. A 1 MHz PA probe at 45° was used with the focal spot in the plane of the simulation. ....	7.21
Figure 7.25.	Average results of the three Voronoi $\Delta V$ tests. This figure is normalized to simulation 06 in Figure 7.22. ....	7.22
Figure 7.26.	Center of mass comparison of two coarse-grained simulations. <i>Left</i> : AAD-3 Run 03. <i>Right</i> : Voronoi 6% Run 06. The red dots indicate the COM. ....	7.25
Figure 7.27.	A polished and etched circumferential section of a CASS specimen. This figure illustrates that a large variety of grain sizes can exist in the same section. ....	7.26

Figure 7.28. Beam simulations using a Voronoi model with increasing accuracy factor. The last two digits of the top label of each panel is the accuracy factor. A 1 MHz PA probe at 45° was used with the focal spot in the plane of the simulation. .... 7.27

Figure 7.29. Beam simulations using the AAD-3 model with increasing accuracy factor. The last two digits of the top label of each panel is the accuracy factor. A 1 MHz PA probe at 45° was used with the focal spot in the plane of the simulation. .... 7.28

Figure 7.30. Image similarity metrics as a function of accuracy factor for Voronoi regions (*left*) and AAD-3 (*right*). Ideal values of *ssim*, *mse*, and *corrcoef* (*p*) are 1, 0, and 1, respectively. .... 7.29

Figure 7.31. Empirical beam map data from AAD-3. *Top row*: Beam map, self-normalized (*left*) and normalized (*right*) to the WSS case (*bottom row*)..... 7.30

## Tables

Table 2.1.	Description of image similarity metrics .....	2.9
Table 3.1.	Ranges of matrix elements used in the metamodel analysis. ....	3.20
Table 4.1	Description of sound field mapping specimens .....	4.3
Table 5.1.	Image similarity metrics comparing the Ogilvy scenarios to the isotropic case.....	5.5
Table 5.2.	Image similarity metrics comparing the Ogilvy scenarios to the average result.....	5.6
Table 5.3.	Similarity metrics calculated for the ten 3-bin scenarios as compared to the simple, isotropic case. ....	5.20
Table 5.4.	Similarity metrics calculated for the ten 3-bin scenarios as compared to the average. ....	5.21
Table 5.5.	Similarity metrics calculated for the ten 7-bin scenarios as compared to the simple, isotropic case. ....	5.23
Table 5.6.	Similarity metrics calculated for the ten 7-bin scenarios as compared to the average. Run 08 is most similar to the average. ....	5.24
Table 5.7.	Similarity metrics of the 128-pixel, 3-bin simulations compared to the isotropic case. ....	5.28
Table 5.8.	Similarity metrics of the 128-pixel, 3-bin simulations compared to the average case. ....	5.29
Table 5.9.	Sound field penetration depth. ....	5.37
Table 7.1.	Similarity metrics of AAD-3 simulations compared to the isotropic case.....	7.12
Table 7.2.	Similarity metrics of AAD-3 simulations compared to the AAD-3 mean. ....	7.13
Table 7.3.	Similarity metrics of Voronoi simulations compared to the Isotropic case.....	7.23
Table 7.4.	Similarity metrics of Voronoi simulations compared to the average cases.....	7.24
Table 7.5.	Image similarity metrics comparing Voronoi and AAD-3 simulations to the isotropic case. ....	7.25
Table 7.6.	Fractional integrated beam of simulations compared to experiment. ....	7.30
Table 7.7.	Comparison of realistic grains and Voronoi regions in beam simulations. ....	7.31

## 1.0 Confirmatory Research in NDE Modeling and Simulation

This section introduces the progression of previous modeling and simulation work at Pacific Northwest National Laboratory (PNNL) and summarizes the basis and technical need for conducting the work by defining the specific motivations that underpin the effort, in terms of the U.S. Nuclear Regulatory Commission (NRC) needs. In addition, the scope and technical objectives of the modeling and simulation task are defined here. Finally, the topical flow of the report is described, and the relevant subject matter is outlined for the remainder of this technical letter report (TLR).

### 1.1 Introduction

Models are essentially simplified approaches to approximating (or simulating) real-world outcomes and may in some cases offer a substitute for experimental measurements. Models provide end-users with a framework for performing ultrasonic simulations and typically incorporate many mathematical approximations that may limit their applicability. Types of ultrasonic models include beam models and flaw response models. Beam models are generally more simplistic, easier to execute, and are used to simulate ultrasonic beam characteristics as the sound energy propagates away from the transducer into a material. Flaw response models are typically more complex, take longer to execute, and are used to simulate the ultrasonic signal response emanating from an insonified flaw. Commercially available tools, such as CIVA (EXTENDE Inc.) and UltraVision (Zetec), can be used for ultrasonic simulations but vary in operational and functional complexity. CIVA provides a semi-analytical simulation platform for generating both ultrasonic beam models and flaw response models in isotropic or non-isotropic materials. While UltraVision (UV) cannot generate flaw response models, it is a data acquisition and analysis tool that includes a beam modeling capability through isotropic materials only.

In commercial nuclear nondestructive examination/evaluation (NDE), models can be used to inform examination procedures, assess beam coverage, predict flaw detection, inform probe and mockup design, and ultimately save time, money, and resources. However, models cannot be used to imitate human factors or equipment limitations, replace empirical measurements, definitively predict beam coverage through complex materials or geometries, or predict unanticipated noise sources, spurious signals, or sources of uncertainty. While the use of NDE modeling and simulation continues to grow, some limited evaluations of strengths and weaknesses of specific modeling tools have been conducted (Cinquin et al. 2007; Bannouf et al. 2014; Chatillon et al. 2015; Holmer et al. 2017). Modeling and simulation limitations must be well understood to effectively and appropriately interpret results. In addition, to ensure confidence in simulations, modeling results must be validated experimentally.

The NRC has identified an assessment of the utility and limitations of modeling and simulation tools as a technical area of focus for confirmatory research. The Office of Nuclear Regulatory Research (RES) initiated a task for PNNL to address these issues. PNNL was directed to assess the modeling and simulation tools currently used for ultrasonic testing (UT), in particular CIVA and UV, using a multi-faceted approach that included:

1. Modeling various component/material/flaw configurations to simulate beam models and flaw signal responses and then conduct laboratory studies to compare and validate the model results; and
2. Identifying and documenting gaps where the models fail to provide effective and reliable results.

This activity was defined as a multi-phased technical effort whereby the research would be sequentially conducted by addressing lesser challenging scenarios first and eventually evaluating more complex scenarios as the work evolved. Each phase of the work includes increasing levels of complexity in terms of material properties and flaw morphologies. In addition, each phase incorporates techniques for the analysis of simulation outputs, in terms of characterizing simulation uncertainty, required noise levels, and interpretation of results for determining inspection effectiveness. The various scenarios evaluated include:

- Simple, machined reflectors such as electro-discharge machined (EDM) notches in fine-grained, homogeneous, isotropic materials, such as wrought stainless steel (WSS), to assess baseline model variability.
- The aforementioned materials using more complex reflectors, where flaws exhibit more realistic morphologies such as thermal fatigue or stress corrosion cracks.
- The evaluation of inspection models using a combination of realistic flaw morphologies coupled with coarse-grained base materials such as cast austenitic stainless steel (CASS) with austenitic welds or dissimilar metal welds (DMWs).

Dib et al. 2017 presented the results of a study with respect to the first bullet above. It was determined, in part, that the procedures used for defining a model have a significant effect on the model's output, which may have a large uncertainty associated with indeterminate or unknown input parameters. The next phase of the work (Dib et al. 2018a) evaluated the effectiveness of beam models with respect to quantifying volumetric coverage and flaw detection capability using thermal fatigue cracks and machined flaws (saw-cut reflectors), i.e., second bullet above. The current report discusses the results from the evaluation of coarse-grained materials and their associated welds (third bullet above). Planned stages of this research will consider the additional uncertainties of noise, attenuation, and scattering. Other confounding factors arise from flaw morphology, challenging weld geometries, and complex material properties/microstructures.

## 1.2 Motivation for the Current Work

The driving factor for this work arose when NRR requested that RES initiate a task to validate nuclear industry activities with respect to ultrasonic modeling and simulation. As the nuclear industry begins to rely more heavily on ultrasonic modeling and simulation as a basis to demonstrate that the examination techniques applied are acceptable, the NRC identified the need to confirm that a solid technical basis exists for conducting, interpreting, and applying the results of ultrasonic modeling.

PNNL has previous experience in employing acoustic modeling and simulation to support NRR in evaluating NDE-related events at operating nuclear power plants (NPPs) and licensee requests for alternative examinations (PNNL 2013c, b, a). Thus, the NRC tasked PNNL with conducting assessments of advanced NDE techniques coupled with theoretical modeling and simulation in order to evaluate signal responses caused by varied microstructures and challenging component geometries. In addition, PNNL was tasked with analyzing and understanding these results and identifying issues to the NRC that should be addressed by the industry to ensure examination reliability and effectiveness. For example, simulations may indicate that 100% of a volume of interest will have coverage, when in actuality beam redirection or partitioning results in some portion of the volume not being insonified. By enhancing their understanding of a model's limitations and key parameters, the NRC will be better equipped to assess simulated predictions of beam coverage.

### 1.3 Scope and Objectives

The goal of this confirmatory research is to provide the NRC with a solid technical basis for conducting, interpreting, and applying ultrasonic modeling to assess the effectiveness of ultrasonic inspections of NPP components. As this work progresses, PNNL is tasked with documenting results in a series of TLRs and a NUREG/CR. These documents, and the associated body of work, will eventually be used to develop guidance and best practices for modeling specific ultrasonic examination scenarios in a more uniform, relevant, and effective fashion. The final deliverable for this multi-year, multi-phased effort will be the development of a framework for a new Regulatory Guide focused on effective use of modeling and simulation tools to support UT examinations of NPP components.

The scope of this work includes a thorough and rigorous evaluation of modeling and simulation tools (specifically CIVA and UltraVision) to determine their potential usefulness for nuclear NDE and better understand their strengths and weaknesses. This work will:

- Determine the sensitivity of simulated flaw amplitudes to model parameter uncertainties
- Quantify sound field and flaw response amplitudes as a function of parameters that may influence ultrasonic amplitudes
- Create metrics for comparing simulation and experimental results when calibration signals are not available
- Identify key variables in typical simulation models that influence coverage extent and flaw detection capability
- Generate accurate models of coarse-grained materials and grain orientations
- Evaluate the accuracy and usefulness of CIVA beam simulations and flaw response simulations through complex grain structures, such as austenitic welds, DMWs, and coarse-grained CASS materials.

### 1.4 Brief Summary of Previous Work

The initial technical evaluation was designed as a basic verification and validation study aimed at CIVA, a semi-analytical modeling software package for simulating UT sound fields and signal responses. In 2016 and 2017, PNNL studied signal responses from simple, machined reflectors (EDM notches) in stainless steel (SS) plates using an array of different conventional<sup>(a)</sup> ultrasonic probes (Dib et al. 2016). Hundreds of empirical data sets were acquired and subsequently modeled. The approach provided a platform for assessing notches of various sizes and orientations, while obtaining UT data using different frequencies, wave modes, refraction angles, and probe dimensions/characteristics. Parametric studies were conducted to isolate, assess, and rank the impact on simulation results of essential variables and inputs to CIVA. This work also focused on developing a better understanding of how CIVA's specific computational models and physics engines performed when certain approximations and assumptions were used. During this initial phase of the work, a numerical example using the Kirchhoff model was

---

(a) Conventional probes are defined as single- or dual-element, pulse-echo or transmit-receive probe configurations operating at frequencies at or above 1.0 megahertz (MHz). The conventional designation, as used here, is meant to associate ultrasonic sound fields propagated in an ordinary manner; that is, having a "dead zone" in the near field with more linear beam characteristics (such as a reduction of sound field intensity and beam divergence) in the far field. Conventional probes are typically designed to generate a sound field at a single fixed angle.

provided to better understand and describe potential simulation inaccuracies resulting from a set of approximations and assumptions.

The approach to this early work was predicated upon a two-step analytical approach for conducting the verification and validation of the simulated CIVA results. A qualitative analysis was performed first, and then a more rigorous, quantitative/probabilistic analysis was conducted. For the latter, a set of metrics was defined and applied to the data and the simulation results to more effectively account for sources of uncertainty in measurements and model inputs. This validation yielded the following conclusion (Dib et al. 2017):

“The procedures used for defining a model have significant effect on the model’s output. Although models are useful for providing insight and visualizing wave fields, there is no evidence that models can be used to replace experiments in applications that require quantification of amplitudes. This is because there is a large uncertainty in the model’s output associated with uncertain, and in some cases unknown, input parameters, and uncertainty and biases in experimental procedures.”

In addition, this work led to many new, unanswered questions and slowly began to shed light on the strengths and limitations of CIVA and under what conditions this modeling tool might be effectively used to provide accurate and representative simulation results for NPP applications.

Efforts continued in 2017 and 2018, focused on evaluating the effectiveness of beam models (transmit-only sound field simulations) for use in quantifying volumetric coverage and flaw detection capability, including identifying key variables that impact these simulations (Dib et al. 2018b). During this phase of the work, a portion of the evaluation focused on assessing the level of variability one might experience when employing two different, but commonly used, beam simulation tools. A study was designed to compute beam profiles in isotropic, homogeneous materials using UV and CIVA and to identify differences between the two platforms. The study evaluated a total of 23 different probes, including single-element shear-wave probes and dual-element transmit-receive longitudinal (TRL) probes. While sound beam structures were qualitatively similar, in 22 out of the 23 probes assessed, CIVA simulations resulted in larger relative beam amplitudes at the backwall than those generated with UV. In addition, both CIVA and UV results indicated larger differences in backwall amplitudes for shear-wave probes in contrast to longitudinal-wave probes.

At this stage, it was necessary to better understand the impact of introducing an austenitic weld or other anisotropic, inhomogeneous material into the path of the propagating sound field. As results from the more simplistic scenarios were obtained, additional questions began to arise, requiring further study. Can CIVA accurately model the effects of welds, complex component geometries, and microstructures in a realistic manner? Will the level of simulation accuracy be sufficient to confidently inform the end-user about insonification volume or flaw detectability? In order to begin to address these questions, a study was conducted to obtain empirical data and physically map out sound fields as they propagated through austenitic welds. In addition, it was determined that the Ogilvy weld parameterization model (included with CIVA) would be used to represent granular structure of the well-characterized austenitic welds. Simulated sound fields were then generated and compared with the measured beam profiles through these welds.

Differences were noted from the analysis of simulations versus empirically-obtained data. Generally, simulated sound fields over-estimated the relative sound beam amplitudes at the specimen backwall. Additionally, the relative beam dimensions of simulated sound fields were

over-sized. These differences were even more significant with higher beam angles. Overall, factors contributing to the differences between simulation and experimental beam models were summarized from Dib et al. (2018a) as follows:

1. No attenuation was considered in the simulations, which might be of high significance for ultrasound propagation in austenitic welds.
2. The weld geometry and microstructure definitions were obtained from the macrographs but were approximated by the Ogilvy model.
3. The material properties of the weld regions were not measured and were taken from the literature. The uncertainties in the stiffness matrix elements and Euler angles is another factor contributing to simulation uncertainties.

While beam models can provide a means to visualize a transmitted sound field through a material, other potential uses include determining the volume of insonification coverage and flaw detectability with a given probe. To address these issues, additional studies were conducted to determine if beam models could be used as surrogates for flaw response models to inform the end-user about flaw detectability. Three metrics were developed to support this assessment: a total beam amplitude metric, the flaw backscatter amplitude (or the specularly-reflected signal from a flaw), and the beam amplitude at the backwall. This effort provided a better understanding of the perils of using beam models as surrogates for flaw detection or for effectively estimating volumetric ultrasonic coverage. Some of the key findings and conclusions from this most recent report included (Dib et al. 2018a):

- Beam amplitudes (relative or absolute) incident on a flaw do not appear to be an informative measure of flaw response or detection reliability. Interpretation of beam simulation results, in terms of flaw detection capability and accurate estimation of coverage, are particularly challenging.
- The probe position that optimizes flaw response for detection may not correlate with the probe position for maximal beam insonification of the flaw. This holds true under limited coverage conditions where the probe is constrained from full translation during an examination.
- Beam simulations in the vicinity of welds are not predictive, and additional material property information, such as weld microstructure, would be required.

Another area of investigation included an initial analysis of flaw response models in and through welds, including the study of both near- and far-side examination scenarios. A comparative analysis was conducted with empirical ultrasonic data. During this stage of the work, only the Ogilvy model was examined, and noise, clutter, and attenuative factors were not simulated. Results showed that flaw specular amplitudes were about 20 dB (10×) different between simulations and experiment for shear-wave probes and about 13 dB (2.5×) for longitudinal-wave probes (phased array [PA] and conventional TRL). A number of potential factors and conditions were discussed in Dib et al. (2018a) that might account for these large discrepancies between simulation and experiment.

From the parametric studies conducted earlier and reported in Dib et al. (2017), it became readily apparent that CIVA simulation results were highly dependent upon the input parameter values chosen for running a model. In order to more effectively quantify uncertainty in CIVA simulation results, another assessment was identified to better understand the impact of variability of the transducer parameters. The idea was to evaluate the variability in performance characteristics of a set of nominally identical transducers and the consequences such variability

would have on simulations. For this work, a set of ten contact transducers was gathered, all with essentially the same design and performance specifications but fabricated by various manufacturers. The set consisted of 12.7 mm (0.5 in.) diameter, circular element contact probes, with a nominal center frequency of 5.0 MHz and  $-6$  dB bandwidths of approximately 60%. Nominal probe design specifications were used as inputs to CIVA to generate beam simulations, and sound field metrics were then calculated from the simulation results. In addition, each transducer was rigorously characterized in the laboratory, and the empirically-derived characterization data were then compared against the CIVA simulations. A few key takeaways were noted in Dib et al. (2018a):

- Using nominal transducer specifications (either noted on the probe or from a vendor-provided specification sheet) as input to CIVA could result in simulation results that do not accurately reflect probe performance.
- The cumulative impact of probe performance variability on flaw detection reliability will depend on the flaw size and location relative to the probe and will need to be quantified using simulation or empirical means.
- Measured variability of transducer specifications can be used to set bounds for particular parameters for modeling; however, these bounds may need to be refined by determining if variation of a particular parameter causes performance deviations exceeding the essential variable tolerance as described in Section XI of the American Society of Mechanical Engineers Boiler and Pressure Vessel Code.

The work documented and summarized in this TLR addresses remaining issues from previous work and will shed light on new questions as they arise, including planned next steps in modeling and simulation research.

Note that all the simulations described herein and all of the CIVA-specific issues that are discussed refer to the 2017 version of CIVA. CIVA 2020 was released after all the work for this report was completed. PNNL intends to use and evaluate CIVA 2020.

## 1.5 Report Organization

Section 2.0 of this TLR provides an overview of the quantitative metrics developed and used for comparisons and analyses reported throughout the document. This includes A- and B-scan representations of flaw responses and beam profiles, as well as image similarity metrics. Section 3.0 provides a discussion of the utility of CIVA and addresses some pertinent issues associated with how wavefront interactions are modeled, how focal laws are handled, how attenuation is modeled, and a host of other CIVA usability attributes. Section 4.0 describes acquisition of experimental beam maps through an austenitic WSS-WSS weld and CASS-carbon steel (CS) DMW. Section 5.0 describes results from beam modeling and flaw response simulations with an austenitic weld model using the CIVA built-in Ogilvy model and using empirically-derived weld geometries from electron backscatter diffraction (EBSD) data. In addition, this section describes results of crack/notch simulations, key factors and considerations that influence these simulations, and weld modeling assessments using accurate true-state inputs. Section 6.0 provides results from simulations of using DMW model. Section 7.0 describes beam simulations in coarse-grained CASS materials using a realistic microstructural representation as well as Voronoi regions. Section 8.0 provides a summary and conclusions from the work and describes ongoing and planned future research in this technical area. Finally, Section 9.0 lists references cited in the TLR. The appendices address some technical aspects, such as computational specifications, CIVA usability tips, brief descriptions of

references used to inform model inputs in Section 5.0, and instructions on how to convert conventional Euler angles into the CIVA reference frame. As discussed in the Summary, this report lays the groundwork for answering important questions using modeling and simulation. In establishing this groundwork, several new workflows were developed. Appendix A contains descriptions of several of the key workflows described and used throughout report.

## 2.0 Quantitative Metrics

### 2.1 Introduction

This section describes metrics that were developed for the purpose of making meaningful, quantitative comparisons between different simulation results and between simulation results and empirical results. Ideally, such comparisons are accomplished by using a consistent calibration signal, such as the echo from a side-drilled hole, that can be normalized across platforms. However, calibration signals are often not available, so other approaches must be explored. Also, calibration signals are not well suited for comparing sound scatter patterns, and visual comparisons are subjective and often inadequate. In this section, an option for quantitatively comparing echo responses is presented. It is based on calculating the sound energy in an echo as a fraction of the total sound energy detected. The metric was developed in 1D for A-scans, then it was expanded to 2D B-scans. Additionally, metrics are presented that can be used to determine the similarity between images. These image similarity metrics can be useful, for example, to compare simulation results when model parameters are varied or to compare simulations to empirical scans.

Figure 2.1 illustrates the synergy between experiment and simulation and the role of comparative metrics. In order to determine whether a model is producing simulation results that adequately predict reality, the simulation and empirical outcomes need to be compared. Such a comparison can be as simple as a qualitative, visual observation, but quantitative comparisons are more rigorous, more objective, and can be better used to justify conclusions. After comparisons are made, and depending on the goals of the work, the results can be used to determine whether the model inputs need to be adjusted and/or whether the experimental approach needs to be altered. This feedback loop allows for parameters to be changed in a controlled and informed manner. Finally, conclusions can be drawn.

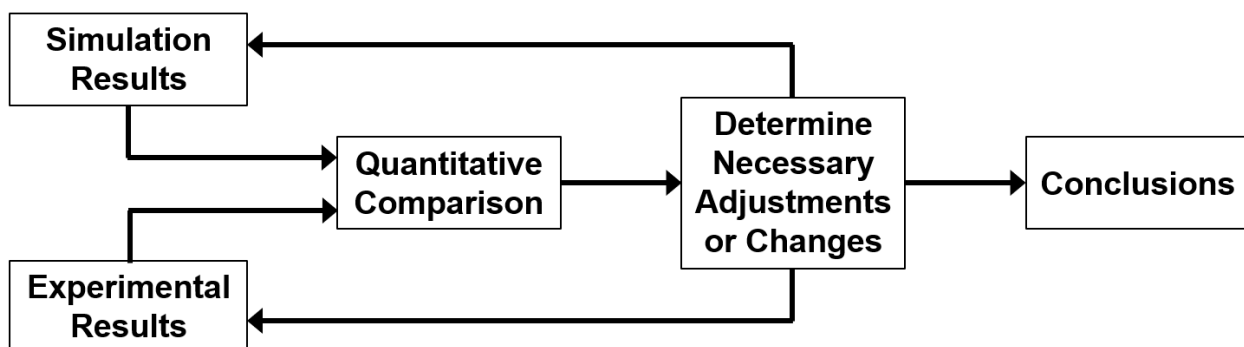


Figure 2.1. The process of comparing simulation and experimental outputs should involve quantitative comparison and informed feedback so that justifiable conclusions can be drawn.

The metrics described in this section are not intended to be exclusive; additional methods may prove useful for quantitative comparisons. Although some of the metrics shown will not be applied in this report, they were developed to lay the foundation for future analyses.

## 2.2 Quantitative Metric for A-scan Comparisons

A-scans can be simulated in situations where adjustments are being made iteratively to model inputs but simulating a full line scan (comprising multiple A-scans) for each iteration may be too time consuming. A metric is necessary for making quantitative comparisons of a flaw's echo response in A-scans under different simulated or experimental conditions. One method is to simply measure the height of the A-scan peak. This is often an adequate estimation of the sound energy of the peak, but such an approach can sometimes lead to incorrect results. A more rigorous approach is to calculate the area of the peak as a surrogate measure of the total sound energy returned to the probe by a particular flaw (Dib et al. 2018a). However, in cases where the probe parameters are not normalized—when different amounts of energy are deposited into the specimen—calculating the absolute area of the peaks is insufficient. For example, if probe one is emitting twice as much energy as probe two, it is reasonable to expect that the echo responses will be weaker with probe two, regardless of other conditions in the specimen. In such cases, calculating the *fraction* of the total received sound energy that is returned by the flaw of interest is more informative. This essentially normalizes the flaw responses and allows for comparison across different probes and experiments.

Figure 2.2 (left) shows an example of a simulated A-scan obtained from a CIVA simulation of a flaw response (the details of the simulation are not important here, only the fact that multiple echoes in an A-scan were the result), and Figure 2.2 (right) shows an example of the envelope of the rectified A-scan. The envelope is used to calculate the area of the peaks.

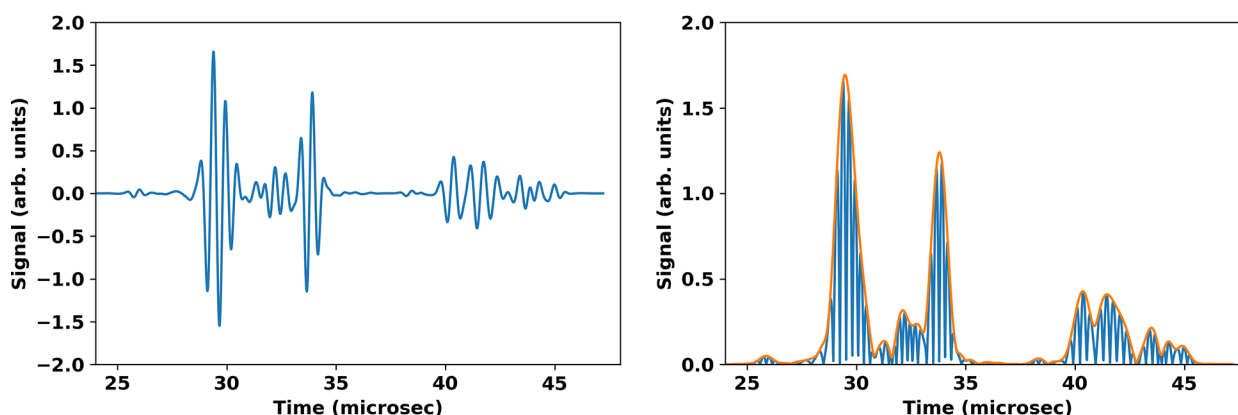


Figure 2.2. Simulated A-scan (left) and rectified A-scan (right) with envelope (orange line).

One key issue in calculating peak areas in A-scans is determining where to set the limits of integration. For example, it is typically straightforward to identify peaks at, say, 50% of their height. Perhaps using points at 10% of the peak height, thereby including more of the overall peak, would be more accurate, but defining these limits is challenging if the peaks are not well separated or if there is substantial noise. A Python script was written to import the A-scans and automatically identify the peaks. The left panel of Figure 2.3 shows red and green markers indicating the 50% of peak height levels for the two peaks, while the right panel shows markers at the 10% levels. The left peak is well isolated, so the 10% peak height locations can be used as integration limits because they do not include adjacent peaks (indicated by the red arrow). However, the right peak is not well isolated, so the 10% peak height markers actually include adjacent peaks, which may be echoes from different reflectors. Thus, the integral would also include these other reflectors and would not be accurate. In situations where the peaks are closely spaced with significant overlap, it would be very difficult to find a level suitable for

integration. One can iterate through the problem to optimize the integration limits on a case-by-case basis, but this would be time-consuming and inconsistent from simulation to simulation. To provide a general solution to this problem, the peaks were fit to Gaussian curves that were then integrated. Figure 2.4 shows the Gaussian fits to the two peaks with the original A-scan envelope included as a dotted line. The fit uncertainties are extremely small, indicating that the peaks can be well approximated by Gaussian curves. Then, finding the area of each peak becomes a simple matter of integrating each Gaussian function independently. This method is desirable because a low-uncertainty Gaussian fit to such curves can typically be obtained even if the peaks overlap substantially, although as the overlap increases the level of fit uncertainty also increases.

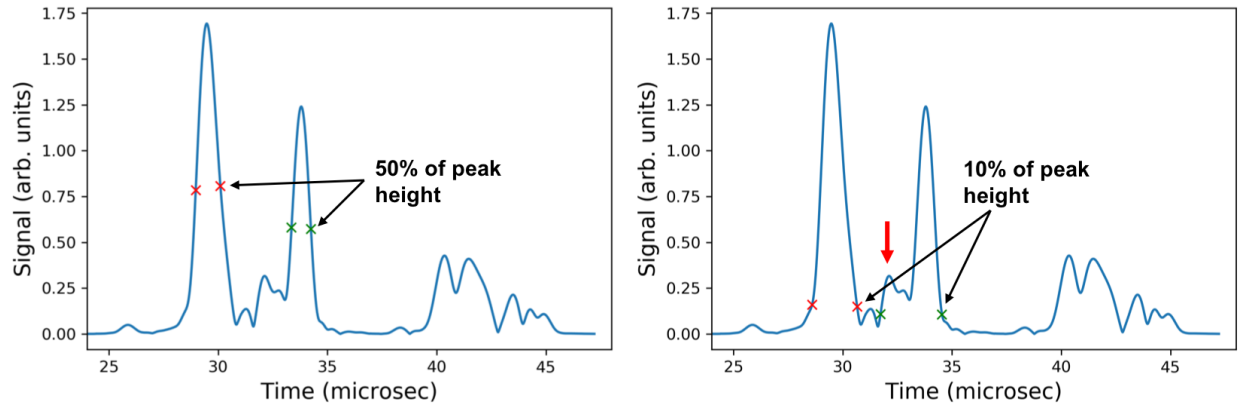


Figure 2.3. An example of a rectified A-scan envelope with two main peaks. The 50% of maximum peak height (*left*) and 10% of maximum peak height (*right*) are identified. The 10% peak height of the right peak (green x's) encompass smaller, neighboring peaks.

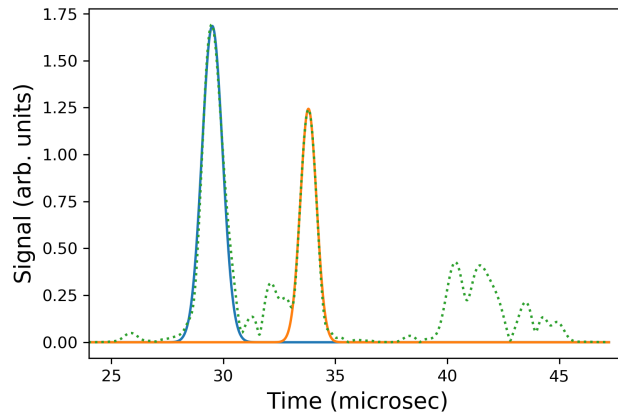


Figure 2.4. Gaussian curve fits (blue and yellow lines) to the two main peaks of the A-scan envelope (dotted line).

Calculating the area under each peak is not sufficient for comparisons across different simulations or with experimental results because of different transducer efficiencies and other issues. Therefore, a normalization process can be used by measuring the total detected signal and calculating the fraction of the total for each peak. To do this, integrate the entire A-scan and the individual peaks of interest, then take the ratio of the peak energy to the total energy. For the example shown in Figure 2.4, the fraction of total energy in Peak 1 (leftmost peak) is 0.40

and in Peak 2 is 0.23. In other words, 40% of the total detected sound energy was from Peak 1 and 23% was from Peak 2. The ratio of these is 1.74 (that is, Peak 1 returned 74% more energy than Peak 2). For comparison, the peak heights were measured. In this example, the peak heights are 1.69 and 1.24 (in arbitrary units). The ratio of these is 1.36 (that is, Peak 1 is 36% higher than Peak 2). Therefore, the integration of the peaks provides a significantly different metric of signal response than simply measuring peak heights, and the normalized integration provides a means by which simulations (and experimental results) can be compared to one another. Measurement of peak heights, on the other hand, does not provide a basis for comparison.

An example of the importance of peak integration versus peak heights is shown in Figure 2.5. In the left panel, the blue line is the raw data, the orange line is the data envelope, and the green dots identify the peak positions as detected by the Python script. The right panel shows the Gaussian fits (the envelope is shown with the dotted line). The first and third peaks from the left have maximum heights of 1.54 and 2.17 (arbitrary units), respectively. However, the integrals of the two peaks are 2.24 and 2.09, respectively. This example shows a case where one peak is much higher than another peak but has a *lower* integrated sound energy.

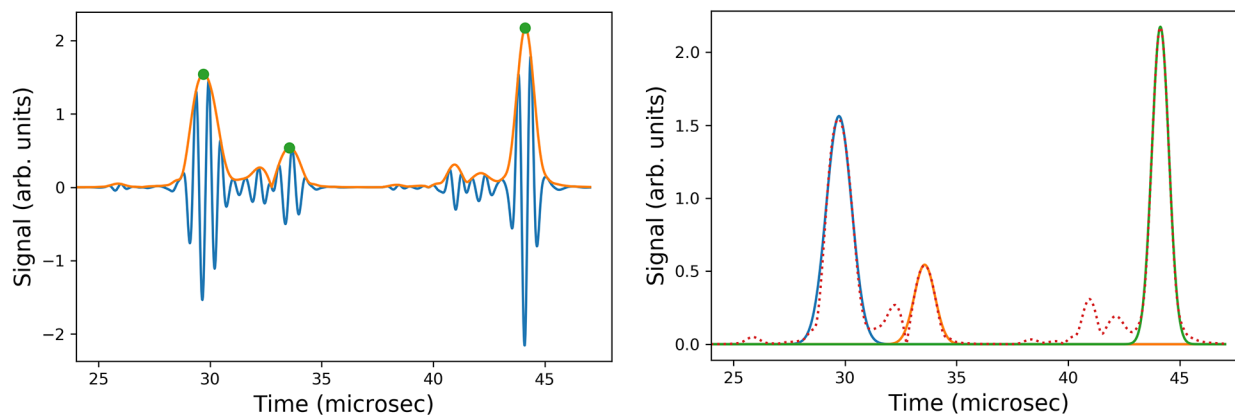


Figure 2.5. *Left:* A-scan (blue line) and envelope (orange line) with three peaks identified (green dots). *Right:* A-scan envelope (dashed line) with Gaussian fits to the three peaks (solid lines). The rightmost peak is highest, but the leftmost peak has the largest integral.

The peak integration method works well with overlapping peaks, as long as each peak is distinguishable and can be fit to a Gaussian curve. The left panel of Figure 2.6 shows an example of an A-scan where the peaks overlap. The right panel shows the Gaussian fits, which clearly separate the two peaks, allowing for integration of each individual peak.

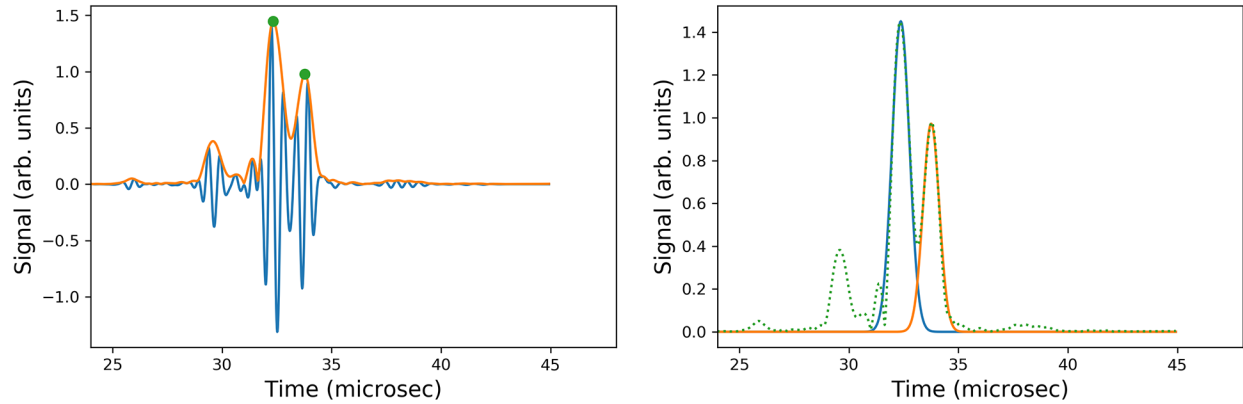


Figure 2.6. *Left:* A-scan (blue line) and envelope (orange line) with two prominent overlapping peaks (green dots). *Right:* Gaussian fits of each peak. The individual fits to the peaks allow for the peaks to be integrated independently.

### 2.3 Quantitative Metric for B-scan Comparisons

The method for comparing 1D A-scans was extended to 2D B-scans so that the flaw responses in line scans can be compared. Although the B-scan metric was not used in this report, work to develop it builds the foundation for future work. For B-scans, the ratio of the peak integral to the integral of the entire B-scan will serve as a metric for direct comparison of simulated and experimental results when a calibration signal is not available. An illustration of the approach is shown in Figure 2.7. Figure 2.7(a) shows a B-scan of a weld region with a crack near the weld. Figure 2.7(b) shows a surface plot of the same data with the peak heights proportional to their intensity. Figure 2.7(c) shows the same surface plot, but with a mask applied so that only the peak from the flaw of interest is visible. In summary, the method should isolate the peak of interest, integrate it, and find the fraction of the total received signal that was contained within that peak. In other words, the method should calculate the total signal of the flaw response shown in Figure 2.7(c) and divide by the total signal of the entire scan shown in Figure 2.7(b).

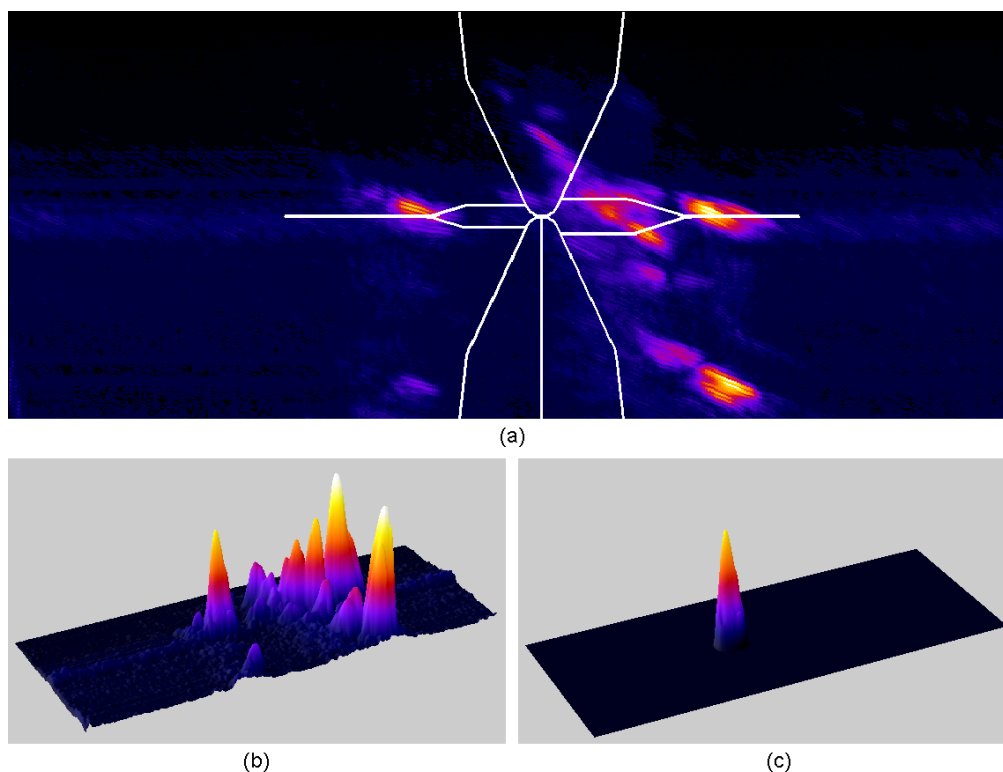


Figure 2.7. Example of isolating a peak in a B-scan for analysis. A: Original B-scan with weld overlay. B: Surface plot of the B-scan with all peaks shown. C: Surface plot of the B-scan with a mask applied to all peaks except for the peak of interest.

The process outlined above is not trivial because it is complicated by the fact that the 2D peaks are difficult to bound or isolate because they do not have a predictable shape. Also, the peaks are not oriented perpendicular with respect to the axes. Therefore, a new method was developed in Python.

The method for the 2D integration is as follows:

1. The user defines the peak of interest by identifying two points along the peak length in the 2D image. Currently, this is done by identifying the coordinates in an image analysis application such as ImageJ<sup>(a)</sup> (Schneider et al. 2012), although this process could be implemented in a graphic user interface if necessary. The user also identifies an approximate peak width (along the short axis of the peak) for the software to use as an initial guess in the fitting process.
2. An initial, constrained Gaussian fit is performed on the identified peak. This is an iterative process to find the x,y location, x,y width and height, and rotation angle of the peak using the Levenberg-Marquardt least squares algorithm.
3. The fit is used to generate a mask for the peak. This isolates the peak to remove any potential background noise or neighboring peaks from the fit.
4. The masked image is used to perform a second, more accurate Gaussian fit, which gives the final result.

(a) ImageJ is a Java-based image analysis software available for free at <https://imagej.nih.gov/ij/>.

An illustration of how this metric was developed and an example of how it can be applied to experimental data is shown in Appendix B.

## 2.4 Image Similarity Metrics

It is often desirable to make comparisons between different simulation outputs or between simulations and empirical results. Comparisons are typically done by visually inspecting the resulting images and making qualitative comparisons between, for example, spatial variations in signal intensity or absolute and relative locations of echoes. In previous modeling and simulation work, comparisons between images of beam simulations and beam-mapping data have been largely qualitative (Dib et al. 2018a; EPRI 2018). Indeed, in many cases, visual inspection is adequate to draw conclusions about differences in results because the differences are obvious to the casual viewer. For example, Figure 2.8 shows the results of two flaw response simulations in which the specimen echo response models were different (Specular [left] and Kirchhoff [right]) but all other model parameters were identical. There is little question that the results differ dramatically, as the echo patterns are not similar. Conversely, in other cases, visual inspection can easily miss subtle differences between images. For example, Figure 2.9 shows the results of two CIVA coarse-grained beam simulations that have different accuracy factors (Accuracy=4 [left], Accuracy=64 [right]). The accuracy factor essentially determines the fineness of the mesh CIVA uses in the simulation calculations. A mesh is a subdivision of the model geometries into cells or elements, such as triangles or squares, which simplifies the geometry into individual units for computational purposes. The mesh should be fine enough to accurately describe the geometry but not so fine that the simulation times become impractically long. In this case, the images in Figure 2.9 are virtually identical except for some signal intensity variations in several of the pixels. In order to objectively determine which image is more similar to an ideal benchmark (e.g., a case with the optimal accuracy factor), a quantitative metric is required.

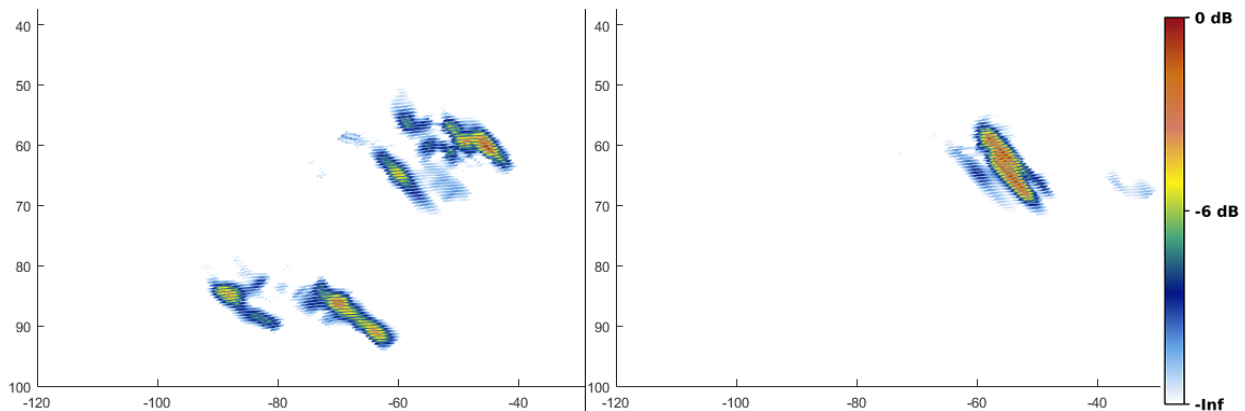


Figure 2.8. Example of two clearly different flaw response simulation results with nearly identical model input parameters. The only difference was the specimen interaction approximation (Specular [left] and Kirchhoff [right]).

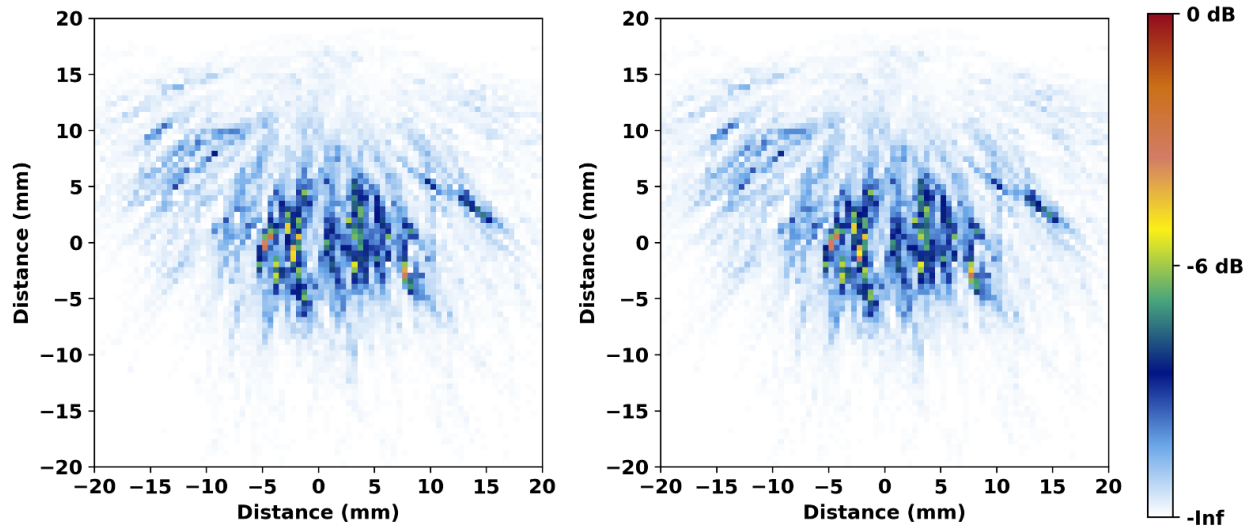


Figure 2.9. Example of two subtly different beam simulation results with nearly identical model input parameters. The only difference between simulation settings was the accuracy factor (accuracy = 4 [left], accuracy = 64 [right]).

There are multiple methods of quantifying image similarity that focus on different aspects of images, such as the effects of blurring, downsampling, contrast, signal intensity, and noise. Because different metrics are sensitive to different effects, selecting just one can be difficult. Therefore, three common metrics were chosen for this work: mean square error (MSE), structural similarity index (SSIM), and the Pearson correlation coefficient ( $\rho$ ). [ENREF\\_60](#) Wang et al. (2004) gave an in-depth description of MSE and SSIM, along with several examples using images with different types of distortions. Very briefly, MSE calculates the mean difference between images on a pixel-by-pixel basis. The SSIM was designed to detect changes in structural information that the human eye is sensitive to, referred to by Wang et al. as “perceived” changes, and does so through a sliding window moved across each image. Finally,  $\rho$  is the linear correlation between images performed on a pixel-by-pixel basis. Using the images shown in Figure 2.9, an example of  $\rho$  is shown in Figure 2.10 with the pixel values from the low accuracy (left) image on the y-axis and values from the high accuracy (right) image on the x-axis. Each dot represents a different pixel pair, and the red line shows the linear correlation between the two images. Individual dots that lie far from the line indicate dissimilar pixels, and if there were many dots far from the line it would indicate poor correlation.

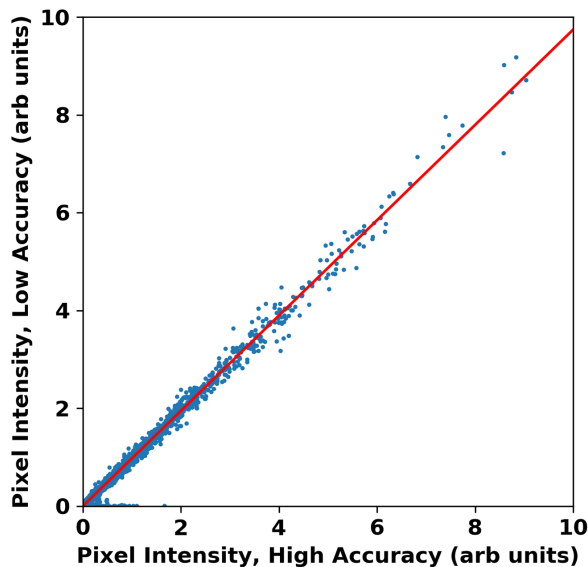


Figure 2.10. The correlation of the pixel intensities from the figures shown in Figure 2.9 on a pixel-by-pixel basis. The red line shows the linear least squares fit.

Table 2.1 summarizes the three metrics. These metrics show promise for comparing different beam simulations that may have differences in local beam intensity, beam scatter, and beam coverage. At this time, it does not appear that any one metric has a significant advantage over the other two for the applications described in this report, so all three will be considered. All three of the metrics have existing implementations in available Python libraries.

Table 2.1. Description of image similarity metrics

Name	Abbreviation	Description	Range
Mean Square Error	MSE	Measures a mean difference in pixel intensities, pixel-by-pixel across the entire image.	$MSE \geq 0$ ; 0 is perfect agreement
Structural Similarity Index <sup>(a)</sup>	SSIM	Accounts for differences in luminance, contrast, and texture to address perceived similarity; uses a sliding window across the image.	$-1 \leq SSIM \leq 1$ ; 1 is perfect agreement
Pearson Correlation Coefficient	$\rho$	Linear correlation of pixel values of one image versus those of a second image. Scatter plots can be generated to show the correlation.	$-1 \leq \rho \leq 1$ , 0 is no relationship, 1 is a perfect agreement, $-1$ is perfect negative agreement (such as an image compared to its inverse image)

(a) A comparison of SSIM and MSE, in addition to instructions for implementation in Python, is presented here: <https://www.pyimagesearch.com/2014/09/15/python-compare-two-images/>

For images that are perfectly identical,  $MSE=0$ ,  $SSIM=1$ , and  $p=1$ . For the images shown in Figure 2.9,  $MSE=0.006$ ,  $SSIM=0.967$ , and  $p=0.996$ . Thus, in this example, the similarity metrics suggest that there are very small differences between the images with Accuracy=4 versus Accuracy=64. Indeed, one may use the metrics to justify that the differences in simulation results are tolerable when weighed against the large increase in computation time for simulations with high accuracy factors. An example of such an application is shown in Section 7.2.

## 3.0 CIVA Usability

### 3.1 Introduction

CIVA (EXTENDE Inc.,<sup>(a)</sup> Norfolk, VA) has emerged as a leading commercial software package for simulating ultrasonic sound fields and flaw responses; cf. (Ginzel 2018; Hopkins et al. 2018; Sy et al. 2018; Hwang et al. 2019). As part of the scope of this project, PNNL has been evaluating the usability and features of CIVA so that NRC staff can be informed on matters of interpreting simulation results when such results are presented to them, for example, in relief requests or technical reports. It is important for both the users and those evaluating results to gain an appreciation of some of the default settings, common options, advanced features, and limitations of CIVA. For approximately the past year, a PNNL research scientist who had no previous experience with CIVA has documented several of the features and usability issues that he has encountered, including communications with EXTENDE support staff. The PNNL research scientist also participated in a week-long CIVA training course early in the year. This section addresses some of the issues encountered, but it is not intended to be an exhaustive review of CIVA. Appendix C addresses additional CIVA tips and potential pitfalls. Please note that the information contained herein is not intended to be a substitute for CIVA training materials; PNNL recommends that the novice user take advantage of EXTENDE resources when learning how to use CIVA.

### 3.2 Specimen Interaction Model

CIVA has two options for the type of model used to simulate the sound field interaction with the specimen surfaces: Specular and Kirchhoff. These options are available under the Specimen tab of the Interactions tab of the Simulation Settings tab. The default option is Specular, but this should only be used if the reflection from the specimen surface is expected to be mirror-like. Otherwise, one should select Kirchhoff. Users who do not understand the differences between the two models may be inclined to use the CIVA default settings. However, failure to select the correct model can have a dramatic effect on the simulation results.

To illustrate the difference between simulation results obtained with the Specular and Kirchhoff approximations, the weld geometry shown in Figure 3.1 was used in a flaw response simulation. The weld material was defined as Inconel and the base material as steel (using the default CIVA material properties) in order to provide some beam-interface interactions. The simulated B-scan results are shown in Figure 3.2, where the top panel is with the Specular model and the bottom is with the Kirchhoff model. The Kirchhoff model shows echoes that better map to geometrical features of counterbore (blue arrow), weld root (black arrow), and the flaw (red arrow). The Specular model, on the other hand, shows a flaw response (red arrow) and a menagerie of other echoes that do not appear to correspond to any geometrical features (encircled in red). The dramatic difference in results underscores the importance of understanding the model and selecting the correct specimen interaction model—in this case, the Kirchhoff model would be the more appropriate choice because the specimen backwall included geometrical features of counterbore and weld root.

---

(a) EXTENDE Inc. is a subsidiary of EXTENDE S.A., Massey, France.

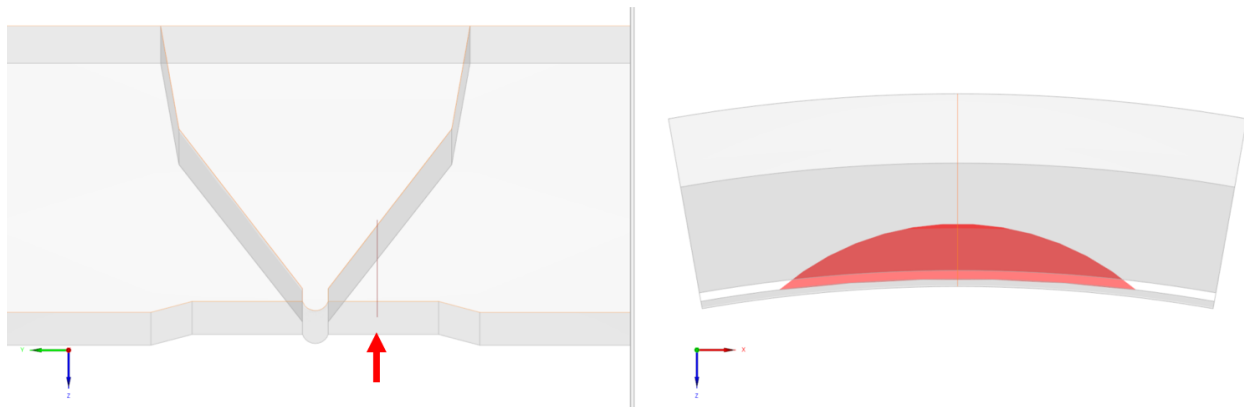


Figure 3.1. Weld geometry used for tests of Specular and Kirchhoff interaction models. *Left*: side view. The flaw position is indicated by the red arrow. *Right*: front view. The red region indicates a circumferential flaw.

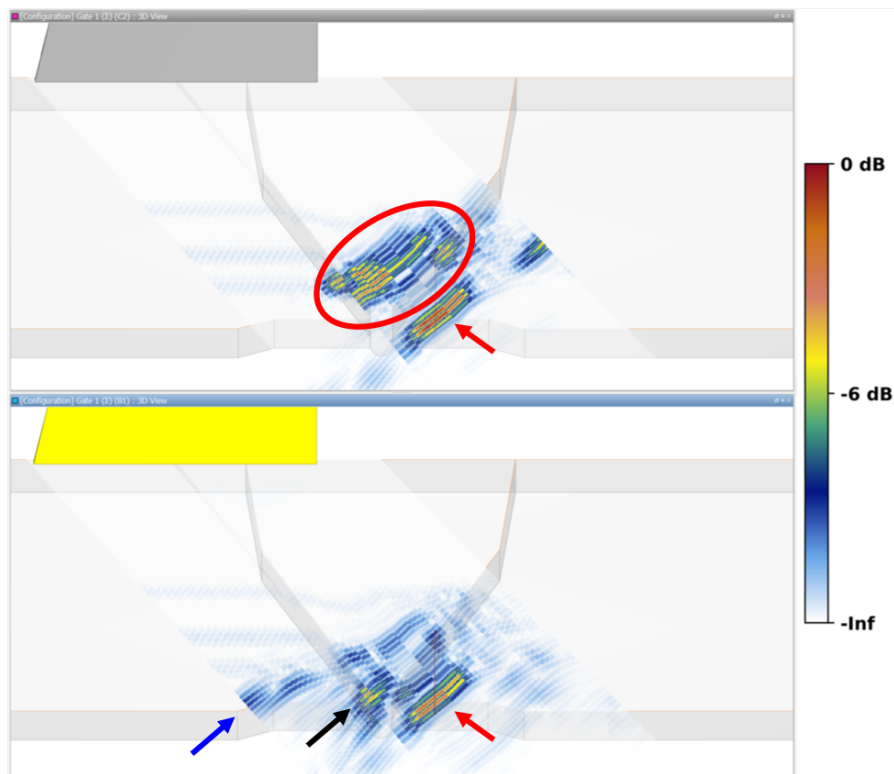


Figure 3.2. Simulation results using the Specular (*top*) and Kirchhoff (*bottom*) specimen interaction approximations. Red arrows indicate the flaw responses of the two simulations. The blue and black arrows indicate the counterbore and weld root responses, respectively. The red circle indicates unidentified echoes in the Specular approximation.

### 3.3 Adapted Focal Laws for Phased-Array Probes

When setting up a PA probe, CIVA requires that the focal laws be calculated and alerts the user to click the Compute button in the Array Settings tab. CIVA automatically computes “adapted” PA laws. That is, the PA focal laws are computed to adapt to the material properties in order to

provide the desired beam focal properties. This is important to keep in mind when performing simulations through non-isotropic welds or materials, because the PA laws will be adapted to whatever material the beam traversed when the focal laws were calculated. To provide some anisotropy for an example, an Ogilvy model was used to define the weld region (Ogilvy 1985); this model was described at some depth in the previous PNNL report (Dib et al. 2018a). Figure 3.3 illustrates beam simulations through the Ogilvy weld model with the focal laws calculated while the probe was situated over isotropic material (top panel) and over the weld (bottom panel); that is, with the focal laws not adapted to the weld and adapted, respectively. Results were normalized to the non-adapted case. The simulations resulted in significantly different sound fields.

In field examinations, focal laws are typically defined on a calibration block and are not adapted to any particular microstructure, because the specific microstructural characteristics of welds in the field are not known. For most simulations, the non-adapted case is a more representative scenario because adapted focal laws will not be calculated in the field. Therefore, when modeling PA probes in CIVA, it is important to calculate the PA laws with the probe completely off of the weld on an isotropic section of the specimen or on a separate isotropic specimen. Fortunately, CIVA allows users to save PA settings to a separate xml file that can be imported into a model; thus, a user is able to set focal laws on an isotropic geometry and then use the same focal laws for multiple simulations by loading the xml file parameters. After loading the PA laws, the user should ignore any notices to recalculate the laws.

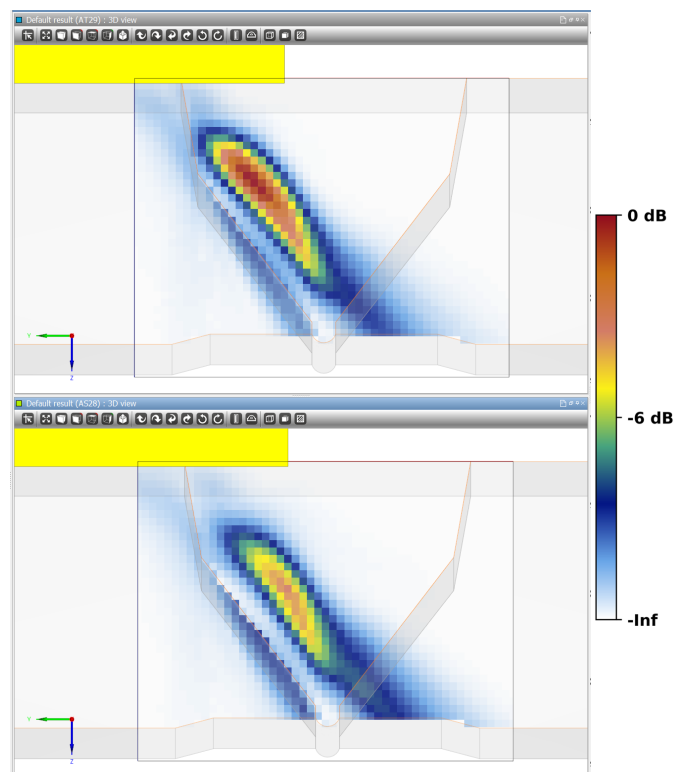


Figure 3.3. Phased-array beam simulations through an Ogilvy weld model. *Top*: Non-adapted focal laws. *Bottom*: Adapted focal laws.

### 3.4 CIVA Metamodels

The 2017 version of CIVA introduced a new metamodel and probability of detection capability, a statistics-based interpolation tool that allows for more complete parametric studies (Ribay et al. 2016; Foucher et al. 2018). Metamodels provide a method of studying how parameters influence simulation outputs and the interdependence of parameters without having to simulate every possible parameter permutation. This promises to help answer key questions, such as how sensitive CIVA is to uncertainties in model input parameters, in a time-saving manner. PNNL team members began to familiarize themselves with the metamodels tool by exploring how the models responded to variation<sup>(a)</sup> inputs of single-element probe parameters. This was done using the measured variability of probe parameters of the 10 single-element probes studied in Chapter 7 of PNNL’s previous modeling and simulation report (Dib et al. 2018a).

Using the nominal and measured values of the probes, a metamodel simulation was run to detect a flaw response of 45° L-waves transmitted through a simple, homogeneous weld geometry. Four simulation parameters were included in the variation: probe bandwidth, phase, diameter (or aperture), and center frequency. The nominal and minimum/maximum values were taken from the measured values in the report. The parent material was defined as steel and the weld as homogeneous Inconel. Figure 3.4 shows a simple ray drawing of the simulation setup, including L-wave interface and backwall reflections. Figure 3.5 shows a CIVA screenshot of the four input parameters of the variation, including their minimum and maximum values. In this case, each parameter was incremented such that there were five evenly-spaced values within each range (this is not shown in the figure). Ideally, for a complete model, one would perform simulations for every possible combination of input variables—625 combinations in this case—but this can be extremely time-consuming. With type “Metamodel” selected, the user can choose the number of combinations, or samples, for CIVA to perform. Here, the key advantage of the metamodel approach is manifest in that the user can have CIVA perform a subset of the total permutations and CIVA can interpolate the rest. In this example, 250 iterations were performed.

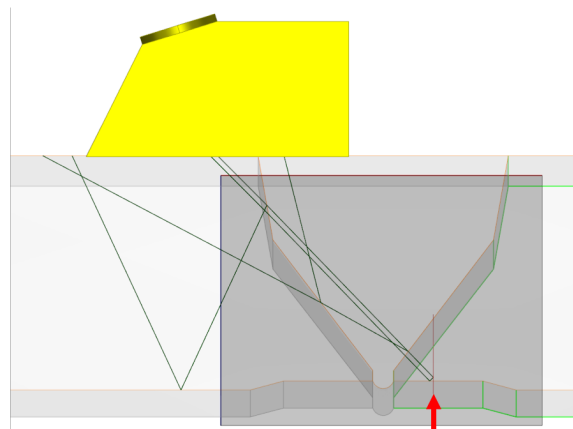


Figure 3.4. Probe and specimen weld profile configuration for metamodel tests. The green lines indicate the L-wave path, including the reflected beam from the flaw (red arrow) and the reflected and refracted beams from the weld interface.

(a) A “variation” is CIVA’s method of allowing the user to perform a parametric study. A set of values for a parameter can be entered and CIVA will compute a simulation for each parameter value and save the result in a single “.var” file.

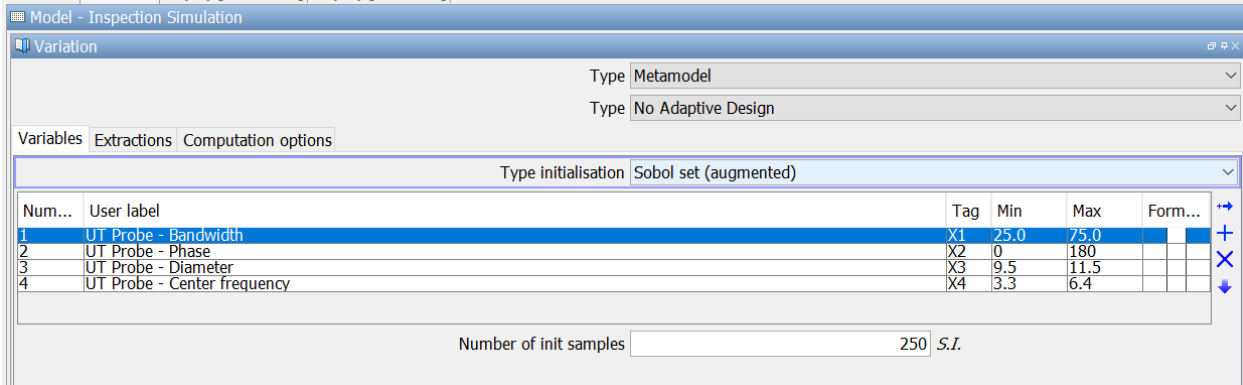


Figure 3.5. Parameters used to define the ranges of the four variables in the metamodel.

CIVA provides an array of output information after the metamodel simulations are complete. Examples will be shown here. Additional examples of the output information are also shown in a recent paper published by the EXTENDE team (Foucher et al. 2018). First is a “parallel plot” that shows the relationships between the different parameters used to build the metamodel; see Figure 3.6. This type of plot is also referred to as a “cobweb” plot (Ribay et al. 2016). Cobweb plots can be used to visualize general trends in relationships between input variables and output values. For example, the plot in Figure 3.6 (top) shows the relationship between the probe parameters of bandwidth, phase, diameter, and center frequency (shown on the four vertical lines from the left) and also the output values (shown on the rightmost vertical line). The pink lines that form the “cobweb” show the connections between the different parameters for each simulation run. Figure 3.6 (top) appears to convey little useful information at first glance. However, the user can further investigate how parameters are interrelated by selecting a subset of the parameter values. For example, Figure 3.6 (bottom) shows a filter applied to the output values (rightmost line) so that only the highest values are selected (yellow bracket). As a practical example, assume that the filter level was chosen such that these highest values represent flaw detection. As a result of applying this filter, the remaining pink lines reveal trends in the input parameter ranges that lead to the selected output values. In this example, the lowest center frequency values (red bracket) and the highest probe diameter values (blue bracket) generally resulted in flaw detection. Values of bandwidth and phase (left two lines) were more uniformly distributed, suggesting that no particular range of bandwidth or phase were advantageous for flaw detection.



Figure 3.6. Parallel plot showing the relationships between the different variation parameters. Top: Unfiltered plot. Bottom: Plot with a filter applied to the output values such that the highest output values are highlighted (yellow bracket). The filter reveals that the lowest values of probe center frequency (red bracket) combined with the highest values of probe diameter (blue bracket) generally resulted in the highest output values.

Next is a meta-analysis screen that shows the quality of the metamodel accuracy; see Figure 3.7. CIVA randomly breaks the data into a user-selectable number of subsets, or folds,<sup>(a)</sup> one of which becomes a training set. Variations between the folds and the training set are calculated as error, or uncertainty, and plotted in the top two graphs for the user to evaluate the quality of the metamodel. The histogram on the top left shows the distribution of the number of metamodel runs related to the error. The user can select threshold values of low (green), medium (yellow), and high (red) errors, depending on user-determined tolerances. The regression plot on the top right shows how the training set (labeled as “True”) compares to the other data (labeled as “Predicted”). A high level of scatter, or deviation of the data points from the regression line, in this plot indicates high uncertainty and potentially poor metamodel results. What constitutes “high” or “low” scatter is up to the judgment of the user and should be based on experience. The bottom graph is a reproduction of the parallel plot with lines color-coded according to uncertainty level. In this case, the error values are included on the rightmost vertical line. This can be a helpful visual to aid determining, for example, if most of the uncertainty originates from a particular range of one of the parameters. In this example, the red bracket highlights that most of the high uncertainty results originate from the lowest center frequencies. However, as shown above, the same range of center frequency values also (hypothetically) resulted in more flaw detections. Therefore, it is necessary for the user to evaluate the results carefully and run additional simulation scenarios to flush out the true implications of using specific probe parameters for inspections.

---

(a) “Fold” is a term that is commonly used in machine learning for cross-validation of data sets. In brief, the data set is randomly divided into  $k$  subsets, or folds. One fold is held out as a training set, and the others are compared to it. An useful introduction to this process is shown here: <https://machinelearningmastery.com/k-fold-cross-validation/>

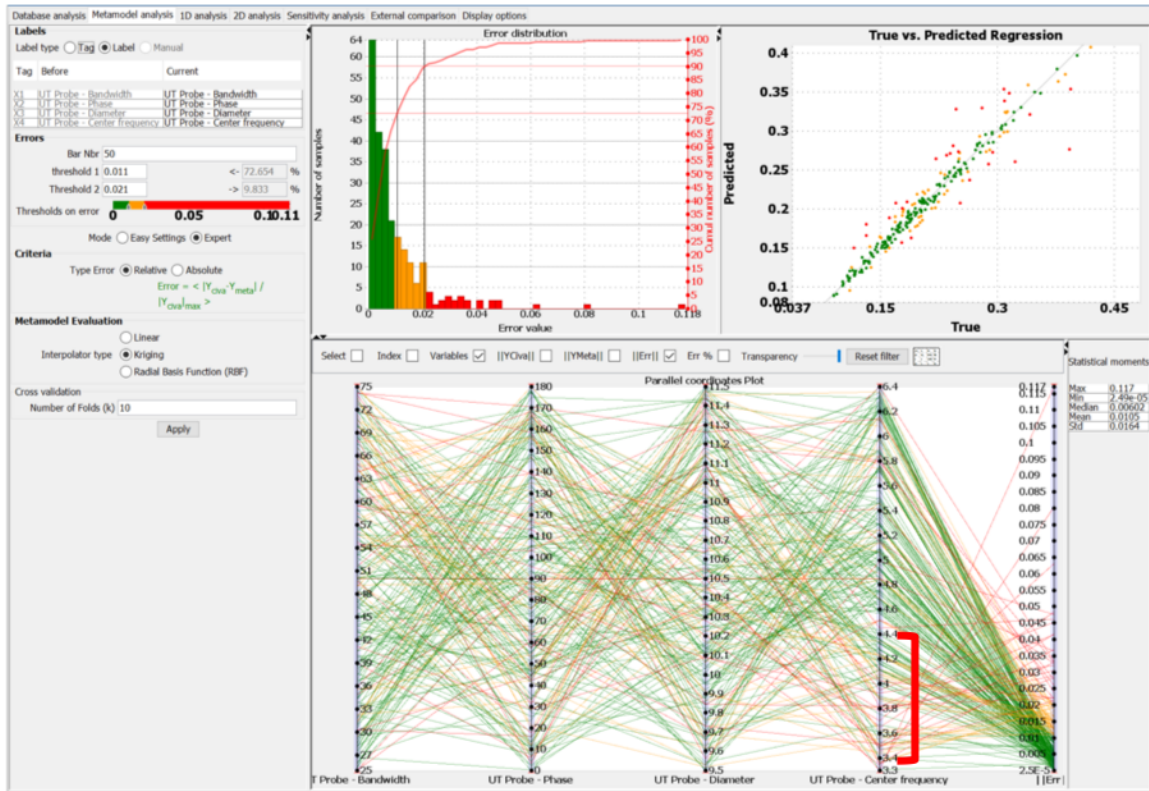


Figure 3.7. Metamodel Analysis screen showing the accuracy of the metamodel. The top two plots illustrate the uncertainty in the metamodel results (red is higher error, yellow is intermediate, and green is low). The lines in the parallel plot are color-coded according to the uncertainty ranges. The red bracket highlights that most of the high uncertainty results originated from the lower end of the range of center frequencies.

Third is a 1D Analysis screen that allows the user to visualize how the simulation output is affected by a single parameter with the other parameters held at constant values. Figure 3.8, for example, shows how the simulation output is expected to change as the bandwidth is varied for user-selected fixed values of the other parameters. The slider bars in the upper left corner allow the user to change the values of the other parameters within the range of each to visualize how the bandwidth (or selected parameter) is affected. In this example, there is little change in simulation output with changes in probe bandwidth as shown by the nearly horizontal line (especially in the center of the bandwidth range). Thus, one can conclude that the simulation outcome for this particular variation is comparatively insensitive to the bandwidth parameter. Note that in practice, probe bandwidth can have a significant effect on ultrasonic signal response by affecting the signal-to-noise ratio and resolution (Murthy et al. 1989; Diaz et al. 1998). Thus, it is important to consider all the parameters of the model and have some working knowledge of how empirical scans respond to such parameters.

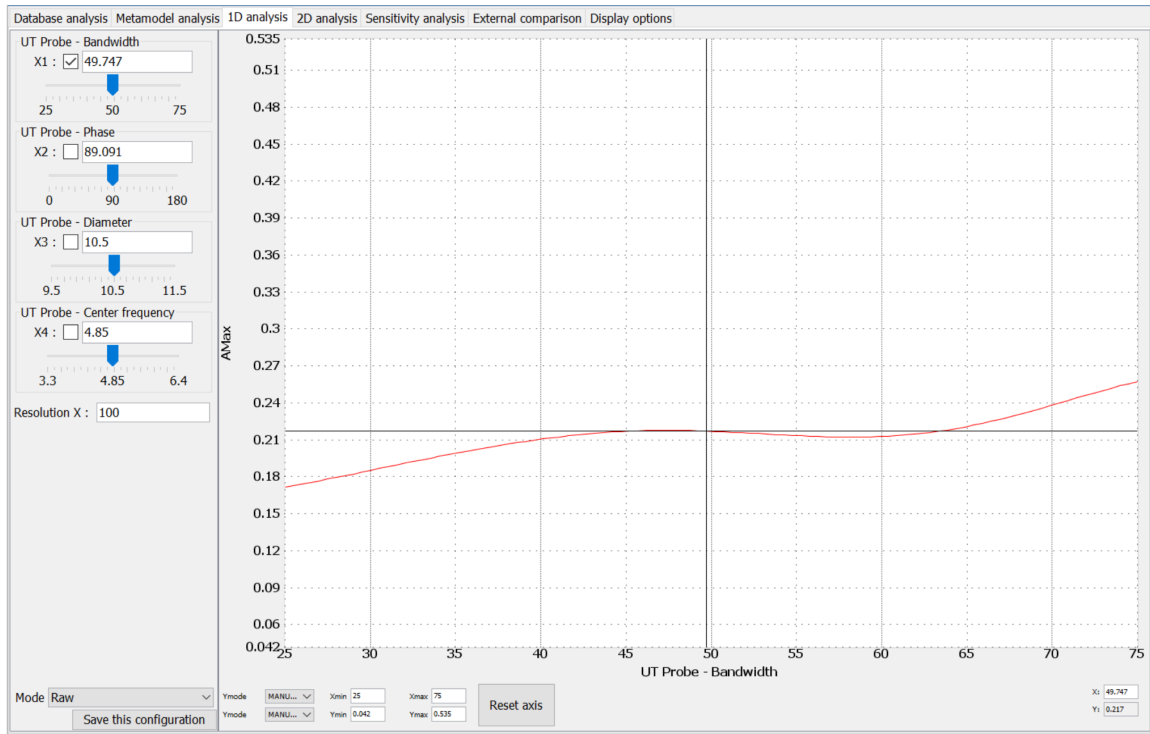


Figure 3.8. 1D Analysis screen. This plot illustrates how the simulation results depend on a selected parameter (bandwidth in this case), with the other parameters held constant.

The fourth screen shows a 2D analysis. Here, the relationship between any two of the variation parameters can be visualized. The example in Figure 3.9 shows how the center frequency (X-axis) and diameter (Y-axis) are related, with the colors indicating the output value for the given frequency/diameter combination. As one varies the frequency (i.e., moves horizontally across the graph), the signal response appears to vary considerably. Similarly, as one varies the diameter (i.e., moves vertically on the graph), there is a non-uniform dependence on center frequency. Therefore, one can conclude from this graph that the diameter and center frequency are related to one another in a complicated manner.

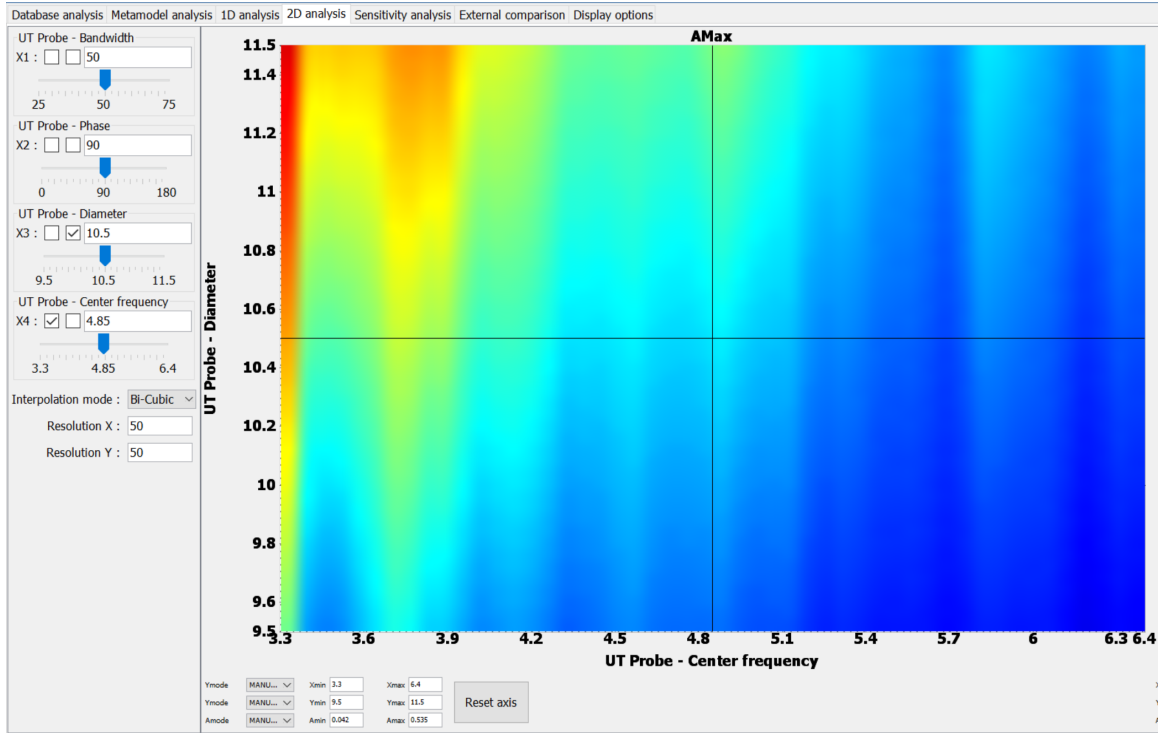


Figure 3.9. 2D Analysis screen. This plot illustrates how the simulation results (represented by the color spectrum) are affected by two variables (diameter and center frequency in this case) while the others are held constant.

Finally, CIVA provides a sensitivity analysis screen. Here, the user can change the “weight”, or the statistical distribution, of each parameter. For example, shown in the upper left of Figure 3.10, the selected parameter is probe bandwidth, and a user-defined Gaussian probability law has been assigned to this parameter (red line on the left). This tells CIVA that the center frequency is most likely to vary based on a Gaussian probability distribution (the user can also choose from other distributions, such as exponential, logarithmic, or uniform). CIVA then recalculates the sensitivity of the simulation output (labeled “sensitivity” on the chart) to the different parameters; this is shown in the bottom charts in bar and pie formats. These charts illustrate the relative impact that changes in each parameter have on the variability of the simulation outcomes. For example, the charts show that changes in the probe center frequency had the largest impact on simulation outcomes while changes to the probe bandwidth and phase had virtually no effect. Note that the bar and pie charts show the same information.

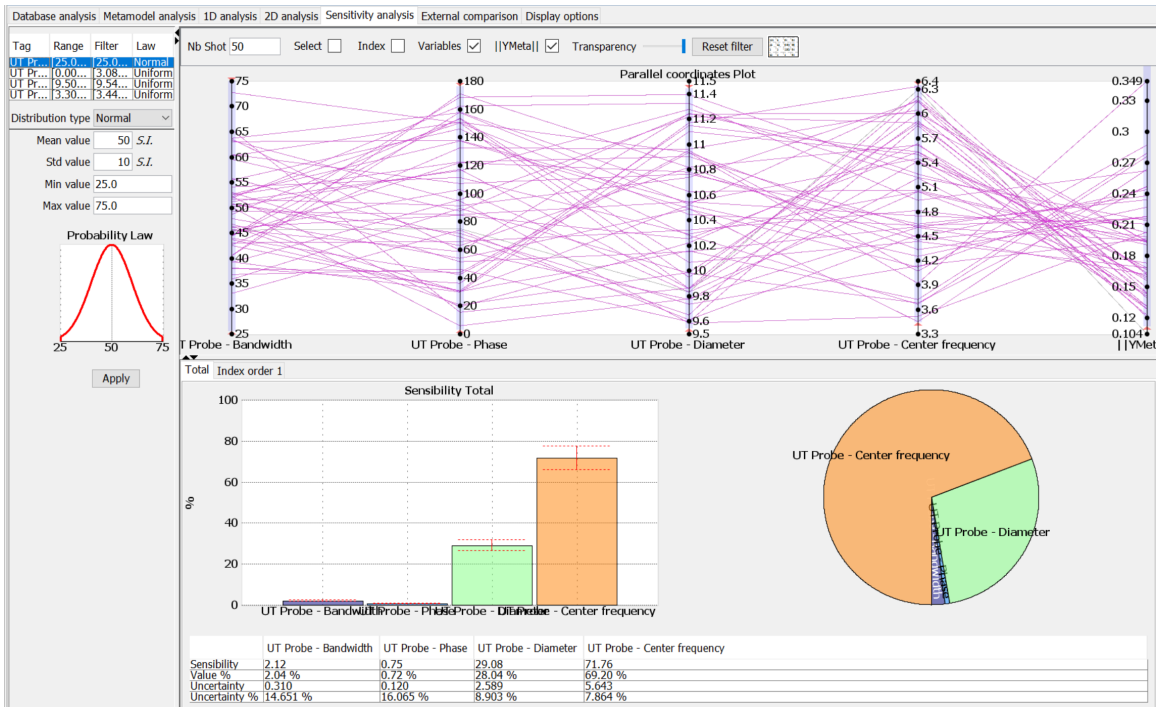


Figure 3.10. Sensitivity Analysis screen. The lower plots illustrate how sensitive the metamodel results are to changes in the individual parameters.

The results of this example study suggest that the probe phase and bandwidth have essentially no effect on the simulation output. However, variations in the probe diameter (shown in green) and center frequency (shown in orange) appear to have a significant impact on the simulation results. The above example was based on parameters and uncertainty ranges measured from a cohort of probes, and the metamodel results were assumed to be accurate. However, if unmeasured parameter values and ranges are guessed at as metamodel variation inputs, then there may be less certainty about the accuracy of the results. This is illustrated in the examples below.

To further explore the utility and limitations of metamodels, metamodel simulations were run with assumed variations of the following wedge parameters: height, radius of curvature, angle, and front length (the distance from the beam exit point to the front of the wedge). In this test, only the range of front length values and the number of metamodel samples (i.e., the number of metamodel test runs) were changed. Three tests were run. First, the wedge front length ranged from 10 to 30 mm (0.40 to 1.2 in.) with 500 samples. Next, the front length range was kept the same but the number of samples was reduced to 360. Last, the front length range was increased to 5 to 30 mm (0.20 to 1.2 in.), again with 360 samples. Figure 3.11 shows the sensitivity results of the three metamodel simulations, or how sensitive the simulation outcomes are to changes in each parameter. As anticipated, there is little difference between the sensitivity results when the number of samples was reduced from 500 to 360 with the same wedge parameters. However, when the front length range was expanded by a few millimeters, the metamodel results changed dramatically. The sensitivity to the front length parameter became virtually insignificant while the importance of the wedge angle dominated. No other parameters were changed, indicating that the metamodel results were highly sensitive to a seemingly innocuous change in a single parameter.

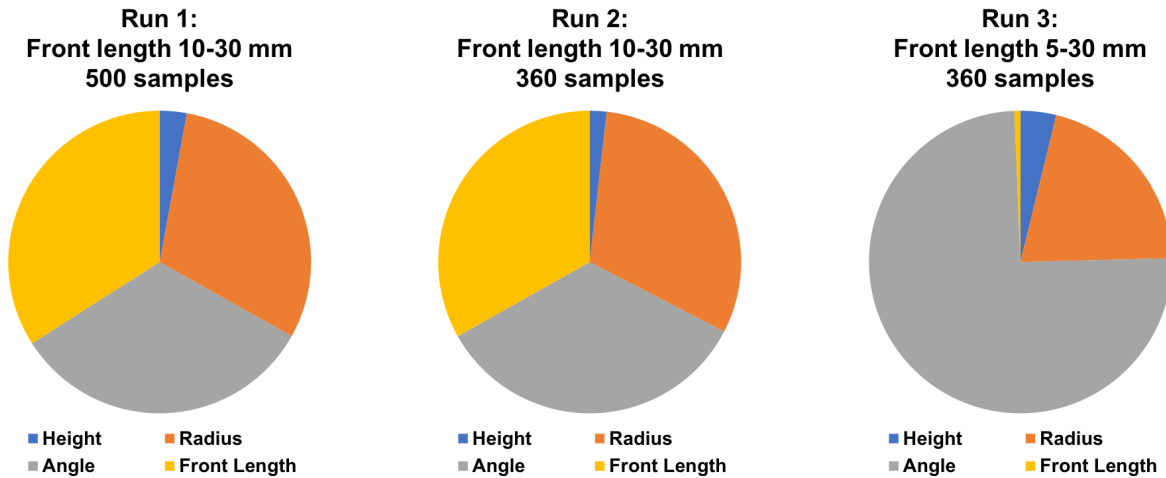


Figure 3.11. Metamodel results from examining wedge parameters. A small change in the front length range between runs 2 and 3 resulted in a dramatic change in the parameter sensitivities.

Similarly, a metamodel simulation was run with flaw parameters being varied: height, position, tilt, and length. In this case, the flaw tilt variation was changed and all other parameters (including the number of samples, 500) were kept the same. Three ranges of tilt were examined:  $-60^\circ$  to  $0^\circ$ ,  $-30^\circ$  to  $30^\circ$ , and  $-30^\circ$  to  $0^\circ$ . For the probe and specimen orientations in these simulations, a negative tilt angle corresponded to tilting the flaw away from the probe and a  $0^\circ$  tilt corresponded to a vertically-oriented flaw. The first range acted as a control, covering a wide array of tilts that could potentially produce a direct specular echo at a tilt of  $-45^\circ$ . The second range covered the same angular span of  $60^\circ$  but eliminated the potential specular response and introduced positive tilt angles. The final range covered a limited range of negative angles only, also excluding the direct specular response angle. Figure 3.12 shows the outcomes. Results show a strong variation in the model dependence based only on the flaw tilt. This may or may not be anticipated, but the point is that if the user is simply guessing at a range of flaw tilt without any empirical basis, the simulation outcomes may not be predictive.

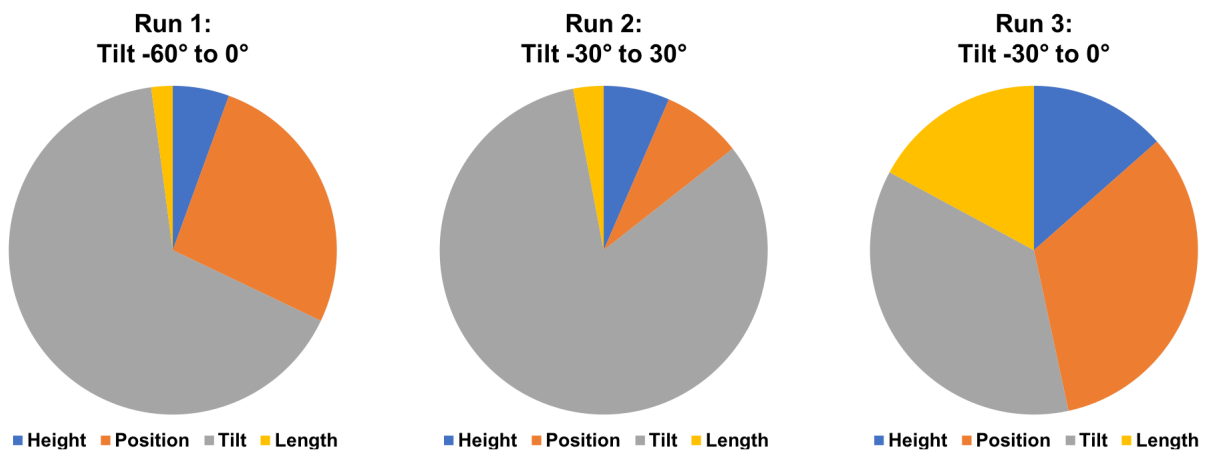


Figure 3.12. Metamodel results from examining flaw parameters. The sensitivity to the flaw tilt depends strongly on the range of the tilt parameter.

Results show that wide variations in metamodel outcomes can stem from seemingly small or assumedly insignificant changes to inputs. Unfortunately, the metamodel documentation is scant, so the reasons behind the large variations in results cannot be investigated at this time (it should be noted that EXTNDE has added options to Metamodels and has expanded the user documentation for CIVA 2020). CIVA metamodels may be useful in situations where the values and ranges of the input parameters are well understood and have been determined by empirical measurements, i.e., in cases where the user does not have to guess at the input parameter ranges. Otherwise, users would do well to perform multiple metamodel tests to determine the sensitivity of metamodel outcomes to relevant input parameter variations. Furthermore, when evaluating metamodel results, one should question the justification for the parameter ranges used and probability laws defined for each parameter range and use empirically-determined values when possible.

### 3.5 Attenuation and Noise

A great deal of flexibility for adding attenuation to models is built into CIVA. For example, users can select “modal” to apply frequency-dependent attenuation described by an exponential, a polynomial, or by the angle of grain orientation; see Figure 3.13. “Global” can be selected to define elements of an attenuation matrix (in units of GPa). Attenuation must be defined independently for each material region, and different attenuation definitions can be made for transverse and longitudinal waves. To date, PNNL has not used attenuation in many simulations, although some limited implementation of attenuation is described in Sections 5.0 and 6.0. PNNL has observed that adding attenuation to the models does not significantly increase simulation time, although this may not be true in all situations. Attenuation properties are defined in the Material tab of the Specimen tab. However, it is important to remember that in order for attenuation to actually be included in the simulations, attenuation must be activated in the model by selecting the “Account for attenuation” option in the Options tab of the Simulation Settings tab. This can be easy to overlook.

In addition to attenuation, structural noise can be added to models (Dorval et al. 2009). PNNL has not yet investigated the noise options in CIVA except for preliminary cursory tests. PNNL observed that adding noise lengthened the simulation times considerably, but PNNL has not yet assessed the realism of simulation noise when compared to empirical noise.

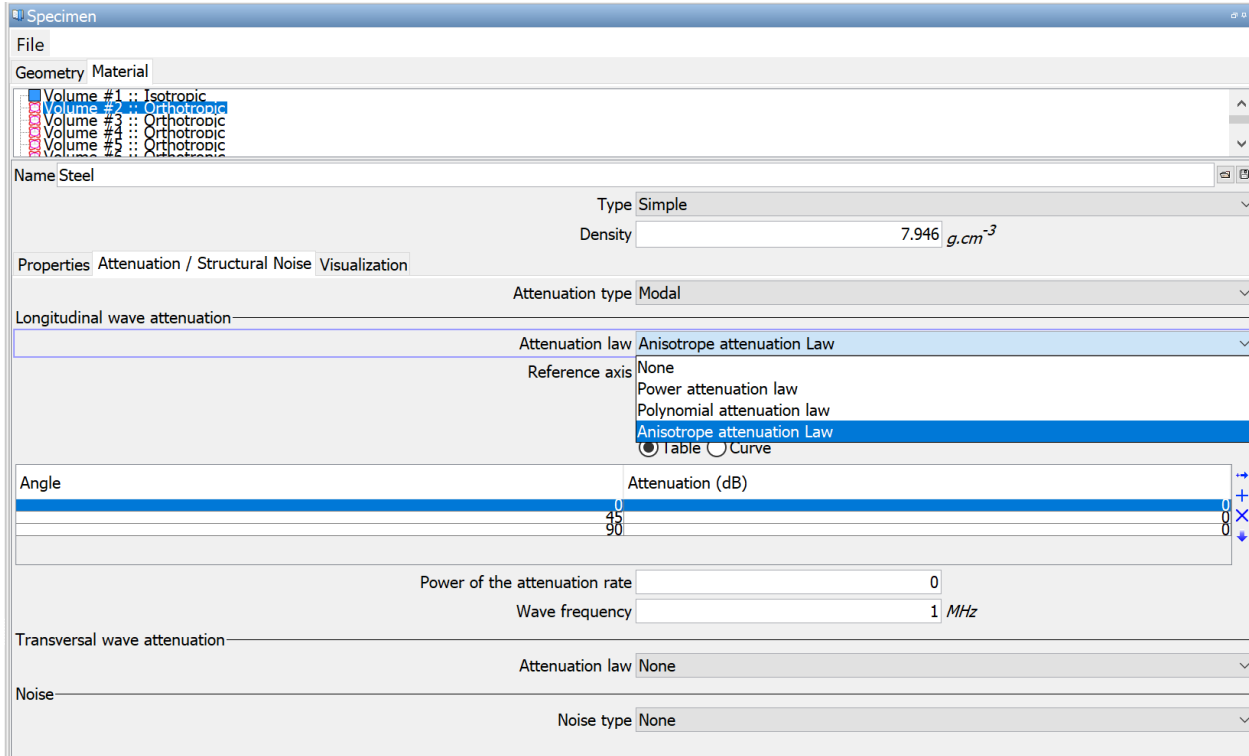


Figure 3.13. CIVA screenshot showing attenuation options.

### 3.6 Ogilvy Weld Model Parameters

The grain orientations in welds can have a significant impact on the direction of sound propagation through the weld material. Because the actual grain orientations are impossible to know without destructive analysis, it is important to understand the impact of applying an approximation to estimate weld grain orientations. CIVA includes a model to define continuously-varying grain orientations in an austenitic weld based on the work of Ogilvy (Ogilvy 1985). This model is attractive for use in simulations because it simplifies the otherwise unwieldy problem of describing individual grains in an austenitic weld. The Ogilvy model and some CIVA applications were described in some detail in the previous PNNL modeling and simulation report (Dib et al. 2018a). Figures 2.3 and 2.4 of Dib et al. are reproduced here as Figure 3.14 and Figure 3.15 to remind the reader of the Ogilvy model.

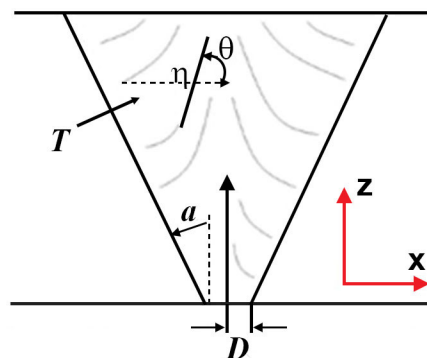


Figure 3.14. Definition of the Ogilvy geometrical weld model. Free parameters  $T$ ,  $D$ ,  $\alpha$ , and  $\eta$  can be defined in CIVA by the user.

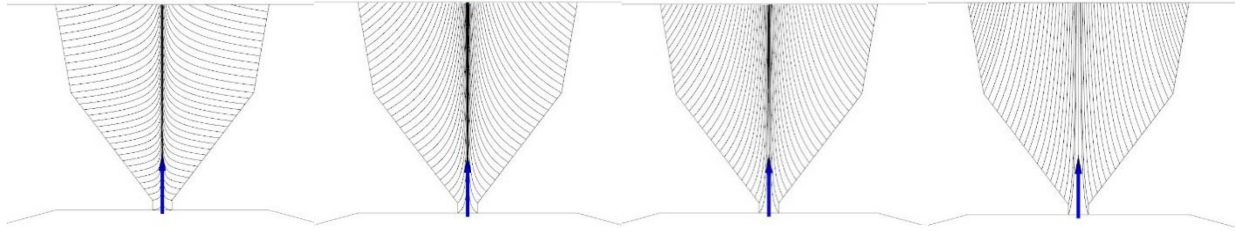


Figure 3.15. Different weld morphologies controlled by the value  $T$ . From left to right:  $T=0.1$ ,  $0.5$ ,  $1$ , and  $2$ . The blue arrows indicate the origin, or center position, from which the Ogilvy model was calculated.

In the current work, PNNL ran a small number of simulations on Ogilvy models of grains that ranged from horizontal to nearly vertical; Figure 3.16 shows the different Ogilvy models tested. The value of  $T$  was changed while other parameters were left constant ( $\alpha=20^\circ$ ,  $\eta=1$ ). The  $T$  values used were  $0$ ,  $0.2$ ,  $1$ ,  $2$ , and  $100$ . Note that  $T=0$  and  $T=100$  are unrealistic scenarios but were included to help understand what happens at the limits of the Ogilvy model. Figure 3.16 also shows a flaw on the right side of the weld root and the ray path of the L-wave emitted from the center, or “exit point,” of a 2 MHz PA probe at a  $45^\circ$  focal law. Using these different Ogilvy scenarios, simple flaw-response simulations were run with the probe in a single position to generate an A-scan. As a control, one simulation was done with an isotropic weld region (i.e., no Ogilvy model). Figure 3.17 shows the envelopes of rectified A-scans with the main echo peaks identified.<sup>(a)</sup> In cases with two peaks, the blue peak is from the weld root and the orange is from the flaw. In cases with a single peak, its origin was not identified. Results show significant differences in the magnitude and locations of echoes in the A-scans. However, in the nominal range of  $T=1$  to  $2$ , the results do not appear to be highly sensitive to the grain orientations. Even so, it is difficult to predict the effects of a particular Ogilvy weld model on simulation outcomes. Therefore, it is important for the CIVA user to understand how the Ogilvy parameters affect the simulated sound propagation so that an informed choice can be made when selecting model parameters.

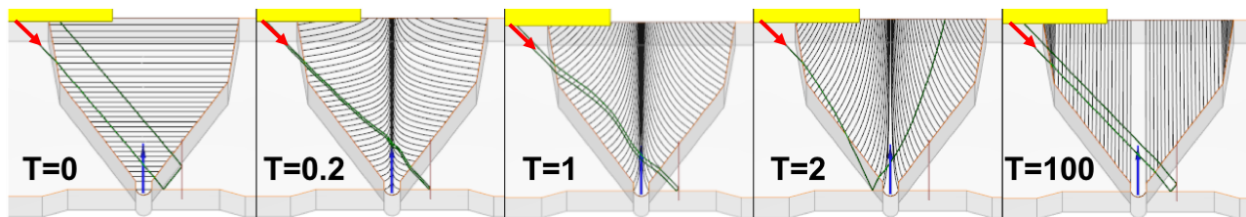


Figure 3.16. Ogilvy grain morphologies tested. The red arrows indicate the origin of the beam path. Note that only the front section of the probe (yellow) is shown. The blue arrows indicate the origins of the Ogilvy models.

(a) Note that only the central beam path is shown; therefore, intuition cannot be used to predict the A-scan response for each of the scenarios. For example, for the  $T=2$  scenario, Figure 3.16 appears to show that the beam misses the root and flaw entirely; however, Figure 3.17 shows two distinct echo peaks.

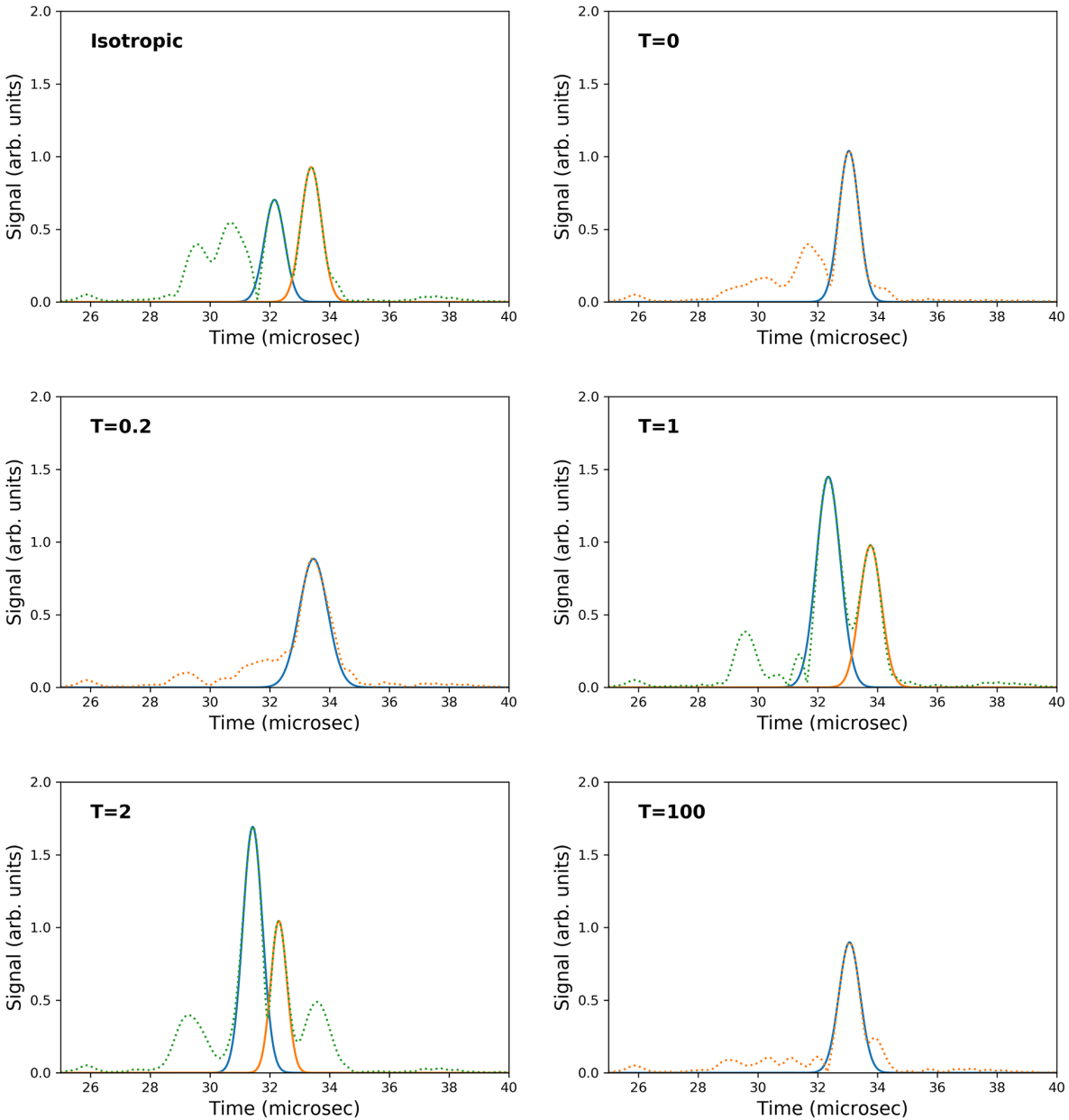


Figure 3.17. Rectified A-scans from simulations with the value of  $T$  varied. The A-scan envelopes (dashed lines) and Gaussian fits to main peaks (solid lines) are shown. In cases where two peaks are identified, the blue peak is from the weld root and the orange peak is from the flaw.

It should be pointed out that CIVA 2017 contains a bug that causes B-scans with the Ogilvy model to not be reconstructed properly.<sup>(a)</sup> This problem is manifest in simulations of line scans that include the exit point of the probe moving onto or across the weld. All data are present in the uncorrected B-scan, but the volume-corrected “True B-scan” (as labeled by CIVA) does not show any of the data that occur when the exit point is over the weld region. An example is

(a) This bug was also observed with non-isotropic welds that did not use the Ogilvy model and welds of complex grain structures, such as used in Section 5.0. The bug was not thoroughly investigated by PNNL, so it cannot be reported under exactly what conditions it persists.

shown in Figure 3.18, the True B-scan result of a full line scan across an Ogilvy-model weld (the T=1 scenario shown in Figure 3.16). The partial reconstruction includes only data with the probe exit point to the left of, and right up to, the weld toe. This problem has also been reported by others (EPRI 2019).

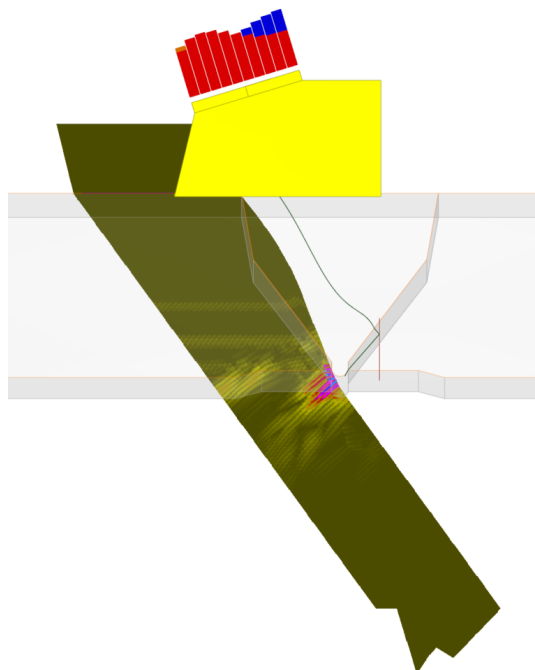


Figure 3.18. Example of the B-scan reconstruction bug.

### 3.7 Stiffness Matrix Parameters and Euler Angles

Sound propagation properties of anisotropic materials can be defined in CIVA using the Stiffness Matrix, which can be found under the Properties tab of the Specimen tab if an anisotropic material type is selected. Different symmetries can be selected, such as cubic, orthotropic, or transverse; the crystallographic details of these symmetries will not be discussed here.<sup>(a)</sup> Figure 3.19 shows an example of stiffness matrix elements that the user is able to edit for orthotropic symmetry. There are nine free stiffness matrix parameters in this example (C11, C22, etc.), and CIVA provides default values for each. These matrix element values are used to calculate the speed of sound in the different crystalline axes. In an initial experiment, PNNL varied the parameters in the stiffness matrix to investigate effects on resulting A-scans. Simulations were run with the CIVA default values and with  $-20\%$ ,  $-10\%$ ,  $+10\%$ , and  $+20\%$  of the default values. For simplicity and to dramatically reduce the number of permutations, all elements of the stiffness matrix were changed simultaneously. A 2 MHz PA probe was used on the Ogilvy weld model shown in Figure 3.16 with T=1. Figure 3.20 shows the simple ray-tracing L-waves calculated by CIVA for the cases that were the default matrix elements and  $\pm 10\%$  of the default values. This figure suggests that the beam path can be considerably altered by

(a) Introductions to the fundamentals of the stiffness matrix and the relation to material anisotropy and sound propagation velocity can be found online at:  
[https://unlcms.unl.edu/cas/physics/tsymbal/teaching/SSP-927/Section%2004\\_Elastic\\_Properties.pdf](https://unlcms.unl.edu/cas/physics/tsymbal/teaching/SSP-927/Section%2004_Elastic_Properties.pdf)  
 and  
[http://web.mit.edu/16.20/homepage/3\\_Constitutive/Constitutive\\_files/module\\_3\\_with\\_solutions.pdf](http://web.mit.edu/16.20/homepage/3_Constitutive/Constitutive_files/module_3_with_solutions.pdf)

relatively small uncertainties in the stiffness matrix values. The variation can be the difference between insonifying the corner of the flaw, the face of the flaw, or missing the flaw altogether.

Geometry Material

- Volume #1 :: Isotropic
- Volume #2 :: Parametric anisotropic orientation (Welding)
- Volume #3 :: Isotropic

Name Steel

Type Parametric anisotropic orientation (Welding)

Density 8.05  $g.cm^{-3}$

Properties Orientations Attenuation / Structural Noise Visualization

Symmetry Orthotropic

Stiffness matrix (GPa) - elastic properties

<b>C11</b>	245	<b>C12</b>	145	<b>C13</b>	110	0	0	0
	145	<b>C22</b>	218	<b>C23</b>	148	0	0	0
	110		148	<b>C33</b>	247	0	0	0
	0		0		0	<b>C44</b>	105	0
	0		0		0		<b>C55</b>	75
	0		0		0			<b>C66</b>
								110

**Euler angles** →

Rotation (X) 0 deg

Skew (Z) 0 deg

Theta (Y) 0 deg

Figure 3.19. Stiffness matrix elements that can be edited for orthotropic symmetry. Stiffness matrix elements are labeled as C11, C22, etc. Euler angles in the specimen reference frame may also be defined on this screen.

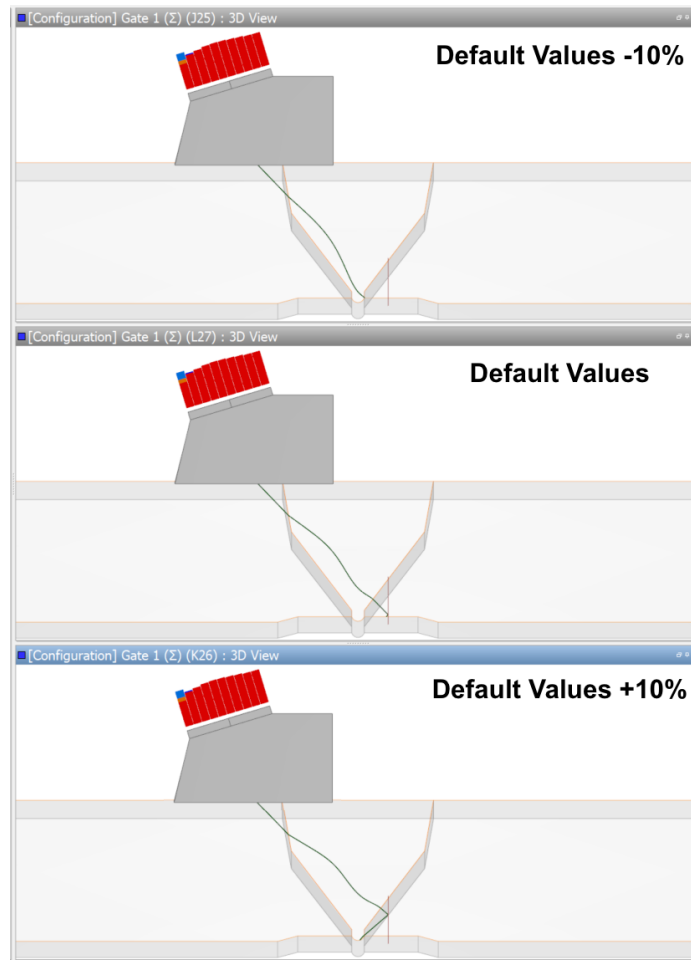


Figure 3.20. Ray-tracing images of the sound path through the weld with default stiffness matrix values and  $\pm 10\%$  of the default values. A circumferential planar flaw is shown on the right side of the weld root.

A metamodel analysis was conducted on the stiffness matrix parameters using C11, C13, C33, C44, and C66 as variation parameters. A 5 MHz single-element probe with a 12 mm (0.5 in.) diameter and a 60% bandwidth was used with a  $45^\circ$  refraction angle. The weld was of the same geometry shown in Figure 3.16, but the material was defined as homogeneous with transverse isotropy. A range of nominal stiffness matrix elements was based on the range of reported values found in the literature (Dewey et al. 1977; Temple 1988; Vijayendra and Neumann 1992; Chassignole et al. 2000; Seldis and Pecorari 2000; Liu and Wirdelius 2007; Tabatabaeipour and Honarvar 2010; Sakamoto et al. 2012; Bannouf et al. 2014; Gardahaut et al. 2014; Fan et al. 2015). Table 3.1 shows the range of each stiffness matrix element in units of GPa. The sensitivity analysis results are shown in Figure 3.21, which indicates that the simulations are most sensitive to changes in matrix element C33 and virtually independent of element C66. Note that, in light of the variability in metamodel outcomes discussed above, one should be cautious about relying on the results of a single metamodel simulation.

Table 3.1. Ranges of matrix elements used in the metamodel analysis.

Matrix Element	Range (GPa)
C11	240–290
C13	120–160
C33	210–290
C44	80–130
C66	55–85

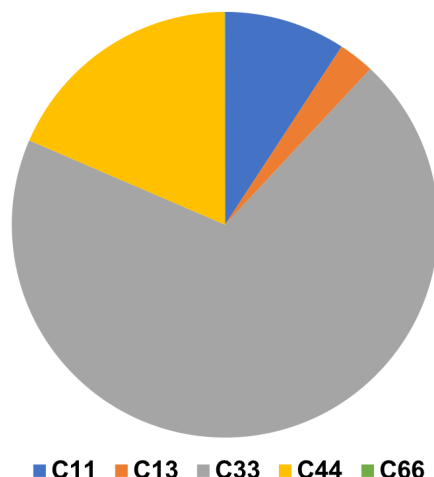


Figure 3.21. Metamodel sensitivity results of varying the stiffness matrix elements. For the ranges of elements used, results were most sensitive to C33 and insensitive to C66.

Measurement of the stiffness matrix elements in real specimens is not trivial and requires destructive analysis or use of material samples, so the matrix elements will be impossible to know for simulations of field testing (Ogi et al. 2002; Sakamoto et al. 2012). Unless values can be taken from the literature and applied with some degree of confidence, one would have to determine whether to use the CIVA default values, other values, or to simply model the material as isotropic. However, if it is important that the properties of non-isotropic materials be modeled, then some effort should be made to understand the properties so that simulation results will be as accurate as possible, keeping in mind that the only way to verify if the simulations are reflective of reality is to collect empirical data on the same materials (Gueudre et al. 2019).

CIVA allows for the user to input crystal orientation angles as part of the material properties. In crystallography, the most common convention is to use Bunge Euler angles, which correspond to rotations in the crystal's reference frame (Bunge 2013). Rotations are done in the following order: a rotation of angle  $\varphi_1$  about the Z axis, a rotation of angle  $\phi$  about the new X axis, then a final rotation of angle  $\varphi_2$  about the new Z axis. Figure 3.22 illustrates this process. Unfortunately, CIVA 2017 does not use standard Bunge angles.<sup>(a)</sup> Rather, it uses rotations about the x, y, and z axes of the fixed reference frame of the specimen. One can use conventional Euler angles in CIVA simulations, but in order to do so, angles must first be transformed from the Bunge angles ( $\varphi_1, \phi, \varphi_2$ ) to the CIVA fixed reference angles (x, y, z). By calculating the rotation matrix R using

(a) CIVA 2020 was changed to allow users to input Bunge Euler angles.

$(\varphi_1, \phi, \varphi_2)$  and solving for  $(x, y, z)$ . Appendix D shows the details on how to do the transformation, including a Python implementation; additional details can be found in Britton et al. (2016). Note that the goal of the work was to determine effects on simulations of realistic but essentially random Euler angle assignments in multiple simulations. Euler angles for this report were taken from the literature simply to provide some basis for crystalline orientations. The angles were taken as reported (as Bunge angles) but were not transformed into the specimen (CIVA) reference frame, because it was incorrectly assumed that CIVA used Bunge angles. The fact that the angles were not in the correct reference frame may affect individual simulation outcomes, but the goal was still accomplished. Therefore, the overall conclusions drawn from the simulation results presented herein are not affected.

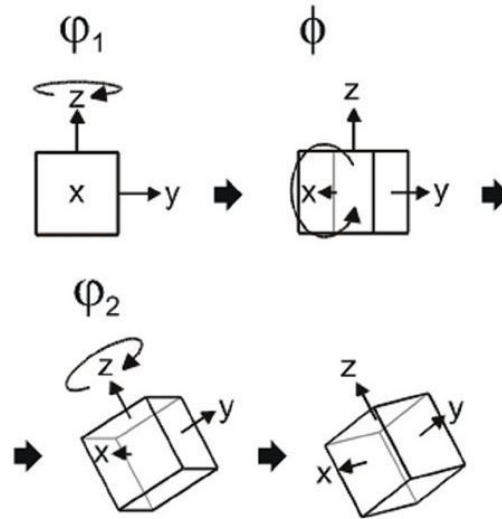


Figure 3.22. Euler angle rotations according to the standard Bunge convention. These rotations are in the crystal's frame of reference and not in the specimen's frame of reference.

### 3.8 Flaw Definitions

CIVA includes a flexible tool for defining and placing reflectors in a model specimen for flaw response simulations. A variety of pre-defined planar flaw profiles are available; these flaws can be placed at arbitrary orientations and positions within the specimen. Additionally, the built-in CAD interface can be used to define and save flaws of arbitrary topography. PNNL noted that when multiple flaws are defined for a given model that significant lag, or latency, can occur in CIVA whenever the user selects or changes a parameter. The latency is due to the meshing (see Section 2.4), because meshing “induces latency because it is performed each time you change a parameter in your CIVA model.”<sup>(a)</sup> A few solutions can be used to minimize this problem: (1) reduce the number of flaws in the specimen model to only those necessary, (2) add the flaws as the last step in the model creation, (3) keep the flaw profiles as simple as possible (e.g., use square flaws instead of semi-elliptical flaws).

CIVA does not have a built-in method of including reflectors in beam simulation models. If a reflector is required for a beam simulation, it must be included as part of the specimen definition. This can only be done if the specimen is defined using the CAD interface. For reflectors

(a) Communication from EXTENDE support staff.

incorporated directly into the specimen, the line segments that delineate the flaw need to be defined appropriately. For example, line segments that compose surface-breaking flaws at the specimen ID should be defined as “backwall” interfaces. Then, in the model, the appropriate interactions (e.g., backwall or interface interactions) should be activated. Also, the Kirchhoff model should be used, even if the remainder of the specimen backwall is smooth, because the assumption of a purely specular reflection is no longer valid.

## 4.0 Experimental

### 4.1 Introduction

Empirical model validation is a critical activity for establishing confidence in simulation outcomes. Most model validation approaches compare echo responses from simulated flaws and easily-replicated empirical scenarios, such as side-drilled holes and ID surface-breaking notches (Wirdelius and Persson 2012; Bannouf et al. 2014; Gardahaut et al. 2014; Dib et al. 2017). Visualization of the sound beam is an important step in UT simulation validation. There must be confidence in beam simulation activities, such as those used in coverage predictions for examination protocols or relief requests. One approach to mapping the sound beam is to use a laser vibrometer to scan the surface of an insonified material (Nakahata et al. 2016). Another approach is to raster-scan the side or end of a specimen with a small-diameter ultrasonic receive transducer, such as a pencil probe, to detect the sound field originating from a transducer on the specimen (Gardahaut et al. 2014). The diameter of the pencil probe defines the point spread function of the system, so the resolution of the acquired image is limited by the probe size. In the previous PNNL modeling report (Dib et al. 2018a), the mapping of sound fields through austenitic welds was described using a pencil probe to detect the sound beam after it had traversed through an austenitic weld. Because such activities record the beam through a specimen cross section, or side, results are referred to as “side-beam” maps. For this TLR, additional side-beam maps were acquired to supplement the previous results and to align with the new modeling and simulation efforts. Previously, data were acquired with focal laws of 30°, 45°, and 60° with the transmitting probe in a static position. For current work, the same angles were used, but data were acquired with the probe at different positions to change the sound path length through the weld for each focal law. Also, sound fields through an additional thick-wall CASS-CS DMW specimen were acquired.

### 4.2 Specimens

Three austenitic weld specimens were used for experimental mapping of the sound fields. The first two specimens, labeled as Specimen 1 and Specimen 2, were removed from mockup 3C-022, described in Anderson et al. (2011). A photo of the 3C-022 specimen with removed samples is shown in Figure 4.1. The mockup is a 71 cm (28 in.) outer-diameter (OD) pipe segment that contains three circumferential welds and one axial seam weld. The pipe material is Schedule 80, ASTM A358 Grade 304 WSS, and the welds are 308/308L stainless steel. Each specimen contains a section of one of the circumferential welds; no specimen overlapped the seam weld. The through-wall thickness of Specimens 1 and 2 was about 36 mm (1.42 in.).



Figure 4.1. Photo of 3C-022 with removed specimens.

The third specimen was removed from a DMW pipe segment mockup, 14C-146; detailed information about this specimen is available in Chapter 7 of Jacob et al. (2019). The pipe mockup is a SA-516 Grade 70 CS nozzle with 308/309 stainless steel cladding welded to SA-351 CF8M CASS. The weld is Inconel 82/182 material. The through-wall thickness was 85 mm (3.35 in.). A photo of 14C-146, with the removed sample, can be seen in Figure 4.2.



Figure 4.2. Photo of DMW pipe segment 14C-146.

For these three specimens, the specimen number, identification number, thickness, and material information are summarized in Table 4.1. A slice of each specimen was polished and etched to reveal the microstructures of the base materials and welds. The microstructures of Specimens 1 and 2 are shown in Figure 4.3 and Specimen 3 is shown in Figure 4.4.

Specimen 1 (identified as 3C-022-02) was welded in a vertical orientation, resulting in a weld grain pattern that is asymmetric with respect to the weld centerline. Specimen 2 (3C-022-03) was welded in a horizontal orientation, resulting in a more symmetric weld grain pattern. Note the gradient of grain sizes in the WSS parent material. The regions near the OD and ID have coarser grains while the centers have fine grains. However, even the largest grains measure a millimeter or less across, so Rayleigh scattering should predominate at 2 MHz.

Table 4.1 Description of sound field mapping specimens

Specimen Number	Identification	Thickness (mm [in.])	Upstream Material	Downstream Material	Weld Material
1	3C-022-02	36 (1.42)	304 WSS	304 WSS	308/308L SS
2	3C-022-03	36 (1.42)	304 WSS	304 WSS	308/308L SS
3	14C-146-01	85 (3.34)	SA-516 CS	CF8M CASS	Inconel 82/182

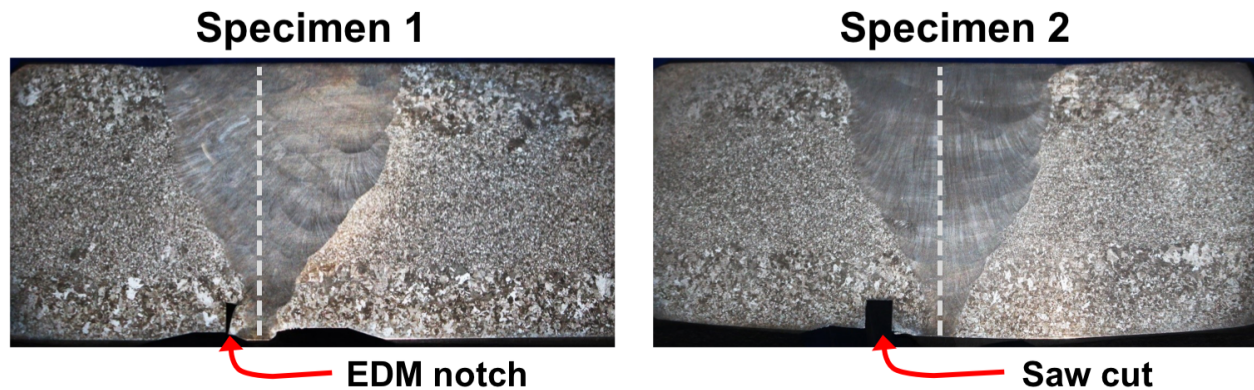


Figure 4.3. Photographs of the weld profiles of Specimen 1 (left) and Specimen 2 (right). The dashed line denotes the weld centerline.

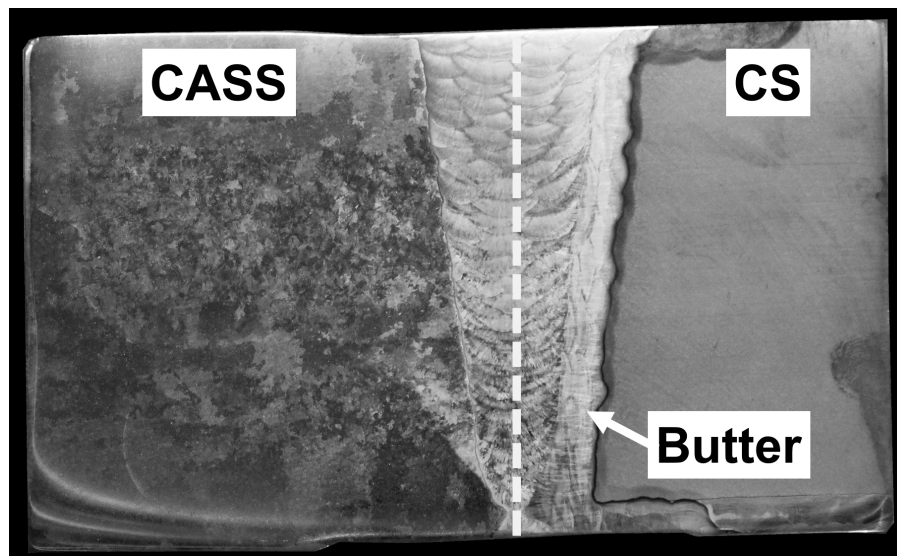


Figure 4.4. Photograph of the weld profile of Specimen 3. The dashed line denotes the weld centerline.

The sides of the specimens were machined flat. Additionally, a flat surface was machined onto the top of the specimens to accommodate a PA probe. This removed the curvature of the pipe to ensure the sound field generated by the probe would remain parallel to the face being mapped for accuracy of measurement.

## 4.3 Equipment

### 4.3.1 Probes

The transmitting probe was a 2.0 MHz PA transducer, typically operated in a TRL configuration. For this study, only the transmit half was used. The transducer contains a 10×5 matrix of piezoelectric elements, each 2.0 mm (0.079 in.) with a spacing of 0.2 mm (0.008 in.) in both the primary and secondary dimension. The overall active aperture is 21.75 mm × 10.75 mm (0.856 in. × 0.423 in.) in the primary and secondary axes, respectively. The transmit PA transducer was mounted on a Rexolite wedge to provide a nominal refracted angle of 45° through stainless steel. A photo of the PA transducer is provided in Figure 4.5. Focal laws were defined at beam angles of 30°, 45°, and 60° for a true-depth focus of 24 mm (0.94 in.) for all specimens and 84 mm (3.31 in.) for Specimen 3.

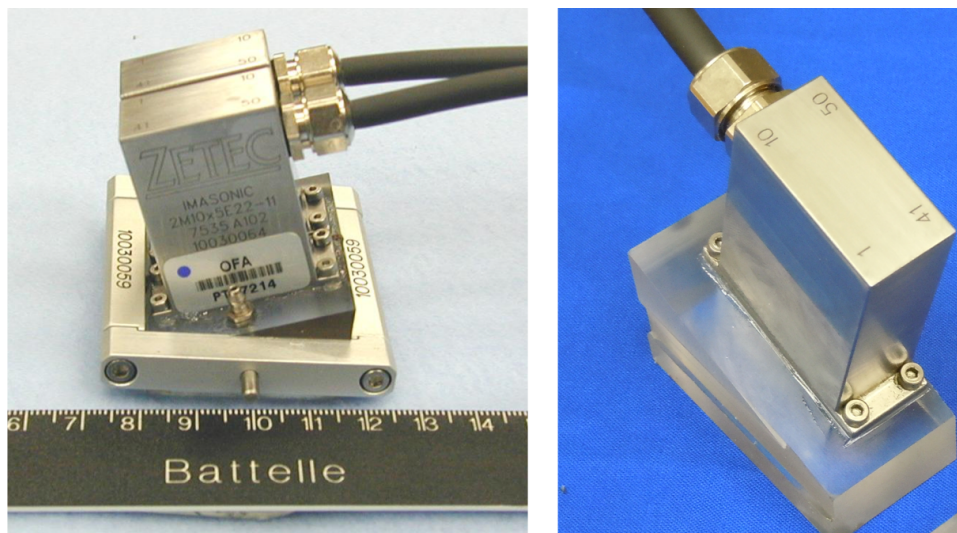


Figure 4.5. 2.0 MHz PAUT transducer. *Left:* Standard TRL configuration. *Right:* The transmit half of the pair, as used for sound field mapping.

A pencil probe was used to receive the ultrasonic waveforms generated by the PA transmitter; see Figure 4.6. Because of the design and fabrication of pencil probes, each has unique frequency characteristics and bandwidths. Thus, five pencil probes were tested in a pitch-catch configuration to evaluate their behavior and find the one that best matched the transmitting frequency. A conventional 2.25 MHz transducer was excited with a 250 ns negative square wave to drive a 2 MHz signal. The frequency response of each pencil probe was analyzed to determine the center frequency and bandwidth. A probe was selected based on the center frequency being near 2.0 MHz and the probe having a sufficient bandwidth to accommodate potential frequency shifts through the specimen material; see Figure 4.7. The calculated center frequency, peak frequency, and bandwidth were 2.10 MHz, 2.05 MHz, and 26%, respectively. The diameter of the pencil probe was approximately 1 mm (0.04 in.)



Figure 4.6. The pencil probe used in this study. The probe is housed within a sleeve, which is mounted inside a holder that can be attached to the scanning arm.

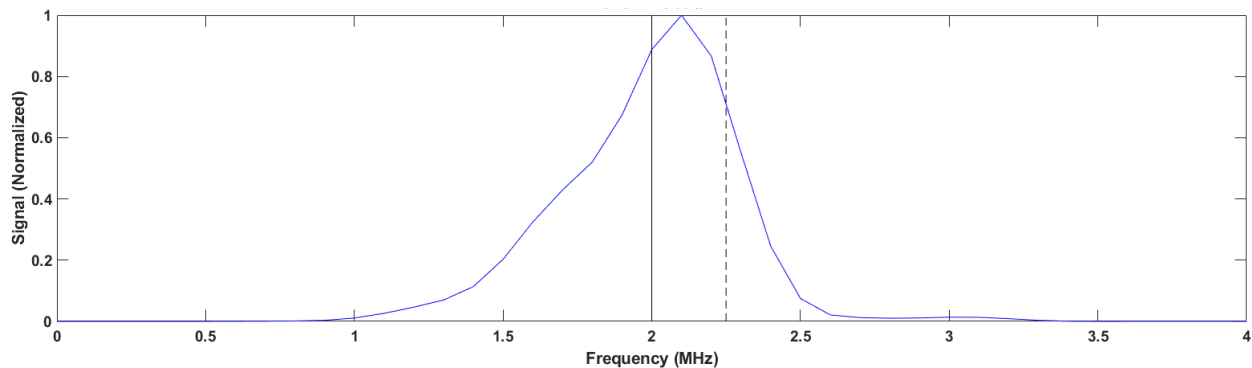


Figure 4.7. Pencil probe frequency response from a 2.25 MHz transducer (dashed black line) driven at 2.0 MHz (solid black line). The signal response was self-normalized.

### 4.3.2 Data Acquisition System

A Zetec DYNARAY, in conjunction with UltraVision 3 software, was used as the data collection system. The DYNARAY can support up to 128/128 transmit/receive elements at a maximum sampling rate of 100 MHz. The 30°, 45°, and 60° focal laws were generated in the same method as discussed in Dib et al. (2018a). A separate computer controlled a scanner, and the encoded position of the scanner was used to synchronize the DYNARAY for data collection.

The pencil probe was mounted on a 3-axis XYZ scanner, used to translate the probe to encoded positions for data acquisition. The resolution of each axis of the scanner is 50  $\mu\text{m}$  (0.0020 in.) for the X-axis and 25  $\mu\text{m}$  (0.00098 in.) for both Y and Z, with shaft encoders on each axis used to feed the scanner position back to the DYNARAY. Figure 4.8 shows the placement

of the PA probe on the specimen with the X and Z translation axes annotated. The relative position of the pencil probe during data acquisition is also shown.



Figure 4.8. Photograph of the locations of the probes during data acquisition.

#### 4.4 Experimental Setup

Figure 4.9 shows the experimental setup. The specimen was submerged in water just above the machined surface to allow for immersion coupling of both the pencil probe and the PA transducer. The PA transmitter was aligned such that the face of the wedge was flush with the face of the specimen, as defined in the focal laws and the focusing plane of the PA transducer in UltraVision. Thus, the focal plane was coincident with the specimen face. Alignment of the specimen was crucial for obtaining a consistent signal response across the scan. A maximum standoff distance of 0.2 mm (0.008 in.) between the pencil probe and the specimen was maintained. The alignment of the specimen was measured by running low-resolution scans in the XZ plane across the face of the specimen while operating the pencil probe in a pulse-echo configuration. The time of flight from the signal response was used to adjust the specimen alignment until the tolerance was met.

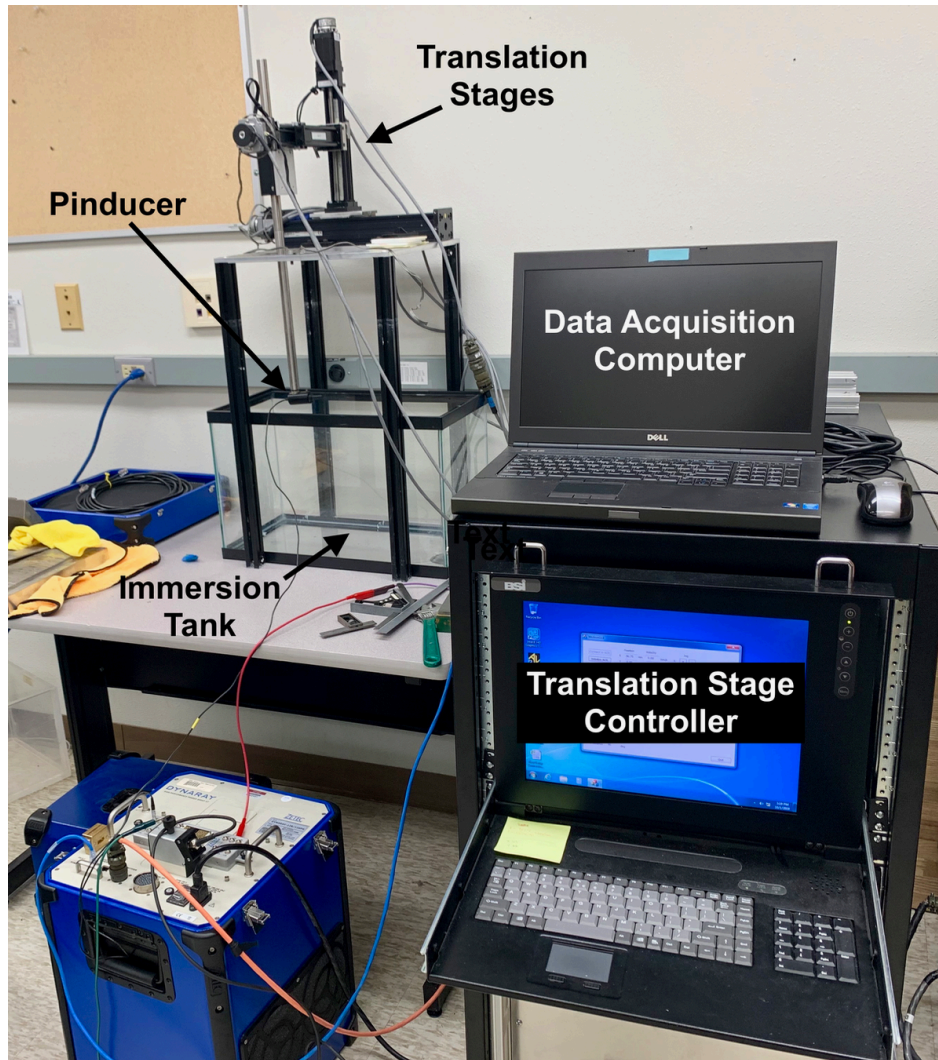


Figure 4.9. Photograph of the experimental setup for side-beam mapping data acquisition.

Beam maps were acquired with the PA probe at four positions with respect to the weld. Three were to maximize the weld path for each refracted angle: the PA probe exit point at the weld centerline (WCL), the exit point just to the left of the WCL, and the exit point to the left of the weld toe. The fourth probe position was away from the weld and over parent material for a control scan.

## 4.5 Results

### 4.5.1 WSS-WSS Welds

Figure 4.10 shows an UltraVision screen capture of the empirically acquired sound field through the isotropic parent material of Specimen 2. Gain was set to 44 dB. The signal was gated to eliminate most backwall bounces and mode-converted signals. This image shows well-formed, symmetric sound beams with minimal scatter.

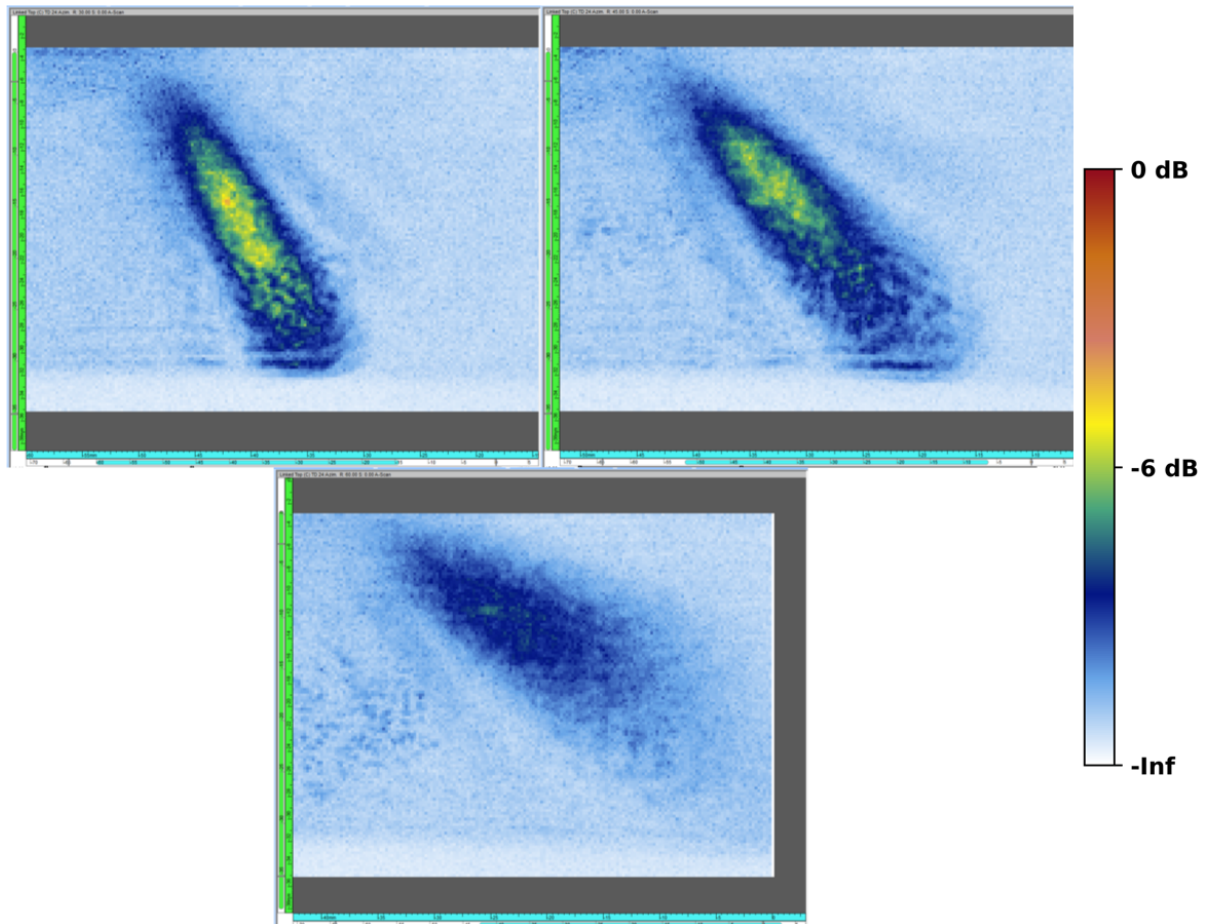


Figure 4.10. Beam maps through WSS parent material. Clockwise from top left: 30°, 45°, 60°.

Figure 4.11 shows the empirical sound fields through Specimen 1 and Specimen 2 with the same gain settings. For these beam maps, the probe was placed so the exit point was near the WCL; the approximate probe position is illustrated at the top of the figure. Similarly, Figure 4.12 shows the sound field through both specimens with the exit point to the left of the WCL. Finally, Figure 4.13 shows the sound field through both specimens with the exit point to the left of the weld toe. Note in Figure 4.12 that the probe position on Specimen 1 was somewhat farther off the weld than that on Specimen 2. This resulted in different scatter patterns that are difficult to compare across specimens.

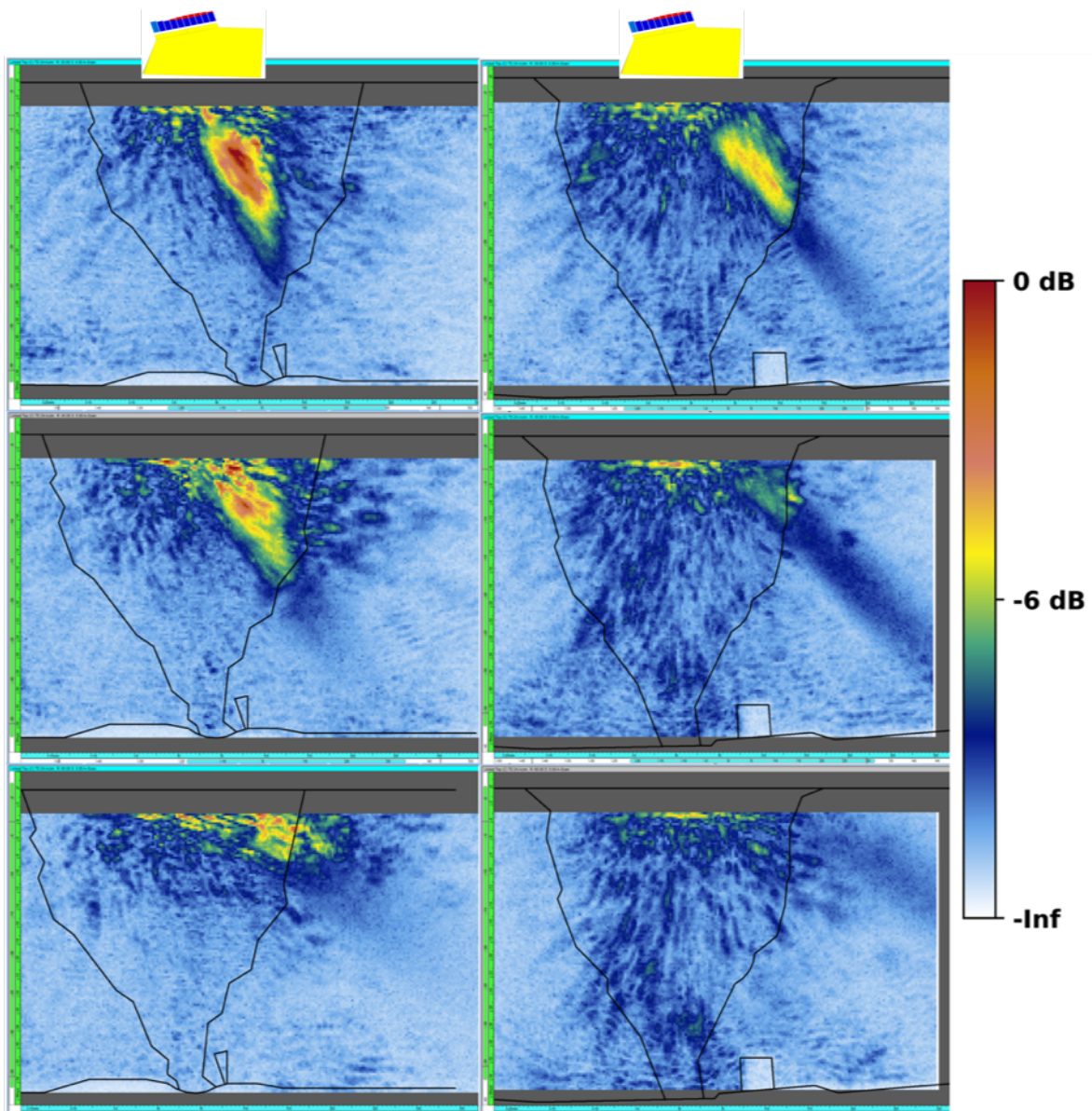


Figure 4.11. Beam maps with the probe exit point near the WCL. *Left column:* Specimen 1. *Right column:* Specimen 2. Rows from top to bottom: 30°, 45°, 60°. Probe positions are shown for illustrative purposes and are not to scale.

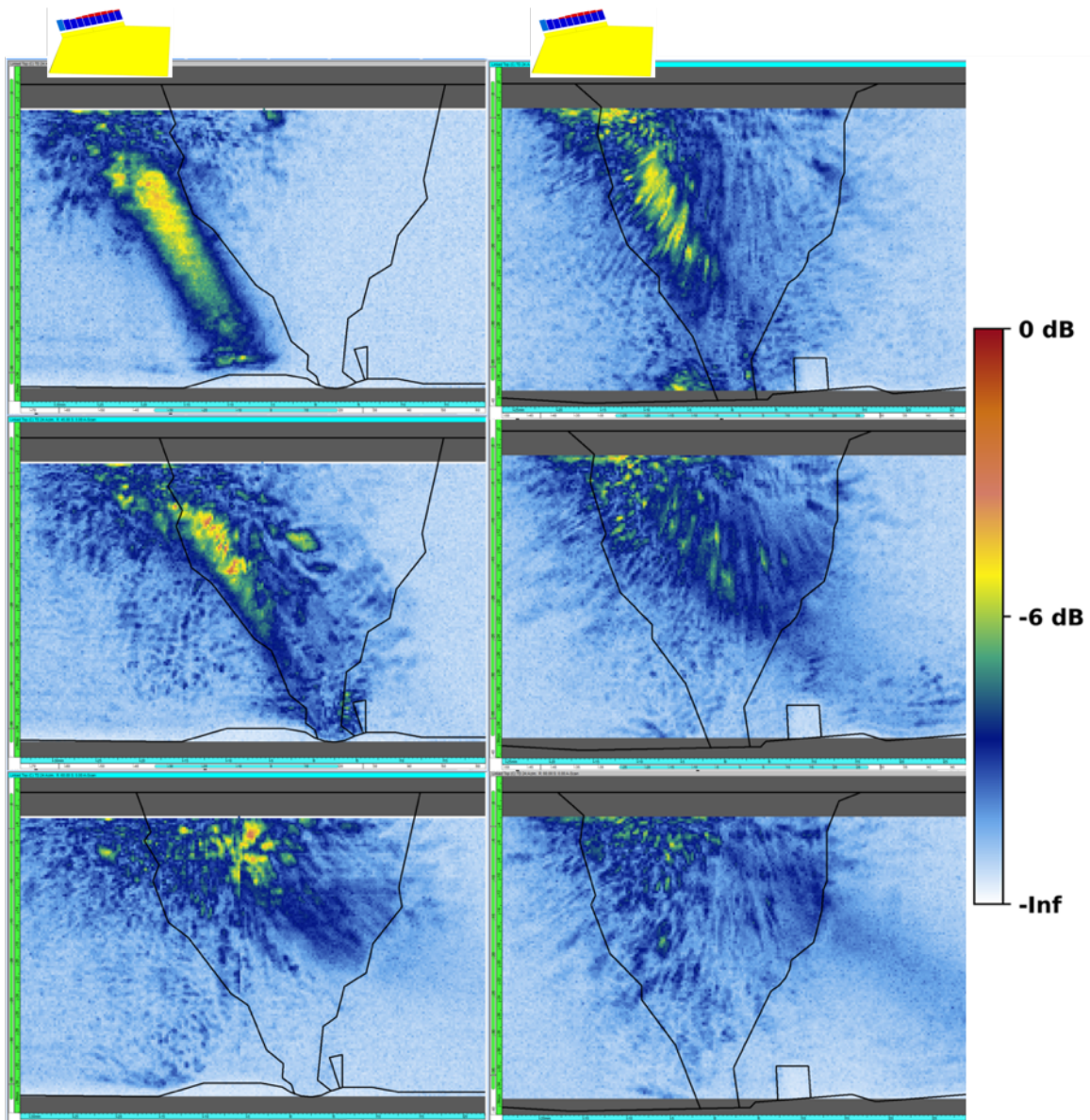


Figure 4.12. Beam maps with the probe exit point to the left of the WCL. *Left column:* Specimen 1. *Right column:* Specimen 2. Rows from top to bottom: 30°, 45°, 60°. Probe positions are shown for illustrative purposes and are not to scale.

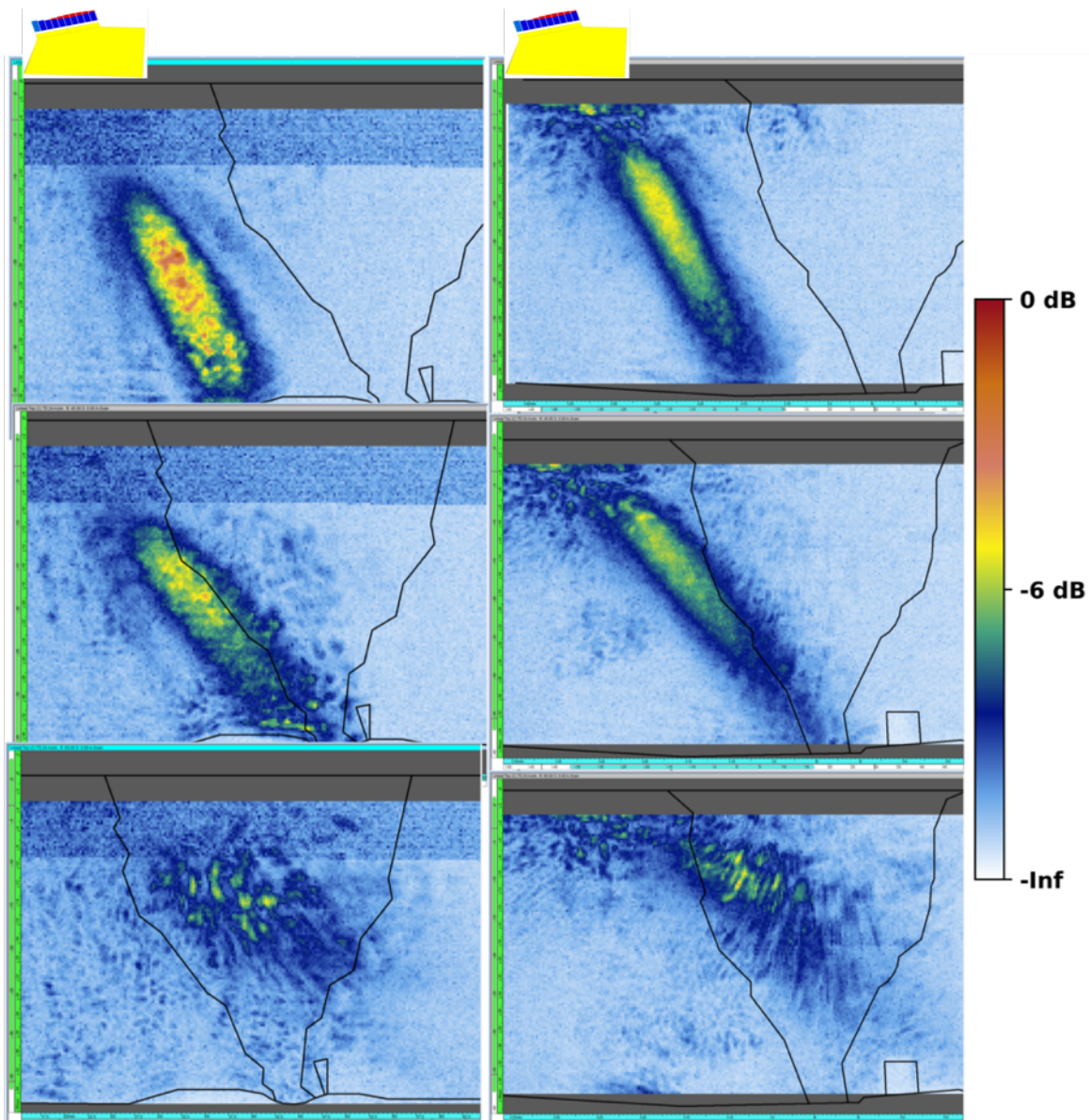


Figure 4.13. Beam maps with the probe exit point to the left of the weld toe. *Left column:* Specimen 1. *Right column:* Specimen 2. Rows from top to bottom: 30°, 45°, 60°. Probe positions are shown for illustrative purposes and are not to scale.

The above images vary considerably from the isotropic sound field maps. In both specimens, the beam through the weld material is not well formed, there is significant scatter (especially near the top surface of the specimen), and the sound field does not penetrate as deeply into the specimen, although some sound energy does appear to reach the backwall. Interestingly, in several of the beam maps, the scatter pattern in the weld appears to be quasi-random, as the sound field somewhat follows the general direction of the weld dendrites. It is important to remember that the crystalline orientation is not the same as the dendritic orientation. That is, the preferred direction of sound propagation as determined by the Euler angles does not necessarily align with the long dimension of the dendrites. Thus, the sound occasionally, but not always, follows the dendritic orientation resulting in a scatter pattern that appears to have some

structure but is mostly random. When the sound does follow the dendritic orientation, it forms an easily identifiable pattern in the image.

It is also interesting to note that the granular structures of Specimen 1 resulted in sound fields that appear markedly different from those of Specimen 2; see Figure 4.3. Prior to this study, both welds were believed to be nominally identical. Even with the ability to visualize the grain structures after cutting, polishing, and etching, the significant differences in through-weld beam maps could not have been predicted.

#### 4.5.2 CS-CASS DMW Weld

Specimen 3, the DMW sample, was mapped with the beam originating from the CS side of the weld. CASS material does not easily propagate sound without large scattering and redirection effects at frequencies at about 1.0 MHz and above because of the wavelength compared to the austenitic grain size of the base material (Jacob et al. 2019). The wavelengths should be larger than the average grain diameter so that the resultant sound fields will be less sensitive to the degradation of beam coherence and other effects on sound field propagation. Grain diameters in typical CASS materials range from very small 0.5 mm (0.02 in.) to very large 41.0 mm (1.61 in.). A PNNL study found that the corresponding wavelength in CASS material employing a 1.5 MHz inspection frequency was approximately 3.8 mm (0.15 in.), and approximately 7.1 mm (0.28 in.) at an 800 kHz inspection frequency (Crawford et al. 2015). Thus, the use of 500 kHz to 800 kHz frequencies is necessary to provide adequate sound field penetration for flaw detection.

To scan the CS side of the weld, two different focuses were used: one at a focal depth of 24 mm (0.94 in.), to match Specimens 1 and 2, and one at a focal depth of 84 mm (3.31 in.), focusing at the ID of the specimen, as might be done in an inspection scenario. Figure 4.14 shows the baseline signal through CS parent material for both focal depths with the same gain setting of 40 dB. Figure 4.15 shows the baseline scans through CS for the 30°, 45°, and 60° cases with the 84 mm (3.31 in.) focal depth. For these scans, the gain was increased to 44 dB. Note that the scans terminated about 4 cm (1.6 in.) from the ID surface due to the specimen support obstructing the path of the pencil probe. Even so, essentially the entire sound field was captured.

Figure 4.16 shows the scans performed through the weld. The top row is the 30° scans, the middle row is 45°, and the bottom row is 60°. The left column is with the front of the probe at the weld centerline, the center column is with the front of the probe 10 mm (0.39 in.) to the right of the WCL, and the right column is 20 mm (0.79 in.) to the right of the WCL. The approximate probe positions are illustrated on the figure. The through-weld beam maps show a poorly focused sound beam that is scattered to the extent that very little sound penetrates through the weld. Virtually no sound energy is incident on the backwall, except in some cases where it preferentially traveled through the buttering. In short, the weld has a dramatically deleterious effect on the sound propagation at the frequency used.

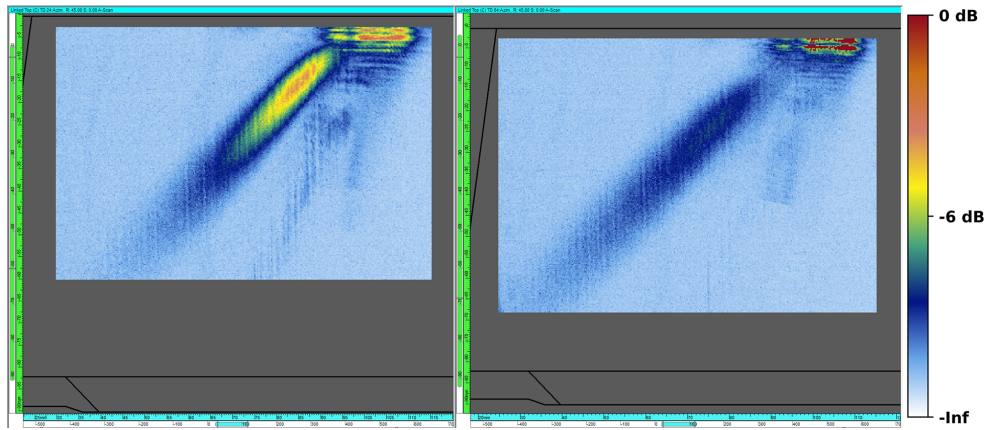


Figure 4.14. Baseline beam maps with focal depths of 24 mm (*left*) and 84 mm (*right*) at 45°.

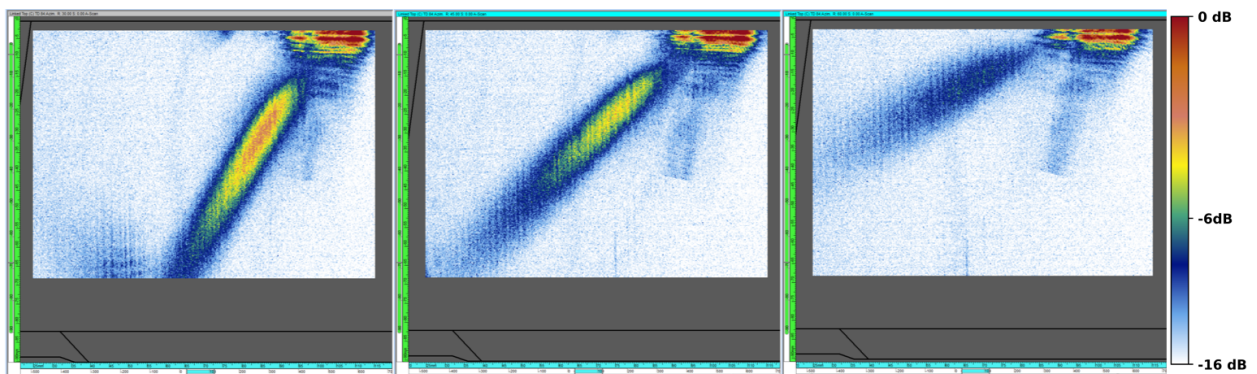


Figure 4.15. Baseline beam maps with a focal depth of 84 mm at 30° (*left*), 45° (*center*), and 60° (*right*).

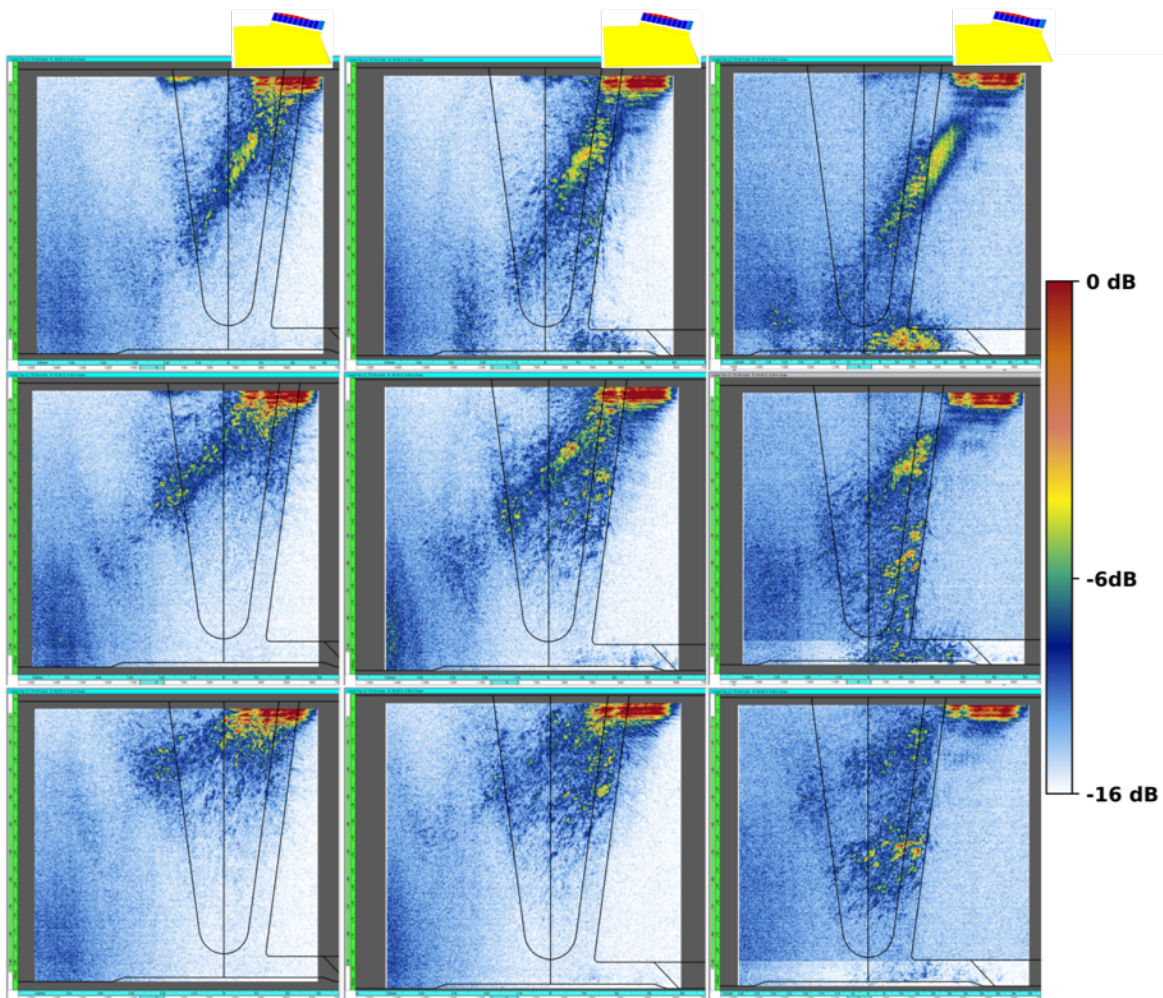


Figure 4.16. Through-weld beam scans with the DMW specimen at a focal depth of 84 mm. *Top row: 30°. Middle: 45°. Bottom: 60°. Left column: 0 mm from WCL. Center: 10 mm from WCL. Right: 20 mm from WCL.* The approximate probe positions are illustrated at the top of each column; probes are not to scale.

## 5.0 Beam and Flaw Response Simulations with an Austenitic Model

### 5.1 Introduction

Regulators at the NRC have received relief requests that include simulated beam coverages to justify the effectiveness (or ineffectiveness) of a proposed examination. In such requests, the weld material is typically treated like homogeneous material, and any scattering effects of the weld microstructure on the sound beam are ignored. Shortcomings of models with such limitations are recognized because austenitic welds can cause significant ultrasonic beam scatter, attenuation, and redirection due to the crystalline microstructure. Previous modeling by PNNL that was used to examine the basis for relief request approvals did not include material anisotropy, and thus the results of the modeling were recognized as a “best-case scenarios” (PNNL 2013c, b, a). In order to make appropriate decisions that affect operational safety, regulators need to have confidence in the modeling and the relationship between simulation results and UT examination outcomes (Cumblidge 2018). Therefore, it is desired that models be investigated that incorporate a higher degree of realism to demonstrate the practical limitations of modeling in predicting beam coverage and flaw responses.

Issues with inspection simulations of austenitic welds have been studied and described thoroughly in the literature (cf. Ploix et al. 2006; Liu and Wirdelius 2007; Carpentier et al. 2010; Gardahaut et al. 2012; Bannouf et al. 2014; Gardahaut et al. 2014; Kim et al. 2016). The fine-grained nature of austenitic welds complicates specimen modeling. Accurate descriptions of weld granular structure, including Euler angles and stiffness matrix elements, require destructive analysis and are often cost- and time-prohibitive. Furthermore, simulations with detailed specimen models can be computationally expensive, requiring days, weeks, or even months to complete on standard workstations. On the other hand, simplified specimen models based on mathematical constructs, such as that described by Ogilvy (1985), can be used to rapidly and efficiently estimate a grain structure in a smoothly-varying manner. However, such simplifications may miss important details, such as beam scatter, that strongly affect the realism of simulation outcomes. In this section, simulation outputs using a simplified Ogilvy weld model and a more rigorous weld model based on destructive analysis will be described and compared to experimental beam maps. Flaw response simulations will also be shown and discussed.

In preparation for beam and flaw response simulations through austenitic welds, PNNL performed a brief literature search to determine nominal values for stiffness matrix elements of common weld and piping materials. The stiffness matrix defines the sound propagation velocity in the different crystalline directions. Several publications were identified, many of which also described the use of modeling for simulation of sound propagation through austenitic welds or coarse-grained materials. The results of this search are presented in Appendix E.

## 5.2 Ogilvy Weld Model

As discussed above (Section 3.6) and in the previous PNNL modeling report (Dib et al. 2018a), the Ogilvy model provides a mathematical approach to representing the grain structure of an austenitic weld. The Ogilvy model is still commonly used in research in ultrasonic modeling of austenitic welds (Kim et al. 2016; Nowers et al. 2016; Jüngert et al. 2018; Zhou et al. 2018; EPRI 2019). The model is a built-in option in CIVA for defining weldments. This model is attractive because it is simple to implement.

In this study, PNNL's evaluation of the Ogilvy weld model focuses primarily on investigating the effects of the stiffness matrix values on beam propagation. The goal of this was to explore the range of different reported material properties on the simulation results—to see if there are significant differences in simulation outputs that arise as a result of stiffness matrix element inputs. Eight different weldment stiffness matrices were used based on those in Nageswaran et al. (2009), Tabatabaeipour and Honarvar (2010), Bannouf et al. (2014), Gardahaut et al. (2014), and Chen et al. (2015). For these simulations, the Ogilvy model parameters were  $T=1$ ,  $D=2$ ,  $\alpha=20^\circ$ , and  $\eta=1$ ; Figure 5.1 shows the weld model. The probe was defined as a  $10 \times 5$  element, 2 MHz PA probe with a 60% bandwidth. The specimen was defined to be 36 mm (1.3 in.) thick, and the beam focal depth was set to 33 mm (1.3 in.) at a focal law of  $45^\circ$  for longitudinal waves. The simulations used PA focal laws that were calculated over isotropic material (i.e., non-adapted focal laws, see Section 3.3). The weld material was defined as “steel” (with the associated default CIVA properties, with the exception of the stiffness matrix values) and the parent materials were defined as “stainless steel 302,” all with a density of  $8.03 \text{ g/cc}^3$  and an L-wave velocity of  $5660 \text{ mm}/\mu\text{s}$ . The probe was placed such that the beam exit point was off of the weld 5 mm (0.20 in.) from the weld toe.

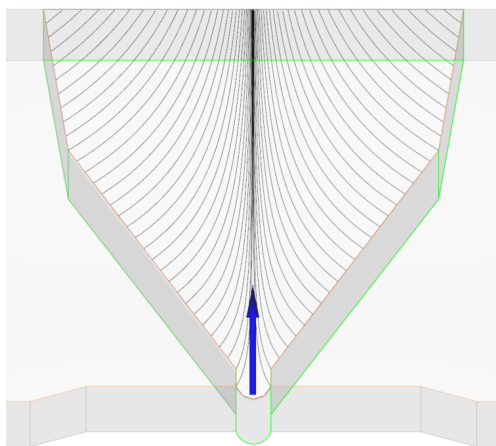


Figure 5.1. The weld region with the Ogilvy-model grains shown. The blue arrows indicate the origin, or center position, from which the Ogilvy model was calculated.

Figure 5.2 shows the simulation results with an isotropic weld to illustrate the beam profile in the ideal scenario. Figure 5.3 shows the eight beam simulation results with the Ogilvy weld model and different stiffness matrix elements. The title of each panel refers to the reference that the stiffness matrix values were taken from (note: Tabatabaeipour et al., abbreviated as “Tabataba,” reported multiple values for different weld scenarios). Images were normalized to the Tabatabaeipour 316L case, which had the highest simulated beam amplitude of the group.

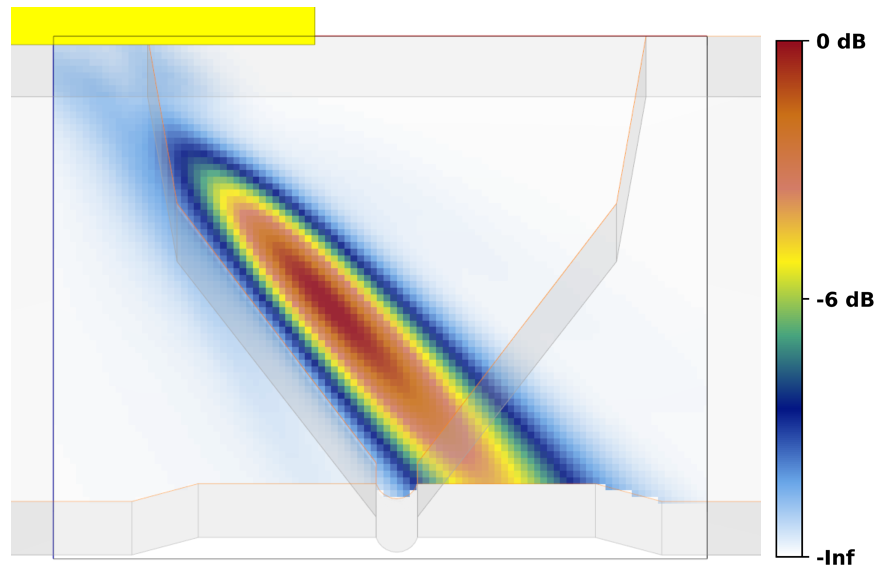


Figure 5.2. Beam simulation from a PA probe at 45° through isotropic weld material.

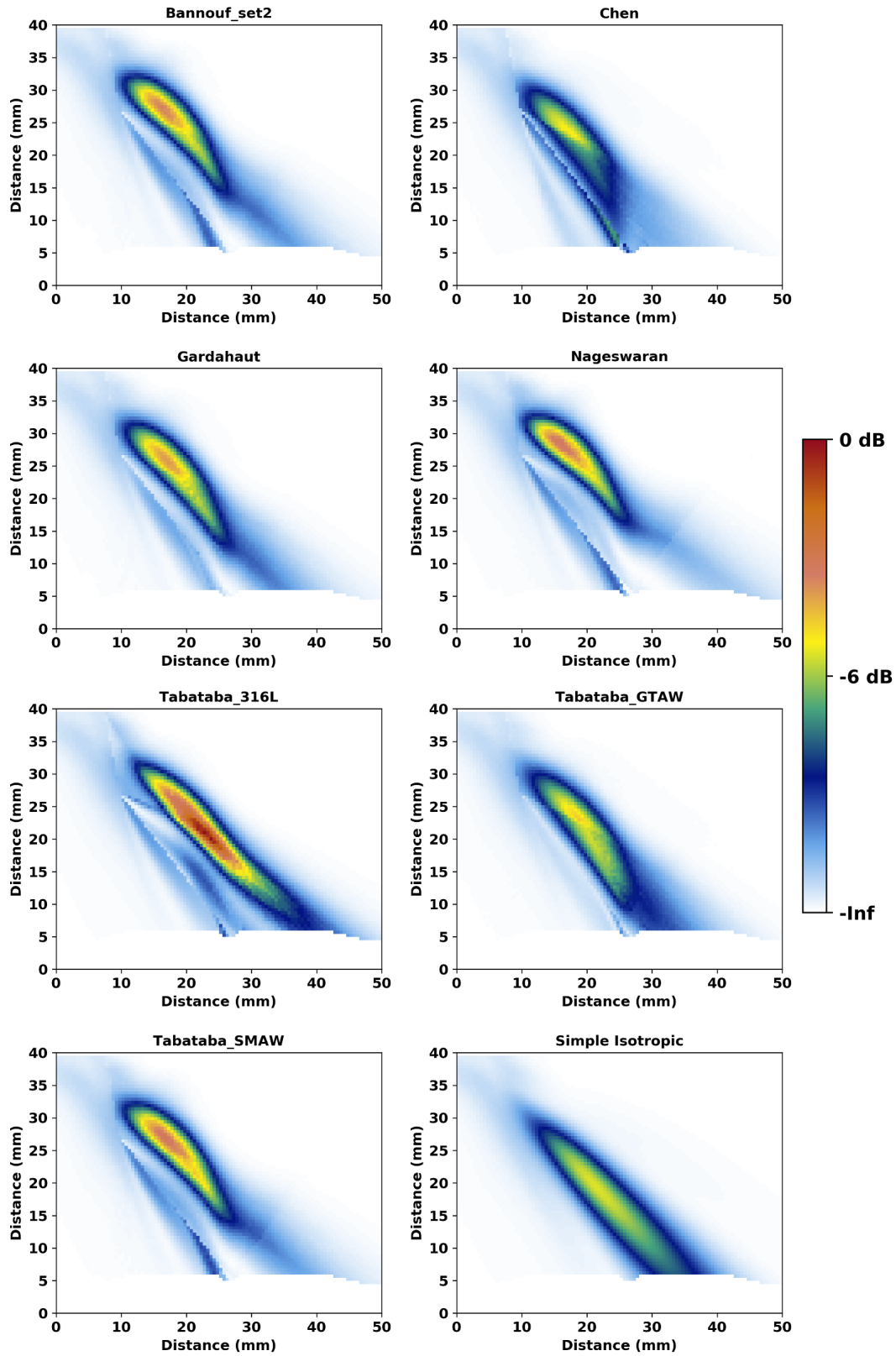


Figure 5.3. Beam simulation results for a simple isotropic weld and Ogilvy-model welds using stiffness matrix elements reported in the literature.

PNNL used the image similarity metrics (see Section 2.4) to compare the results of the Ogilvy simulations to the isotropic weld simulation; Table 5.1 summarizes the results. Considering all three metrics, the Tabatabaeipour GTAW (gas tungsten arc weld) scenario agreed most closely with the isotropic case: SSIM was closest to 1, MSE was closest to 0, and p was closest to 1. Note that the relatively high standard deviations (SD) of the metrics indicates a large spread of the data. That is, the different stiffness matrix elements had a strong impact on the sound propagation, causing large differences between simulations. This is an important result, because it confirms that **the choice of material properties in the model can have a strong impact on simulation outcomes.**

Table 5.1. Image similarity metrics comparing the Ogilvy scenarios to the isotropic case.

Run	SSIM	MSE	p
Bannouf_Set2	0.640	6.28	0.717
Chen	0.738	3.87	0.823
Gardahaut	0.711	3.93	0.823
Nageswaran	0.535	10.5	0.521
Tabataba_316L	0.602	9.39	0.715
Tabataba_GTAW	0.863	1.31	0.943
Tabataba_SMAW	0.621	6.87	0.706
Average	0.673	6.02	0.750
SD	0.108	3.24	0.132

The image similarity metrics can also be used to compare the individual results to the group average to find the scenario that is most “representative.” This average scenario, which was taken as the mean result of all the Ogilvy cases, is shown in Figure 5.4. Table 5.2 shows the image similarity comparisons of the different cases with the average. Results suggest both the Bannouf Set2 and Tabatabaeipour SMAW (shielded metal arc weld) cases are in approximately equally good agreement with the average scenario: both have the same SSIM, the MSE of Bannouf is lower, but the p of Bannouf is also lower, but only slightly. One could conclude that a representative Ogilvy weld scenario could probably be well described by either the Bannouf Set2 or Tabatabaeipour SMAW stiffness matrix elements. Therefore, these results could be used, for example, to justify the choice of nominal or typical stiffness matrix elements for flaw response simulations through Ogilvy welds. The advantage of having a nominal or representative geometry is that it allows one to forgo having to run time-consuming flaw response simulations on multiple geometries in order to determine a nominal flaw response. It is important to point out that beam simulations are often faster to run in CIVA than inspection simulations (depending on the options selected and the number of interactions calculated). Thus, for informative flaw inspection simulations, it is valuable to first determine nominal or representative weld parameters with multiple beam simulations, and then apply those parameters to the inspection simulation. Hence, quantitatively comparing each simulation result to the average result in order to find a representative case is useful.

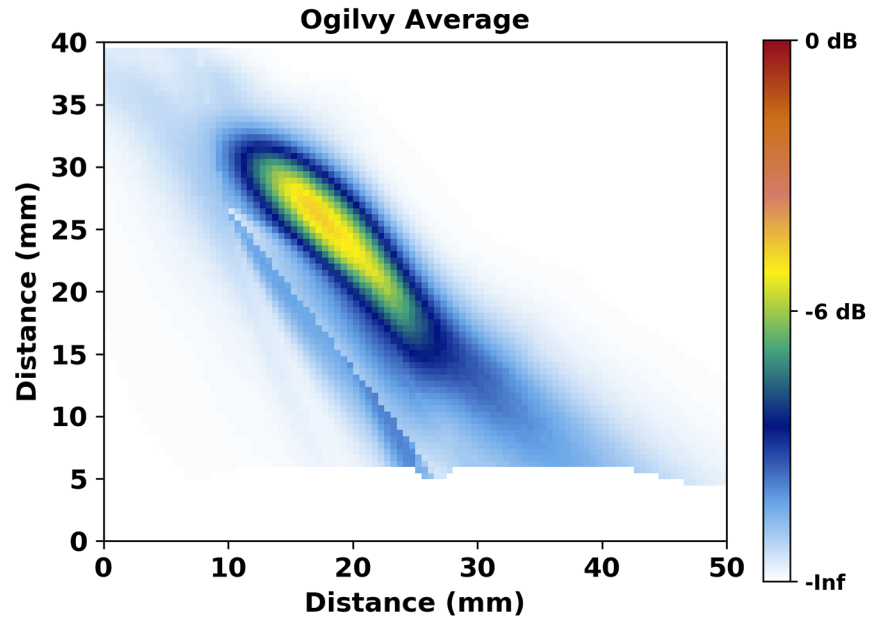


Figure 5.4. Average of the seven Ogilvy simulation results.

Table 5.2. Image similarity metrics comparing the Ogilvy scenarios to the average result.

Run	SSIM	MSE	p
Bannouf_Set2	0.931	0.429	0.979
Chen	0.700	2.83	0.843
Gardahaut	0.896	0.514	0.975
Nageswaran	0.822	1.80	0.908
Tabataba_316L	0.820	4.67	0.891
Tabataba_GTAW	0.782	2.02	0.898
Tabataba_SMAW	0.931	0.498	0.982
Average	0.840	1.82	0.925
SD	0.085	1.56	0.054

To attempt to predict the potential effects of the beam distortion in the different Ogilvy simulations on the ability to detect a flaw on the far side of the weld, the total sound incident on the specimen far-side backwall was calculated for each case; results are shown in Figure 5.5. In almost every case, the beam distortion due to the non-isotropic weld resulted in a significant decrease in sound energy incident on the far side of the weld. Again, the only difference between the simulations was the definition of the stiffness matrices.

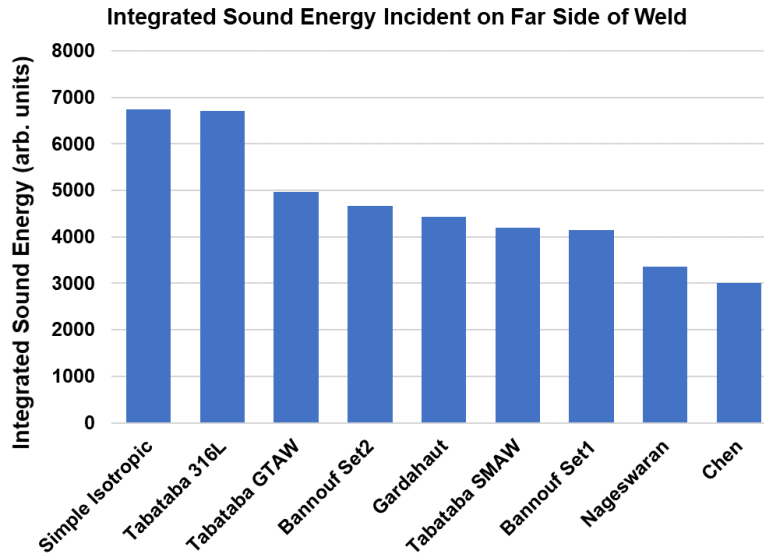


Figure 5.5. Total sound energy incident on the specimen backwall on the far side of the weld.

Additional simulations were run to investigate the response from a flaw on the far side of the weld. To save time, single A-scans were simulated. As described in Section 2.2, the flaw responses were calculated by fitting the individual peaks to a Gaussian curve and integrating the peaks. In this case, the root response was also prominent, so it was integrated separately. For example, Figure 5.6 shows the A-scan (left) and the Gaussian fits (right) for the isotropic case and for the Gardahaut case. Figure 5.7 shows the ratio of the flaw response to the root response, which was taken as a measure of how pronounced the flaw echo would be compared to a prominent geometrical feature. For the simple isotropic case, the flaw and root had responses that were nearly identical, resulting in a ratio of about 1. In every other case, the flaw response was somewhat lower or much lower than the root response, suggesting lower flaw detectability. For the Gardahaut case shown in Figure 5.6, the root and flaw responses were too overlapping to obtain reliable peak integrals, and for the Bannouf Set1 case, there was no identifiable flaw response. In the Nageswaran and Chen cases, there was a third distinct peak between the root and flaw responses whose origin was not identified.

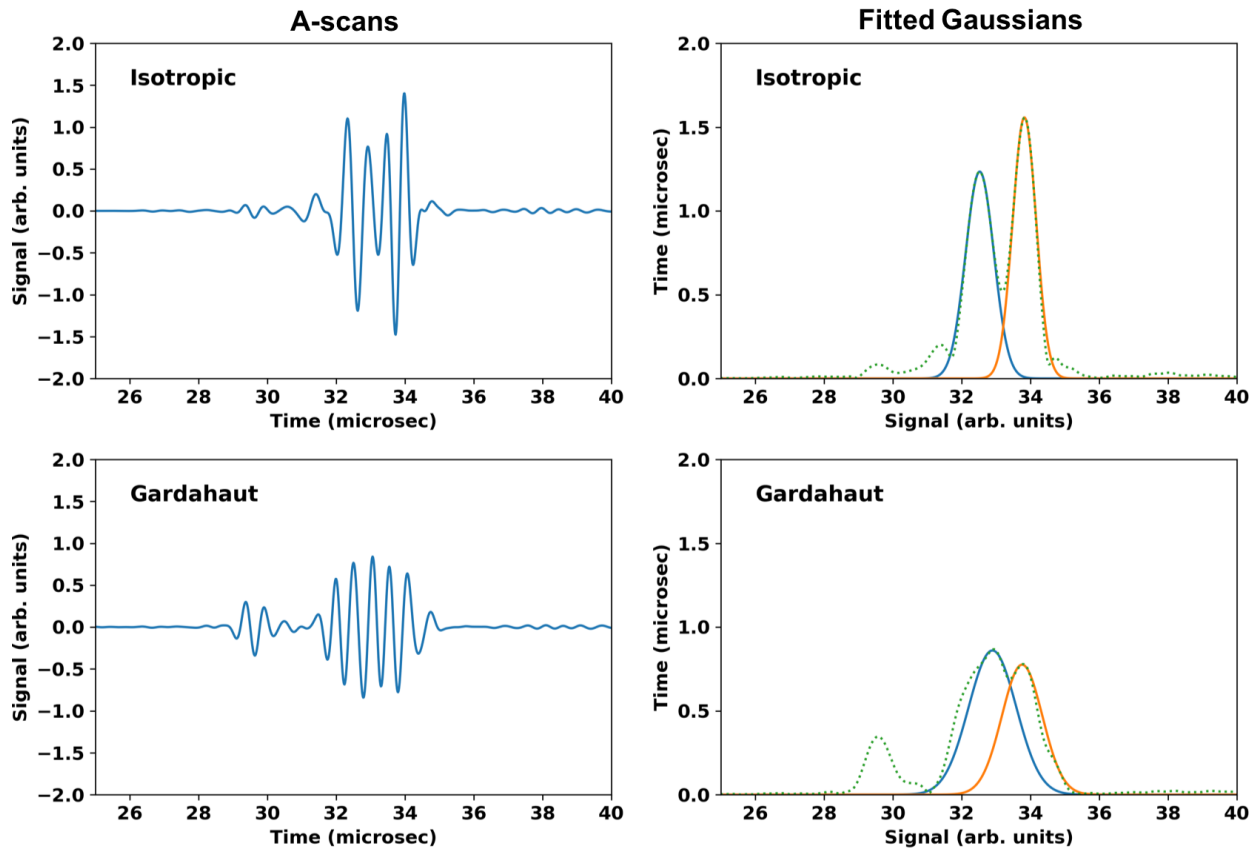


Figure 5.6. A-scans and Gaussian fits for the isotropic case (top row) and the Gardahaut case (bottom row). For the Gardahaut case, the peaks were too close together to obtain accurate area measurements.

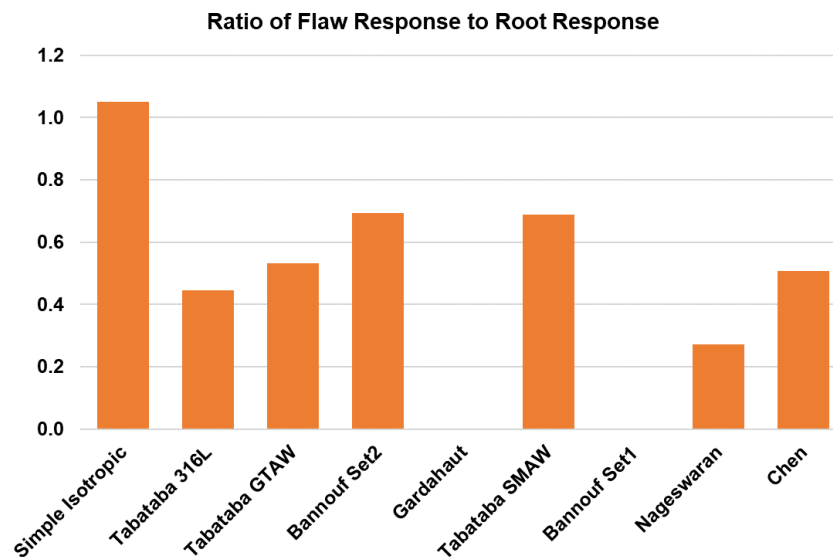


Figure 5.7. Ratio of the flaw response to the root response.

Results show that the stiffness matrices play a significant role in the propagation of the beam, which is consistent with the findings of EPRI (2019) and Gueudre et al. (2019). Consequently, the level of incident sound energy on the far side of the weld is strongly affected, as is the ability to distinguish the flaw signal from the root signal. Because it is difficult or impossible to predict *a priori* the effects of specific stiffness matrix elements on the sound propagation through the weld, PNNL suggests running multiple beam and/or flaw-response simulations with a range of realistic material properties obtained from direct measurements or the literature in order to determine a nominal scenario and a range of potential uncertainty. Naturally, the exact material properties should be used when available; however, for field inspections, it is not expected that such information will be available.

A qualitative comparison of the beam simulation results shown in Figure 5.3 can be made with the experimental results shown in Section 4.5 and in Figures 4.9 and 4.10 in Dib et al. (2018a). A comparable comparison was also done by Gardahaut et al. (2014) using a beam-mapping technique similar to that used by PNNL. In the simulations, the Ogilvy weld model shows virtually no beam scatter and good beam formation. However, prominent beam scatter and little or no beam formation was observed experimentally through austenitic welds. **Therefore, the Ogilvy model, which does not include grain boundaries and relies on a continuous gradient of preferred sound propagation, is not suitable for austenitic weld simulations.**

### 5.3 Austenitic Weld Model

Results from the Ogilvy model simulations indicate that any simulations through austenitic welds should include grain structures that result in realistic beam scatter. An approach with more geometric realism will likely require complex weld geometry models and may therefore push the limits of simulation software and users' ability to generate appropriate geometries. More simplistic approaches may be easier to simulate but lack important attributes of realism and may therefore overestimate (or underestimate) beam coverage or flaw detection capabilities. This section describes a modeling approach where the model specimen geometry was based on direct measurements of grain structures.

#### 5.3.1 Model Development

PNNL initiated a study to characterize weld microstructures for use in simulations. This study was done in an effort to investigate the effect of realistic geometries on simulation outputs and the extent to which uncertainties in weld microstructure contribute to simulation accuracy. A section of a WSS-WSS austenitic weld from Specimen 3C-022 (Figure 5.8) was cut and polished in preparation for EBSD (electron backscatter diffraction) measurements (Schwartz et al. 2000; Humphreys 2001). EBSD is a scanning electron microscope technique that measures grain shape, size, and crystalline orientation, which is described by a set of Euler angles. Along with published (or measured) anisotropy information on ultrasonic wave speeds and attenuation, the grain geometry information can be incorporated into the weld model used in the simulation studies (Nageswaran et al. 2009; Carpentier et al. 2010; Mark et al. 2014). The EBSD measurements described herein were performed at PNNL. Three separate scans were required to obtain a full dataset on the weld sample due to its size. The sample was held at different orientations for the three scans to facilitate access in the EBSD instrument. Data sets were then rotated to the same orientation and combined in post-processing.

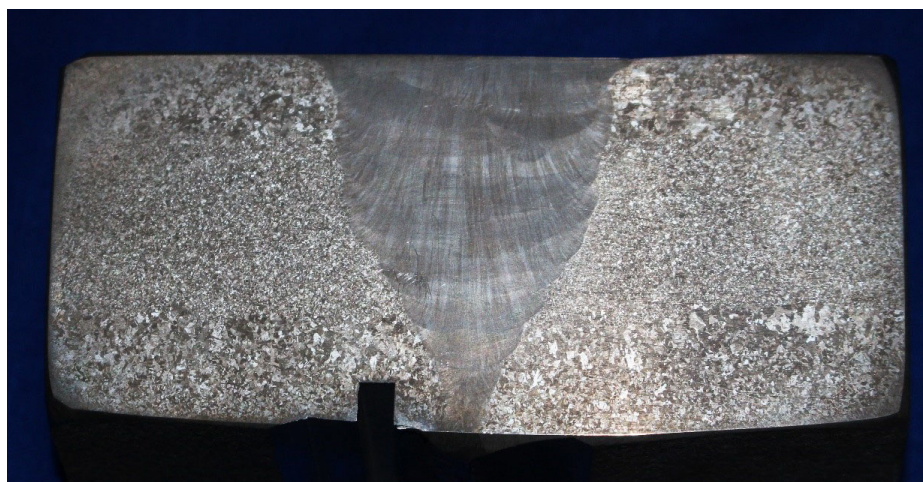


Figure 5.8. Cross section of the austenitic weld used for EBSD data acquisition.

EBSD results are often shown in inverse pole figures (IPF); see Figure 5.9. These figures show the x, y, and z components of the crystal orientation with respect to the sample (Schwartz et al. 2000). From the IPF data, the information needed to calculate the Euler angles can be derived on a pixel-by-pixel basis. However, the EBSD data were acquired at  $4\ \mu\text{m}$  (0.00016 in.) resolution, which is several orders of magnitude smaller than the wavelength of sound that will be used in the simulations and is therefore much smaller than the resolution required for generating a useful model. Thus, significant downsampling of the images was required to generate a geometry that can be imported into CIVA. For an adequate simulation of scattering, the smallest grain size should be no smaller than about 10% of the wavelength (in steel at 2 MHz, the wavelength is about 3 mm [0.12 in.]) (Nageswaran et al. 2009; Chen et al. 2015). Therefore, the resolution of the raw EBSD data is about 100 times too high. As the exact level of downsampling required to generate a realistic model is unknown, an important question to answer is: how much detail is needed in defining the grain shapes and orientations in order for CIVA to produce suitably accurate simulation results? To answer this question, the same geometry with multiple levels of downsampling needs to be tested.

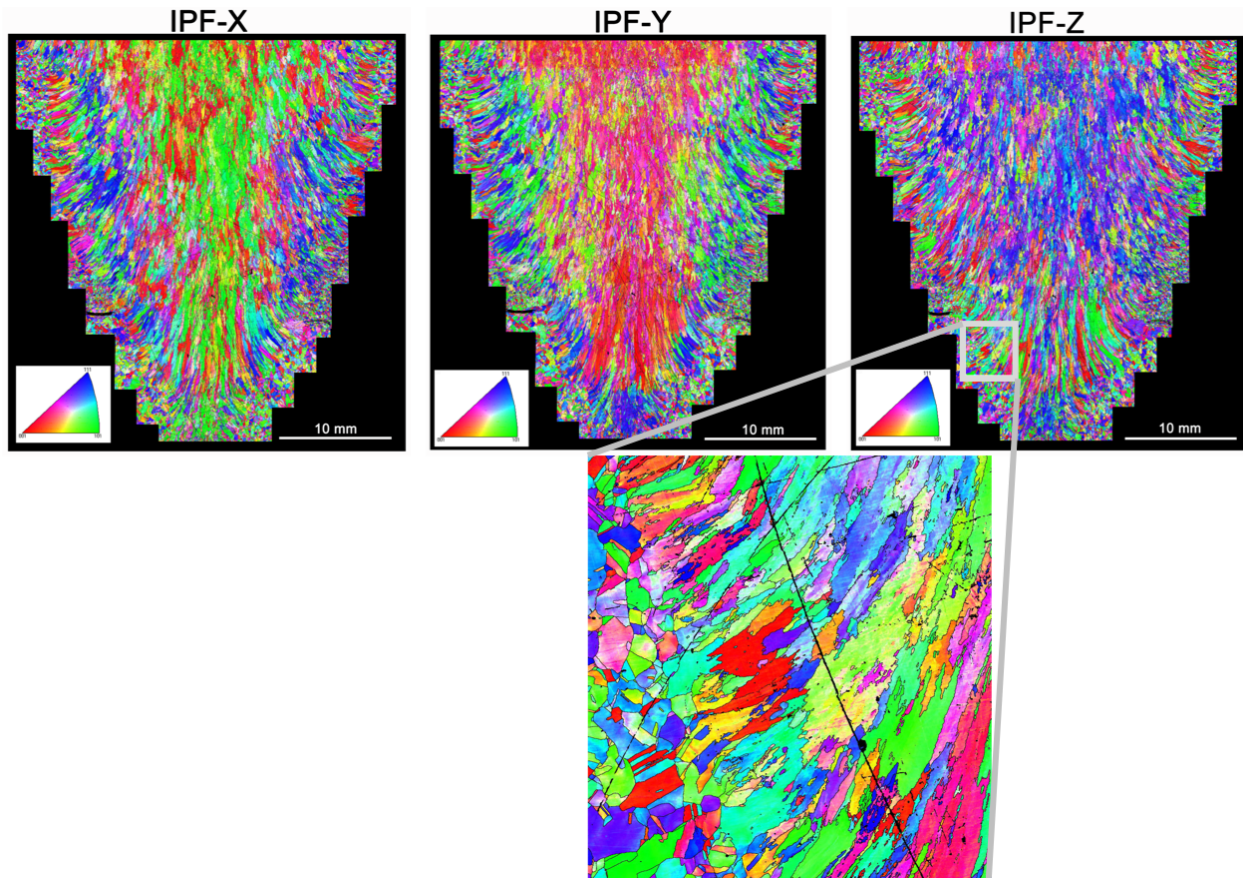


Figure 5.9. EBSD inverse pole figures for the X, Y, and Z axes. Each color represents a different crystalline direction, each of which can be defined by a set of Euler angles. The black line on the inset is an artefact from a subtle scratch on the specimen surface.

There are several approaches to doing the image processing. For example, Nageswaran et al. (2009) used an “orientation unification” technique, which combines neighboring grains and assigns the Euler angle value of the dominant grain. This method produces excellent representations of the grain structure, but it is not easily scalable without loss of information. PNNL desired a technique where the same weld could be tested at different grain-size scales. A downsampling method that is well suited for this application and is objective, rapid, repeatable, and robust is called “quadtree decomposition.” This method is used in, for example, image processing, image compression, and mesh computerized tomography (CT) generation. A shortcoming of the quadtree approach is the fact that it produces square grains instead of naturally-shaped grains. With a small number of grains, this could be a problem for modeling; however, if the number of grains is high enough, then the effects of the grain shapes should become less important as diffusion-like effects of sound scatter dominate.

The quadtree process essentially involves recursively subdividing an image into squares, or quads, and interrogating each quad based on a metric of homogeneity. The metric of homogeneity can be the standard deviation (SD) of the pixel values within the quad. If the SD exceeds a pre-set threshold value, then the quad is decomposed into daughter quads (e.g., moving from left to right in Figure 5.10). If the threshold value is not exceeded, then the quad is left alone. The process is repeated until all the quads are either below the threshold value or

until they reach a pre-determined minimum size. At the end, all quads are assigned the mean value of the image pixels within the quad. An example of a quadtree decomposition is shown in Figure 5.11. This is a photograph of Times Square that has been downsampled using quadtrees—notice that each square contains a single color value, so there are no color variations within a given square. An advantage of quadtrees is that they preserve edges and features while minimizing processing time. Regions with high detail are characterized by small quads while large quads dominate in relatively homogeneous regions. Furthermore, decomposed images are easy to index, because each quad can be fully defined by four numbers: a mean value, an edge length, and spatial x and y coordinates of one corner.

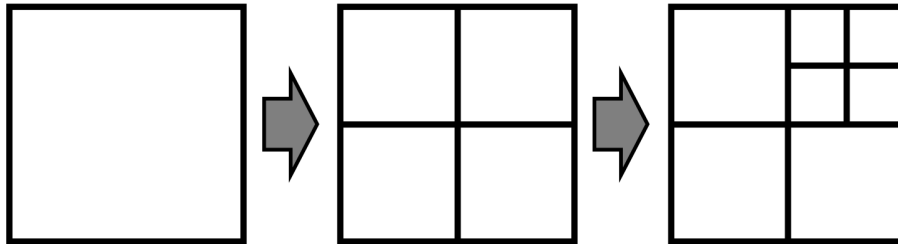


Figure 5.10. An illustration of the quadtree decomposition process. Large quads are decomposed into smaller quads depending on if a homogeneity metric has been reached.

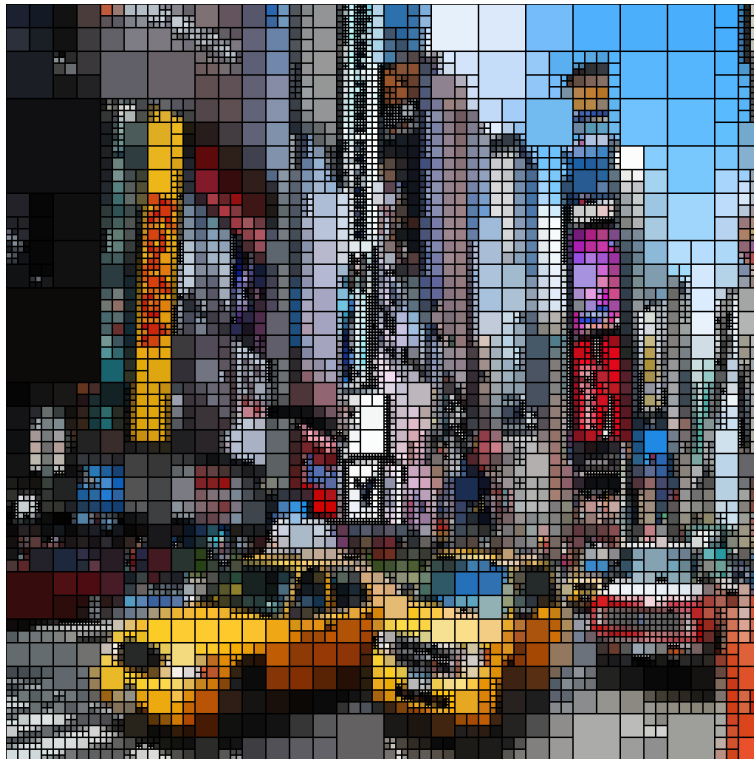


Figure 5.11. Example of a quadtree decomposition. This image is the result of a quadtree decomposition of a photograph of Times Square.

Source: <https://imgur.com/gallery/7qtkL> by “AndrewVetovitz”.

In pilot work, PNNL automated the quadtree process in MATLAB and applied it to the IPF images. The homogeneity threshold used was a measure of grain orientation uniformity, and the

interrogation was done by calculating the mean and SD of the grain orientations within a quad. PNNL used trial-and-error to determine ideal threshold values for the decomposition. Work is ongoing as of this writing to apply the process directly to the raw EBSD Euler angle data, which is complicated by the file size and assembling of multiple EBSD scans.

Even with the quadtree decomposition, the geometry needs to be further simplified to minimize the time that CIVA needs to process the geometry and compute the simulation. The image was simplified by reducing the total number of sets of Euler angles and, by extension, the total number of regions without affecting the minimum region size. For example, say the decomposition resulted in 100 regions and therefore 100 unique sets of Euler angles. The geometry can be simplified by consolidating the 100 sets of angles into a smaller number of bins, such as 10, each bin containing a group of closely-related Euler angles and assigned the average value. Reducing the number of sets of Euler angles has the effect of reducing the total number of regions, because bordering regions that end up in the same bin will become one region, as they share the same material properties. The number of grain regions and complexity of the geometry increases with additional downsampling and with increasing the number of bins.

Figure 5.12 shows examples of IPF images decomposed to quads with a minimum size of  $256 \times 256$ ,  $128 \times 128$ , and  $64 \times 64$  pixel resolution, and then binning was applied to group similar mean EBSD values of each square (the different bins are indicated by color). Recall, the original IPF images represent EBSD data acquired with  $4 \mu\text{m}$  ( $0.00016 \text{ in.}$ ) resolution; that is, each pixel of the IPF images represents a  $4 \mu\text{m} \times 4 \mu\text{m}$  area. The target grain size for the modeling is one tenth of a wavelength (at 2 MHz in steel), which equates to about 70 IPF pixels in length. Therefore, the  $64 \times 64$  pixel decomposition, which will result in quads that are  $0.26 \text{ mm} \times 0.26 \text{ mm}$  ( $0.010 \text{ in.} \times 0.010 \text{ in.}$ ), will be used as a lower bound for testing necessary grain resolution. An advantage of the quadtree downsampled images is that they are straightforward to convert into a CAD format that CIVA can import because they comprise straight line segments.

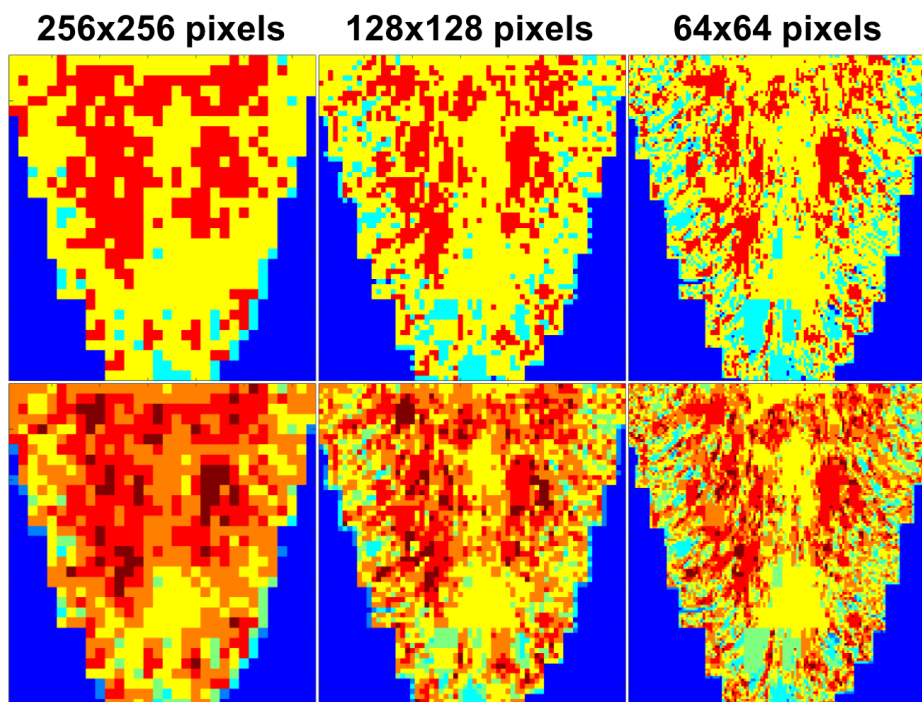


Figure 5.12. Examples of decomposed and binned IPF image data. Top row: 3 Euler angle bins. Bottom row: 7 Euler angle bins.

Unfortunately, PNNL encountered significant problems with importing the geometries into CIVA 2017. First, the method that CIVA uses to organize and sequence the different regions of the geometry is not straightforward and includes a rounding-error bug. Second, CIVA's CAD interface has a bug preventing it from handling perpendicular intersections of line segments very well, so CIVA often rejects geometries that contain such intersections. PNNL's approaches to working around these two problems are described below.

First, it is critical to assure proper correspondence between each region and its material properties measured from EBSD in order to have a model that faithfully represents the true-state. Typically, the CIVA user will manually assign material properties region-by-region (this is the usual approach with simple geometries) using a dropdown menu, but with hundreds or thousands of regions this approach is time-prohibitive and prone to errors. Alternatively, one can leverage the fact that CIVA uses xml files to store definitions of specimen geometries and region properties. Ideally, the specimen interface boundaries generated by the quadtree decomposition and the corresponding region material properties would be written sequentially to an xml file by the user and imported into CIVA where the regions would be read-in in the proper sequence. However, the regions are not listed sequentially in the xml file, nor are they labeled. Furthermore, determining the "proper sequence" is challenging because of the algorithm that CIVA employs. CIVA sequences the regions based on the relative positions of the iso-barycenter,<sup>(a)</sup> or centroid, of each shape, moving across the image top-to-bottom, left-to-right. However, CIVA's calculation of the iso-barycenter is extremely complicated, and there are special cases that increase the complexity, such as when the iso-barycenter lies outside of the shape boundary or inside a grain that lies inside another grain. PNNL could not duplicate the

(a) The iso-barycenter is the centroid, or "center of gravity," of a shape based on the endpoints of the line segments, with each endpoint given equal weight.

CIVA sequencing algorithm, even with multiple, increasingly detailed explanations from EXTENDE. To add to the problem, PNNL found that rounding errors in CIVA were contributing to some arbitrary region sequencing, to the point that CIVA itself was changing the ordering after a simple scale factor was applied to the geometry. So, even if PNNL could duplicate the region sequencing algorithm, these rounding errors could unpredictably affect the final region sequencing.

To work around the problems with CIVA, PNNL created a multi-step process that was guaranteed to successfully duplicate the correct region sequencing. However, this came at the expense of additional geometrical complexity and potentially longer computation times. The crux of the workaround was to guarantee that the calculation of the centroids is trivial, consistent, and unambiguous by using only rectangular, columnar regions. Figure 5.13 shows an example of this for the 256-pixel decomposition with 7 Euler angle bins. The additional columns add to the geometrical complexity by increasing the number of regions and region interfaces. Fortunately, based on simulation tests, it appears that CIVA ignores interfaces between regions that have identical material properties, so the additional interfaces between such regions (i.e., regions of the same color in Figure 5.13) do not appear to add a significant amount of simulation time. However, CIVA does spend significant resources on rendering and processing the geometry, so additional regions slow down the process of loading the geometries and displaying simulation results. Some of the more complex geometries take upwards of an hour to open in CIVA, if they open at all.

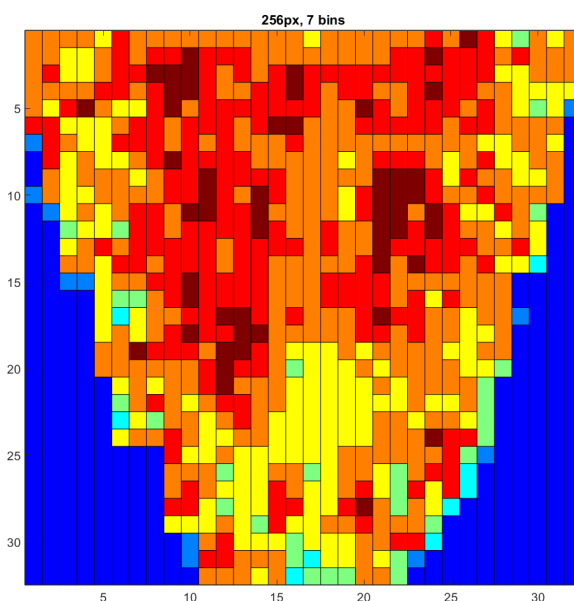


Figure 5.13. The 256-pixel, 7-bin geometry with columnar regions used for simulations. Different colors indicate different bin regions.

Second, CIVA's CAD interface often rejects cases where four perpendicular line segments meet at a single point, termed "quadpoint intersections." The quadtree-decomposed images, by their very nature, have many such intersections. To work around the problem, PNNL redefined such intersection points by moving a y-coordinate of one of the segments by 0.01 units, the smallest resolution unit that CIVA can recognize. Figure 5.14 shows an example of this approach. All of the quadpoint intersections were adjusted so that CIVA could process the geometries. This step has a negligible effect on the final geometry, except that each quadpoint requires the addition of a vertical line segment, which adds to the complexity of the geometry and slows down CIVA.

Caution was exercised when implementing this workaround, because moving the corner points of a region could affect the location of the centroid. The effect would be only slight, but, as PNNL observed, it could be enough to affect the sequencing of the regions. Because the sequencing is done top-to-bottom then left-to-right, adjusting only the y-coordinate of a corner point does not affect the region sequencing.

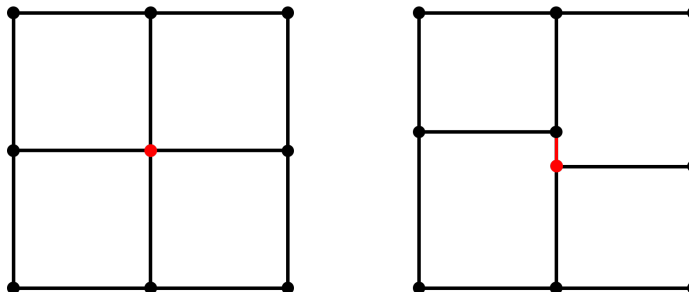


Figure 5.14. Illustration of how quadpoint intersections were treated so that CIVA would process the geometry. Left: Dots indicate line segment termini, and the red dot indicates a quadpoint intersection. Right: The red line segment and red dot indicate new elements that were added to the geometry. The size of the red segment was exaggerated to illustrate the concept.

PNNL used MATLAB to create the custom weld geometries and assign material properties to each region. The final process requires multiple steps in order to work around the CIVA complications and is summarized below:

1. Apply the quadtree decomposition and binning to create the desired weld geometry.
2. Modify the geometry to be CIVA friendly by removing all quadpoint intersections.
3. Define the different interfaces and surface types (i.e., frontwall, backwall, and sidewall).
4. Export the geometry as a dxf (CAD) file.
5. Open the dxf file in CIVA's 2D CAD editor and verify that CIVA can validate the geometry for use in a model.
6. Export the geometry file from CIVA as an xml file. This file contains all of the original line-segment definitions as well as placeholders for the material property information for each region, such as Euler angles and stiffness matrix elements.
7. Edit the xml file in MATLAB to add material property information for each region. (This is where it is critical that the region sequencing algorithms of CIVA and MATLAB agree.)
8. Import the edited xml file back into CIVA. The geometry will be the same as before but now will include the material properties of each region. The model geometry is ready for simulations.

PNNL automated and generalized the above steps so that they can be applied to arbitrary grain structures, such as coarse-grained CASS, where the grain boundaries are determined through light photography (see Section 7.2).<sup>(a)</sup>

(a) CIVA 2020 was released after this work was complete. PNNL found that many of the problems with importing complex geometries were addressed. In particular, geometries with quadpoints are no longer a problem, so Step 2 above can be eliminated. Also, the algorithm used to define the geometries is much more efficient; geometries open faster, and geometries that would not open in CIVA 2017 will open in CIVA 2020.

### 5.3.2 Beam Simulations

Beam simulations were performed using the 3-bin and 7-bin austenitic weld geometries generated from the quadtree approach. The probe used in the simulations shown below was a 2 MHz dual-element, TRL probe with a 45° refraction angle and 37 mm (1.46 m) crossover depth in steel. The exit point was placed just off the weld such that the bulk of the sound beam would have to traverse through parent material, weld material, and parent material again to reach the inner-diameter (ID) surface on the far side of the weld. The probe position was the same for all simulations. Beam simulations were initially run with a 3D computation zone and 0.5 mm (0.02 in.) isotropic resolution and later a 2D computation zone to reduce simulation time. The simulation included L-waves only and no reflections at surfaces or interfaces. For more rapid simulation times at this stage, the accuracy factor was set to 1. Figure 5.15 shows the simulation results through a simple, isotropic weld.

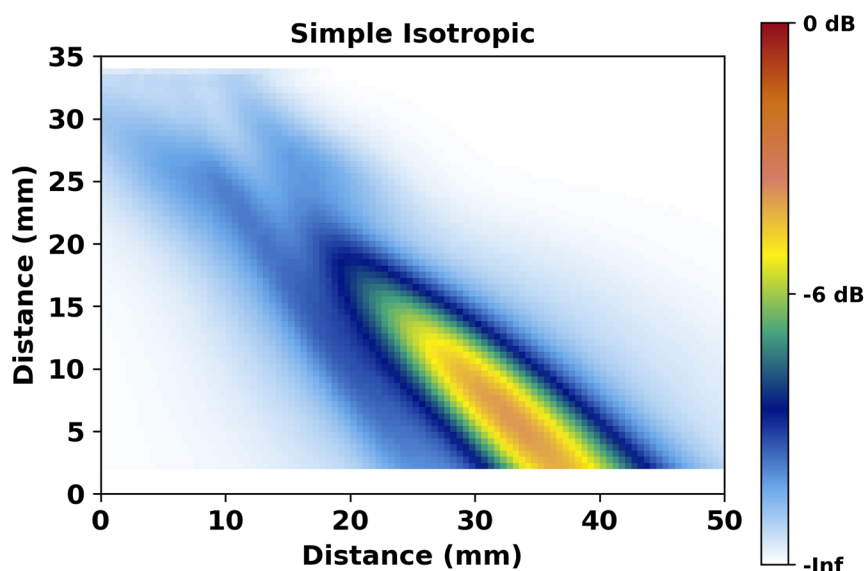


Figure 5.15. Beam simulation through isotropic material with a 2 MHz TRL probe at 45°.

The first weld geometry investigated was the simplest case generated from the IPF images, using the largest quads (256 pixels) and the smallest practical number of different grain orientations, or Euler angles (3 bins). For reference, 256 pixels in this geometry is approximately 40% of a wavelength at 2 MHz. This geometry is pictured in Figure 5.16. The geometry consists of 272 regions and 832 line segments, or interfaces, most of which separate regions with identical material properties and are therefore essentially ignored by CIVA. The geometry was extruded in the z-direction (into the page); thus, there is no variation of grain geometries in that dimension. Ten different welds with this geometry were prepared, each with the same stiffness matrix elements but different sets of Euler angles. Multiple geometries (defined by the same grain structure but different sets of Euler angles) can be thought of as imitating different positions on the weld of a given specimen, because grain structures vary spatially. Nominal stiffness matrix values were adapted from the literature (Liu and Wirdelius 2007; Tabatabaeipour and Honarvar 2010; Gardahaut et al. 2012; Bannouf et al. 2014), and Euler angles were randomly assigned to the regions from those reported in Chen et al. (2015) such that each of the ten cases had a unique assignment of Euler angles. This choice of angles is largely arbitrary, but those from the literature provide an adequate basis for performing the initial simulation tests in CIVA. Note that the process of assigning angles was started prior to the final

EBSD Euler angle data being available, because of issues with interpreting and exporting the raw EBSD data, so values from the literature were used instead of the measured values.

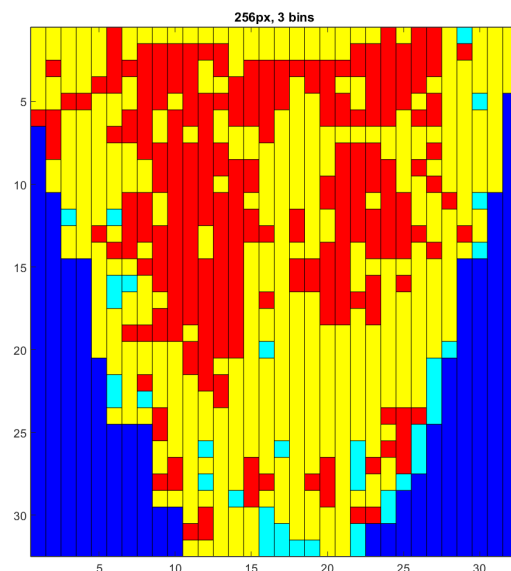


Figure 5.16. The 256-pixel, 3-bin geometry with columnar regions used for simulations. Different colors indicate different bin regions.

Figure 5.17 shows the beam profile results of the ten different weld scenarios. Data were normalized to the maximum sound intensity of the entire image set. Qualitatively, results suggest that significant differences exist between the simulation scenarios shown in Figure 5.17. Recall, the only change made between each scenario was the assignment of different Euler angles—all other model parameters were identical. Note some of the scenarios appear to have strong sound fields and others do not. Upon further investigation of the ray drawings of the sound beam paths in CIVA, it was observed that some scenarios prevented the transmit and receive beams from intersecting because of redirection of the sound in the z-direction. This may be exaggerated by the fact the grains were extruded in the z-direction, essentially resulting in elongated grains that may have a stronger impact on beam propagation in the elongated direction than if a true 3D weld geometry was used. Even so, results clearly illustrate the significant effect crystalline orientation alone can have on beam propagation.

By comparing Figure 5.17 and Figure 5.3, one can readily observe that beam scatter, or the spreading of the sound field across the image, is virtually nonexistent in the Ogilvy cases but is prominent in the 3-bin quadtree case. The Ogilvy model does a good job of representing the overall grain structure but not the crystalline orientations. In the Ogilvy depiction, the grain orientations are varied smoothly and continuously from one grain to the next, resulting in gentle bending of the sound beam and minimal scatter. In a real weld, on the other hand, the relationship between the crystalline orientations of neighboring grains appears to be largely random; cf. Figure 5.9 and Nageswaran et al. (2009). Thus, in the Ogilvy-model simulation, beam steering and redirection are smooth and continuous, whereas in a more realistic, multi-grained geometry, significant beam scatter is the result.

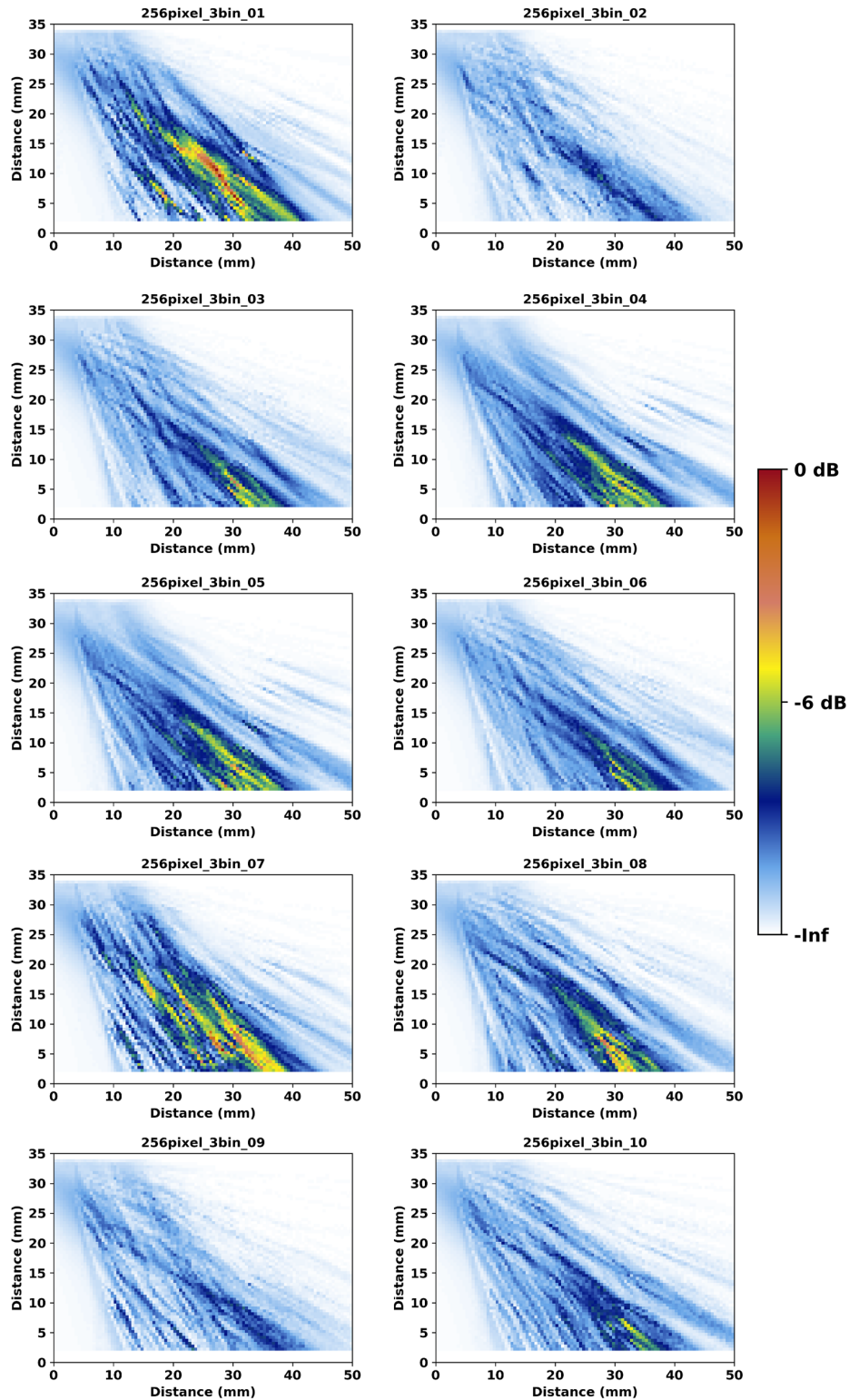


Figure 5.17. Beam simulation results of the ten 3-bin, 256-pixel scenarios with the 2 MHz TRL probe at 45°. Data were normalized to the peak signal of the image set. The X-axis is in mm from the beam exit point, and the Y-axis is in mm from the ID surface.

Results can also be considered quantitatively using the image similarity metrics. Table 5.3 shows the metrics resulting from comparison to the simple, isotropic case shown in Figure 5.15. Notice that SSIM values are much lower and MSE values are much higher than their counterparts in Table 5.1. This indicates that these scenarios differ more strongly from the isotropic case than the Ogilvy scenarios do, probably because of beam scatter. Additionally, the SDs are much lower (as a fraction of the average) in Table 5.3 than in Table 5.1. This is because the scatter tends to smear out the sound beam, making all of the simulation scenarios more similar to one another in the 3-bin scenarios than in the Ogilvy scenarios. Again, beam scatter is a prominent feature of simulation results from the austenitic weld model and of empirical beam maps but is lacking from the Ogilvy model.

**Table 5.3. Similarity metrics calculated for the ten 3-bin scenarios as compared to the simple, isotropic case.**

Run	SSIM	MSE	p
256_3bin_01	0.370	32.8	0.859
256_3bin_02	0.340	64.2	0.825
256_3bin_03	0.391	41.5	0.837
256_3bin_04	0.360	39.3	0.812
256_3bin_05	0.355	40.4	0.805
256_3bin_06	0.411	38.7	0.871
256_3bin_07	0.365	36.3	0.851
256_3bin_08	0.265	45.1	0.780
256_3bin_09	0.318	65.6	0.771
256_3bin_10	0.289	46.3	0.821
Average	0.346	45.0	0.823
SD	0.045	11.2	0.033

While SSIM and MSE are much different in the 3-bin results as compared to the Ogilvy results, the correlation coefficient metrics tend to show less variation. The lack of variation is because the vast majority of data points have low signal intensity or are background, which gives a strong weighting to the data correlation. All scenarios are similar in this regard, so the correlations do not vary as strongly as the other metrics. A fix to this issue may perhaps involve removal of low-intensity pixels (below, say, the 20 dB threshold), but this has not yet been tested.

Figure 5.18 shows the average of the 3-bin simulations. This image is also normalized to the maximum response of the ten simulation images. The average case shows considerable scatter while at the same time a good degree of beam formation. Table 5.4 shows the results of the similarity metrics with the average image as the reference. Naturally, the metrics indicate much stronger image similarity to the average case than to the isotropic case in Table 5.3. Using these data, one can determine that Run 04 has the closest agreement with the average image, according to two of the three similarity metrics (with MSE only slightly higher than that of Run 06). Therefore, the metrics suggest that Run 04 may be a good representative weld model for use in inspection simulations through this austenitic weld model.

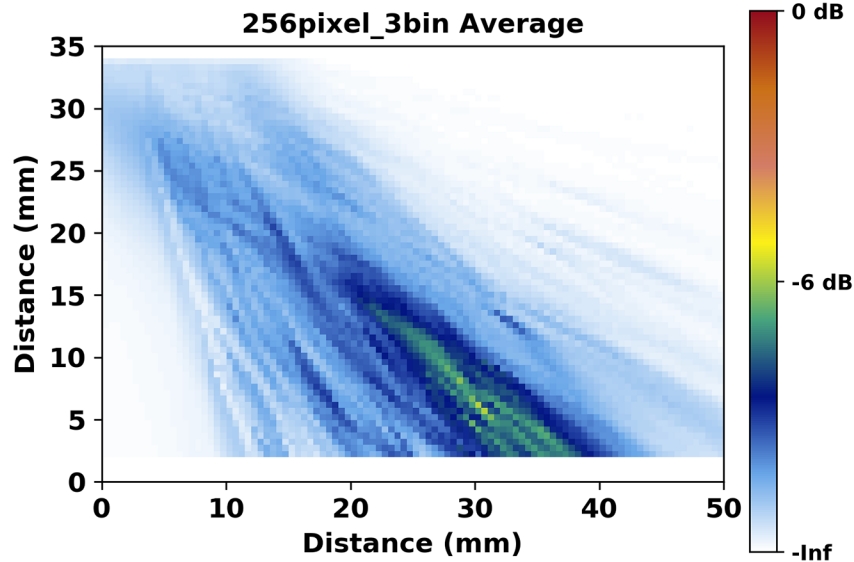


Figure 5.18. Average image of the 256-pixel, 3-bin simulations.

Table 5.4. Similarity metrics calculated for the ten 3-bin scenarios as compared to the average.

Run	SSIM	MSE	p
256_3bin_01	0.537	32.0	0.914
256_3bin_02	0.458	17.2	0.878
256_3bin_03	0.517	7.45	0.925
256_3bin_04	0.684	6.39	0.959
256_3bin_05	0.670	7.78	0.952
256_3bin_06	0.547	6.22	0.937
256_3bin_07	0.540	38.7	0.898
256_3bin_08	0.539	11.6	0.912
256_3bin_09	0.543	16.8	0.856
256_3bin_10	0.528	9.58	0.899
Average	0.556	15.4	0.913
SD	0.069	11.3	0.032

For the next test, a somewhat more realistic and complex weld geometry with 7 bins was created, and comparisons were made with the simple 3-bin case. Figure 5.13 shows the 7-bin, 256-pixel geometry. This geometry consists of 453 regions and 1360 line segments. As with the 3-bin case, Euler angles from Chen et al. (2015) were randomly assigned to the 7 bins to create 10 unique cases. Other than the geometry and Euler angles, all 3-bin and 7-bin model parameters were identical.

Figure 5.19 shows the beam simulation results of the ten 7-bin scenarios. Images are normalized to the overall maximum of the image set. Qualitative comparisons to the 3-bin cases in Figure 5.17 suggest there is more beam scatter and generally less beam formation in the 7-bin scenario, while more simulation-to-simulation signal intensity variations are visible in the 3-bin results. For reference, Figure 5.15 shows the simple, isotropic case.

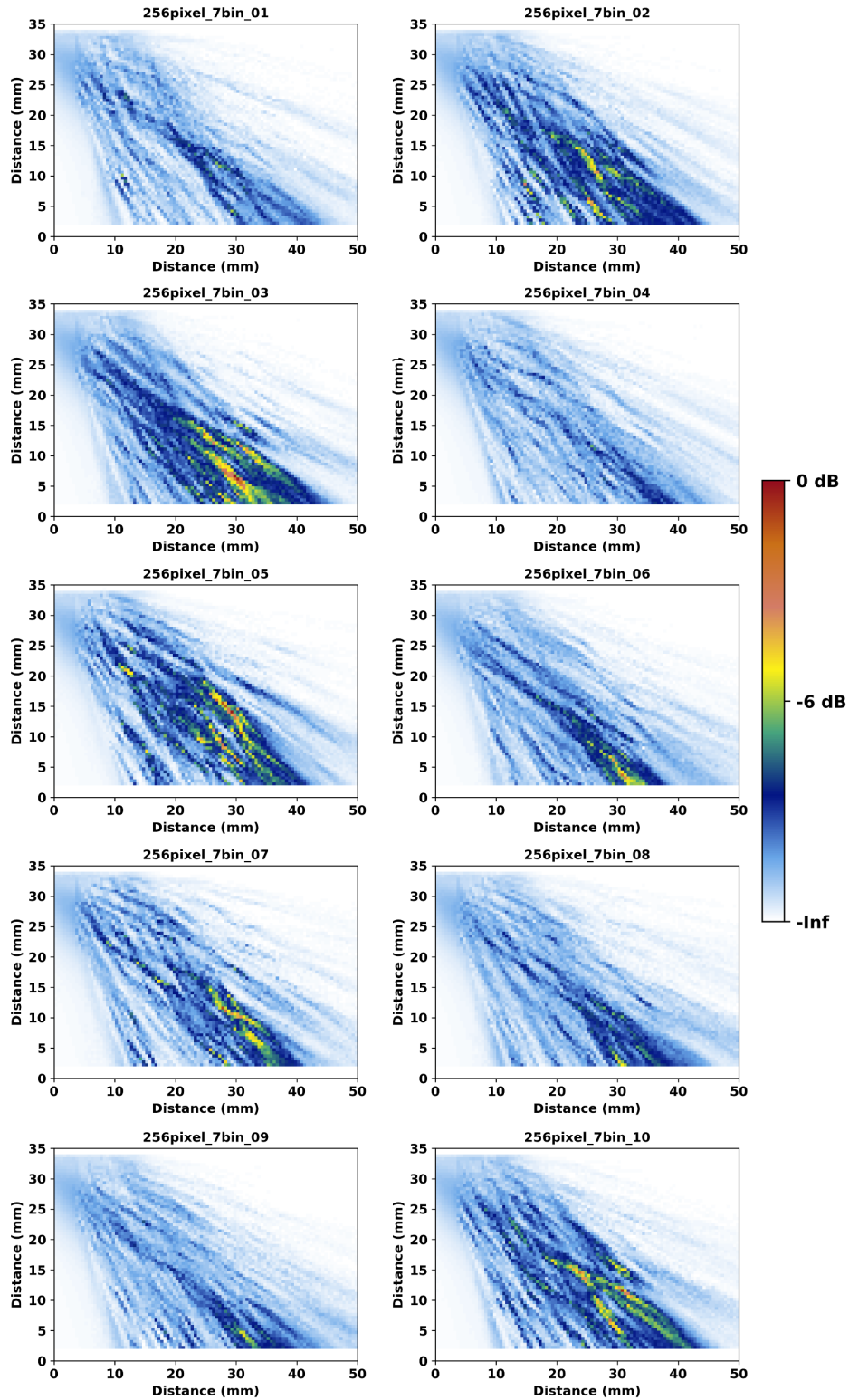


Figure 5.19. Beam simulation results of the ten 7-bin, 256-pixel scenarios with the 2 MHz TRL probe at 45°. Data were normalized to the peak signal of the image set. The X-axis is in mm from the beam exit point, and the Y-axis is in mm from the ID surface.

Table 5.5 shows the similarity metrics of the 7-bin scenarios compared to the isotropic case. Comparison of the average values in this table to those in Table 5.3 indicate the 7-bin scenarios are overall less similar to the isotropic case than the 3-bin scenarios. For example, the average SSIM in the 7-bin case is 0.298 but for the 3-bin case it is 0.364, which is suggestive of less beam formation and more beam scatter in the 7-bin scenarios. In the 3-bin geometry, a few large regions resulted in less overall scatter and more cohesive beam redirection; such large regions are absent in the 7-bin geometry. Because there are more grain volumes, or scattering centers, and more grain orientations in the 7-bin geometry, it is hypothesized that the 7-bin scenarios are more representative of reality than the 3-bin scenarios.

**Table 5.5. Similarity metrics calculated for the ten 7-bin scenarios as compared to the simple, isotropic case.**

Run	SSIM	MSE	p
256_7bin_01	0.268	70.5	0.745
256_7bin_02	0.313	43.6	0.791
256_7bin_03	0.328	32.4	0.846
256_7bin_04	0.304	71.3	0.779
256_7bin_05	0.288	47.7	0.764
256_7bin_06	0.321	59.1	0.744
256_7bin_07	0.257	46.1	0.804
256_7bin_08	0.279	53.7	0.823
256_7bin_09	0.343	64.3	0.768
256_7bin_10	0.276	41.9	0.794
Average	0.298	53.0	0.786
SD	0.028	13.0	0.033

As with the 3-bin case, the average of the 7-bin images was taken; this is shown in Figure 5.20. Compared to the average 3-bin image Figure 5.18, the 7-bin average case shows less beam formation and more scatter, as expected. The individual 7-bin scenarios can be quantitatively compared to the 7-bin average image; this is shown in Table 5.6. It was concluded that Run 08 is closest to the average case and is therefore may provide a nominal 7-bin geometry. However, other scenarios are also very similar to the average case. This is because additional scatter in the 7-bin scenarios had the effect of spreading out the sound beam and making the images more similar to one another than in the 3-bin scenarios. This is another indication scatter in the 7-bin scenarios was higher overall.

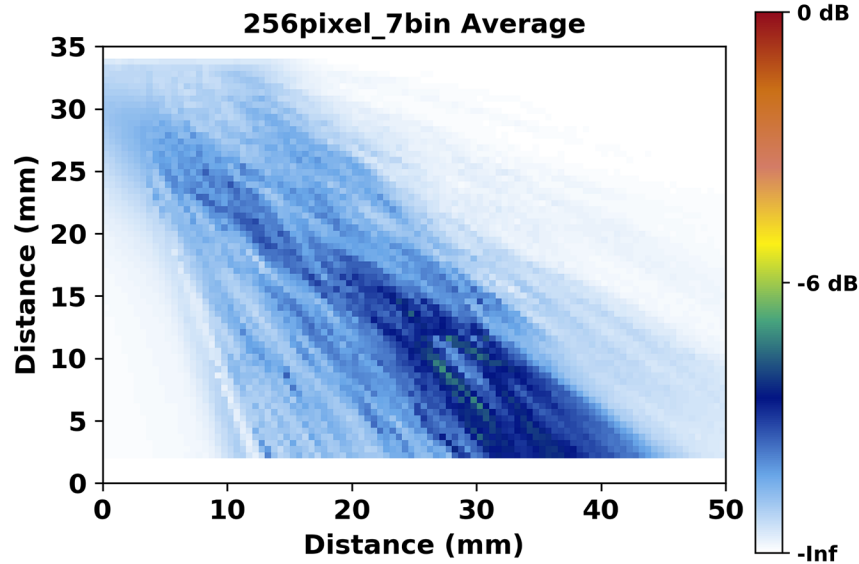


Figure 5.20. Average image of the 256-pixel, 7-bin scenarios.

Table 5.6. Similarity metrics calculated for the ten 7-bin scenarios as compared to the average. Run 08 is most similar to the average.

Run	SSIM	MSE	p
256_7bin_01	0.446	12.3	0.829
256_7bin_02	0.499	14.3	0.897
256_7bin_03	0.505	20.9	0.921
256_7bin_04	0.445	11.5	0.854
256_7bin_05	0.430	26.3	0.846
256_7bin_06	0.463	11.6	0.843
256_7bin_07	0.429	14.8	0.836
256_7bin_08	0.511	7.61	0.888
256_7bin_09	0.510	9.12	0.870
256_7bin_10	0.505	19.7	0.883
Average	0.474	14.8	0.867
SD	0.035	5.8	0.030

Results of the 7-bin simulations indicate that the simulation results tend to converge as additional geometrical complexity is added to the model, as suggested by the lower SDs in Table 5.6 than in Table 5.4. If this holds true, then the specific geometry and assignment of grain orientations may not be as important as the grain boundary definitions, especially as the grain size is decreased. That is, with sufficient geometrical complexity, beam simulations through each weld would look essentially like the next.<sup>(a)</sup> This would simplify future austenitic weld modeling by allowing for a single, representative weld geometry with random grain

(a) Thanks to improvements in the way CIVA 2020 handles complex geometries, PNNL is currently investigating the effects of smaller grain sizes to see if there is any convergence in simulated beams as grain size decreases.

orientations to be used. For example, in Section 5.4, a single representative weld geometry was used based on the image similarity metrics. However, as observed in Section 4.0, different welds do scatter the sound beam differently, so the notion of a single, representative weld geometry for modeling may not be realistic. Additional through-weld beam simulations with different probe positions, additional empirical side-beam maps, and through-weld flaw detection data are currently planned to elucidate whether relying on a representative geometry is realistically feasible.

PNNL investigated the implications of the different simulation scenarios on flaw detection by calculating the sound intensity incident on the specimen backwall. This was done in only the simulation plane shown in Figures 5.18 and 5.20. Figure 5.21 shows the sound intensity versus distance (in mm) from the beam exit point for the average 3-bin (blue line), average 7-bin (green line), and isotropic (orange line) cases. Beam scatter reduced the overall peak height of the 7-bin case compared to the 3-bin case and of both cases compared to the isotropic case. (Note that Figure 5.21 shows the intensity of incident sound energy on the backwall, but sound energy incident on a flaw of arbitrary depth is easily calculated as well.) Based on these results alone, it is impossible to tell whether a far-side flaw at, say, the 35 mm (1.38 in.) position would be detected. For the 7-bin case, the signal reaching the flaw was diminished by about a factor of two compared to the isotropic case; it is reasonable to assume the reflected signal would be diminished by about the same factor as the sound traversed back through the weld. So, if a factor of about four reduction (or 12 dB) in signal compared to the isotropic case still provides a defect signal, then detection is likely. This is a simplified scenario; noise and attenuation were not included in the simulations. There would be much more noise introduced by the weld than in an isotropic case, and attenuation would further diminish the signal. Note these results are based on B-scan beam simulations with a single probe position; it is likely detection would be enhanced by scanning through multiple positions and/or probe angles. Nevertheless, beam simulations with the probe at multiple positions could be used, along with representative weld structures, to help inform coverage calculations and the likelihood of flaw detection while preventing the need for very long flaw inspection simulations. It is anticipated that predictions of limited coverage scenarios would particularly benefit from such an approach.

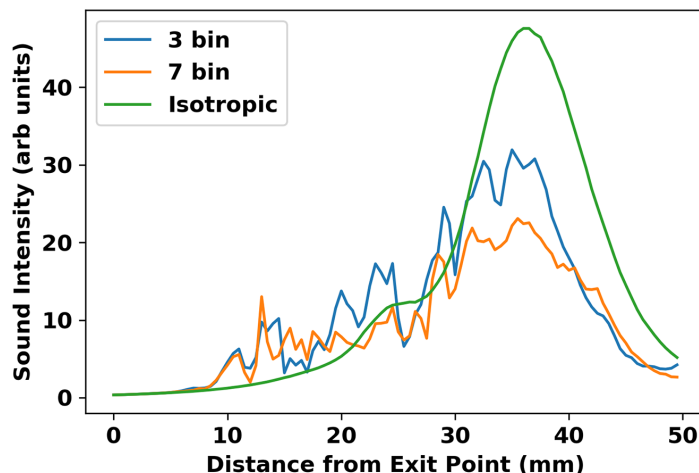


Figure 5.21. Sound intensity incident on the backwall versus position. The average 256-pixel, 3-bin case (blue), 7-bin case (orange), and the isotropic case (green) are shown.

Additional simulations were performed using the finer 128-pixel quadtree decompositions with 3 and 7 bins. The 3-bin geometry comprised 3193 line segments and 1064 regions, while the 7-bin geometry comprised 5215 segments and 1738 regions. Starting with the 3-bin geometry, it was found that CIVA would not complete a simulation with a 3D computation zone. EXTENDE suggested limiting the simulation to a 2D plane through the center of the probe. Although this will not give a complete picture of the sound beam, CIVA was able to complete the 2D simulations. As was done previously, ten simulations with random assignments of Euler angle sets were performed, with each simulation finishing in under two hours. Note that it can take tens of minutes to open the data files; this is not because of the file size; rather, it is due to the complexity of the weld geometry. The simulation results are shown in Figure 5.22. Note that, as with the previous 256-pixel simulations, there is considerable beam scatter. However, also note much larger disparities in the maximum signal intensity between the simulations than were noted in previous simulation sets. Also of interest are multiple, apparently random regions in some of the simulations where pixel values appear to be missing. Because the missing pixels are not consistent from simulation to simulation, they must be related to the Euler angle assignments and not the geometry. This problem is most likely related to the accuracy factor, which was set to 1 in order to minimize simulation time. Interestingly, missing pixels were not a problem with the 256-pixel weld models that had the same type of rectangular grains.

Data were analyzed to assess the similarity metrics as compared to the isotropic case (see Figure 5.15) and the average case (Figure 5.23). Results are shown in Table 5.7 and Table 5.8, which show that Runs 04 and 05 appear to be closest to the isotropic case, while Run 10 is the most comparable to the average and would therefore represent a nominal case for use in future modeling. (Recall that ideal similarity metrics are SSIM=1, MSE=0, and p=1.) The average similarity metrics of the 128-pixel, 3-bin simulations are similar to those of the 256-pixel, 7-bin scenarios, implying that the two different geometries produce beam simulation results that are comparably different from the isotropic case. This suggests that the simpler 256-pixel, 7-bin geometry (453 regions) can be used in lieu of the more complex (and time-consuming) 128-pixel, 3-bin geometry (1064 regions) to obtain comparable simulation results but without the missing points in the beam simulation data.

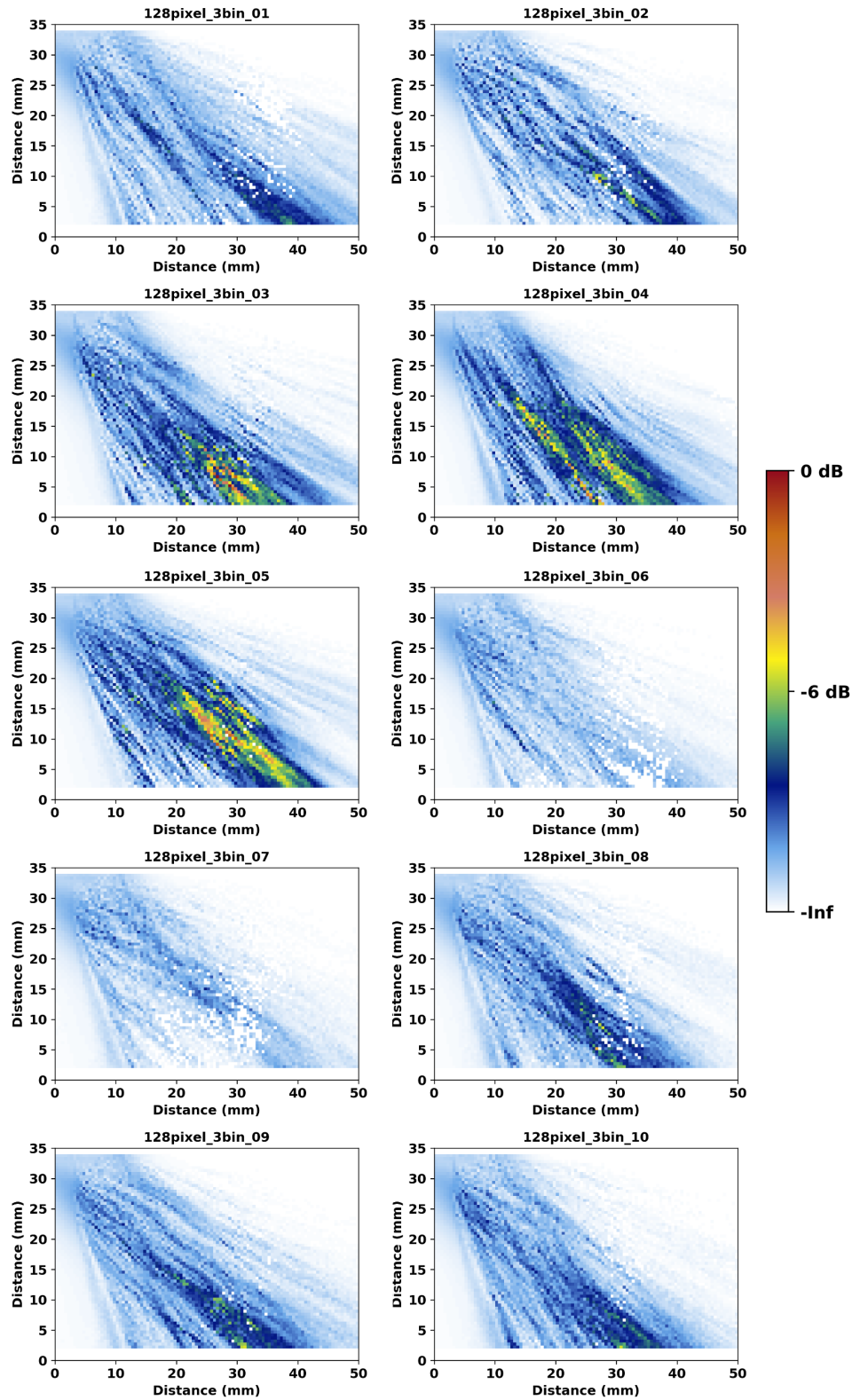


Figure 5.22. Beam simulation results of the ten 3-bin, 128-pixel scenarios with the 2 MHz TRL probe at 45°. Data were normalized to the peak signal of the image set. The X-axis is in mm from the beam exit point, and the Y-axis is in mm from the ID surface.

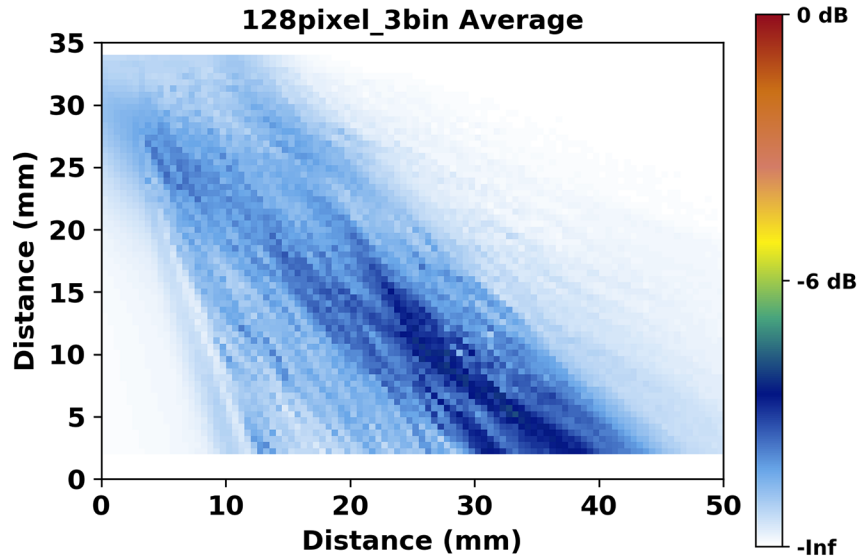


Figure 5.23. Average image of the 128-pixel, 3-bin scenarios.

Table 5.7. Similarity metrics of the 128-pixel, 3-bin simulations compared to the isotropic case.

Run	SSIM	MSE	p
128_3bin_01	0.311	67.7	0.761
128_3bin_02	0.291	66.8	0.736
128_3bin_03	0.315	48.6	0.768
128_3bin_04	0.408	36.0	0.827
128_3bin_05	0.346	32.1	0.846
128_3bin_06	0.263	115	0.447
128_3bin_07	0.263	114	0.481
128_3bin_08	0.265	69.8	0.721
128_3bin_09	0.341	60.2	0.779
128_3bin_10	0.288	67.3	0.747
Average	0.309	67.8	0.711
SD	0.046	28.1	0.136

Table 5.8. Similarity metrics of the 128-pixel, 3-bin simulations compared to the average case.

Run	SSIM	MSE	p
128_3bin_01	0.493	7.60	0.834
128_3bin_02	0.407	9.77	0.815
128_3bin_03	0.433	19.9	0.860
128_3bin_04	0.477	26.5	0.894
128_3bin_05	0.410	35.5	0.851
128_3bin_06	0.433	15.8	0.703
128_3bin_07	0.418	17.4	0.662
128_3bin_08	0.477	6.60	0.874
128_3bin_09	0.489	5.78	0.894
128_3bin_10	0.522	5.14	0.900
Average	0.456	15.0	0.829
SD	0.040	10.1	0.082

PNNL attempted to run simulations with 128-pixel, 7-bin geometries. These geometries can take over an hour just to load into CIVA. Unfortunately, the simulations would not finish, even after several days and when limited to 2D. An inquiry was sent to EXTENDE, and they were able to run such simulations with a coarser 1 mm (0.4 in.) resolution instead of the finer 0.5 mm (0.02 in.) resolution in the previous simulations. PNNL confirmed on its computer system that the 1 mm (0.4 in.) resolution simulation did finish, and the simulation time was less than one hour. Then, PNNL sought to determine what resolution between 0.5 and 1 mm (0.02 and 0.4 in.) would be CIVA's limit for computing the simulation. First, a simulation at an intermediate resolution of 0.67 mm (0.03 in.) was attempted, and it finished successfully. A simulation at 0.51 mm (0.02 in.) also finished successfully. Finally, a simulation at 0.455 mm (0.018 in.) also finished—this is *higher* resolution than the 0.5 mm (0.02 in.) that would not finish. Apparently, something with this model geometry is incompatible with precisely 0.5 mm (0.02 in.) resolution; this information was forwarded to EXTENDE. Figure 5.24 shows the 0.455 mm (0.018 in.) simulation results. The results show a large number of uncomputed pixels, likely due to the low accuracy factor. Further simulations with this geometry have not been pursued.

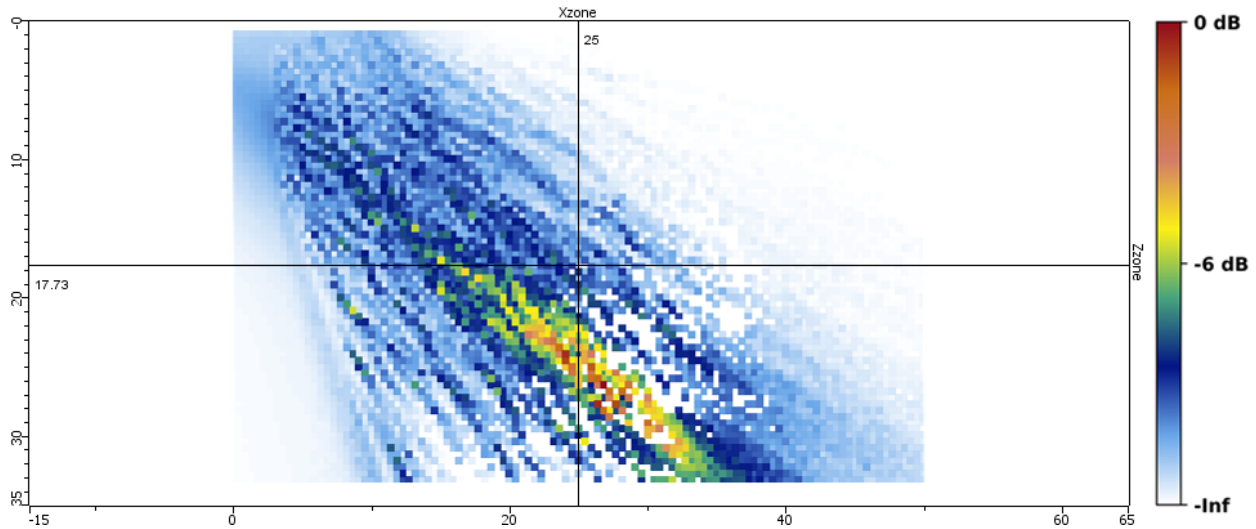


Figure 5.24. CIVA screen capture illustrating the results of the 0.455 mm resolution simulation.

In addition to trying different resolutions with the 128-pixel, 7-bin geometry, EXTENDE suggested moving the probe to a slightly different position by 0.1 mm (0.004 in.). This may avoid having some of the computation points fall exactly on the corners of specimen volumes, which can cause holes because “the beam is not computed on the triple point associated with the intersection of three volumes.”<sup>(a)</sup> It is unclear why this problem did not present itself in the previous simulations with similar geometries; the only differences between simulations were the sizes of grains, the number of grains, and the number of interfaces, so the 128-pixel, 7-bin geometry must be exceeding the limits of CIVA’s capabilities.<sup>(b)</sup> Even so, PNNL attempted moving the probe position slightly. However, when setting this up, it was noticed that the small perturbation of probe position caused the sound beam direction to change considerably. This is shown in the simple ray-tracing diagram in Figure 5.25. The beam redirection suggested that probe position is an important variable in beam simulations with complex geometries. This does not compromise the integrity of simulations that were run; however, moving the probe from one simulation set to the next would preclude direct comparison between simulations sets. Therefore, the simulation with the new probe location was not executed.

(a) Received in communication from EXTENDE technical support.

(b) PNNL has found that CIVA 2020 is able to open the 128-pixel, 7-bin geometries in only a few minutes, and simulations with this geometry are executed without any apparent problems.



Figure 5.25. Transmit (light green) and receive (dark green) rays at different TRL probe positions at  $45^\circ$ . *Left*: Probe position = 95.0 mm. *Right*: Probe position = 94.9 mm. All previous simulations were done with the probe at 95.0 mm.

Geometries with the 64-pixel resolution were generated, but they would not even load into CIVA after several hours. The complexity of these geometries appears to exceed CIVA's capabilities. Note that the amount of computer memory allocated to CIVA was 96 Gb and several Tb of hard drive space was free, and the PNNL hardware specifications exceeded those recommended by EXTENDE (see Appendix F), so the limitation was not likely to be hardware related.

PNNL recognizes that significant compromises may have to be made to limit simulation complexity. However, it is part of the purpose of this exercise to determine what level of detail is necessary to achieve through-weld simulations that adequately reflect experimental results while balancing the limitations of the software. That level of detail can only be determined by evaluating simulation results with several different degrees of weld model complexity (e.g., 256-pixel, 128-pixel, and 64-pixel resolution). Unfortunately, the 128-pixel, 3-bin geometry, which still provides a relatively coarse weld grain representation, will probably be the finest geometry that can be tested; going to higher numbers of bins or finer decomposition resolution (e.g., 64 pixels) will not be possible with CIVA 2017 at this time.

So far, results show that realistic geometries scatter the sound beam in ways that are not duplicated by Ogilvy models. Additionally, results show that for a given geometry or microstructure, the angular orientations of the grains play a critical role in the beam formation, scatter, and the amount of sound energy incident on the ID surface.

### 5.3.3 Comparison with Experimental Beam Maps

The simulation results shown above were performed using a 2 MHz dual-element TRL probe with a beam crossover depth of 37 mm (1.46 in.). Ideally, this same probe would be used for the sound field maps; however, because of the probe size and pinducer size, the receive portion of the probe extended beyond the edge of the specimen, preventing the pinducer from accessing the top third of the specimen. Instead, the sound field maps were performed with the transmit-only portion of a 2 MHz PA probe focused at a focal depth of 24 mm (0.95 in.) (see Section 4.3 for details), so additional simulations were run to duplicate this configuration. Figure 5.26 shows the results of PA beam simulations through the ten 256-pixel, 7-bin austenitic weld models used previously. Results were normalized to the highest-intensity image. Figure 5.27 shows the average result and Figure 5.28 shows the isotropic result, both of which were normalized to the peak signal of Figure 5.26. These are very similar to the simulations performed previously using the two-element TRL probe with the main difference being the probe focal depth.

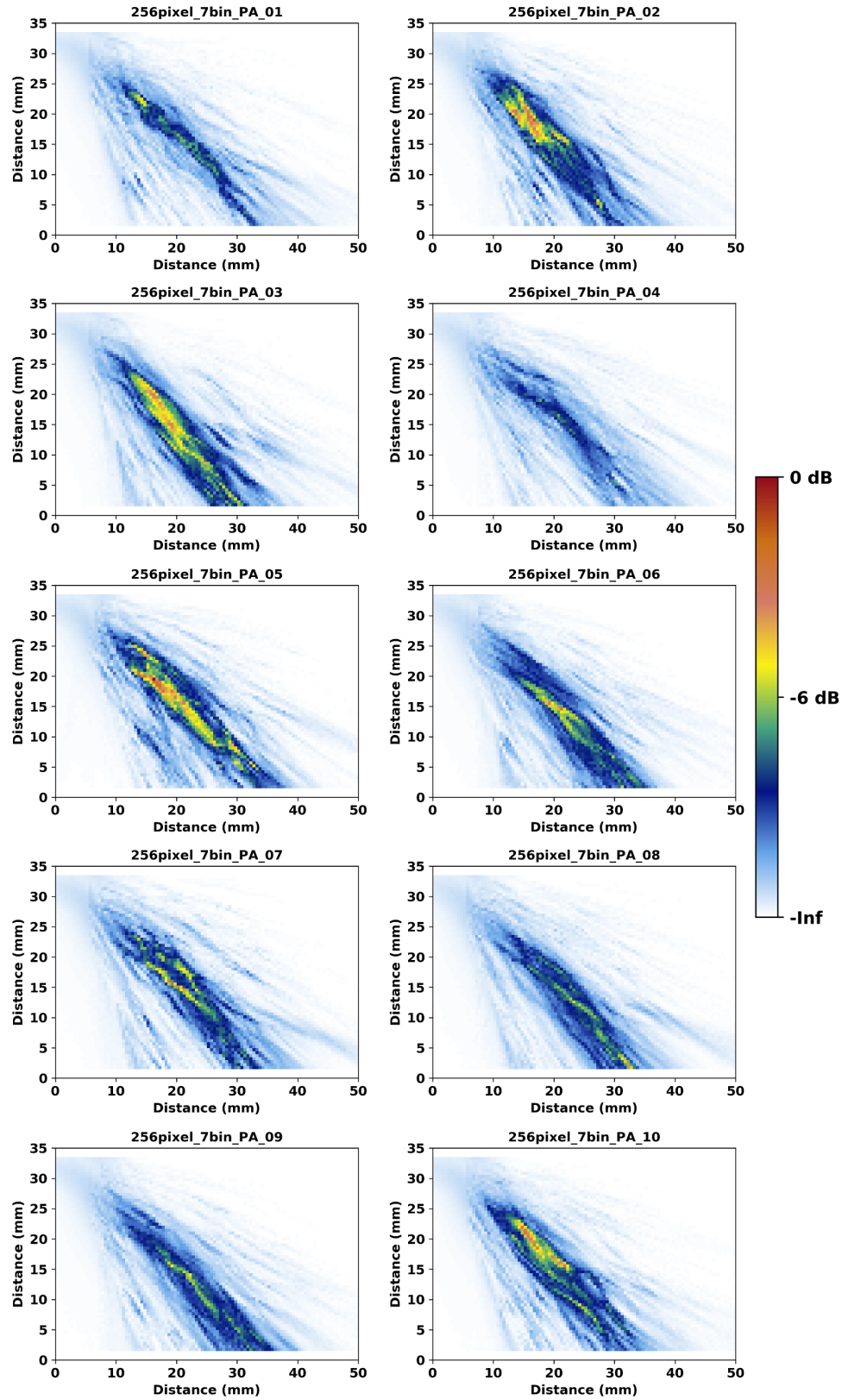


Figure 5.26. Beam simulation results through the 256-pixel, 7-bin austenitic weld model with a 2 MHz PA probe at 45° with a focal depth of 24 mm (0.95 in.).

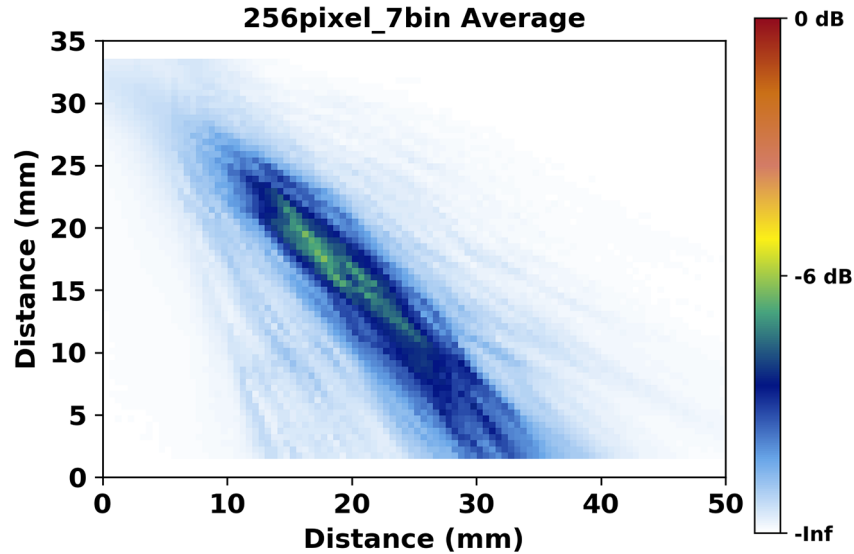


Figure 5.27. Average of the 10 PA beam simulations, normalized to Figure 5.26.

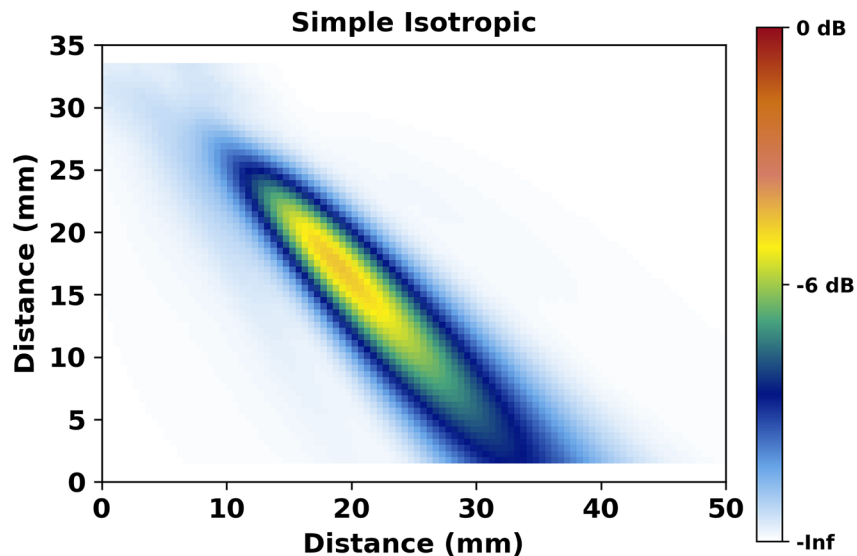


Figure 5.28. PA beam simulation through isotropic material, normalized to Figure 5.26.

Figure 5.29 shows an UltraVision screen capture of the empirically acquired sound field through the isotropic parent material of the specimen with the PA probe at  $45^\circ$ . The software gain was increased until the maximum signal intensity reached 100% FSH, and the minimum displayed intensity was then set to  $-16$  dB (15.8% FSH) to eliminate most of the noise floor. The signal was gated to eliminate most backwall bounces and mode-converted signals. This image shows a well-formed, symmetric sound beam with minimal scatter, and it can be qualitatively compared to the self-normalized isotropic simulation shown in Figure 5.30. Aside from noise and peak signal intensity variations, the beam maps appear qualitatively similar. The empirical beam map has more apparent beam spread and some scatter. The refraction angles of both the empirical and simulated beams were measured in ImageJ to be  $43^\circ \pm 1^\circ$ . The empirical beam shows less sound reaching the specimen backwall, which may be a result of the lack of attenuation in the simulated beam; this will be addressed below.

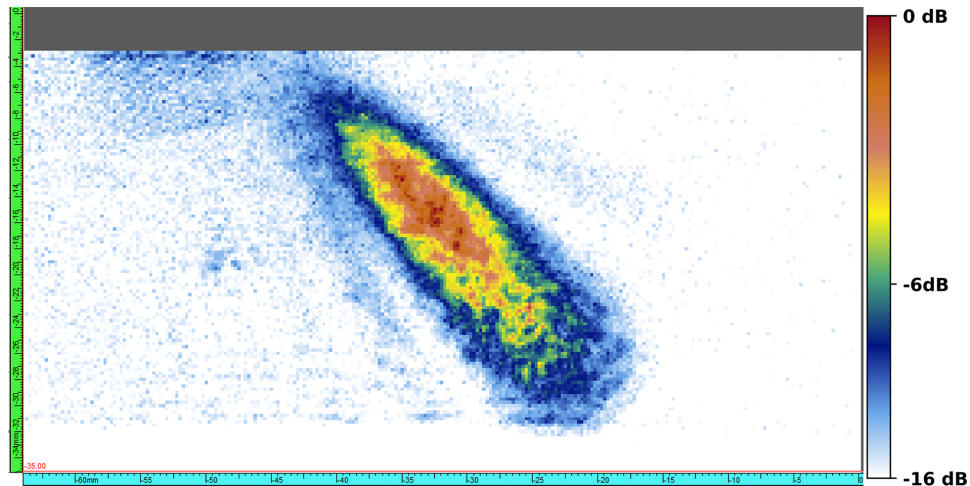


Figure 5.29. Empirical sound field through isotropic wrought stainless steel with the PA probe at  $45^\circ$  and a focal depth of 24 mm (0.95 in.).

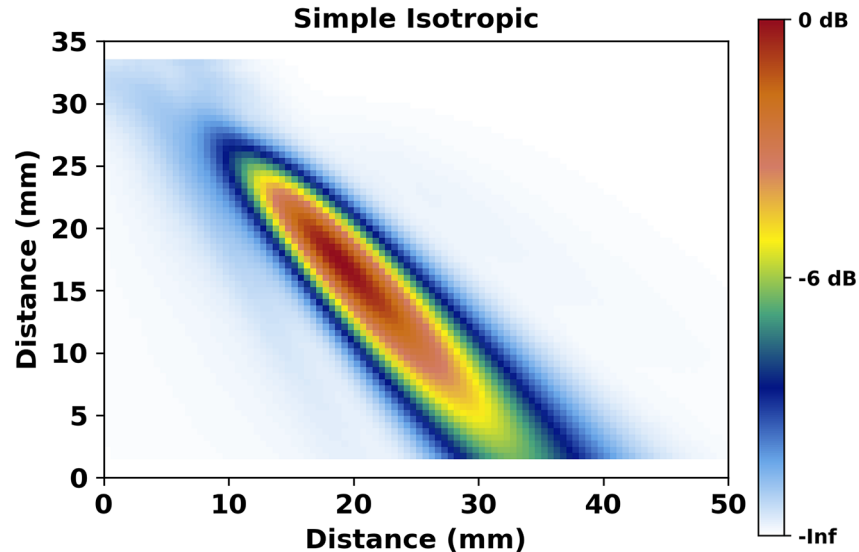


Figure 5.30. PA beam simulation through isotropic material with the PA probe at  $45^\circ$  and a focal depth of 24 mm (0.95 in.), normalized to itself.

Figure 5.31 shows a screen capture of the empirical sound field through Specimen 1 with the same probe parameters and data acquisition settings (see Figure 4.12). The red vertical line indicates the weld centerline. As with the isotropic scan above, the soft gain was increased until the maximum signal reached 100% FSH, and the minimum intensity was set to  $-16$  dB. It can be seen that this image varies noticeably from the isotropic sound field map in Figure 5.29. The beam is not well formed, there is considerable scatter (especially near the top surface of the specimen), and the sound field does not penetrate as deeply into the specimen, although some sound energy does appear to reach the backwall on the far side of the weld. Similarly, Figure 5.32 shows the sound field through Specimen 2. The different granular structure of the weld resulted in a sound field that appears markedly different from that of Specimen 1.

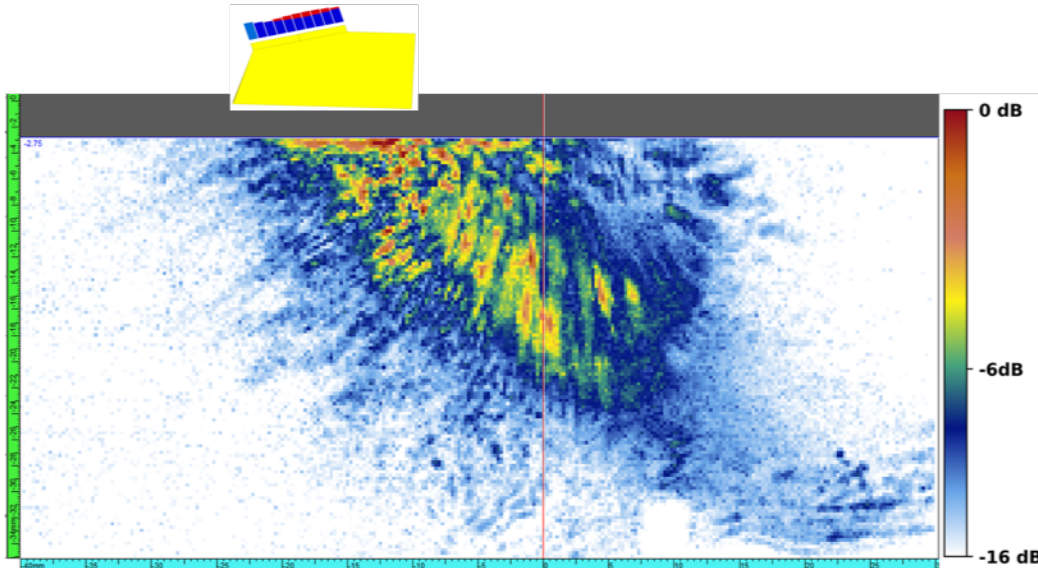


Figure 5.31. Sound field through the weld of Specimen 1 with the 2 MHz PA probe at 45°. The probe position is shown for illustrative purposes and is not to scale.

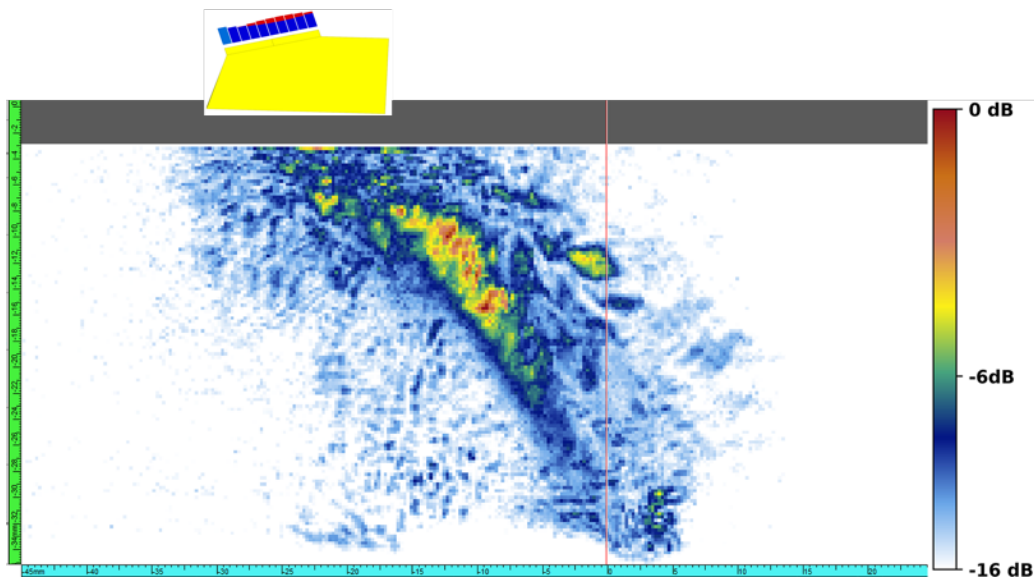


Figure 5.32. Sound field through the weld of Specimen 2 with the 2 MHz PA probe at 45°. The probe position is shown for illustrative purposes and is not to scale.

Empirical results can be compared qualitatively to the simulation results in Figure 5.26. Both results show a high amount of scatter.<sup>(a)</sup> However, the empirical results indicate that little sound energy reached the backwall, whereas the simulation results predicted that comparatively more sound energy should reach the backwall. The difference may be due to attenuation in the specimen that was not accounted for in the simulations. A brief literature search found several

(a) PNNL has not yet developed a metric to quantify scatter, although this could be done, for example, by creating a -20 dB mask of the isotropic simulation result, overlaying the mask onto the weld simulation result, and summing the signal that lies outside the mask boundary. This would be similar to the approach used in Jacob et al. (2010).

papers that provided data on sound attenuation through austenitic steel and welds (Seldis and Pecorari 2000; Ploix et al. 2006; Gardahaut et al. 2014). The literature shows that attenuation is strongly dependent on the sound frequency and grain orientation. Even so, based on these papers, a reasonable value for austenitic steel of approximately 0.2 dB/mm (59% decrease per inch) at 2 MHz was chosen. For the 33 mm (1.3 in.) thick specimen, this equates to about a 6.6 dB (2.1×) signal loss.

In CIVA, attenuation parameters must be added separately to each region of the specimen geometry—it is not a global parameter. Unfortunately, one cannot select a group of regions and assign the same properties to each member of the group. The geometries being modeled were custom generated with hundreds of individual regions, so adding the attenuation parameters region-by-region in CIVA was not practical. Instead, the geometries were exported from CIVA as xml files and edited off-line by using a text editor's *find and replace* function to copy the same attenuation properties to each region. It is critical to remember that defining the attenuation properties in the Specimen tab is not sufficient. One must also “turn on” the attenuation in the Simulation tab by selecting a checkbox. This can be an easy step to overlook, because the user has already defined attenuation in the specimen properties and may easily forget that it needs to be activated in the simulation properties. Failure to activate the attenuation will result in no attenuation in the simulation results.

Beam simulations were re-run on the austenitic weld geometries with attenuation added. First, Figure 5.33 shows the isotropic beam with attenuation. Comparing this figure with Figure 5.28 shows that the attenuated sound field does not penetrate as far into the material and consequently the region of peak sound intensity is closer to the probe. Thus, the depth of the center of the sound field was taken as a simple metric for comparing the empirical data and both isotropic simulations (with and without attenuation). The results are shown in Table 5.9. The depth of the empirical sound field is about midway between the depths of the simulated fields, suggesting that adding attenuation to the simulation was necessary to bring empirical and simulation results into better agreement, but that 0.2 dB/mm may have been too high.

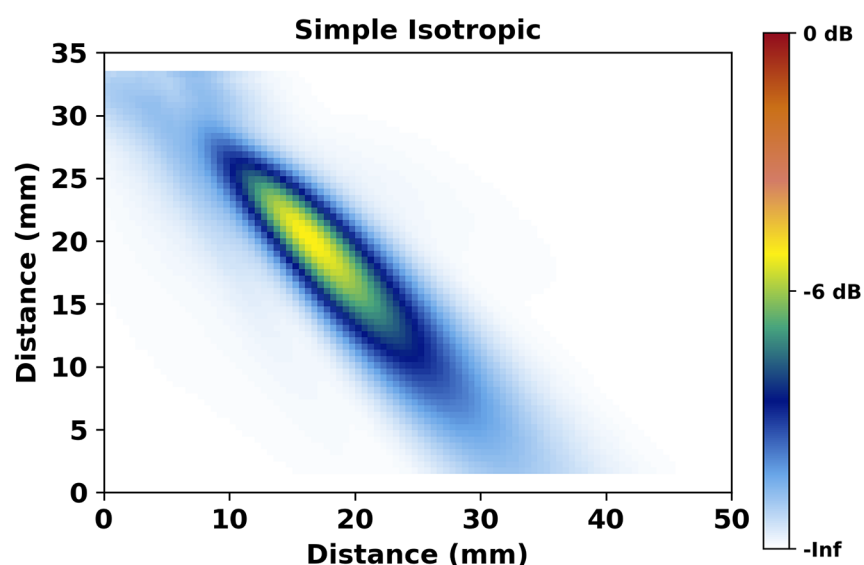


Figure 5.33. PA beam simulation through isotropic material at 45° with 0.2 dB/mm attenuation.

Table 5.9. Sound field penetration depth.

Image	Depth of Peak Sound Field, mm (in.)
Empirical Isotropic	15.0 (0.59)
Simulated Isotropic without Attenuation	16.5 (0.65)
Simulated Isotropic with Attenuation	13.6 (0.54)

Figure 5.34 shows the results of the ten simulations with attenuation, and Figure 5.35 shows the average of the ten, normalized to the maximum of Figure 5.34. Comparison of Figure 5.35 and Figure 5.27 reveals that attenuation added to the simulation resulted in less sound intensity reaching the specimen backwall. This may be difficult to see, because the figures were normalized to different values. For a quantitative comparison, the total sound that was incident on the backwall of the specimen was calculated in both cases. For the case without attenuation, the total was 196, and for the case with attenuation the total was 26 (both in arbitrary units). Thus, nearly eight times less sound energy was incident on the backwall when attenuation was added to the simulation.

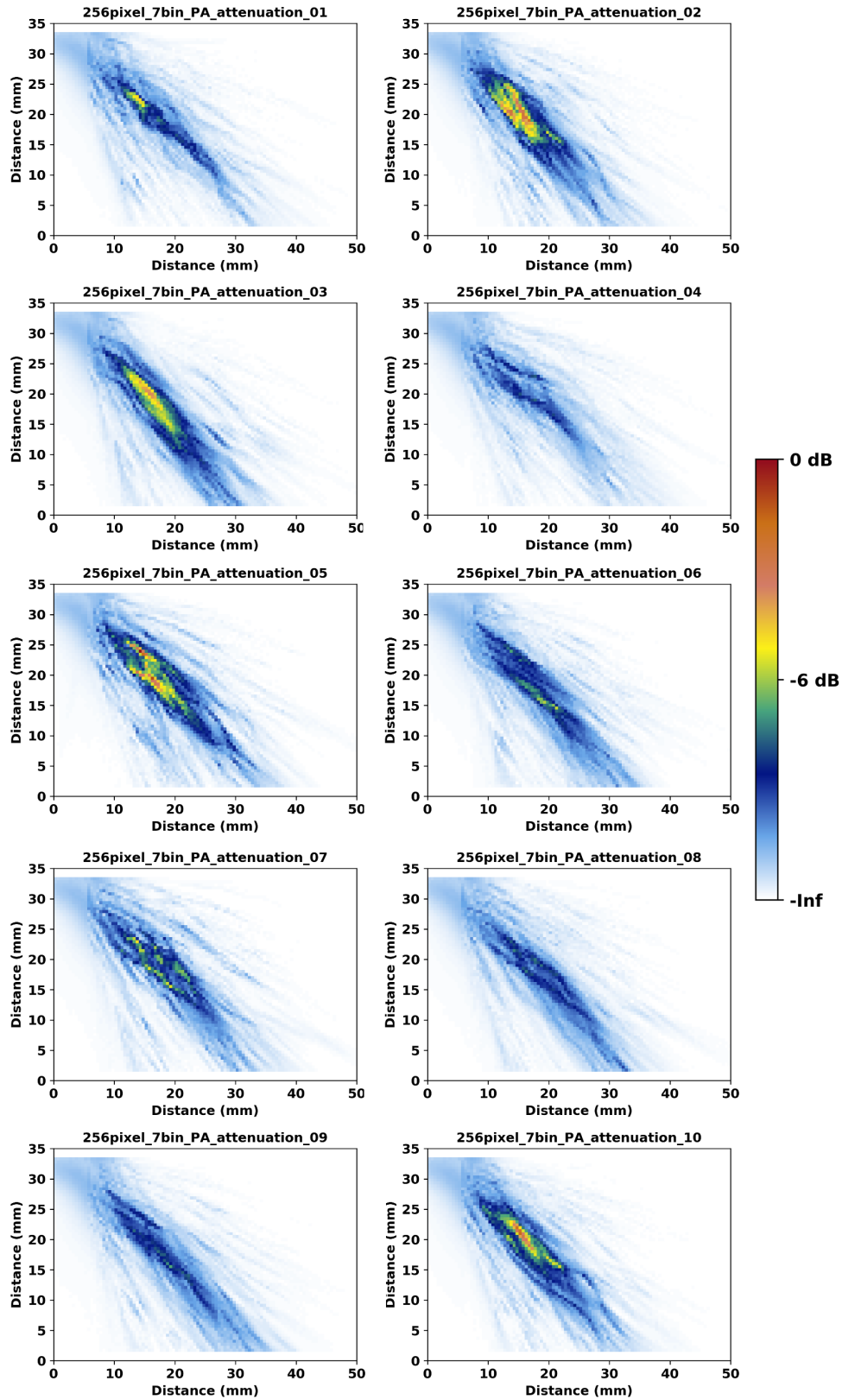


Figure 5.34. Beam simulation results through the 256-pixel, 7-bin austenitic weld model with a PA probe at 45° with 0.2 dB/mm attenuation.

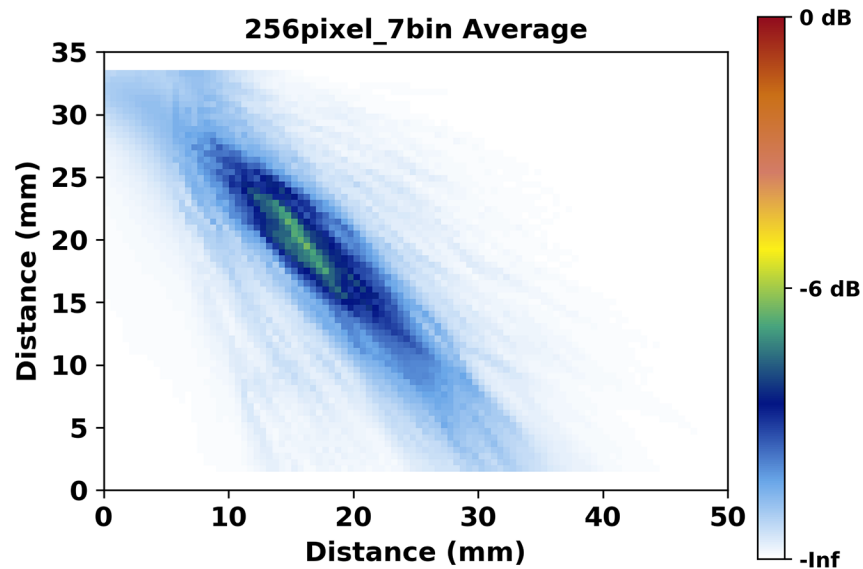


Figure 5.35. Average of the ten PA beam simulations with 0.2 dB/mm attenuation.

### 5.3.4 Summary

Overall, the following conclusions were drawn from the austenitic weld simulations:

- CIVA simulations are capable of representing beam scatter through complex geometries that represent austenitic welds. However, CIVA cannot handle geometries that have too many regions or interfaces. The balance between useful geometries and too-complex geometries can only be determined experimentally.
- Beam scatter through the austenitic model geometries is significantly greater than that in isotropic model geometries.
- Ogilvy models of austenitic welds are not suitable for austenitic weld simulations because they do not depict beam scatter; rather, they rely on a continuous gradient of preferred sound propagation. Any simulations through coarse-grained materials or austenitic welds should include grain structures that result in realistic beam scatter.
- The degree of beam formation can vary considerably from one weld model scenario to the next for the same geometry with only the Euler angles changed. Such variations may be somewhat dependent on the grain structure extrusion in the Z-dimension.
- An average beam map can be determined based on multiple beam simulations, and a representative weld structure can be deduced from the average beam map using image similarity metrics. This may be particularly useful for follow-on flaw inspection simulations that can make use of a nominal weld model.
- Quantitative image metrics are useful and effective for evaluating and comparing different beam simulation scenarios.

## 5.4 Other Influential Parameters and Considerations

### 5.4.1 Probe Position and Implications for Flaw Detection

Thus far, results of through-weld beam simulations have been shown with the probe in a fixed position. The next group of simulations was performed with the probe at different positions across the weld. The 7-bin, 256-pixel weld model using file number 08 was determined to be the nominal geometry, because the similarity metrics showed that it was most comparable to the average case of the ten weld models tested. Beam simulations were conducted with the probe position, as measured by the beam exit point, incremented by 5 mm (0.20 in.) facing both the positive (right) and negative (left) directions. Figure 5.36 shows the simulation results with the probe moving from left to right facing toward the right. The X-axis position is the absolute position on the specimen. Results are normalized to the simulation with the highest signal intensity. The nominal beam exit point is in the title of each panel. Figure 5.37 illustrates three of the probe positions and the weld geometry. The figures show the evolution of the sound field intensity and beam scatter pattern as the probe is incremented across the weld. Interestingly, the sound field shows good beam formation when the exit point is above the weld and the focal region is outside the weld, as seen in the bottom four panels (110 mm, 115 mm, 120 mm, and 125 mm). The beam formation suggests that initial scattering of the beam by weld material can be overcome to an extent if the beam path through the weld is short, although some sound intensity is lost. Similarly, Figure 5.38 shows the simulations with the probe facing toward the left, and Figure 5.39 illustrates three of the probe positions and the weld geometry.

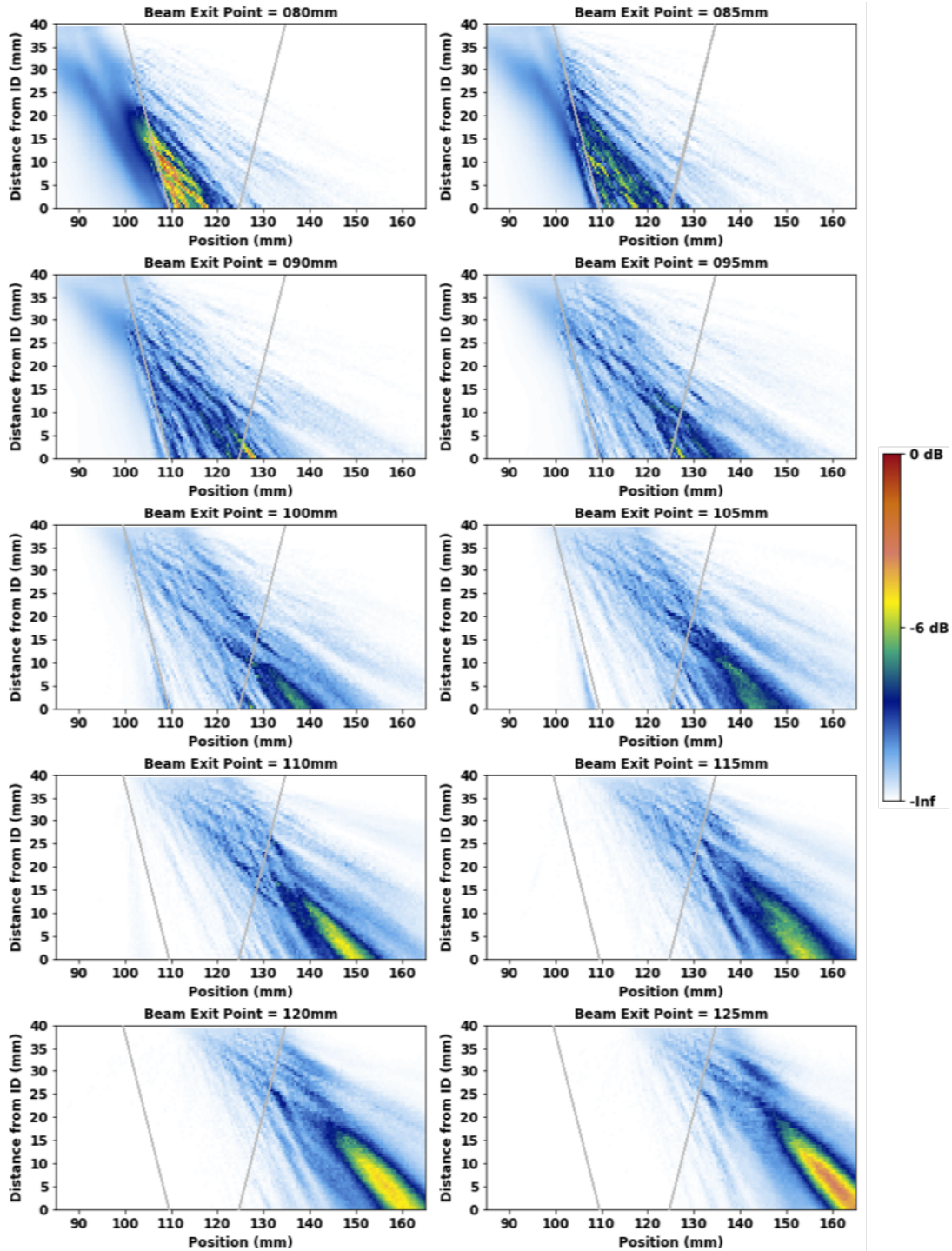


Figure 5.36. Beam models through the weld at different positions with a right-facing, 2 MHz TRL probe at 45°. The approximate weld boundaries are shown in grey.

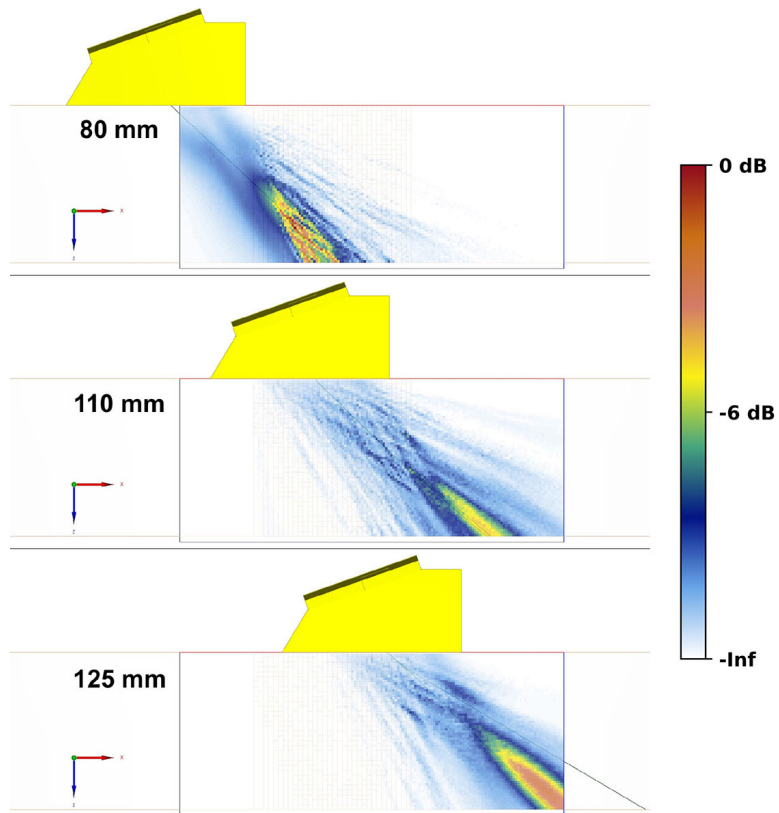


Figure 5.37. Example of three beam models showing the weld geometry and probe positions with the right-facing probe.

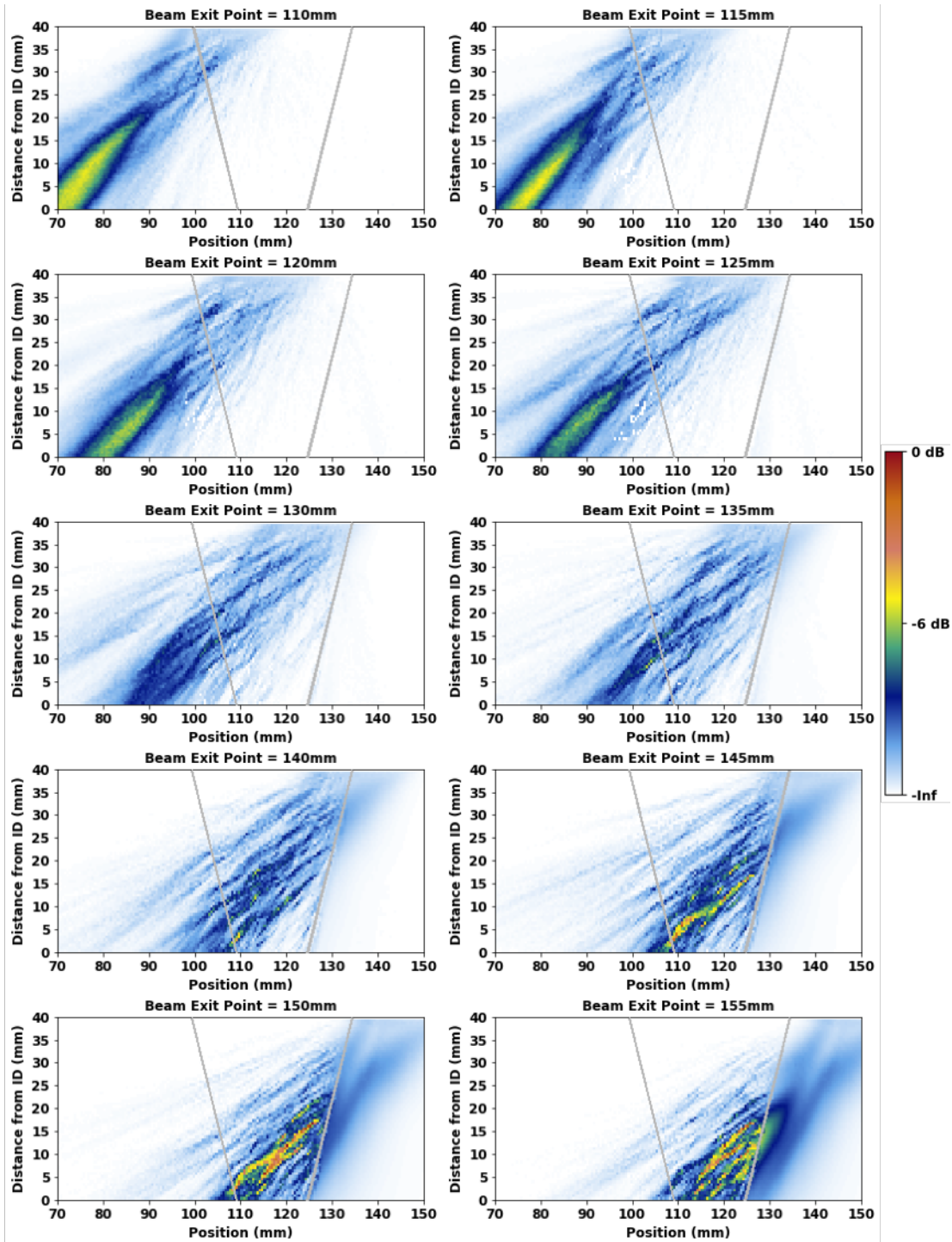


Figure 5.38. Beam models through the weld at different positions with a left-facing, 2 MHz TRL probe at 45°. The approximate weld boundaries are shown in grey.

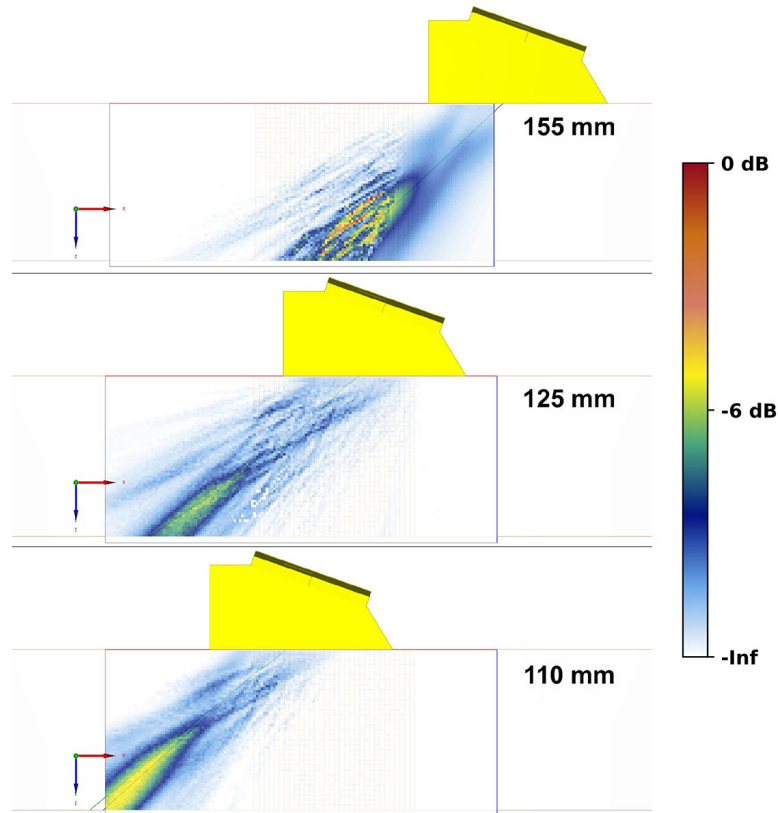


Figure 5.39. Example of three beam models showing the weld geometry and probe positions with the right-facing probe.

To determine what, if anything, the beam simulations might indicate about flaw detection capability, the sound incident on the entire specimen ID was integrated for each probe position to a height of 3 mm (0.12 in.). This height allows for an estimation of the sound intensity incident on a flaw corner. Figure 5.40 shows the results for the right-facing probe, and Figure 5.41 shows the results of the left-facing probe. The blue lines are the integrated signal for each probe position. For comparison, the orange line was added to show the integrated signal through an isotropic material. This was done for only one position of the probe, because the profile would not change as the probe was translated across the isotropic specimen—hence, the orange line is static. Interestingly, in the first panel of Figure 5.40 (labeled “080mm”), the height of at least one of the peaks exceeds that of the isotropic beam. This is an example of localized beam focusing caused by the weld grain structure, and the implication is that a flaw at that position would have a stronger signal response with the weld present than without. Finally, the integrals were summed to generate a total picture of the backwall-incident sound energy. This is shown in Figure 5.42. Note that both summations have local minima (troughs) and maxima (peaks) of sound intensity on the specimen backwall.

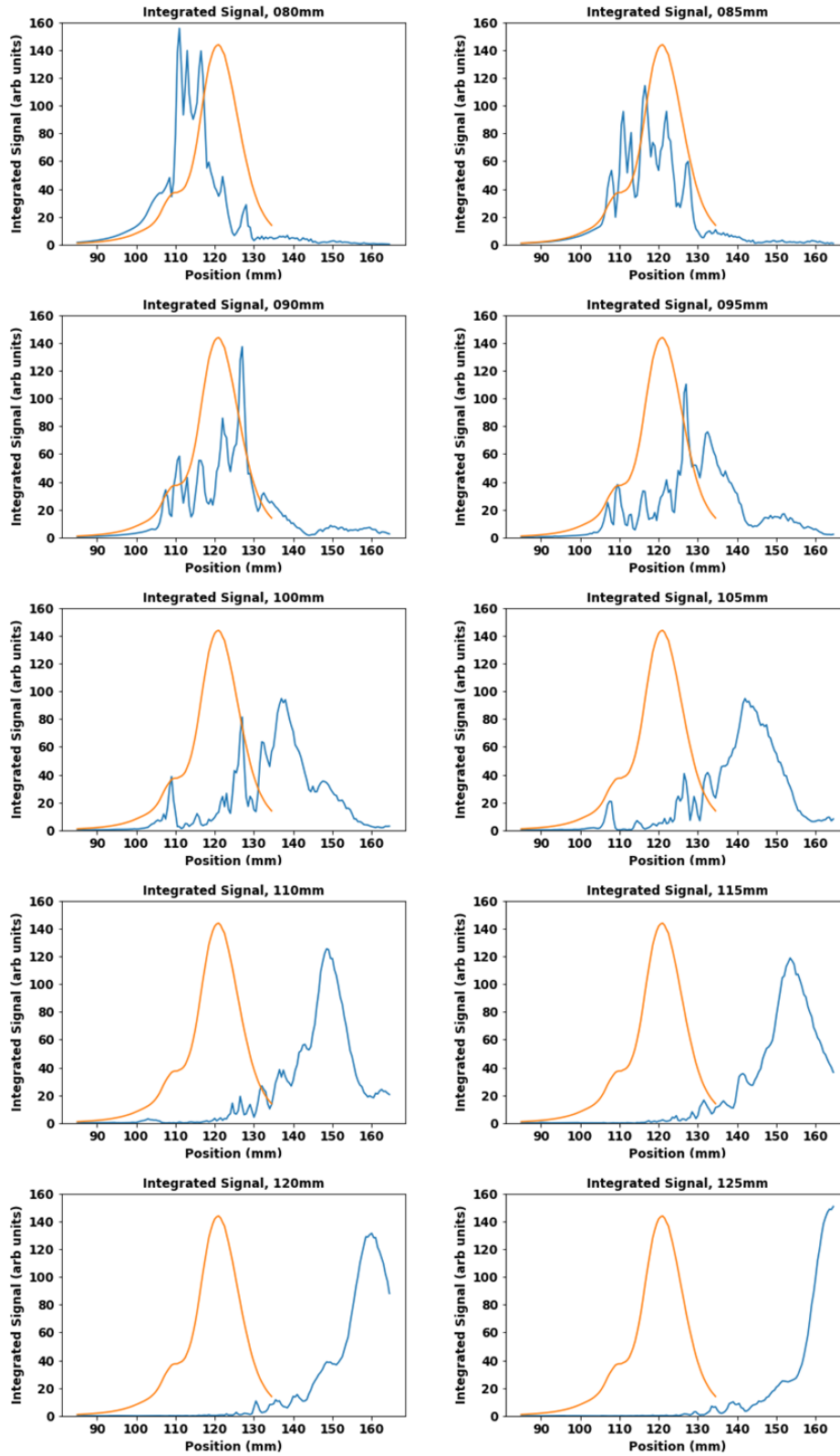


Figure 5.40. Integrated sound energy incident on the specimen backwall for the right-facing probe as a function of position. For comparison, the orange line illustrates the static isotropic beam.

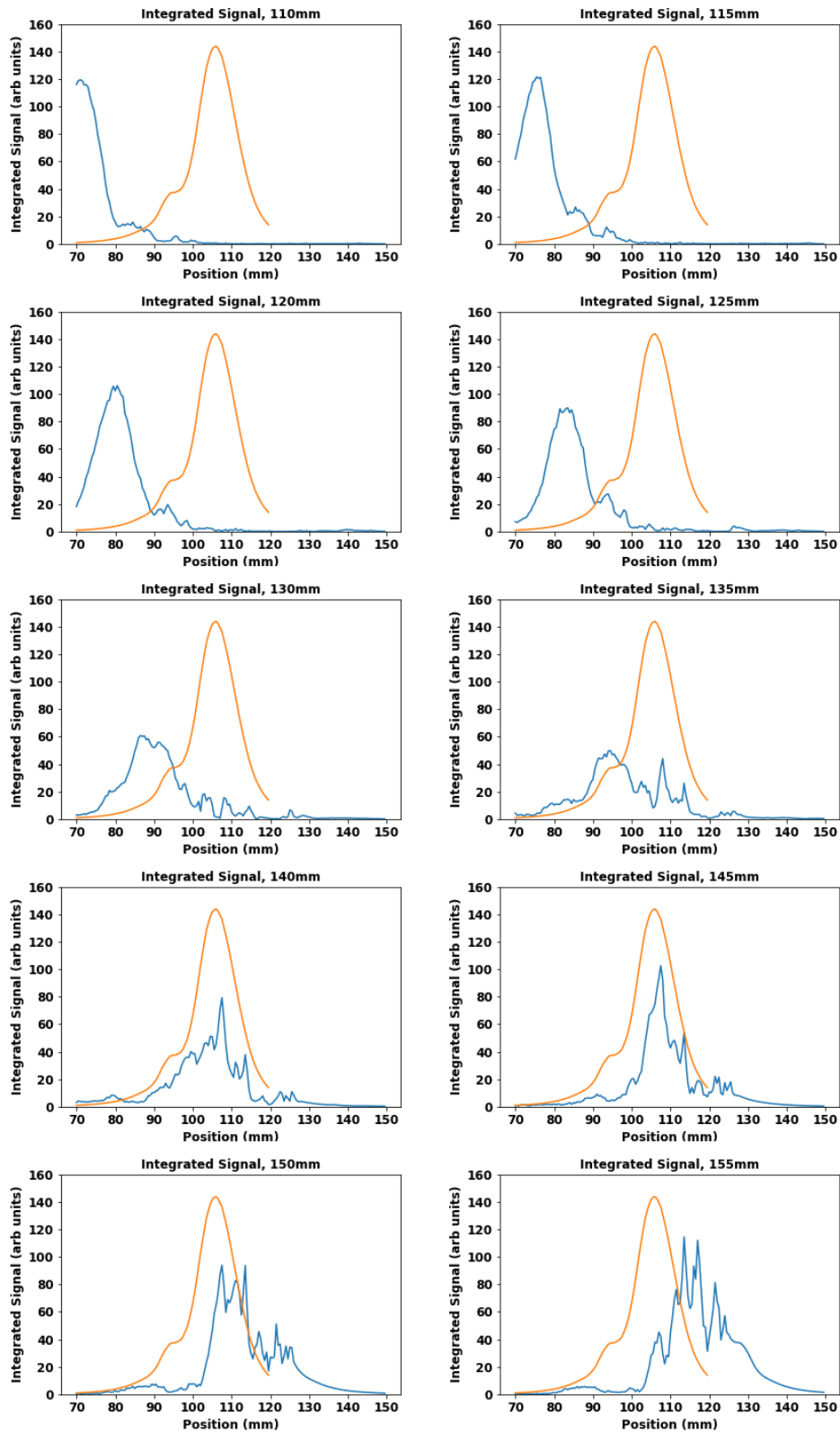


Figure 5.41. Integrated sound energy incident on the specimen backwall for the left-facing probe as a function of position. For comparison, the orange line illustrates the static isotropic beam.

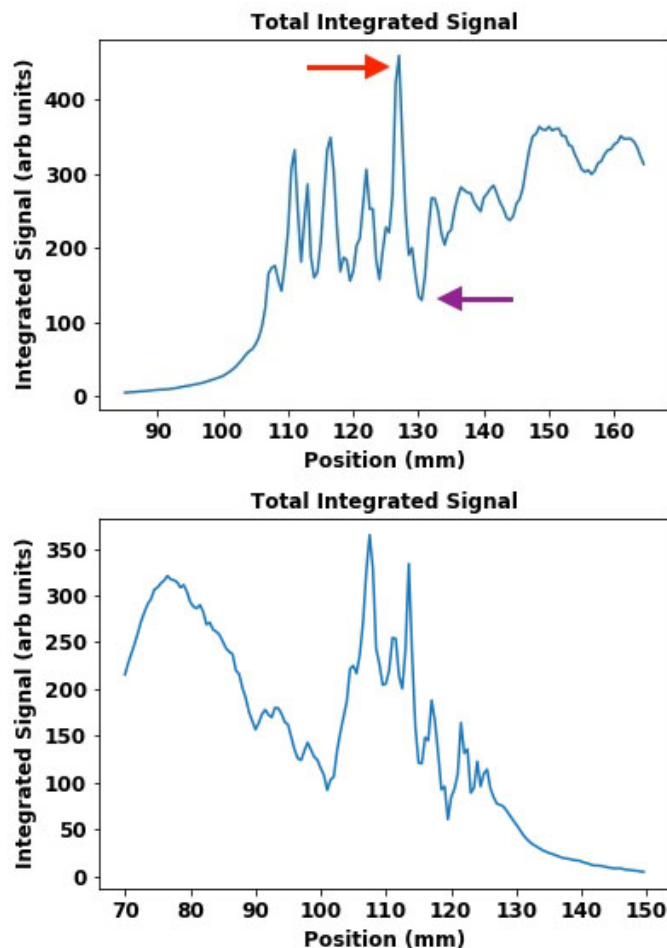


Figure 5.42. Total integrated signal for the right-facing probe (*top*) and the left-facing probe (*bottom*). The maximum (red arrow) and local minimum (purple arrow) of the right-facing probe are only 3.5 mm (0.14 in.) apart.

In Figure 5.42 (*top*), two features are indicated by arrows: the absolute maximum (red arrow) at 127 mm (5.0 in.) and a local minimum (purple arrow) at 130.5 mm (5.14 in.). Both features occur on the far side of the weld and are separated from each other by only 3.5 mm (0.14 in.). If the beam simulations are indeed predictive of a flaw response, then flaw response simulations with flaws placed at 127 mm and 130.5 mm (5 in. and 5.14 in.) should show a stronger response from the flaw at 127 mm (5.0 in.). This hypothesis was tested by adding a 3 mm (0.12 in.) flaw to the weld geometry at the two positions and running flaw response simulations with the probe moving across the weld. Figure 5.43 shows the results, including a control scan (through isotropic material) with the flaw far from the weld. (Recall that CIVA has a problem reconstructing B-scans when the beam exit point is above a complex geometry, so partial volume-corrected B-scans are shown on the left and uncorrected B-scans on the right.) The flaw response simulations show that the peak signal from the flaw at 127 mm (5.0 in.) was 4.5 dB (1.7 $\times$ ) higher than that of the flaw at 130.5 mm (5.14 in.). Interestingly, the response from the flaw at 127 mm (5.0 in.) was also higher than that of the flaw in the control scan by 2.7 dB (1.4 $\times$ ). It is known that the weld region can unpredictably disperse the sound field, resulting in lower flaw responses. However, results again suggest that the weld region can also unpredictably focus the sound field, resulting in localized stronger flaw responses at very specific positions. For example, it is feasible that a recorded flaw signal may be greater than the

calibration signal in a test block or corner trap. Such positions would never be known a priori in the field or in the lab, but it is important to be aware of the possibility.

Figure 5.42 (top) shows that the peak indicated by the red arrow is about four times higher than the trough indicated by the purple arrow. This implies that there is about four times more sound energy, or about 12 dB, incident at 127 mm (5 in.) than at 130.5 mm (5.14 in.). However, the difference in the flaw responses in Figure 5.43 was only 4.5 dB. We point out that the beam simulations were acquired with 5 mm (0.20 in.) spacing between each scan, whereas the flaw response simulations were acquired with 1 mm resolution. This difference may account for the apparent discrepancy between what the beam simulation predicted and what the flaw response showed. Also, the beam simulation only shows sound emitted from the probe and does not take into account the sound reflection from the flaw back to the probe, as it would be for the flaw simulation. The reflected sound moving back through the weld to the probe is subject to additional scatter or redirection, resulting in a lower measured flaw response.

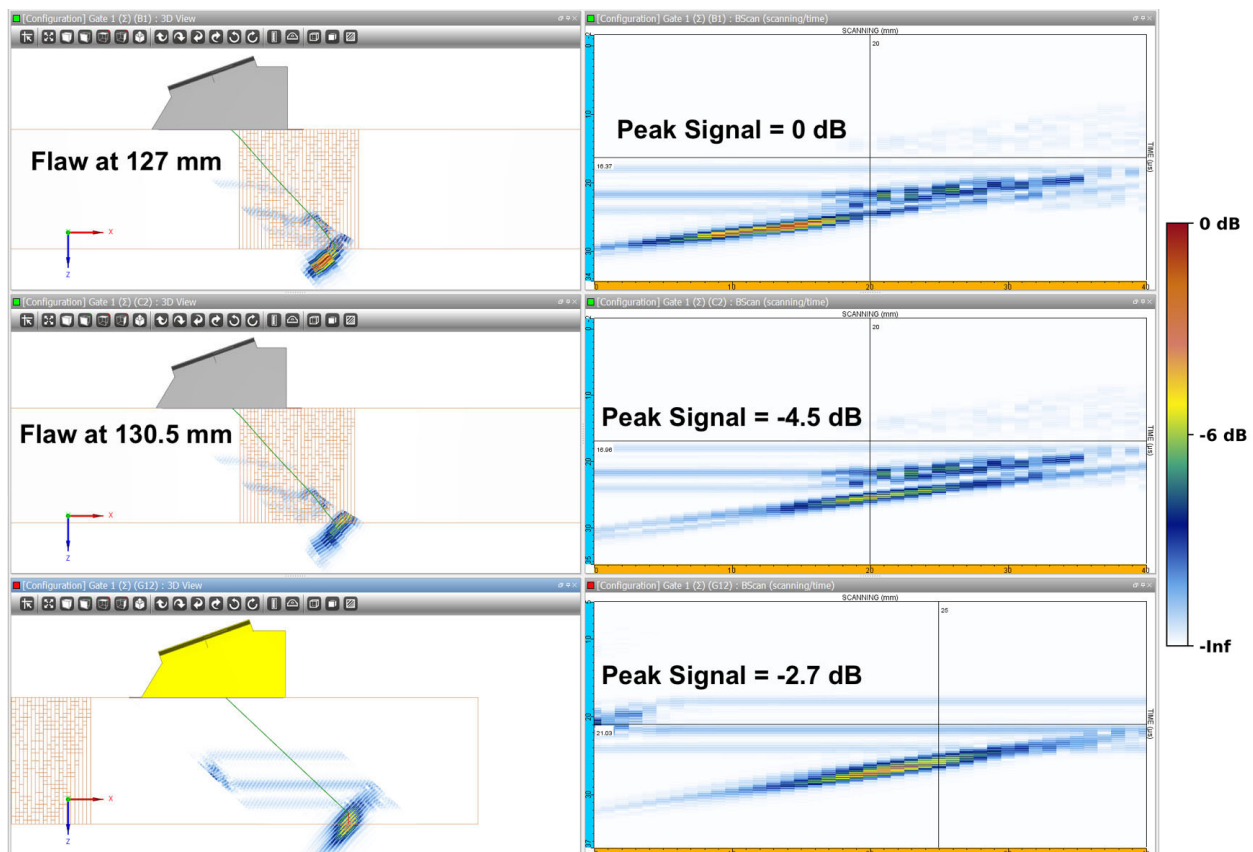


Figure 5.43. Flaw response simulations with the right-facing probe. A 3 mm (0.12 in.) deep flaw was located at 127 mm (5 in.) (top) and 130.5 mm (5.14 in.) (center). A control simulation was performed away from the weld (bottom).

## 5.4.2 Crack Detection Simulations

For crack detection simulations, a test case was modeled after a wire-EDM “crack” that was created in an Electric Power Research Institute (EPRI)-owned test specimen that was on loan to PNNL. The specimen is pictured in Figure 5.44. The crack is of moderate complexity, comprising several small branches. Importantly, the crack is at a 37° tilt, which allows it to be

added close to the model weld geometry without encroaching into the weld itself. Figure 5.45 shows the CAD drawing (dashed lines) and simplification for CIVA input (solid lines). The crack outline was incorporated into the 256-pixel, 7-bin weld model, as shown in Figure 5.46. For flaw response simulations, CIVA allows the user to create custom-shaped cracks using a 2D CAD editor. In this case, the crack was added directly to the geometry that had been previously generated so that beam simulations could also be run. The crack borders were defined in CIVA as backwall interfaces for simulation purposes because beam models do not allow for flaws to be defined.

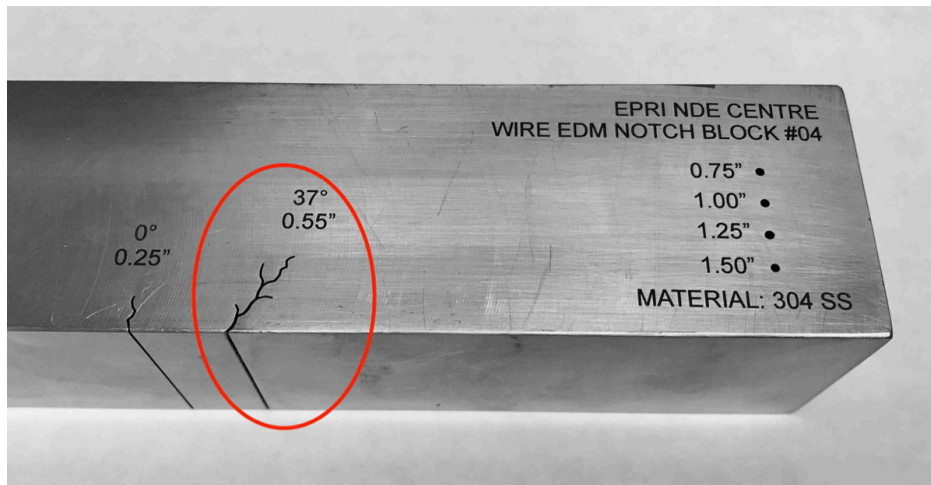


Figure 5.44. EDM “crack” in a stainless steel test block (specimen on loan to PNNL courtesy of the EPRI NDE Center).

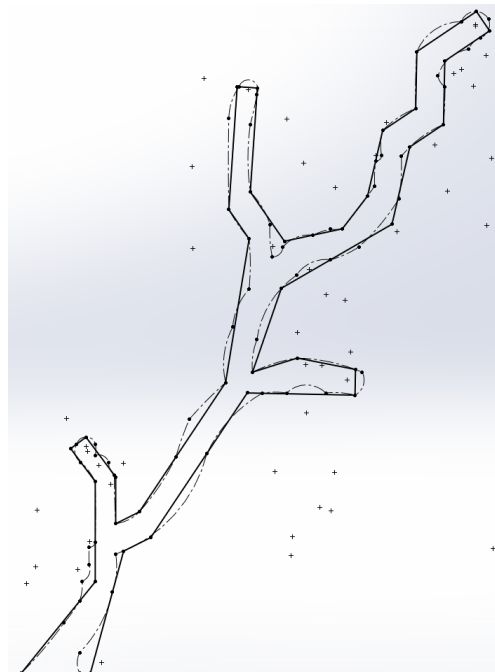


Figure 5.45. CAD rendering of the EDM “crack.” Dashed lines are the outline of the crack, and solid lines show the simplified outline for CIVA import.

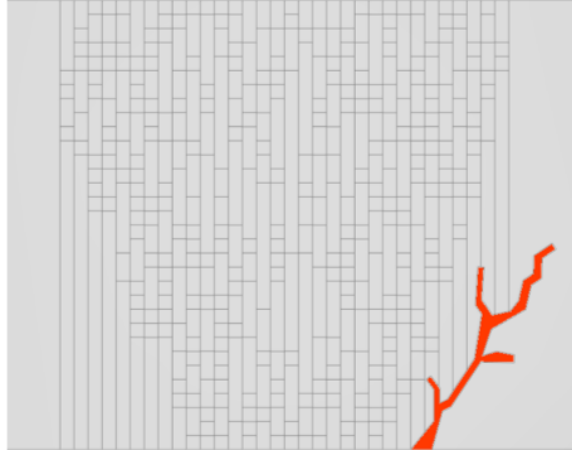


Figure 5.46. The austenitic weld model with the EDM crack added.

The EDM crack was scanned with a 2 MHz TRL probe with a 45° refraction angle and a focal depth of 37 mm (1.46 in.). A simulation was run with the same probe on isotropic material that contained the replication of the crack. Relevant simulation settings included Kirchhoff specimen echoes, backwall interactions only, five half skips,<sup>(a)</sup> full incident beam, an accuracy factor of 1 for both field and defect, no attenuation, no mode conversions, and L-waves only.

Figure 5.47 shows the results of the simulated and experimental scans; note that these are shown for qualitative comparison only, as the size scaling and color scales are not the same. The red arrow indicates the target flaw and the green arrow indicates a second, smaller flaw that is about 17 mm (0.65 in.) away. This smaller flaw was not included in the simulations. The red and blue horizontal cursor lines in the experimental scan indicate the positions of the crack corner and tip, respectively. The results of the two scans are similar in that they both reveal the presence of the flaw, the full depth of the flaw, and about the same flaw tilt angle (the true angle of the crack's tilt is 37°, the empirical data showed a tilt of 33°, and the simulation showed a tilt of 38°). However, the simulation does not show any specular reflection from the flaw face and shows a comparatively weak tip response versus the corner response. The empirical image, on the other hand, shows a consistent response from the entire flaw.

---

(a) This number of skips is typically excessive, but here it assures that any reflections between branches of the crack would be accounted for.

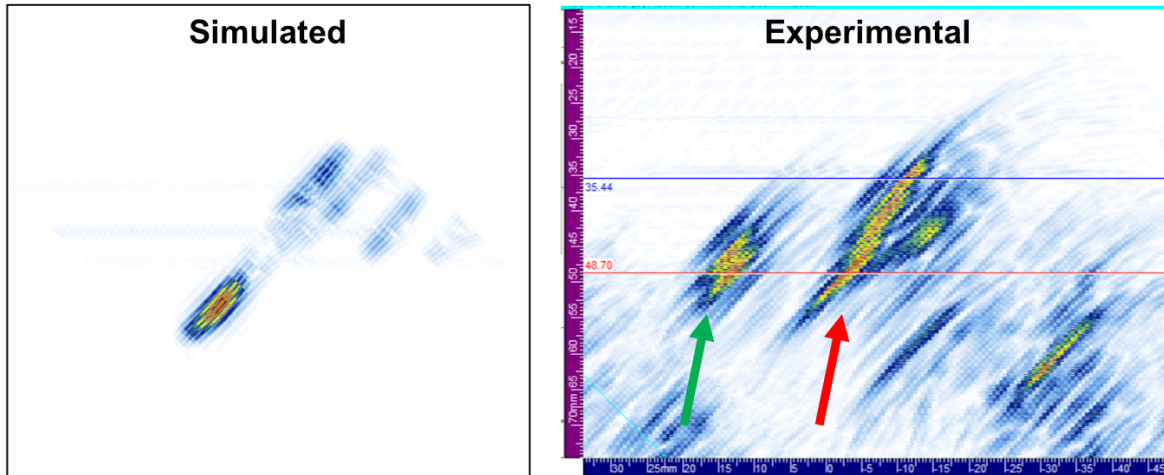


Figure 5.47. Qualitative comparison of a flaw response simulation and empirical data of the EDM “crack.” The 2 MHz TRL probe at 45° was used. The red arrow indicates the target flaw and the green arrow indicates a second, smaller flaw that is about 17 mm (0.65 in.) away. The smaller flaw is visible in Figure 5.44.

### 5.4.3 Limited Coverage Scenarios

PNNL also performed several beam and flaw-response simulations with coverage limitation scenarios for different refraction angles. All simulations used the same 2 MHz, 45° probe that was used for most weld simulations to date and the same settings described above. The wedge angle was adjusted to also give refraction angles of 60° and 70°. The roof angles were adjusted to keep the beam crossover point at about the specimen ID surface.

Figure 5.48 shows beam simulations through an isotropic (left) and austenitic (right) weld model. The probe was placed such that the front of the wedge was adjacent to the weld toe. Results illustrate flaw insonification at the different angles. The 45° beam did not reach the flaw. The 60° beam was nearly normally incident on the flaw, but the tip was not insonified in the austenitic model. The 70° beam insonified the tip, but the sound field intensity was considerably weaker than those of the other angles. It is interesting to note that in the austenitic weld model, beam scatter can also result in beam focusing. This is evident in the 60° and 70° simulations where some parts of the beam had higher sound intensity than in the isotropic model.

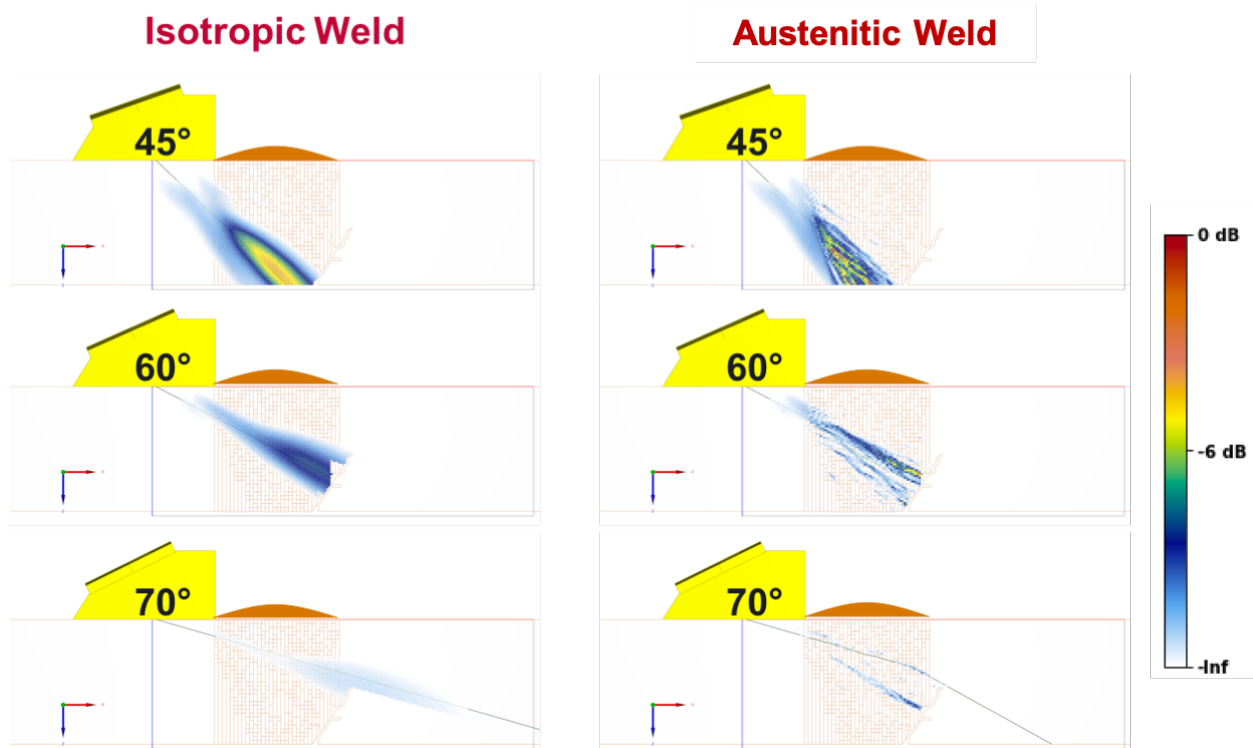


Figure 5.48. TRL-probe beam simulations through isotropic material (*left*) and the austenitic weld model (*right*) with the EDM crack.

Flaw response simulations were also run with the same weld crown limitation. Figure 5.49 shows the total flaw response and the ray path when the probe was at the weld toe. The response from the 45° beam was so weak that it would not realistically be distinguishable from noise. For comparison, Figure 5.50 shows the flaw response from the 45° beam with no coverage limitations. (Note that the appearance of the flaw response in this image is slightly different than usual because this image was reconstructed in MATLAB due to of the B-scan reconstruction bug in CIVA.) The 60° beam provided a strong response as the sound beam was directly incident on the flaw. However, the tip signal was not present so the flaw depth cannot be determined. The 70° beam resulted in a relatively weak response from the tip of the flaw that would likely be taken for noise or a weld fabrication flaw due to its position and intensity. Note that no corner response was observed with the 70° beam. This is because of an unintended coverage limitation—the probe was not able to translate back far enough to insonify the flaw corner due to the defined size of the specimen model.

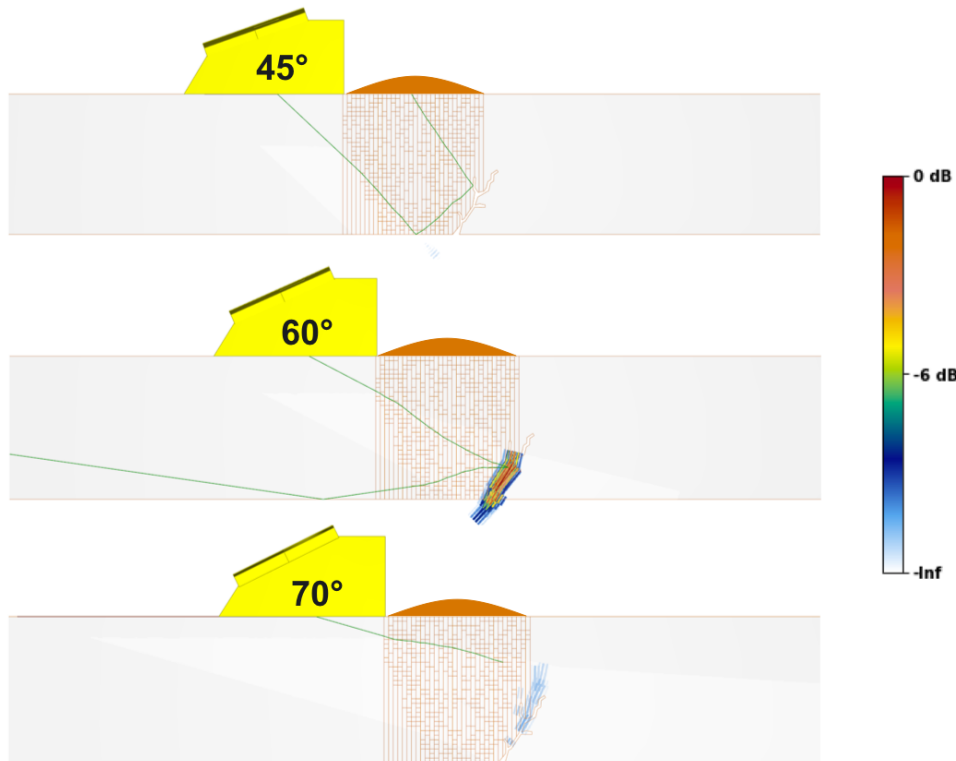


Figure 5.49. TRL-probe flaw response simulations through the austenitic weld with the EDM crack.

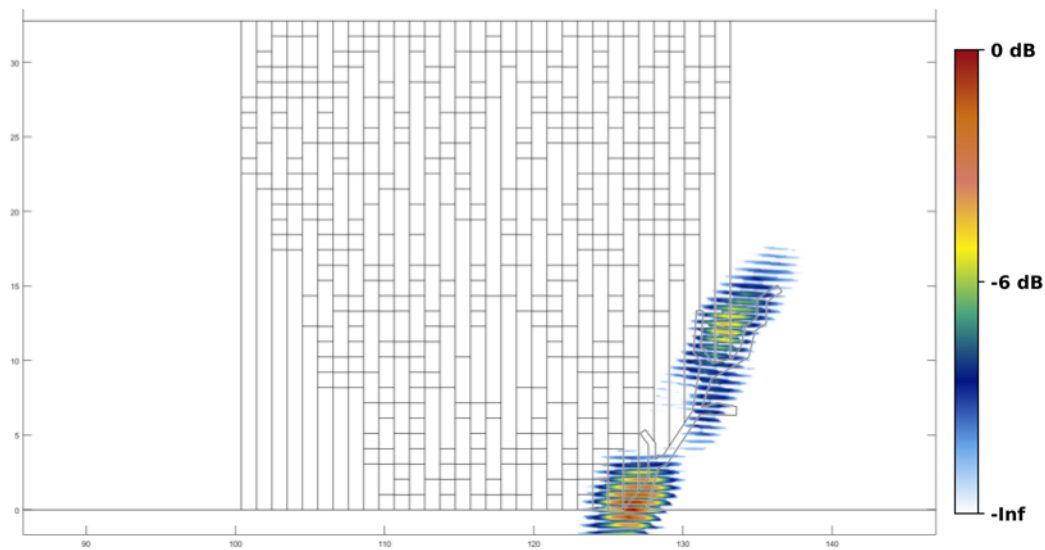


Figure 5.50. Flaw response simulation with the 45°, 2 MHz TRL probe through the austenitic weld model and no coverage limitations.

A second set of flaw response simulations was done on the austenitic weld model with a 6 mm (0.24 in.) deep notch on the far side of the weld; see Figure 5.51. Coverage limitations were implemented as above. Again, the 45° beam resulted in a very weak corner signal that would not be distinguished from the noise. At 60°, the entire flaw was insonified; however, because no tip signal was visible it may be unclear to an examiner whether the limitation allowed the entire

flaw to be insonified or not. At 70°, the corner was not insonified due to the backward limit on probe motion and may not provide the full picture of the flaw response.

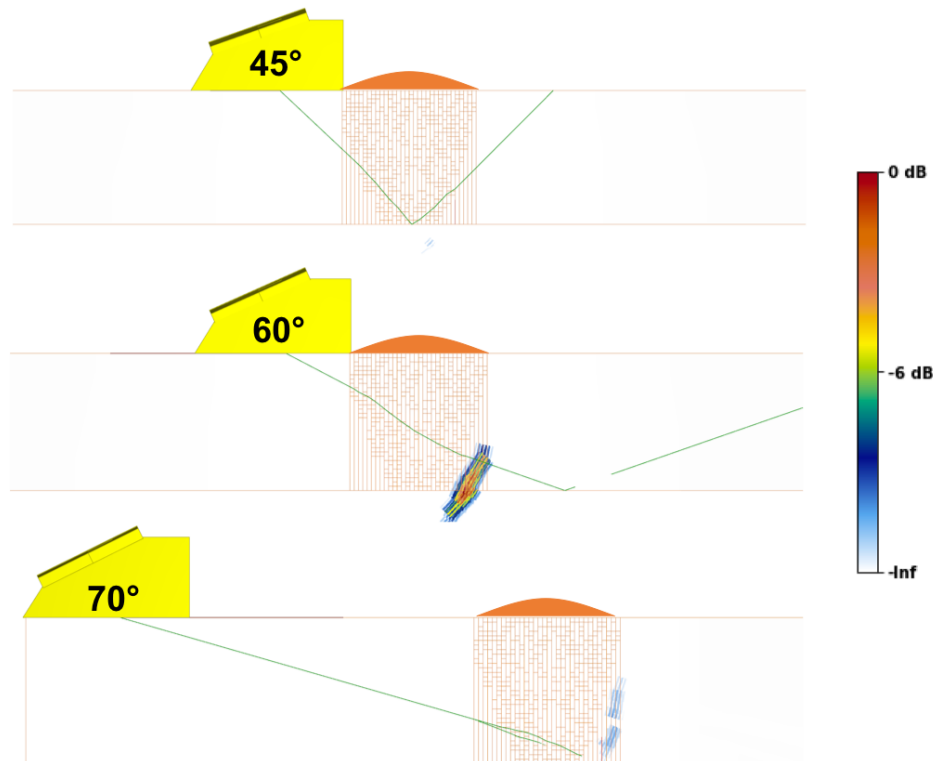


Figure 5.51. Flaw response simulations using the 2 MHz TRL probe through the austenitic weld model with a 6 mm (0.24 in.) deep notch on the far side.

Simulation results suggest that basic flaw response modeling may be useful for indicating whether a flaw will be sufficiently insonified under limited coverage scenarios. However, the simulation results remain to be verified with experimental measurements. These simulations did not include mode conversions, interface interactions, or other complexities. Hence, they only took about 10–15 minutes to run.

#### 5.4.4 Probe Frequency

The 7-bin, 256-pixel weld model number 08, which was determined to best represent the nominal case from the simulation set, was used to test the effects of different probe frequencies in beam simulation models. Four different TRL probes from PNNL's library of pre-defined probes (that is, probes whose parameters had previously been defined and saved in CIVA) were used. The probe frequencies were 1, 1.5, 2, and 4 MHz. Each probe had an element size of 20 mm × 34 mm (0.79 in. × 1.34 in.), a focal depth of 30 mm (1.2 in.), a refraction angle of 45°, and a bandwidth of 60%. Results of the simulations are shown in Figure 5.52 and are normalized to the peak signal intensity of the 1 MHz simulation. Results show a dramatic drop in signal intensity from the 1 MHz to the 4 MHz probes, which is consistent with the known effects of austenitic welds on higher frequencies. As the wavelength decreases with respect to the size of the scattering centers, scatter becomes more stochastic and more prominent.

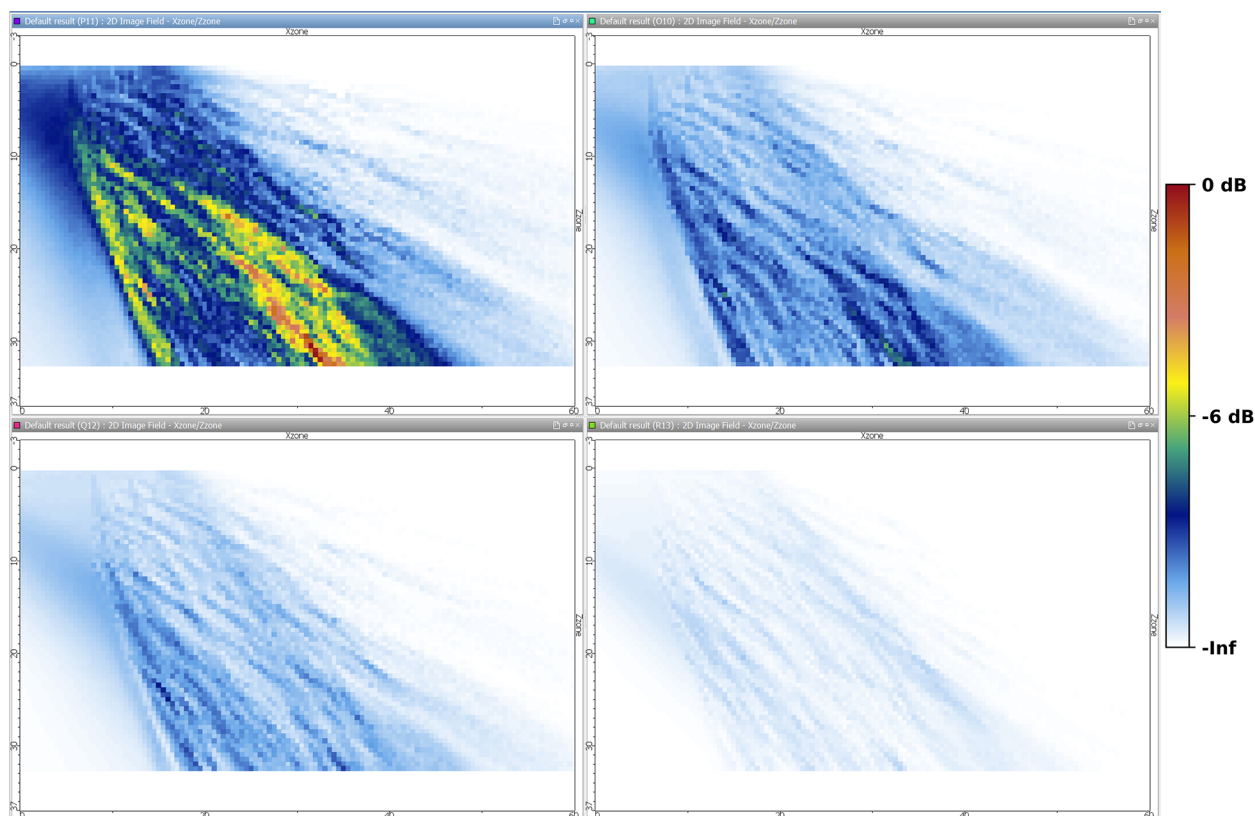


Figure 5.52. Beam simulations in an austenitic weld with different probe frequencies. Clockwise from top left: 1 MHz, 1.5 MHz, 4 MHz, and 2 MHz. Results are normalized to the peak signal intensity of the 1 MHz simulation.

### 5.4.5 Simulation Complexity

An important issue in modeling is the relationship between the simulations' complexity and the time required for them to run. So far, weld simulations have been run with the most basic CIVA options. This does not include interface interactions (sound interactions at internal weld or grain interfaces), mode conversions, attenuation (with the exception of the limited example discussed above), or noise. Activating any of these may increase simulation time dramatically. Also, the accuracy factor will likely need to be increased to eliminate the holes, which further adds to simulation time.

To illustrate the issue, flaw response simulations were run with the 256-pixel, 7-bin austenitic weld model, the 2 MHz TRL probe at 45°, and a notch on the far side. The first simulation used the basic settings, and the second simulation added interface interactions but had no other changes. Both simulations finished, but the basic simulation took 12 minutes while the other simulation took about 127 hours (~7600 minutes, or 635× longer). Figure 5.53 shows the results of the basic simulation and a ray trace of the sound beam. For comparison, Figure 5.54 shows the results of the same simulation, but with interface interactions activated. The ray trace of the L-wave sound beam is so complicated, with hundreds of reflected and refracted beams, that it entirely obscures the specimen. However, comparison of the flaw responses shows little difference between the two simulations. The simulation with interface interactions had some additional low-intensity signal near the flaw (circled in the figure). The open questions then are: Are these differences significant? If so, is it worth the extra time to run the complex simulations?

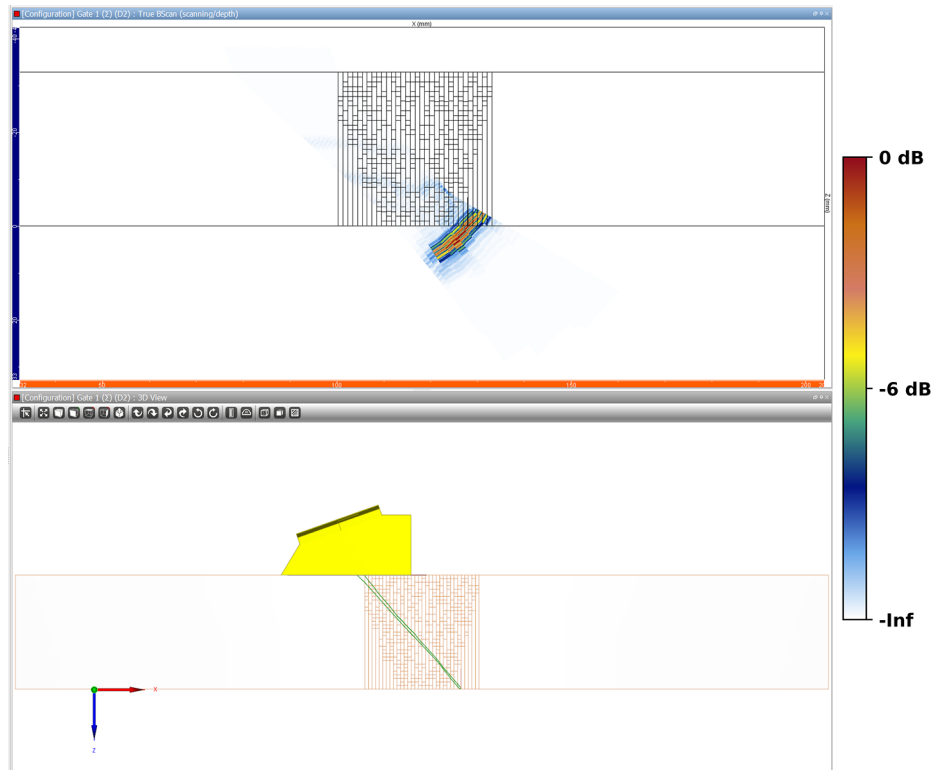


Figure 5.53. Flaw response simulation through the austenitic weld model using the 2 MHz TRL probe at  $45^\circ$  with no interface interactions. The green line is the transmitted and reflected beam.

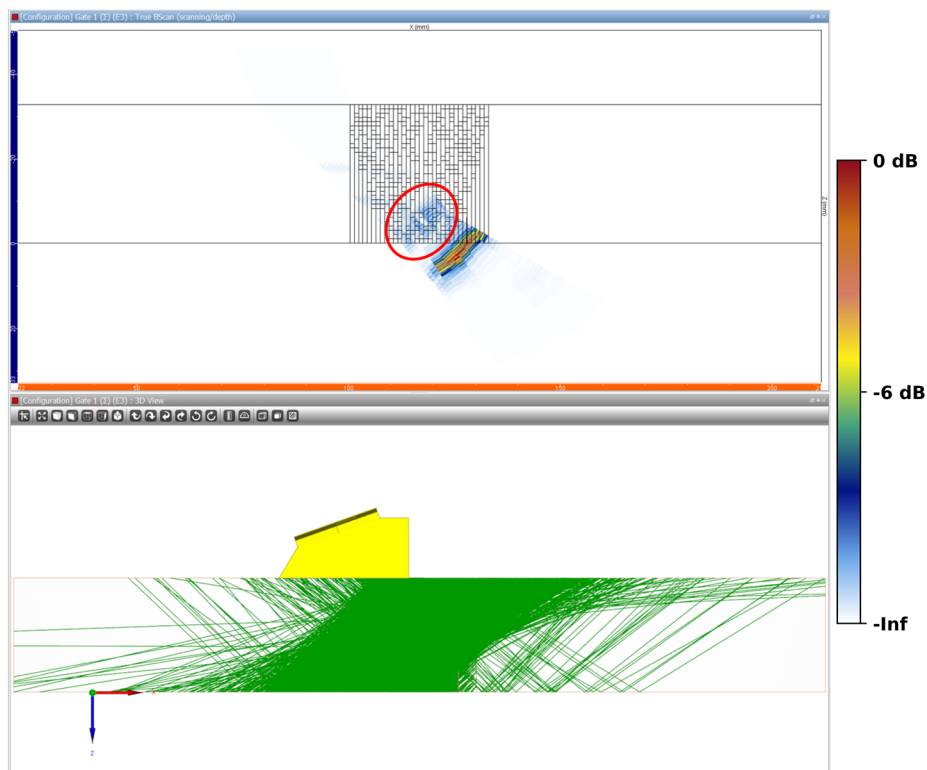


Figure 5.54. Flaw response simulation through the austenitic weld model using the 2 MHz TRL probe at 45° with interface interactions. The green lines indicate the beams reflected from the interactions with the weld model grains.

Based on PNNL's experience examining empirical scans of austenitic welds, PNNL concludes that the differences between the two simulations are not significant. Indeed, the extra signal in the complex simulation would likely be at or near the noise level in an empirical scan and does not appear to originate from a flaw. It would therefore most likely be ignored by an analyst. Thus, adding interface interactions to these flaw response models is probably not necessary. However, as this is a very limited study, *caution should be exercised when generalizing these findings to other simulation scenarios and geometries*. The addition of mode conversions, attenuation, and noise has not yet been investigated.

## 5.5 Summary

This section described simulation results through multiple austenitic weld models and geometries. Simulation results were compared to isotropic cases and empirical beam-mapping data. It is important to emphasize this point: **a single simulation, no matter how well conceived, is not adequate to predict the sound field coverage in a complex situation, such as an austenitic weld or a coarse-grained material**. In particular, PNNL advises against basing examination protocols or coverage calculations on individual simulation results. Rather, multiple simulations are required that explore the practical limits of both the inspection scenario and simulation parameters. There are many options and settings in CIVA, some of which considerably extend computation times. It would therefore not be feasible to run a comprehensive parametric study to determine which optimal combination of settings and specimen geometries provide simulation results that exactly match empirical data. Furthermore, because grain structures in real specimens vary spatially within the same specimen, not to

mention the significant variations from specimen to specimen, hunting for “ideal” simulation parameters is not practical. The parameters that are ideal for one scenario may not be ideal for another scenario. However, simulation results may be useful in predicting sound fields and flaw responses with consideration of the following:

- It is important to understand the modeling software and its limitations. CIVA has many options and settings, some of which can have a significant impact on simulation outcomes. When questions arise, expert technical support from EXTENDE should be engaged.
- Empirical data is critical for validation of simulation accuracy. Otherwise, it is impossible to know whether the models are producing useful results or if model parameters should be adjusted. It is neither practical nor possible to fingerprint every weld with destructive analysis, so a database of weld profiles and grain structures could be developed from mockups or specimens from cancelled plants. It would then have to be assumed that the welds in the database were representative, but at least a range of realistic options would be available.
- Compromises in selecting model parameters will be inevitable, such as including interface interactions or limiting the number of beam skips, to maintain reasonable computation times while balancing simulation realism.
- Results show that realistic geometries scatter the sound beam in ways that are not duplicated by Ogilvy models. As much realism as possible, understanding that there are practical limits, should be used in defining specimen geometries and grain structures. Additionally, for a given geometry or microstructure, the Euler angles play a critical role in the beam formation, scatter, and the amount of sound energy incident on the ID surface.
- Enough simulations should be run in order to cover a range of anticipated real-world variation of material parameters, such as geometry, anisotropy, crystalline orientations, and sound velocity.
- Quantitative methods should be used when applicable to compare images and simulation results. Obvious differences between images can be observed qualitatively, but more subtle differences may require an analytical approach.

The difficulties of real-world, through-weld inspections are already well appreciated, and the results shown in this section suggest that similar difficulties exist in simulated through-weld inspections. In field inspections, the variables are limited to what can be controlled by the examiner. Properties such as weld geometry and attenuation are fixed attributes of the specimen, but with proper examination technique and choice of probe frequency and wedge angle, reliable results can usually be obtained. Simulations, however, require a complete description of the specimen, in addition to all the other variables. Thus, it is important to maintain realistic expectations of model usefulness. If the limitations are understood and enough simulations are run to obtain a spectrum of anticipated outcomes, then results are expected to provide reliable guidance on beam coverage, flaw detectability, and probe performance.

## 6.0 Dissimilar Metal Weld

### 6.1 Introduction

Inspections of DMWs are challenged by the grain structure of the weld and butter material that can scatter and redirect the ultrasonic beam. Thorough inspections of such welds are critical due to the potential of stress corrosion cracking, thermal fatigue cracking, and mechanical fatigue cracking in NPP components. Models that can predict probe behavior, beam coverage, and flaw responses can save time and resources by informing inspection protocols and requests for relief. However, the geometry and orientations of the weld granular structures are not known, which makes it difficult to set up the models and interpret the simulation results. There are several publications describing the application of different weld geometry models and simulation tools that may be useful for predicting the behavior of ultrasonic beams through DMWs. An Ogilvy model, or an adapted Ogilvy model for DMW geometries, has been used to simulate beam propagation and flaw responses with CIVA (Gardahaut et al. 2014) and with finite element modeling (Kim et al. 2016; Hwang et al. 2019). Others have used EBSD-derived grain structures and CIVA to simulate flaw inspection through DMWs (Nageswaran et al. 2009; Carpentier et al. 2010). CIVA has also been used with other weld characterization techniques based on photographs of polished and etched weld sections (Gardahaut et al. 2012; Szávai et al. 2016). In this section, preliminary modeling and simulation work on a DMW specimen is described. Results are compared to those of austenitic weld simulations shown in this report and to empirical data.

### 6.2 Specimen Description

A large-bore, DMW specimen was used in this study. This is a CASS-to-CS mockup labeled 14C-146 that was described in depth in Section 7 of Jacob et al. (2019). A section of the mockup weld region was cut, polished, and etched so that the microstructure of the weld could be replicated for modeling. To characterize the grains, photographs were taken with a light source from different angles. (Note: this process will be described in Section 7.2.) Figure 6.1 shows a photograph of one of the sections under ambient light. The CASS side is to the left of the weld. In an attempt to characterize the grain structure, additional photographs were taken with oblique light sources. Unfortunately, the sections were not etched well enough to sufficiently discern the grains. Figure 6.2 shows one of the sections with the light source to the left. Visible in the images are the different features of the specimen, such as the weld, the buttering, and the cladding on the CS parent material to the right of the weld. Some of the grain structures of the weld and buttering are visible, revealing predominantly horizontal grains in the buttering and predominantly vertical grains in the weld.

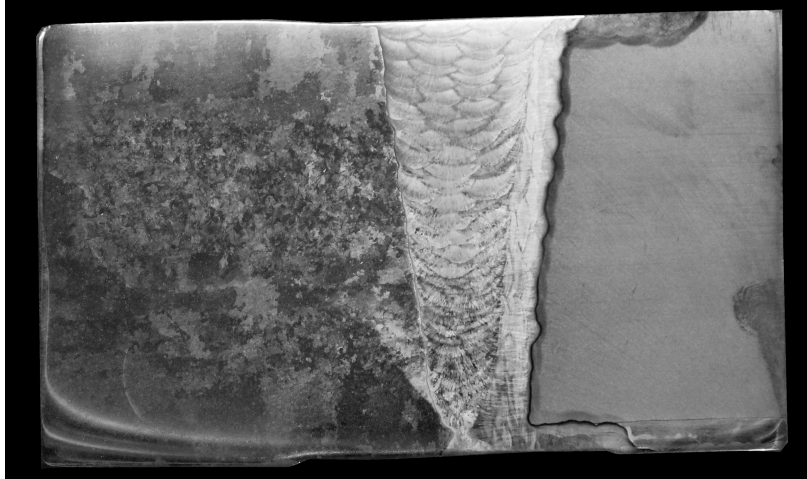


Figure 6.1. Photograph of a polished and etched DMW weld section under ambient light. The CASS side is to the left.

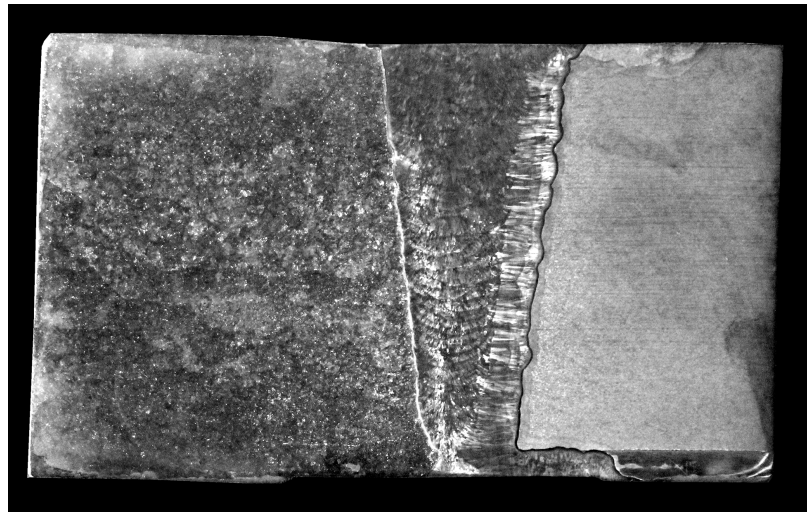


Figure 6.2. Photograph of the polished and etched DMW weld section with the light source to the left.

The grain extraction method described in Section 7.2 could not be used to replicate the grain boundaries due to poor etching, so a simplified geometry of the weld was traced using Photoshop. It was then converted to a CAD format that could be read by CIVA. Figure 6.3 shows the trace with the different regions labeled. The wall thickness of the CASS side of the model is 88 mm (3.5 in.). A similar model was created that includes a crack located on the CS side of the weld; see Figure 6.4. This is the same crack geometry used in austenitic weld simulations (see Section 5.4.2). Note that the grain structure represented here is much coarser than that used in our previous austenitic weld models. Although a finer representation of the DMW weld is not feasible at this time, this weld outline will serve to provide an intermediate level of weld model detail somewhere in between the fine austenitic weld model used in Section 5.0 and an isotropic weld region or Ogilvy model. This level of weld model detail is also consistent with that used by others (Chassignole et al. 2000; Liu and Wirdelius 2007; Mahaut et al. 2007; Nageswaran et al. 2009; Carpentier et al. 2010).

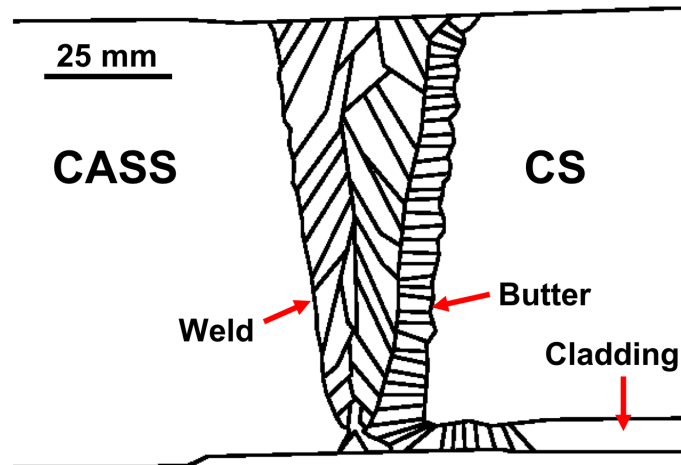


Figure 6.3. DMW CAD drawing with weld regions labeled.

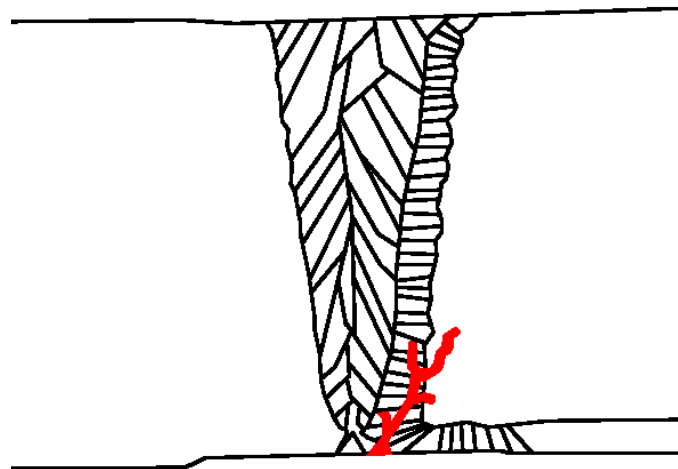


Figure 6.4. DMW model with a crack in the butter region.

### 6.3 Beam Simulations

The initial intention was to create coarse grains in the CASS side in CIVA using Voronoi regions. However, CIVA is currently only able to create Voronoi regions in two simple scenarios: flat-plane or cylindrical geometries that comprise single-region, isotropic materials. Voronoi regions cannot be generated in any weld models or 2D CAD drawings of specimens. Therefore, in order to create a realistic CASS-CS DMW model (representative of mockup 14C-146), the grain boundaries on the CASS side would have to be added off-line or extracted from photographs of the specimen. To save time in the initial testing, only the weld region was represented with granular structures and the bulk materials were assumed isotropic. Thus, for initial simulations, it was assumed that the CASS side of the DMW was isotropic WSS material.

Sets of ten Euler angles were assigned to the weld and buttering regions to create ten different model geometries. The cladding and SS side were assigned CIVA default parameters of isotropic SS 304, and the CS side was assigned default parameters of isotropic steel. The probe used was a 2 MHz, dual-element, TRL probe with a bandwidth of 50%. The beam crossover depth was 78 mm (3.1 in.) at a fixed refraction angle of 45°. Figure 6.5 shows the placement of the probe with respect to the weld for the simulations. The simulation results are shown in Figure 6.6 and were normalized to the peak amplitude of DMW\_03. Note that DMW\_09 had a peak amplitude about twice as high as that of DMW\_03, because of an apparent beam focal point that happened to occur in the simulation plane. The DMW\_09 peak amplitude value was not used for the normalization, however, because doing so caused the other results to appear so faint that virtually none of the features remained visible. For comparison, the isotropic simulation, also normalized to the peak level of DMW\_03, is shown in Figure 6.7. Finally, the mean image of the ten simulations is shown in Figure 6.8.

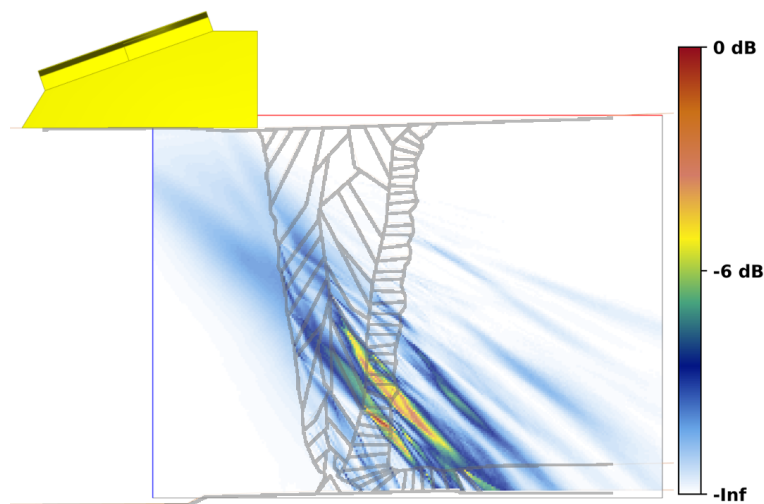


Figure 6.5. Probe placement with respect to the DMW model for beam simulations.

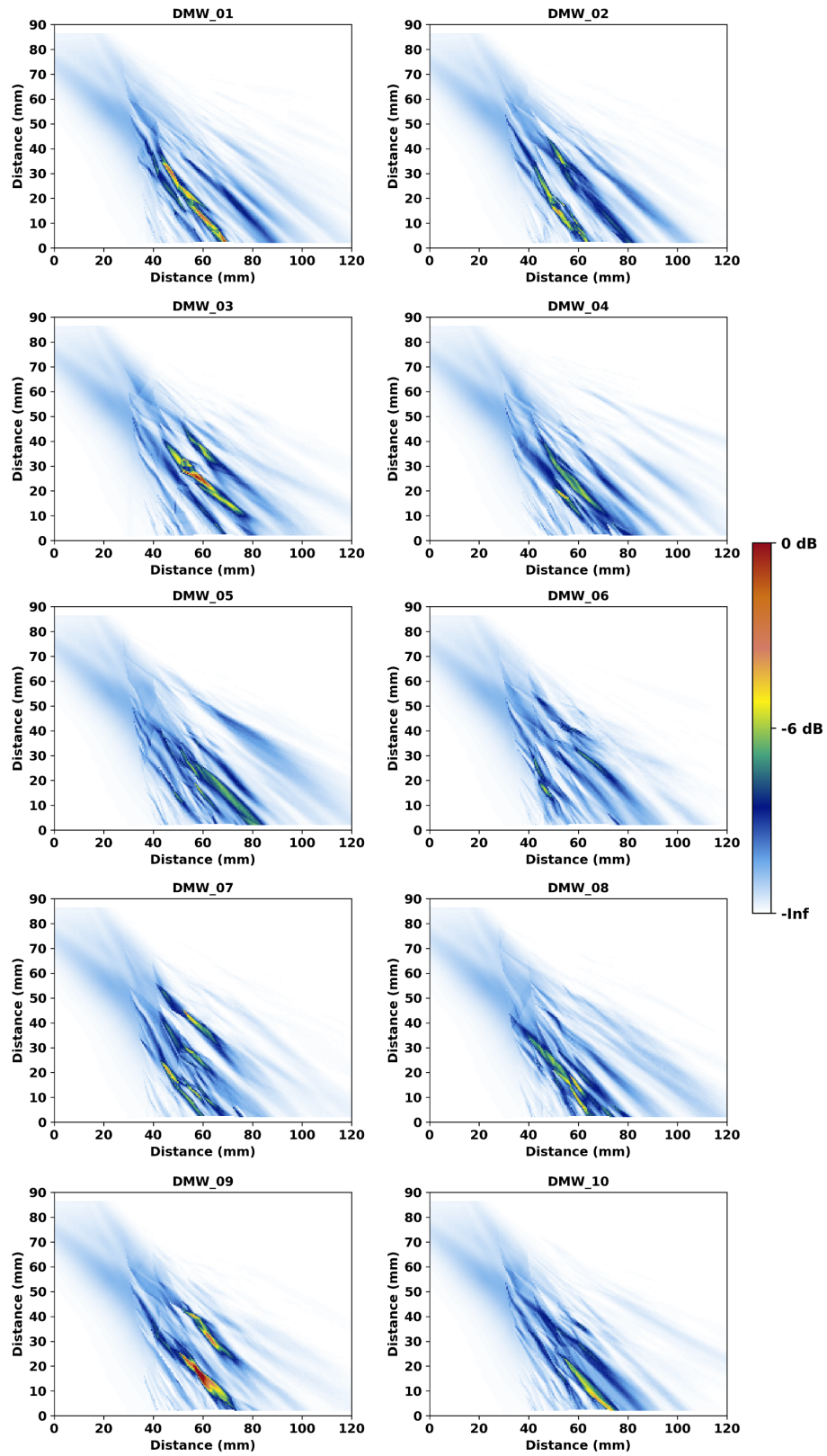


Figure 6.6. Beam simulation results using a 2 MHz TRL probe at 45° through the DMW with 10 different Euler angles.

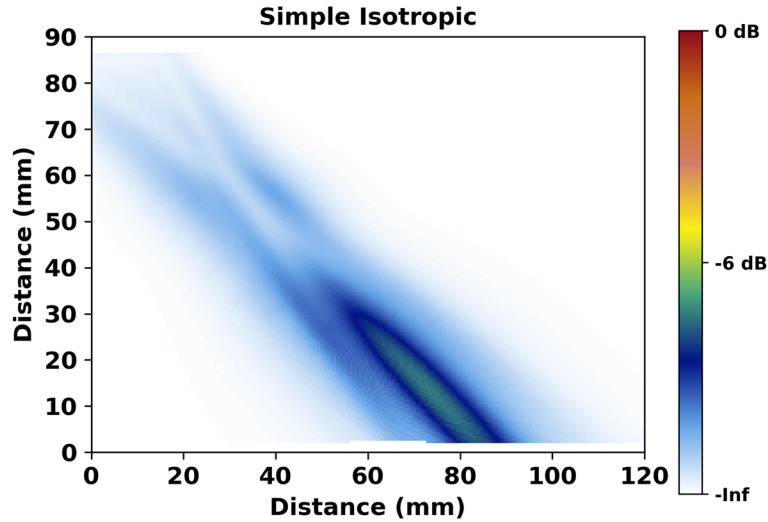


Figure 6.7. Normalized beam simulation through isotropic material.

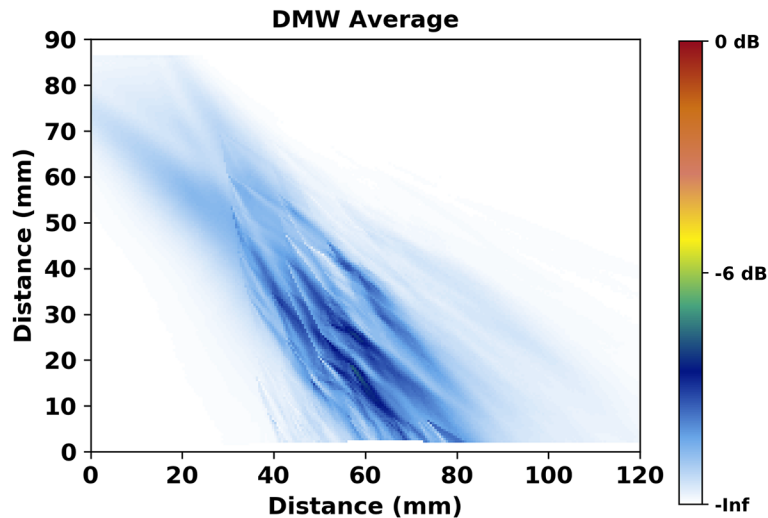


Figure 6.8. Average of the ten DMW beam simulations.

As observed with the simulations on the austenitic weld shown in Section 5.0, DMW model results show significant beam scatter and simulation-to-simulation variations due only to different Euler angle assignments. With the DMW model, however, the scatter appears to be occurring on a larger or coarser scale. That is, the scattering effects of individual “grains” are more prominent. In the specimen models with smaller grains, as shown in Section 5.3, the scattering is more random, resulting in a more even or smooth appearance of the sound field. Results therefore confirm that grain size matters when setting up specimen models. This is expected, because in the Rayleigh scattering regime, where the wavelength is much larger than the grain size, larger grains will have a disproportionately large effect on the sound propagation direction and scattering (Wan et al. 2017). At 2 MHz in steel, the wavelength of sound is about 3 mm (0.12 in.), and from Figure 6.3 it is clear that the smallest dimension of the drawn grains generally exceeds this. In actual DMW microstructures, the average dimension of the grains is typically much smaller than 3 mm (0.12 in.). Therefore, these DMW models are closer to the geometric or stochastic scattering regimes than the Rayleigh regime (i.e., the DMW model grain

sizes are too big), so the simulation results are not expected to be representative of scatter through actual DMW component welds.

As an aside, it is interesting to consider that it is common for some very large grains to exist in CASS microstructures. In Section 7.2 it is reported that the average grain size of a particular CASS specimen (AAD-3) was about  $7 \text{ mm}^2$  ( $0.011 \text{ in.}^2$ ) and the maximum grain size was about  $430 \text{ mm}^2$  ( $0.67 \text{ in.}^2$ ). The grain size distribution is far from Gaussian and tends to be heavily weighted by small grains that are well into the Rayleigh scattering regime. Such findings are supported by data shown in Papadakis (1964). However, as pointed out by Wan et al., “the effect of one large grain on wave scattering is greater than the sum of the effects of many small grains in the same volume.” One might therefore conclude that the use of large grains in a model that should contain only small grains—such as the DMW weld shown in Figure 6.3—will not produce simulation results that are representative of reality. Whether or not such simulations are suitable for making coverage predictions is currently an open question.

For completeness, beam simulation results of the DMW model with a crack are shown in Figure 6.9 with the signals normalized to the group maximum. Although the crack itself is not shown in the figure, the effects of the crack are seen in the simulation results because a “shadow” is cast behind the crack where no sound energy is present. This is shown by the white or empty triangular region between about 40 and 80 mm (1.6 and 3.2 in.) on the X-axis. The average of the simulations is shown in Figure 6.10. As with the austenitic welds shown Section 5.0, the DMW results suggest that the grain structure and Euler angles can affect how evenly the crack is insonified and, by extension, how well one could expect to measure the crack position, size, and depth in a field exam. Note that because CIVA cannot include flaws in beam simulations, the flaw was added to the geometry as part of the backwall. The added line segments that defined the crack altered the weld geometry enough that it was more efficient to reassign Euler angles to the new geometries. As a result, the beam simulations shown in Figure 6.6 do not correspond with those of Figure 6.9.

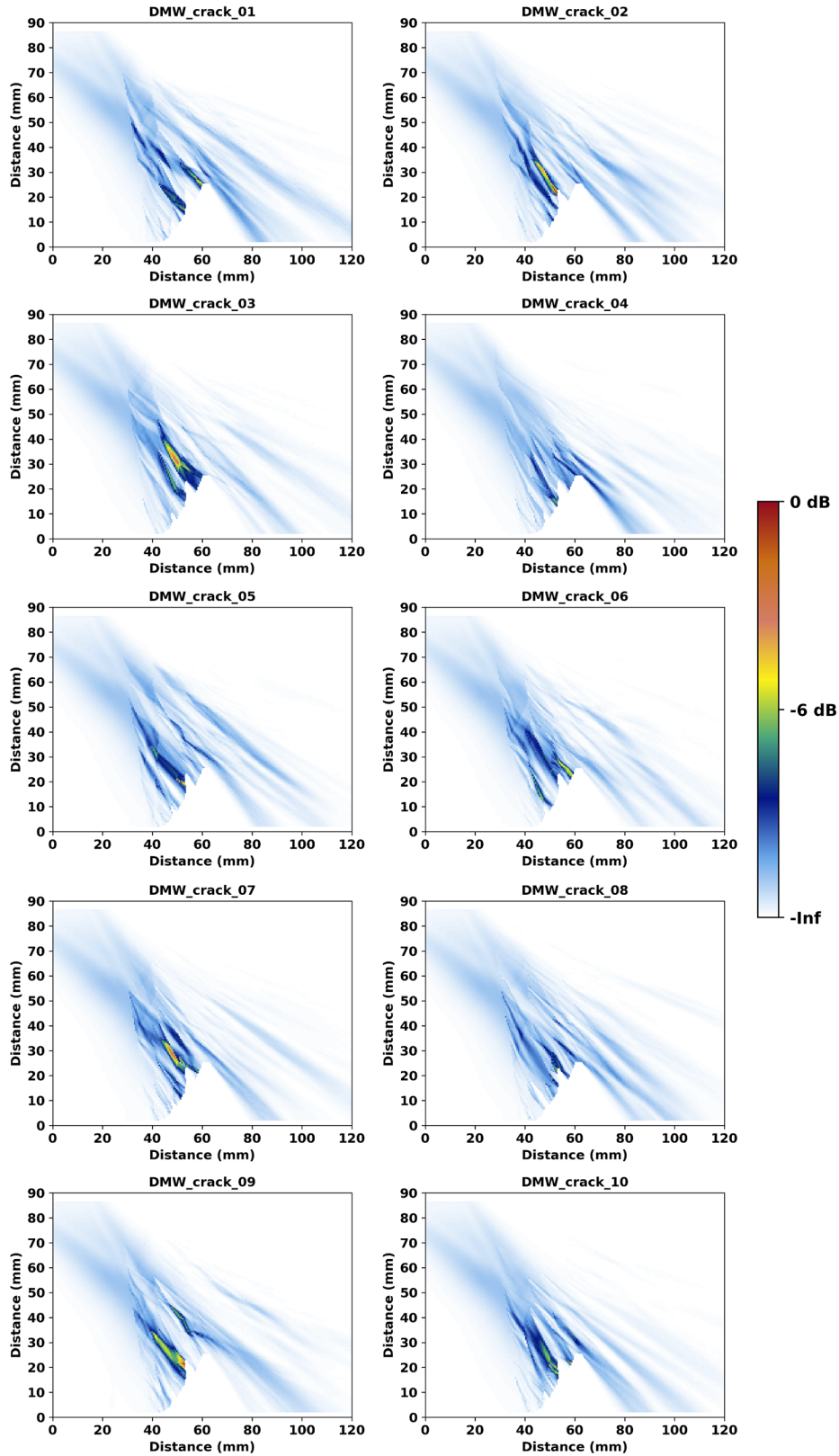


Figure 6.9. Beam simulation results using a 2 MHz TRL probe at 45° through the DMW with a crack in the butter region.

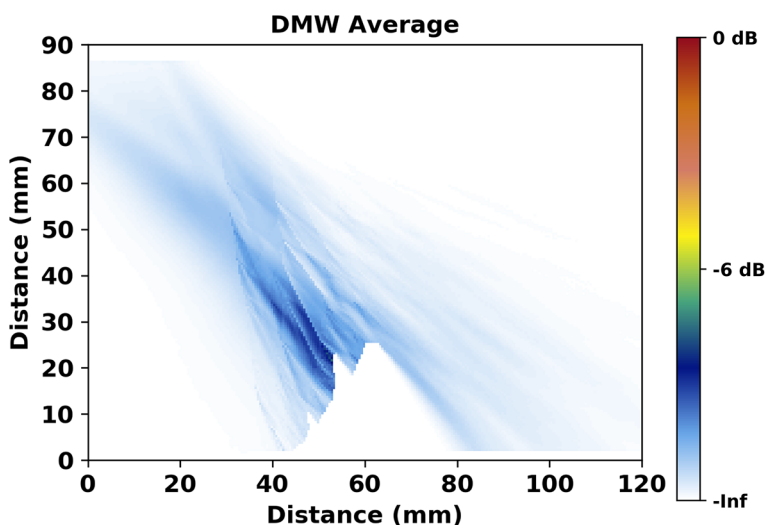


Figure 6.10. Mean of the beam simulations of the DMW with the crack.

## 6.4 Flaw Response Simulations

Two flaw response simulations were run on the DMW model, one included only backwall interactions while the other included both backwall and interface interactions. Both simulations used the same weld model with the same Euler angles. Simulations used the 2 MHz TRL probe as described in Section 6.3. Both simulations used L-waves only and had the option of one half-skip activated. No mode conversions, attenuation, or noise were included. Figure 6.11 shows the results of the simulation without and with interface interactions. The former simulation finished in 2.0 hours, and the latter finished in 61.5 hours. Results are normalized to the peak response of the simulation with interface interactions; it had about a  $3\times$  (10 dB) stronger signal response than the simulation with no interface interactions. A similar comparison was shown in Figures 5.53 and 5.54 with the austenitic weld model. In the austenitic model, activating the interface interactions made virtually no difference in the simulated flaw response. However, with the DMW model, the interface interactions resulted in a significantly stronger flaw response signal and more image clutter (i.e., echoes that do not appear to map to the flaw position). The DMW simulation had a thicker specimen model and therefore used a probe with a deeper focal depth. Otherwise, all key parameters were identical. Simulation time differences between the two models were due primarily to the larger number of grains and interfaces in the austenitic weld model. PNNL assumes that the main difference between the DMW and austenitic weld simulation results is due to the coarser grains in the DMW model; this hypothesis can be tested with a fine-grained DMW model. In the meantime, results suggest that the nature of the specimen model (e.g., coarse-grained, fine-grained, Ogilvy, etc.) has a significant impact on flaw response simulation results when options such as interface interactions are selected. This is an excellent reminder that it is important to understand the nature and limitations of the model before drawing conclusions from the results, especially when simulation times are so dramatically affected by clicking on a single checkbox in CIVA. For example, in this DMW case, turning on one interface interaction increased the simulation time by  $30\times$  but the benefits to the simulation outcomes were unclear.

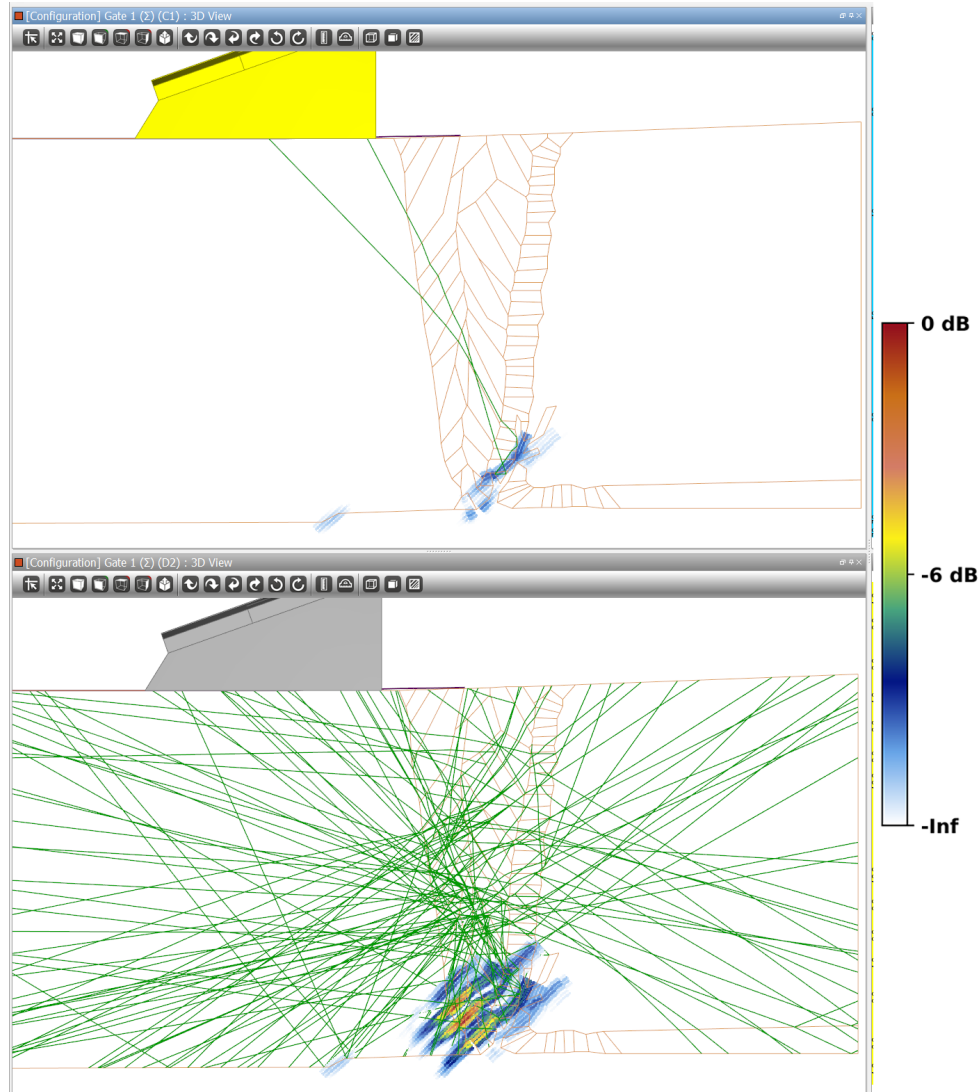


Figure 6.11. Flaw response simulation without (*top*) and with (*bottom*) interface interactions using a 2 MHz TRL probe at 45°. The L-wave transmit trajectory and reflections are shown by the green lines.

## 6.5 Comparison with Experiment

Experimental beam maps were acquired using a 2 MHz PA transmit-only probe with 84 mm (3.3 in.) focal depth (see Section 4.0). Additional simulations were performed to match the experimental conditions. The probe was placed at the edge of the buttering on the CS side of the weld. A 45° focal law was used, and a frequency-independent attenuation of 0.1 dB/mm (2.5 dB/in.) was added to each region of the specimen model. Note that this was lower than the 0.2 dB/mm (5.1 dB/in.) used in Section 5.3.3, because the 0.2 dB/mm (5.1 dB/in.) was found to be somewhat too strong when compared to experiment. Initial simulations were run with isotropic weld models. Figure 6.12 shows the beam simulations through isotropic weld material with and without attenuation, normalized to the no-attenuation result. The attenuation dramatically reduced the beam intensity and penetration depth, as expected. The experimental beam map shown in Figure 4.15 (2 MHz PA transmit-only probe with 84 mm [3.3 in.] focal depth on the CS side of the weld) was compared to the simulation results. The angle of the beam was

measured to be  $45^\circ$  for both the simulation and the beam map. The depth of the beam maximum was measured to be  $25 \pm 2$  mm ( $1.0 \pm 0.1$  in.) for the beam map and  $27 \pm 2$  mm ( $1.1 \pm 0.1$  in.) for the simulation. The attenuation level of 0.1 dB/mm (2.5 dB/in.) resulted in agreement between the simulation and the experimental beam map.

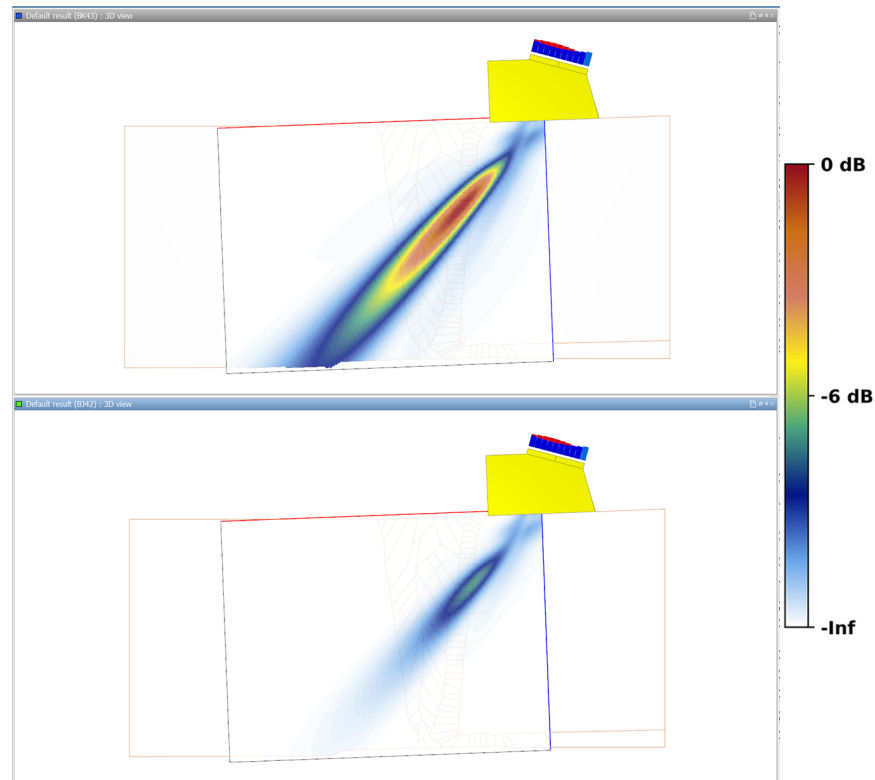


Figure 6.12. Beam simulations through isotropic material without (*top*) and with (*bottom*) 0.1 dB/mm (2.5 dB/in.) attenuation. A 2 MHz PA probe at  $45^\circ$  with a 84 mm (3.3 in.) focal depth was used.

Additional simulations were run with the PA probe on the same ten DMW weld models used in Section 6.3 above but with 0.1 dB/mm (2.5 dB/in.) attenuation added. Figure 6.13 shows the results of the ten simulations normalized to the highest signal intensity of the group, and Figure 6.14 shows the average result. The edge of the weld region is evident by the beam scatter, which is otherwise absent to the right of the weld in the CS material. Results show that almost no sound energy reaches through the weld and to the backwall of the specimen. These observations are consistent with those made from the empirical beam scans shown in Figure 4.16. However, the scatter patterns are dramatically different. This is likely due primarily to the coarse-grained pattern used for the DMW model. Even so, for the purposes of beam coverage predictions, the coarse-grained weld model may be sufficient to show that beam scatter and attenuation preclude far-side beam coverage from the modeled probe position with this probe. It should be noted that coverage would be improved as the probe is moved across the weld. This is evident by the data shown in Section 7.5 of Jacob et al. (2019), where the 2 MHz PA probe was able to detect circumferential flaws with good signal-to-noise ratio in the same DMW specimen that the current weld model was based on, although length sizing was generally poor. Note, however, that the axial flaws within the weld were not detected with the 2 MHz probe. Comparable flaw response simulations have not yet been completed.

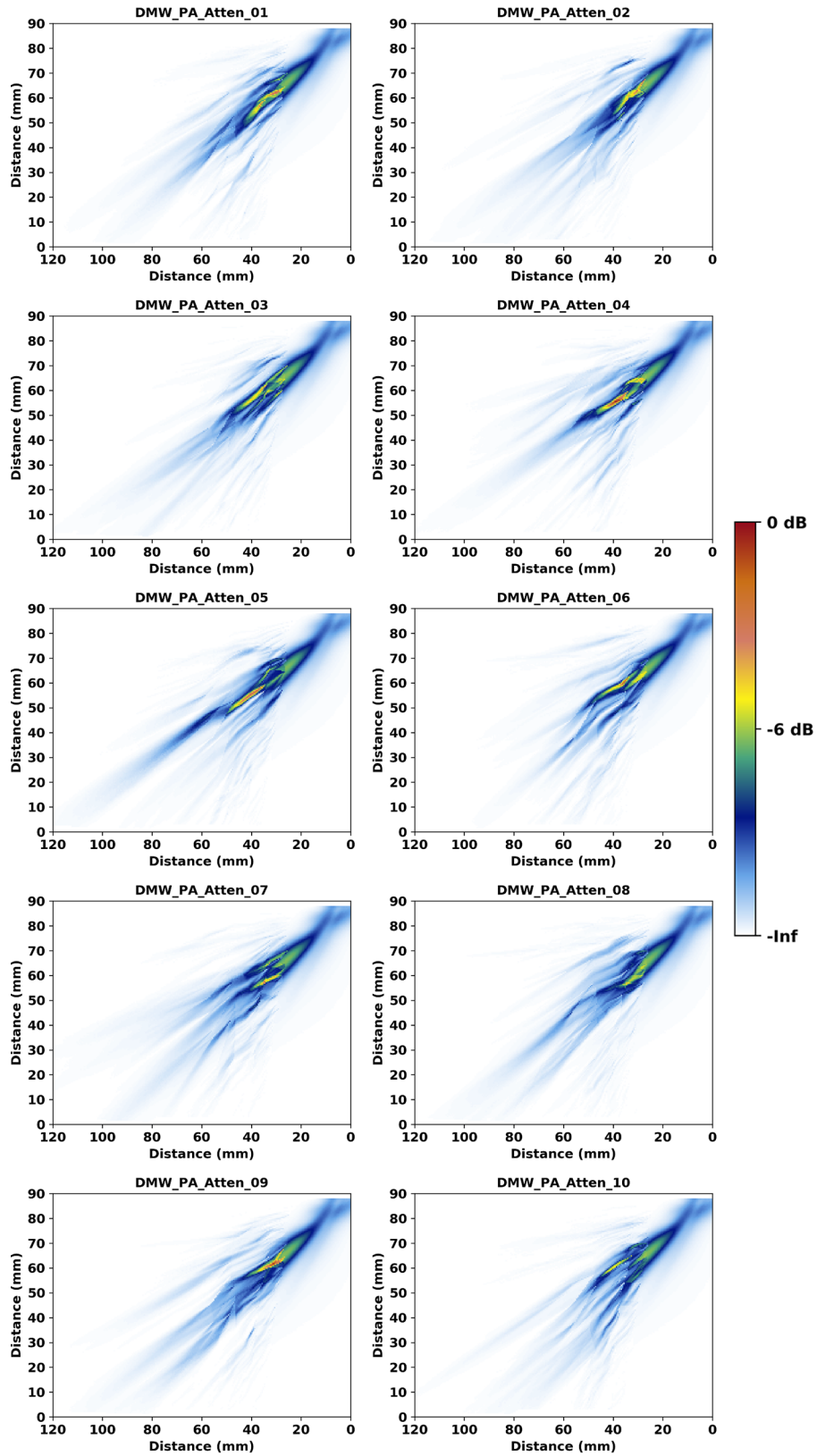


Figure 6.13. Simulation results with the 2 MHz PA probe at 45° on the CS side of the DMW model. An attenuation of 0.1 dB/mm (2.5 dB/in) was added to the simulation.

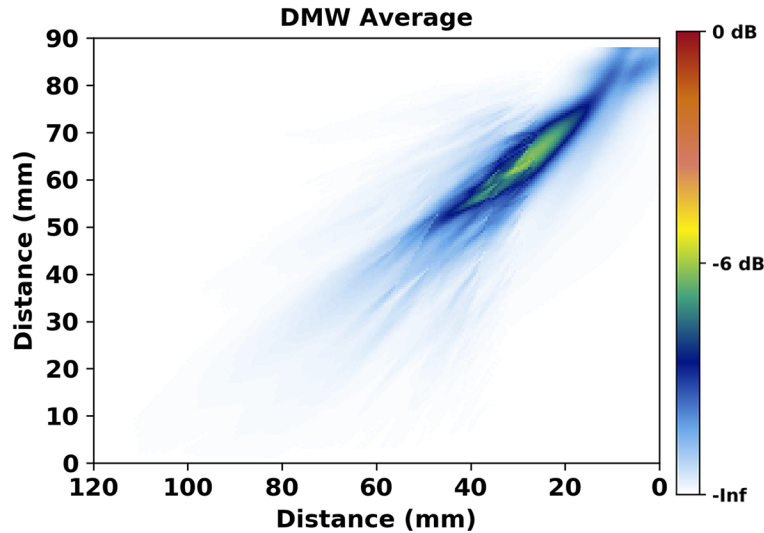


Figure 6.14. Average of the images in Figure 6.13.

## 6.6 Summary

Simulations were executed using a model of a DMW. This model differed from the austenitic weld model used in Section 5.0 due to the typical grain size. Overall, the DMW model had fewer, larger grains. Results showed that the larger grain structure had a direct effect on the beam scatter and general appearance of the resulting simulation: the sound beam was less scattered with the larger grains. Even so, simulation results (with attenuation added) were generally consistent with experimental beam maps; in both cases, the sound beam only weakly penetrated the weld region to insonify the specimen backwall on the far side of the weld. For coverage predictions, results illustrate the importance of performing beam simulations through an appropriate weld model geometry with beam attenuation, even if the model lacks detail in the representation of the actual grain structure.

## 7.0 CASS Model

### 7.1 Introduction

Model-based inspection simulations can be used to understand and improve ultrasonic inspections of heterogeneous polycrystalline and coarse-grained materials, such as CASS. Several publications describe aspects of research in creating coarse-grained materials for computational modeling while executing different types of models.

Nearly exact specimen models can be generated from EBSD measurements. CASS specimen models were created from EBSD scans by Chen et al. (2015). The researchers showed that simulations with the CASS models produced noise and signal distortion that were consistent with experimental results. They suggested that the accurate description of specimens is key for modeling, and that the EBSD approach to defining specimen models is highly effective. Nakahata et al. (2016) used EBSD data to create elongated grain structures for simulating sound propagation through coarse- and fine-grained CASS parallel to the grain elongation direction. They showed that at 2 MHz, average grain diameters of 0.3 mm behave similarly to homogeneous material, whereas average grains of 1.1 mm cause significant scatter and attenuation.

Other methods can be used to generate specimen models as well. Van Pamel et al. (2016) used 2D Voronoi models and a full matrix capture approach with finite element modeling to study the effects of aperture size and array type on predicted signal-to-noise ratio. They concluded that a 2D array would be beneficial over a 1D array, and that pitch-catch probe configurations can be advantageous when trying to minimize noise. Shivaprasad et al. (2018) also used Voronoi models in different simulation studies of the effects on sound propagation on grain size, orientation, and randomization. Wan et al. (2017) used specimen models with a regular square lattice and models based on a physical specimen to investigate the effects of grain size on sound attenuation in coarse-grained materials. They showed that different grain sizes resulted in different types of scattering (i.e., Rayleigh, stochastic, or geometric), but that a few large grains in a fine-grain model can have a disproportionately large effect on the scatter at a given frequency. They also showed that higher inhomogeneity of grain size distributions may introduce a stronger frequency dependence to attenuation.

Finally, CIVA has been used by several different research groups to model various effects in coarse-grained materials. For example, noise and attenuation were simulated using CIVA's built-in point-scattering, noise-simulating capability (Dorval et al. 2009). Beam propagation and flaw response were modeled by EPRI (2018) using Voronoi models, and results were compared to experimental scans. In addition, probability of detection calculations were simulated under various scenarios in CIVA (Ribay et al. 2017).

Due to the nature of CASS, realistic predictions of beam coverage and flaw detection through such materials must include an appropriate representation of the polycrystalline structure. Otherwise, the beam scatter, redirection, and attenuation that is well known to occur in such materials will not be adequately accounted for and the coverage predictions will not be accurate. In this section, models of a realistic coarse-grained CASS structure are tested in CIVA by generating beam simulations. Results are quantitatively compared to simulations generated from a Voronoi model to determine whether the Voronoi model is an adequate representation of the realistic structure. Finally, results are compared to empirical beam maps. In addition, the

appropriate CIVA accuracy factor is evaluated and determined for both the realistic and Voronoi cases.

## 7.2 Realistic Model of Vintage CASS Microstructure

### 7.2.1 Specimen Model Preparation

CASS specimens can be used to create a realistic specimen model that describes a coarse-grained material. Cut, polished, and etched sections can reveal individual grains, and EBSD can be used to characterize the grain boundaries and crystalline orientations (Sakamoto et al. 2012; Chen et al. 2015; Nakahata et al. 2016). This approach was taken by PNNL for studies with austenitic welds (see Section 5.0), and PNNL has access to many polished specimens from a previous beam-mapping study (Crawford et al. 2014). However, the specimens were too large for the EBSD equipment at PNNL. Instead, an alternative approach using light photography was used to capture grain geometries, and Euler angles in CASS material were taken from the literature and used to define crystalline orientations.

It was observed that the grains from polished and etched specimens reflect light differently when light is incident from different angles. It was therefore inferred that acquiring photographs with a light source of different incident angles would provide a more complete depiction of the grain boundaries than single photographs. This method was tested on a section from a coarse-grained specimen that was labeled as AAD-3 (this specimen was described in Crawford et al. (2014) for beam-mapping studies). Figure 7.1 shows a photograph of the section with ambient light. Figure 7.2 shows the same section photographed with two different lighting angles. A portable halogen light was used as the light source in an otherwise dark room, and an SLR camera was mounted on a tripod and operated with a wireless remote shutter control to prevent any camera motion between shots. Notice that the visibility of the grains in Figure 7.2 changes as the lighting angle is shifted. Testing was done with additional lighting angles, but it was found that two angles were generally sufficient.

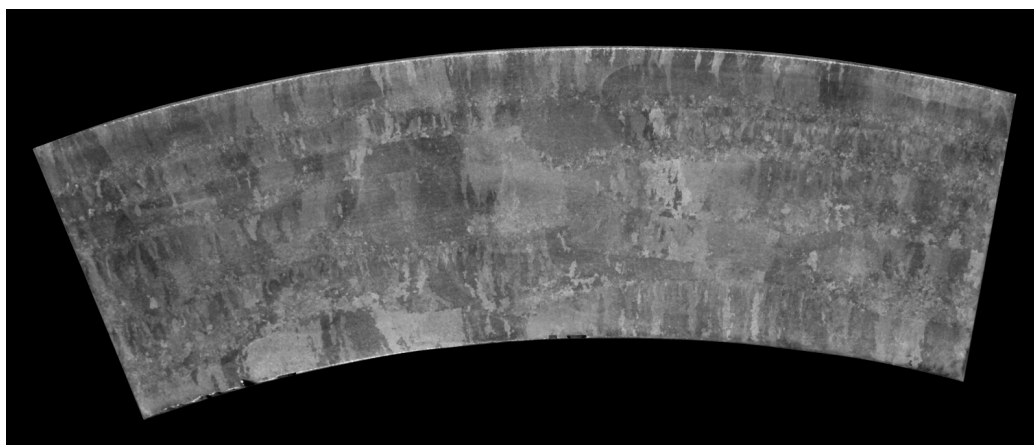


Figure 7.1. Coarse-grained CASS specimen AAD-3 photographed with ambient light.

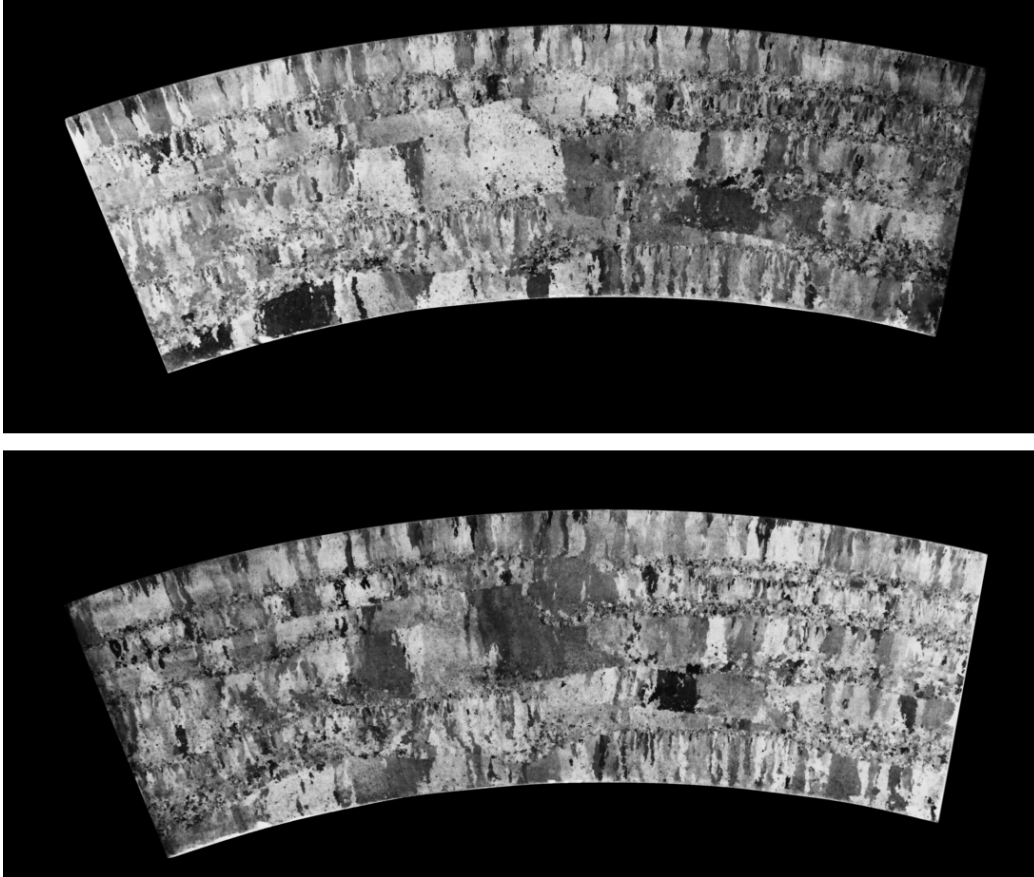


Figure 7.2. The section shown in Figure 7.1 with illumination from the left (*top*) and the right (*bottom*).

Image analysis software ImageJ was used for image processing and grain boundary extraction. Figure 7.3 illustrates the image processing steps used to create the grain outlines. The process is as follows:

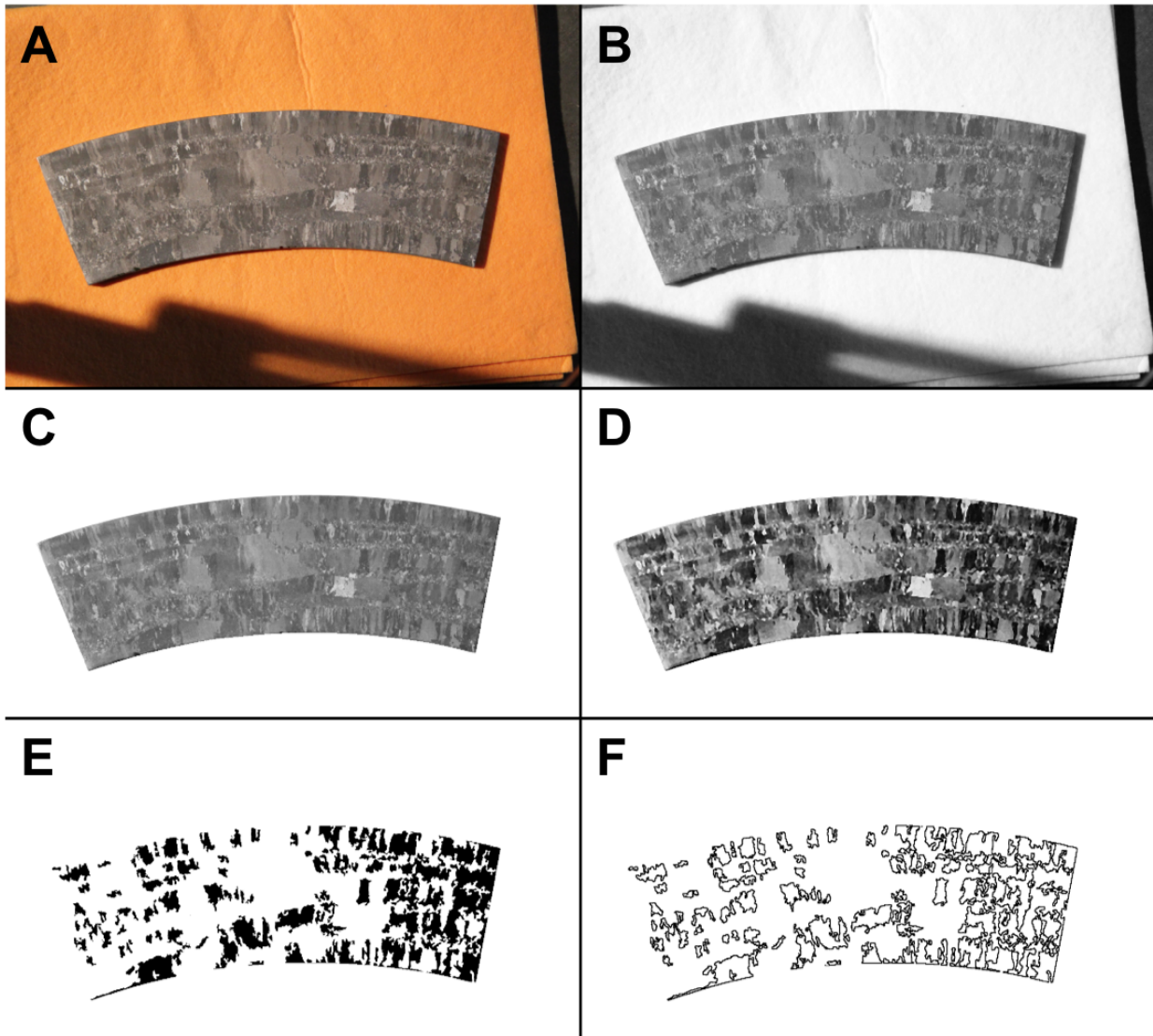


Figure 7.3. Illustration of the steps used to extract the grain boundaries from photographs. A: Example photograph with lighting from the left. B: The red channel of the RGB image. C: Image from Panel B with the mask applied. D: Image from Panel C with image filtering applied. E: Binary image of highlighted grains. F: Boundaries from the grains in Panel E.

1. Color photographs (Panel A) are split into separate RGB (red/blue/green) channels, which results in three grey-scale images. The histograms of these images are evaluated to determine the one with the largest spread of grey-scale values (i.e., the image with the greatest contrast), and this image is retained. In this case, the red channel was retained (Panel B) and the others discarded.
2. A mask is created from the specimen outline to remove all image background, and the mask is applied to the grey-scale image (Panel C).
3. The masked image is filtered to enhance contrast, remove speckles and noise, and sharpen grain boundaries (Panel D). This is done in three steps with the Enhance Contrast filter, a

Median filter, and an Unsharp Mask filter. Optimal filter parameters are determined by trial-and-error.

4. The window/level of the image is set to two different ranges—one to emphasize the bright grains and the other to emphasize the dark grains. A binary (black and white) image is created from each of the window/level settings. Panel E shows the binary image with the dark grains emphasized. Note that more than two window/level settings can be used if necessary; this may be helpful if image contrast is poor.
5. A particle removal algorithm is run to eliminate any grains that are below a size threshold, typically about 1/10 of the wavelength that will be used for simulations. Panel E shows the binary image with particles already removed.
6. An edge-finding algorithm is used to outline the region boundaries in the mask images and create a partial grain skeleton (Panel F).
7. Steps 4, 5, and 6 are repeated as necessary with different window/level settings until all the grains have been outlined.
8. Repeat the process for both photographs.
9. The partial skeleton images are summed to create a single image with all the grain outlines. Some additional processing is done to clean up regions where edge outlines did not line up exactly due to filtering and where grain boundary segments did not form an enclosed region. This may include a final particle removal step and/or region dilate/erode steps. Figure 7.4 shows the final grain skeleton.

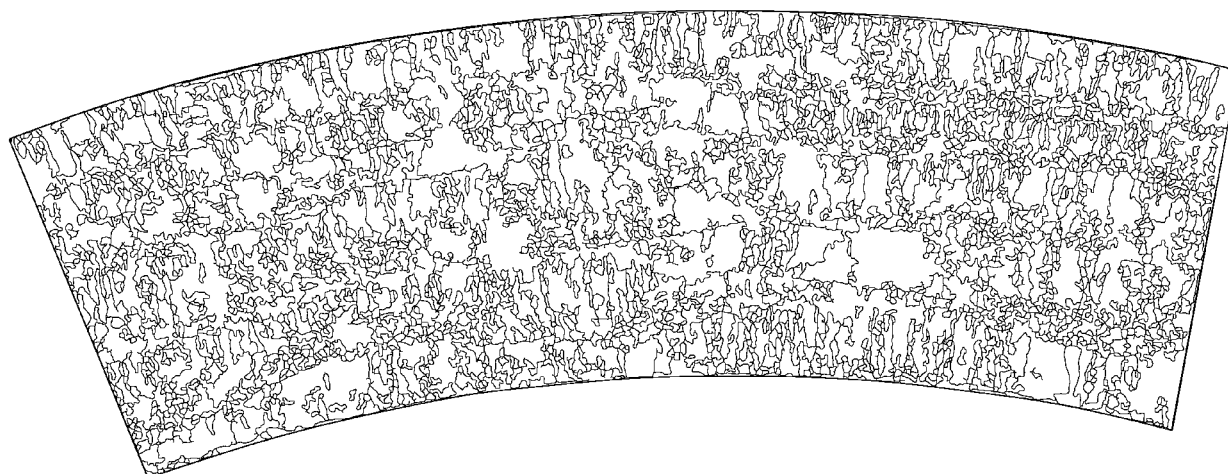


Figure 7.4. Final grain outline image of AAD-3.

Most steps in the above procedure can be automated, and the original photographs can be processed into a grain skeleton in only a few minutes. Some trial-and-error may be needed to optimize filtering and to find the optimal window/level settings. A similar but less-involved approach was described briefly by Ribay et al. (2017) to measure grain size.

To import the grain outlines into CIVA for use as a specimen geometry, the outlines must be in a CAD file format comprising line segments. However, because the grain outlines resulting from the above method are generally not straight lines, converting the outlines directly into a CAD file would result in tens of thousands of individual line segments, most of which would only be one or two pixels long. To eliminate this problem and to make a CAD file that is simple enough for

CIVA to handle, PNNL applied a line reduction algorithm that can minimize the number of line segments.<sup>(a)</sup> This is essentially a one-dimensional meshing process. Careful attention was paid to the locations of the segment endpoints and the deviation of any segment from the curved grain boundaries in order to retain the original geometry as closely as possible but without creating quadpoint intersections that CIVA 2017 cannot handle (see Section 5.3.1). Figure 7.5 shows the line reduction algorithm applied to a subsection of the AAD-3 grain boundary image with three different threshold values: 3, 7, and 14. The number of line segments with each threshold value is 4548, 2937, and 2248, respectively. As the threshold is increased, the number of segments needed to define the geometry decreases, but at the same time the representation of the grain boundaries loses fidelity. In this case, a good balance appears to be reached with the threshold value of 7—the grain boundaries are well represented without resorting to an unwieldy number of line segments. The final specimen model, shown in Figure 7.6, was  $80 \times 80$  mm ( $3.1 \times 3.1$  in.) and had 810 regions, or grains. The average grain size was measured to be about  $7 \text{ mm}^2$ , the grain size standard deviation was  $25 \text{ mm}^2$ , and the maximum grain size was about  $430 \text{ mm}^2$ . This represents a large range of grain sizes, with the distribution heavily weighted by small grains. Recall, this was after the smallest grains were removed during image processing.

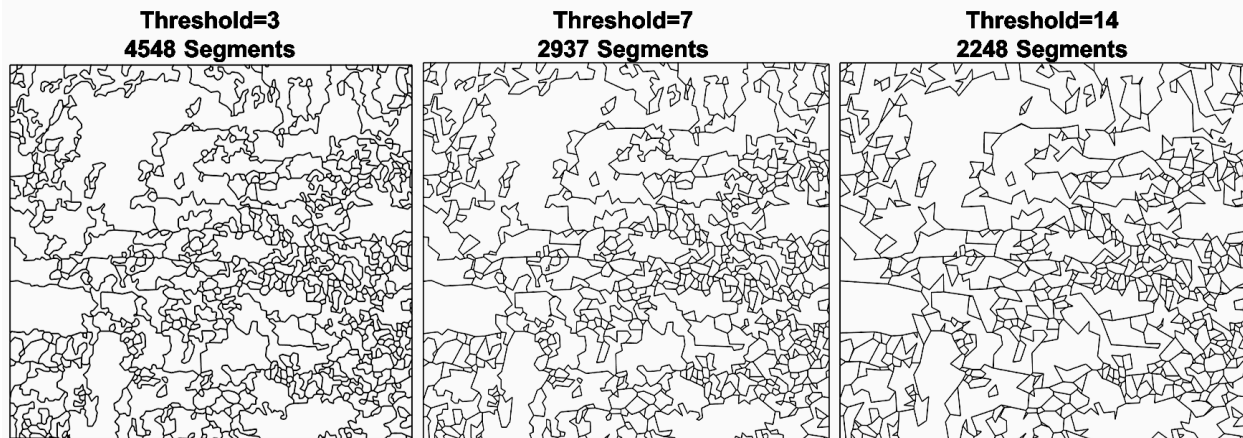


Figure 7.5. Results of applying the line reduction algorithm with different threshold values to a section of the AAD-3 skeleton.

(a) The method was adapted from the MATLAB “reducem” algorithm described at <https://www.mathworks.com/help/map/ref/reducem.html>.

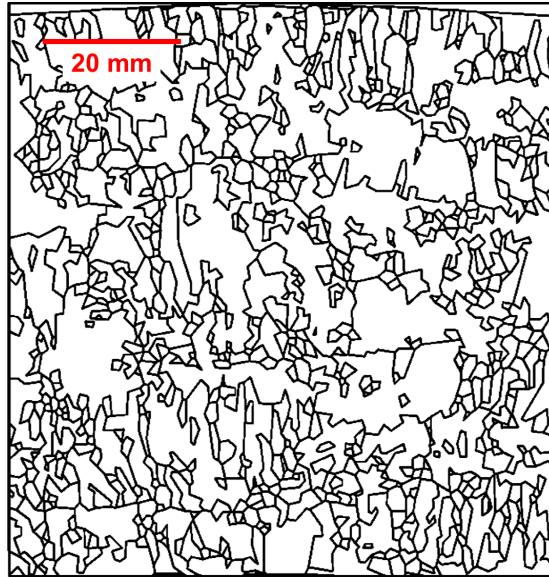


Figure 7.6. Specimen model of AAD-3 used for simulations.

The process was repeated on a second specimen, labeled B-519C (columnar). This specimen was also described in Crawford et al. (2014). Figure 7.7 shows a photograph of B-519C under ambient light, and Figure 7.8 shows the grain skeleton. The line reduction algorithm resulted in the image shown in Figure 7.9.

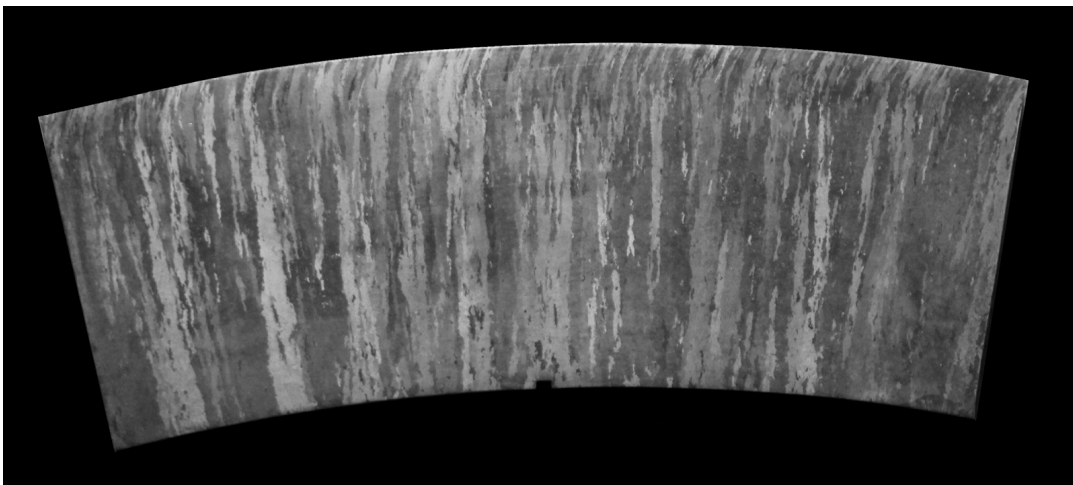


Figure 7.7. Ambient-light photograph of B-519C, a columnar-grained CASS sample.

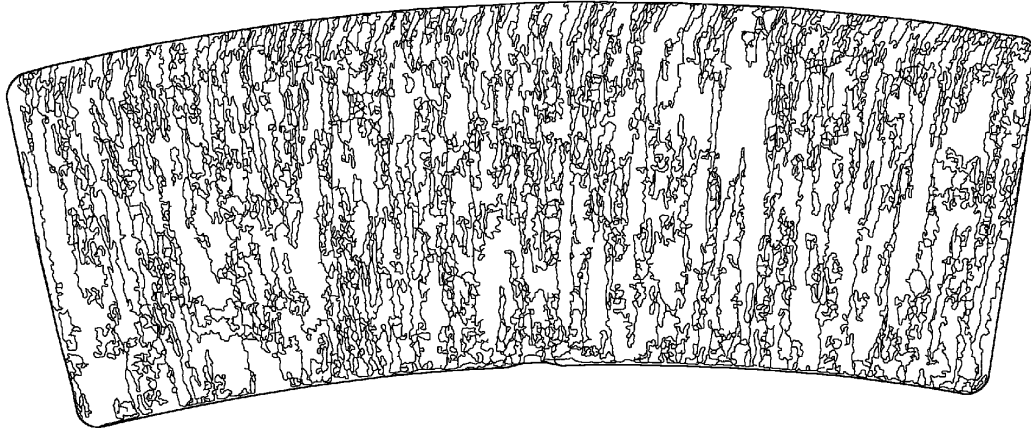


Figure 7.8. Grain skeleton of Specimen B-519C.

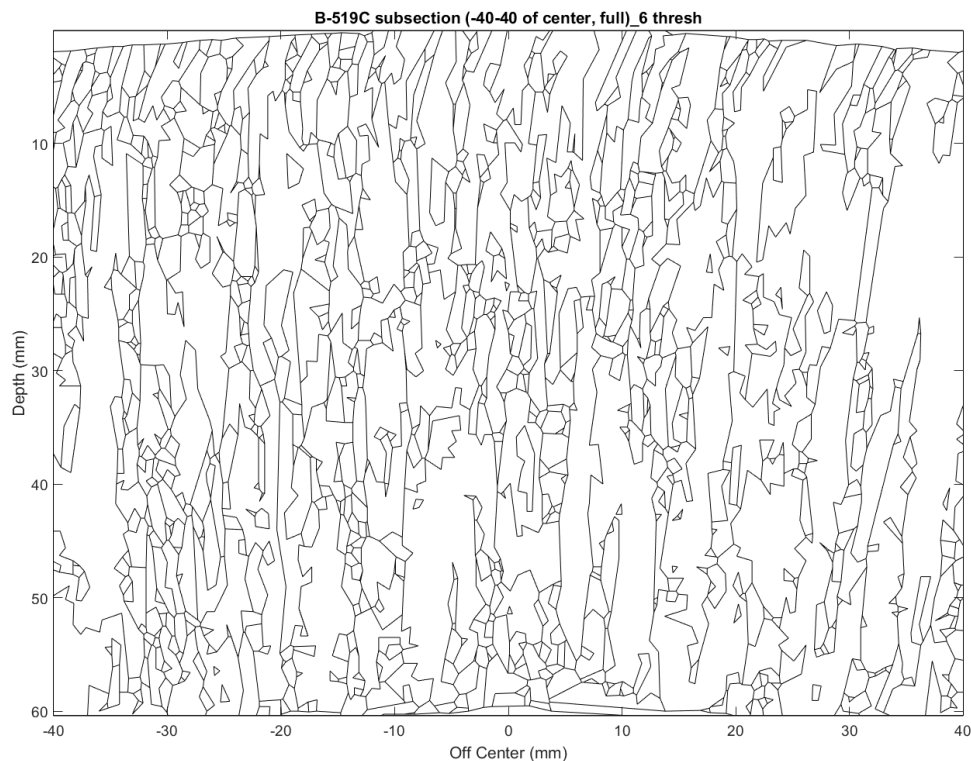


Figure 7.9. Skeleton of B-519C with the line reduction algorithm applied.

## 7.2.2 CIVA Simulations

The specimen model was created in 2D; therefore, it was extruded in the third dimension by 200 mm (7.9 in.) for purposes of running simulations. The speed of sound in the specimen was set to 5.90 mm/ $\mu$ s (0.232 in./ $\mu$ s). A 2D-matrixed PA probe (1.1 MHz, 58% bandwidth) in TRL configuration with a 45° refraction angle was used—these parameters were taken from those used in previous simulation work and were based on the 1 MHz PA probe used for data acquisition described in Crawford et al. (2014). To reduce computation time, the simulation was run in 2D in a computation zone through the specimen cross section at the focal point of the beam.

The first simulation, to be used as a benchmark, was of an isotropic specimen. That is, every grain was given the same material properties. The results are shown in Figure 7.10. As expected, the simulated beam cross section was symmetric and exhibited no scatter. To give a sense of scale of the beam size in relation to the grain sizes, the grain structure was superimposed on the simulation results.

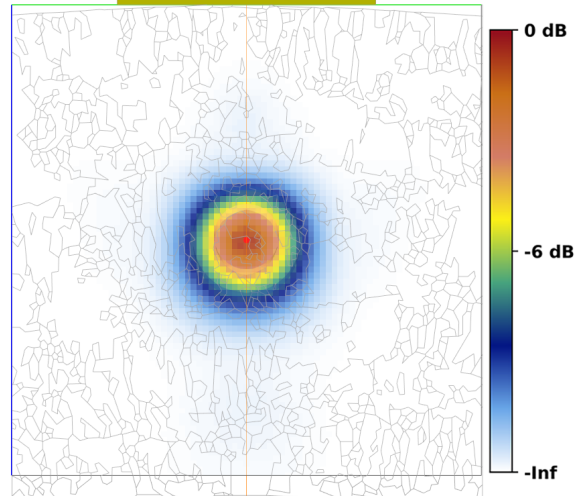


Figure 7.10. Simulation results with a simple isotropic specimen. A 1 MHz PA probe at 45° was used.

For the next simulations, each grain in the specimen model was defined with one of ten different sets of Euler angles taken from Chen et al. (2015); elastic constants were defined by a single stiffness matrix that was based on the default CIVA values for steel. The grain definitions were implemented with a CIVA xml file in a manner similar to that described in Section 5.3.1. The Euler angles were assigned quasi-randomly such that regions that share a boundary would not have the same set of angles. If two neighboring regions did have the same Euler angles, the two regions would behave as one region in the simulation and the grain boundary would be ignored, so this was prevented. Ten different specimen models were generated, each with a different distribution of Euler angles. Figure 7.11 shows an example of the Euler angle assignments for one of the models; each color represents a different set of angles.

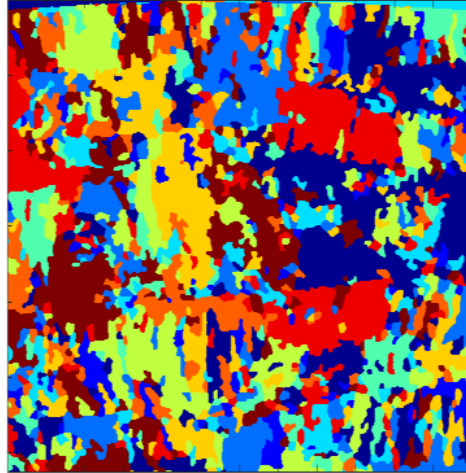


Figure 7.11. Color-coded image illustrating the distribution of Euler angles in one of the AAD-3 models. Each of the ten colors represents a different crystalline orientation.

The simulation results are shown in Figure 7.12. Each image covers an 80 mm × 80 mm (3.1 in. × 3.1 in.) area. Note that many of the simulation results include missing or uncalculated pixels. Such pixels seem to be randomly located from image to image, suggesting that they are not related to the grain geometry, resolution, or probe position as had been suggested by EXTENDE when similar issues arose in the weld simulations (Section 5.3.2). Because the only variable that was changed from simulation to simulation was the Euler angle assignments, the random failure of CIVA to calculate some pixel values must somehow be related to that; however, the reason why is unclear. At any rate, these simulations exhibit considerable beam scatter and a less well-focused beam than the isotropic case. Simulations in Figure 7.12 can be qualitatively compared to the empirical beam maps reported on page B.46 of Crawford et al. (2014), which are reproduced in part in Figure 7.13. Simulation results illustrate the well-known effects that CASS has on sound propagation of beam scatter, redirection, and attenuation. More importantly, qualitative comparison with empirical beam maps illustrates that CIVA beam simulations through CASS geometries provide at least somewhat realistic characteristics.

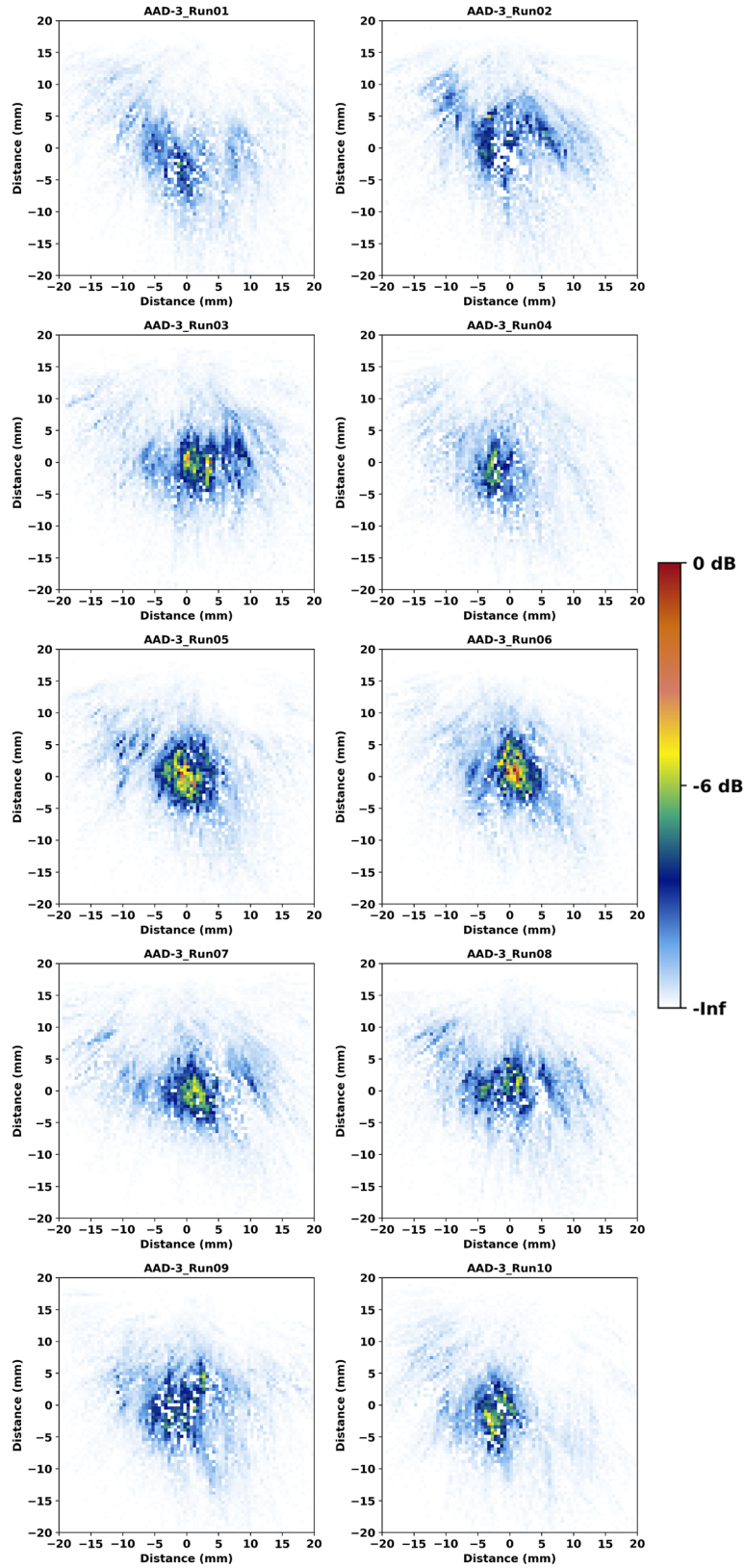


Figure 7.12. AAD-3 beam simulations. A 1 MHz PA probe at 45° was used with the focal spot in the plane of the simulation.

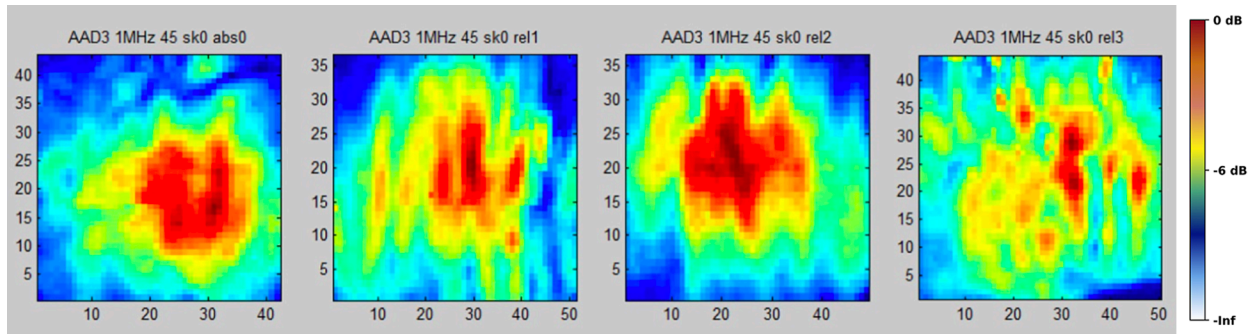


Figure 7.13. Empirical beam maps from AAD-3, reproduced from PNNL-23393 (Crawford et al. 2014). A 1 MHz PA probe at 45° was used with the focal spot in the plane of the beam map.

Table 7.1 shows the similarity metrics calculated for the ten AAD-3 cases compared to the isotropic case. Overall, the metrics indicate that there is little similarity between the isotropic case and the simulations with the realistic geometry. This is due to the high degree of beam scatter, which is expected through CASS materials. The low SD of the SSIM and MSE metrics indicates that there is little spread in the data—all of the geometries were comparably different from the isotropic case. Figure 7.14 shows the AAD-3 average result (average of the ten images). Note that missing pixels are included as zeros when calculating the average and may therefore affect the mean image by reducing the overall intensity.

Table 7.1. Similarity metrics of AAD-3 simulations compared to the isotropic case.

Run	SSIM	MSE	Correlation Coefficient
AAD-3_01	0.241	144.1	0.570
AAD-3_02	0.241	141.8	0.510
AAD-3_03	0.233	128.2	0.773
AAD-3_04	0.236	139.7	0.664
AAD-3_05	0.251	118.4	0.891
AAD-3_06	0.269	121.4	0.839
AAD-3_07	0.209	127.6	0.843
AAD-3_08	0.247	133.9	0.707
AAD-3_09	0.289	135.8	0.669
AAD-3_10	0.204	136.3	0.662
Average	0.242	132.7	0.713
SD	0.025	8.6	0.123

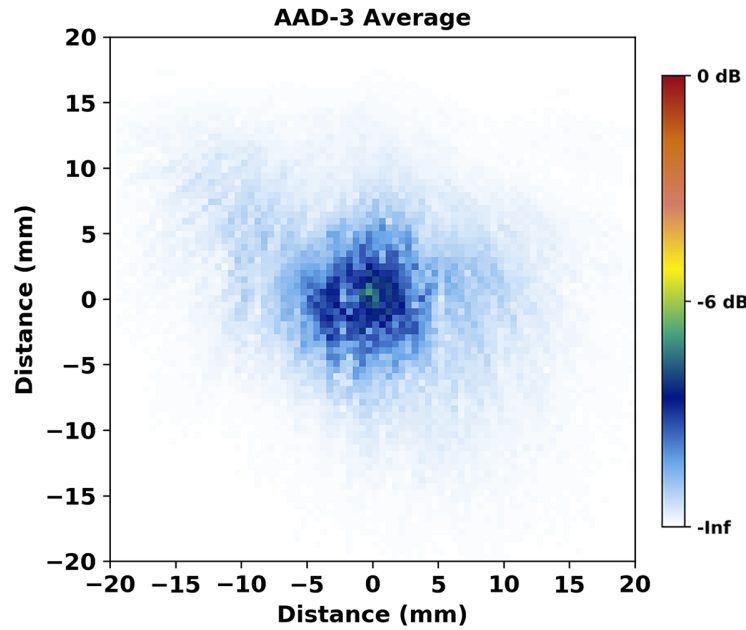


Figure 7.14. Average of the ten AAD-3 simulations.

Table 7.2 shows the similarity metrics for the AAD-3 cases compared to the mean. Results are again characterized by a low SD and no outliers, indicating that there are no individual simulations that stand out as being most (or least) similar to the group average, as the simulations vary from the average by about the same amount. This consistency of results is interpreted as an indication of the randomness in the beam scatter caused by the grains. In particular, the use of ten different sets of Euler angles resulted in enough scatter that all simulations appear to have about the same degree of randomness. That is, the 10 Euler angle approach appears to produce a good model where any of the cases could be used to represent the group. Note that Nakahata et al. (2016) used 25 sets of Euler angles for similar work, but the 10 most prominent sets of angles represented 85.2% of the specimen.

Table 7.2. Similarity metrics of AAD-3 simulations compared to the AAD-3 mean.

Run	SSIM	MSE	Correlation Coefficient
AAD-3_1	0.438	0.649	0.685
AAD-3_02	0.459	0.724	0.707
AAD-3_03	0.466	0.823	0.804
AAD-3_04	0.475	0.567	0.756
AAD-3_05	0.489	0.924	0.898
AAD-3_06	0.462	1.076	0.845
AAD-3_07	0.439	0.556	0.854
AAD-3_08	0.499	0.488	0.841
AAD-3_09	0.487	0.596	0.790
AAD-3_10	0.422	0.760	0.741
Average:	0.464	0.716	0.792
SD:	0.025	0.184	0.069

The realistic coarse-grained model based on specimen AAD-3 produced satisfactory simulation results. However, this specimen model proved to push CIVA's limits, as it took upwards of an hour to simply load each geometry and about as much time to run a simulation. Furthermore, the process of generating the geometry requires a cut, polished, and etched specimen, precision photography, and image processing expertise. This onerous process is time-consuming and expensive. PNNL already had several cut and polished sections that were available to be characterized, but most organizations that may be interested in these types of simulations do not. Fortunately, CIVA provides a built-in alternative coarse-grained specimen model that uses Voronoi regions; this alternative is explored below.

### 7.2.3 Voronoi Model Simulations

A Voronoi diagram is a partitioning of a plane or volume into regions based on a random or quasi-random distribution of seed points.<sup>(a)</sup> A Voronoi diagram is usually created by populating a region with seed points, then the Voronoi cells, or regions, are defined as the set of points that are closer to a seed point than to any other seed point. An example is shown in Figure 7.15. The result is a set of convex polyhedra that lack the intricate and complex grain shapes that can be seen in the real specimen (Figure 7.6), including “islands” and “peninsulas.” Voronoi diagrams are used for modeling in a wide variety of scientific disciplines, including simulations of sound propagation in coarse-grained materials (Ghoshal and Turner 2009; Jenson et al. 2009; Sakamoto et al. 2013; Shivaprasad et al. 2018).

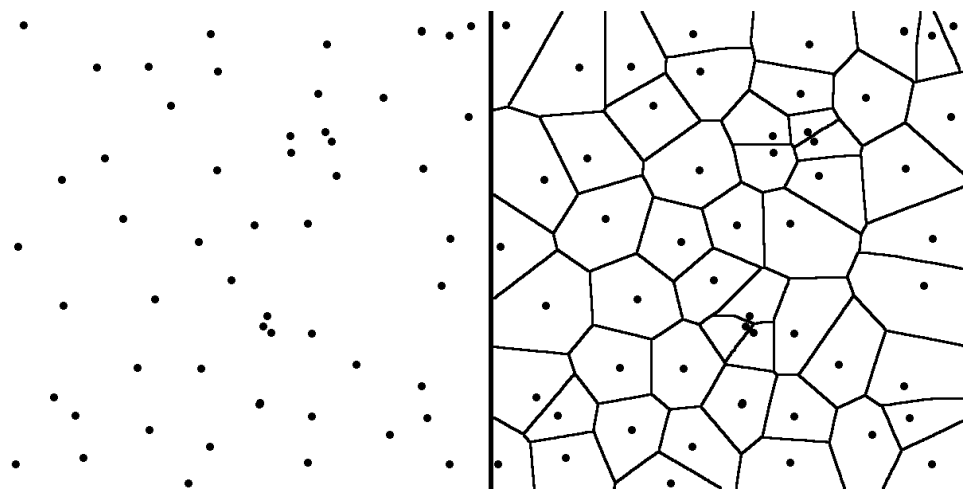


Figure 7.15. Example of Voronoi regions. *Left:* Seed points. *Right:* Voronoi regions drawn from the seed points.

Several preliminary simulations were run to investigate CIVA's built-in Voronoi region function of creating coarse-grained model structures and to compare simulation results to those of the realistic grain structure of AAD-3. An important fundamental difference between the realistic grain model and the Voronoi regions is the way that variations in grain properties are defined in CIVA. With Voronoi regions, CIVA allows the user to define an overall mean velocity of the entire specimen and a grain-to-grain velocity variation “ $\Delta V$ ,” or velocity range, such as  $\pm 10\%$ . That is, the sound speed of each region can vary from the average sound speed by as much as 10%. The user cannot, however, define crystalline orientations with Euler angles using the

(a) A detailed description of Voronoi diagrams can be found here: [https://en.wikipedia.org/wiki/Voronoi\\_diagram](https://en.wikipedia.org/wiki/Voronoi_diagram).

Voronoi model. For the realistic grain model, each grain had the same speed of sound and elastic constants, but the crystalline orientations were rotated relative to one another by the Euler angles to create preferred sound propagation directions. This is consistent with many modeling approaches found in the literature (see Appendix D). The practical effect of both the sound speed variation and Euler angle approaches is an impedance mismatch at grain interfaces that results in beam refraction, which is ultimately manifest as scatter.

To illustrate the difference between varying the velocity and varying the crystalline orientation, a simple specimen model was created with two regions stacked horizontally. In the first case, both regions had the same properties. In the second case, the regions were assigned different sound velocities. The top region was  $6.2 \text{ mm}/\mu\text{s}$  ( $0.244 \text{ in.}/\mu\text{s}$ ) and the bottom region was  $5.6 \text{ mm}/\mu\text{s}$  ( $0.220 \text{ in.}/\mu\text{s}$ ) (this was based on the extremes of a nominal  $5.9 \text{ mm}/\mu\text{s}$  [ $0.232 \text{ in.}/\mu\text{s}$ ]  $\pm 5\%$ ). In the third case, the regions had the same sound velocity but different Euler angles. The angles were (in the CIVA, or specimen, reference frame)  $X=0^\circ$ ,  $Y=25^\circ$ ,  $Z=45^\circ$  for the top layer and  $X=45^\circ$ ,  $Y=45^\circ$ ,  $Z=45^\circ$  for the bottom layer; Figure 7.16 shows the beam simulation results. As expected, the isotropic simulation shows no beam redirection or discontinuities at the interface and produces a symmetric beam spot. The second simulation shows some distortion of the beam but no redirection and almost no beam discontinuity at the interface. The third shows significant beam redirection and some beam discontinuity at the interface. Results illustrate the fundamental difference between the methods that CIVA uses to handle custom geometries and Voronoi models. In a real specimen, every grain should have the same crystal symmetry and the same speed of sound. It is the crystalline orientation, described by the Euler angles, that determines the preferential direction of sound transmission, and the angles should be essentially random from grain to grain. Therefore, it must be determined whether the speed of sound variations from grain to grain in a Voronoi model adequately approximate realistic differences in the crystalline orientations. Some simple investigatory experiments were conducted to try to address this.

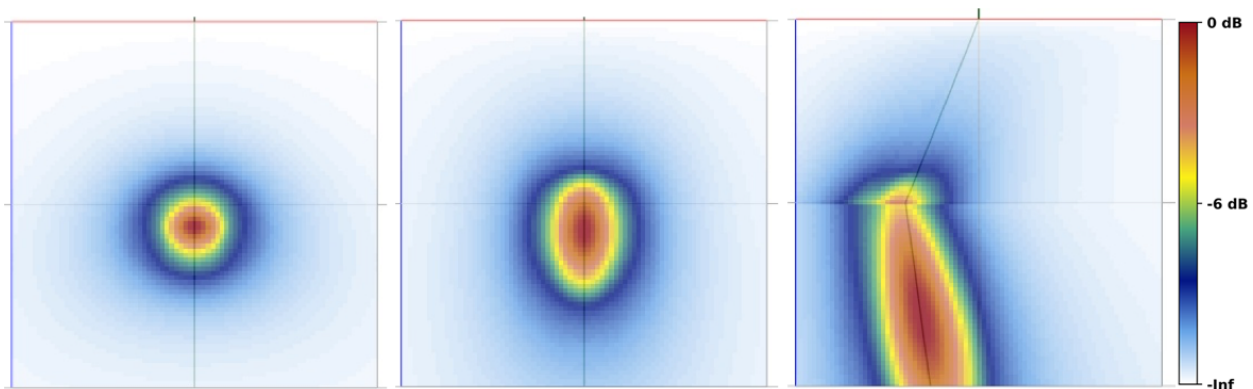


Figure 7.16. Testing beam redirection in a two-layer specimen. *Left:* Isotropic material. *Center:* Different sound speeds. *Right:* Different Euler angles.

A first geometry was created using the same specimen volume as was used for the AAD-3 model. This geometry comprised 1000 Voronoi regions. Note that CIVA creates the Voronoi regions in three dimensions, so for this case the grains were not extruded as was done with the realistic grains. The sound speed was set to  $5.9 \text{ mm}/\mu\text{s}$  ( $0.232 \text{ in.}/\mu\text{s}$ ) and the  $\Delta V$  to  $\pm 10\%$ . Figure 7.17 shows the  $80 \times 80 \text{ mm}$  ( $3.1 \times 3.1 \text{ in.}$ ) cross section of the Voronoi regions in the simulation plane. Approximately 50 of the 1000 regions are intersected by the plane. Note that the large apparent range of region sizes is because the cross section intersects some regions near their centers and other regions near their corners. In 3D, all the regions are approximately

the same size. Figure 7.18 shows the results of the simulation. The maximum amplitude is normalized to that of Figure 7.10. The large size of the Voronoi regions is reflected in the coarse-beam-scatter pattern; this is not indicative of the beam scatter observed in the empirical measurements.

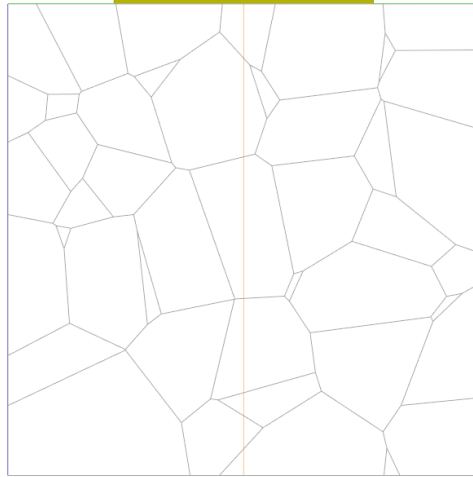


Figure 7.17. Simulation volume with 1000 volumetric Voronoi regions. Shown are the Voronoi regions that intersect the simulation plane.

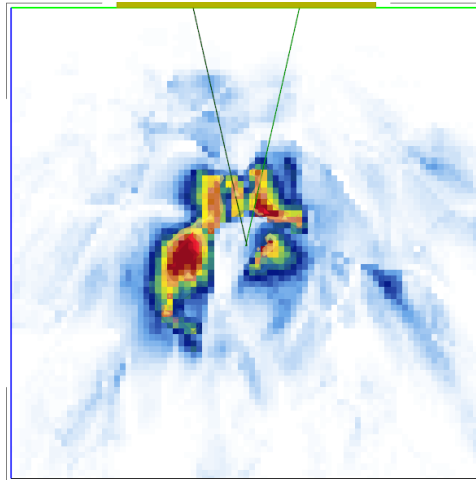


Figure 7.18. Beam simulation with 1000 volumetric Voronoi regions. This image is normalized to Figure 7.10. A 1 MHz PA probe at  $45^\circ$  was used with the focal spot in the plane of the simulation.

A second model geometry was defined, this time with 5000 Voronoi regions. This geometry is depicted in Figure 7.19. Figure 7.20 shows the results of the beam simulation with the 5000 regions. The peak signal was normalized to that of Figure 7.10. When compared to the 1000-region simulation results in Figure 7.18, the 5000-region simulation shows more beam scatter and much lower peak sound intensity. Overall, the 5000-region simulation more closely matches the AAD-3 simulations. It is important to note that the computation time of the 5000-region Voronoi simulation was about 7.5 minutes, whereas it was about 42.5 minutes for the realistic AAD-3 geometry plus approximately one additional hour to open the AAD-3 simulation results because of the time required to render the geometry.

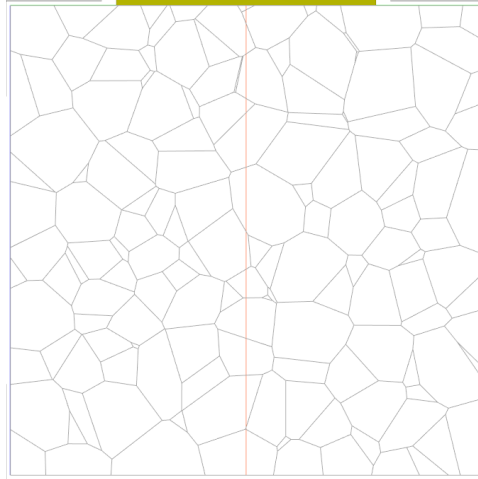


Figure 7.19. Simulation volume with 5000 volumetric Voronoi regions. Shown are the Voronoi regions that intersect the simulation plane.

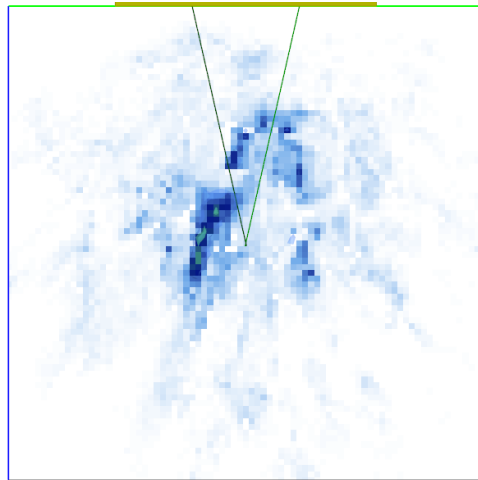


Figure 7.20. Beam simulation with 5000 volumetric Voronoi regions. This figure is normalized to Figure 7.10. A 1 MHz PA probe at  $45^\circ$  was used with the focal spot in the plane of the simulation.

A key question of this work is to determine whether the Voronoi regions can adequately model realistic grain structures in beam and inspection simulations such that the simple Voronoi models can be used instead of the expensive, complex, and time-consuming realistic geometries. Initial tests appear to indicate that this may indeed be possible, because the 5000-region simulation results have qualitative similarities to some of the empirical results.

To make a more direct comparison between the Voronoi approach and the realistic grains modeled above, PNNL performed additional sets of simulations with the realistic geometry from AAD-3 and with Voronoi regions. For consistency, the same specimen dimensions were used, and the number of Voronoi regions was the same as the number of grains in AAD-3. Figure 7.21 shows the Voronoi geometry side-by-side with the AAD-3 geometry. The grains in AAD-3 were defined in a 2D plane and extruded in the third dimension, so the same was done with the Voronoi specimen by giving the regions a high aspect ratio of 100. This resulted in about 750 of the 810 regions intersecting the simulation plane. The Voronoi model had an average grain

cross-section of about  $7 \text{ mm}^2$  ( $0.011 \text{ in.}^2$ ), a SD of  $5 \text{ mm}^2$  ( $0.008 \text{ in.}^2$ ), and a maximum grain size of about  $26 \text{ mm}^2$  ( $0.040 \text{ in.}^2$ ). The SD of the AAD-3 model was  $25 \text{ mm}^2$  ( $0.039 \text{ in.}^2$ ) and the maximum grain size was  $430 \text{ mm}^2$  ( $0.67 \text{ in.}^2$ ), so there was a much larger range of grain size in the realistic model. A further measure of the differences between the grain shapes in the two models is the solidity.<sup>(a)</sup> The average solidity of the AAD-3 regions was  $0.82 \pm 0.12$  and for the Voronoi regions was  $0.91 \pm 0.05$ .<sup>(b)</sup> The lower solidity and higher SD of the AAD-3 regions indicates a larger variety of shapes that includes concavities.

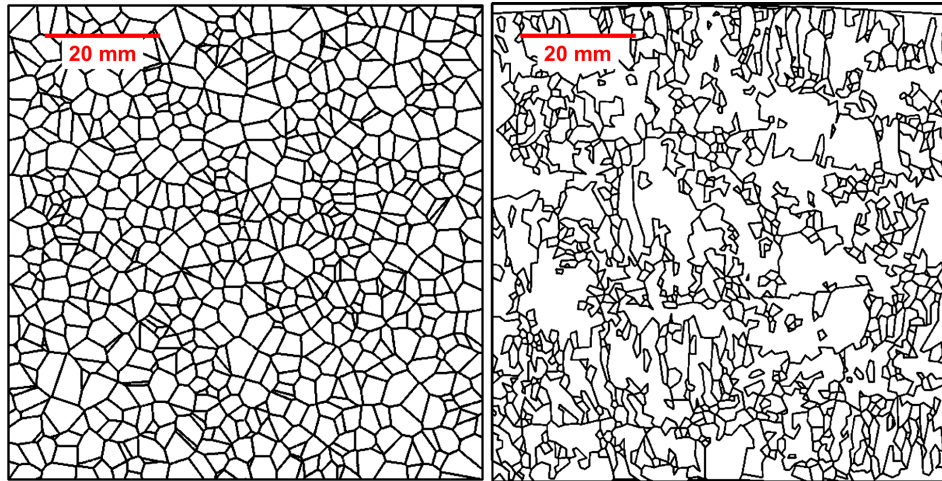


Figure 7.21. Coarse-grained specimen models. *Left: CIVA-generated Voronoi. Right: AAD-3.* Both models are the same size and have the same number of regions in the 2D plane.

CIVA allows the user to randomly reassign the distribution of Voronoi regions, essentially creating a new specimen, or randomly reassign velocities to the existing regions without changing the region boundaries. For this work, simulations were run with the same Voronoi geometry but with the sound velocity of each region changed. The average sound velocity used for the Voronoi geometry was  $5.9 \text{ mm}/\mu\text{s}$  ( $0.232 \text{ in.}/\mu\text{s}$ ). Six simulations were performed for each of three different values of  $\Delta V$ : 4%, 6%, and 8%. Simulations were done using the same probe and specimen size as described for AAD-3. Figures 7.22 through 7.24 show the simulation results; all results were normalized to the same peak value, which occurred in simulation 06 of the 4% group. Figure 7.25 shows the average result for each group, also normalized to the peak value of the 4% group. As the value of  $\Delta V$  increased, the signal intensity decreased because of increased scatter, as expected.

- 
- (a) Solidity is a measure of the smoothness of a surface. It is calculated by dividing the area of the shape by the area of the convex hull, which is defined as the smallest convex polygon that encloses the shape. Surfaces with concavities or projections will have a lower solidity.
- (b) For convex polyhedrals that comprise the Voronoi regions, the solidity should be nearly equal to 1. However, due to pixelation in the screen-capture image, a small amount of surface roughness was introduced.

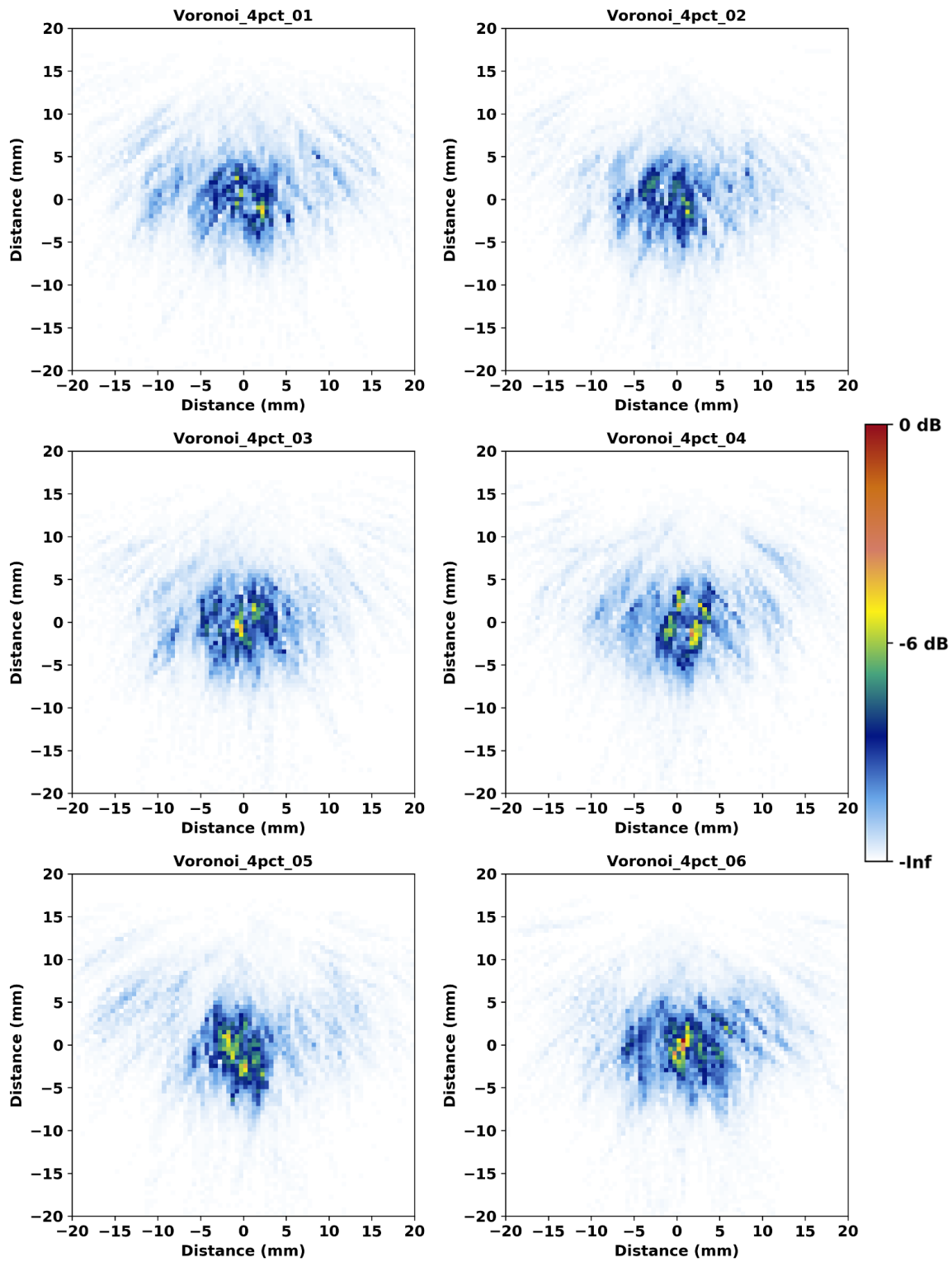


Figure 7.22. Voronoi simulation results for  $\Delta V = 4\%$ . A 1 MHz PA probe at  $45^\circ$  was used with the focal spot in the plane of the simulation.

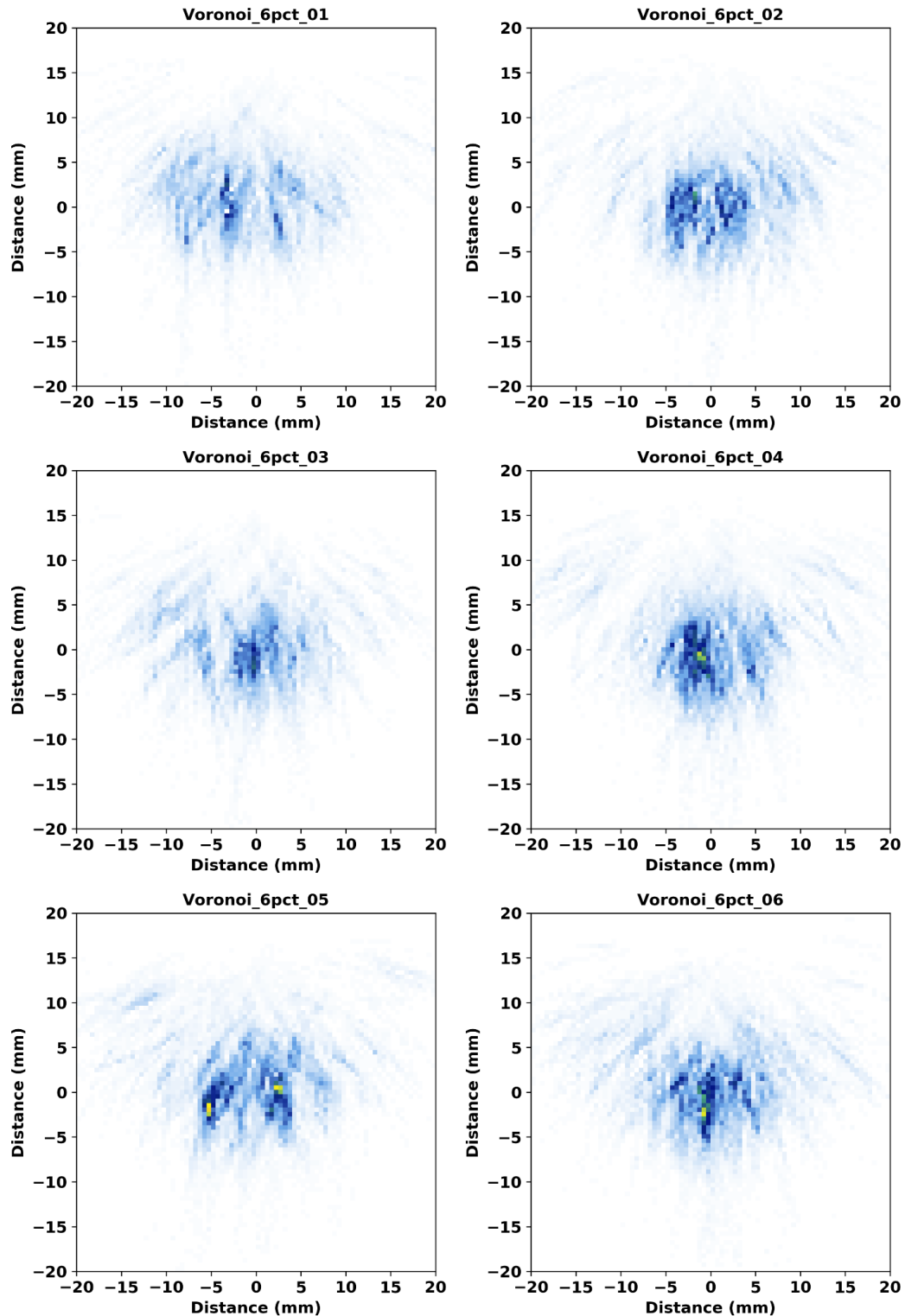


Figure 7.23. Voronoi simulation results for  $\Delta V = 6\%$ . This figure is normalized to simulation 06 in Figure 7.22. A 1 MHz PA probe at  $45^\circ$  was used with the focal spot in the plane of the simulation.

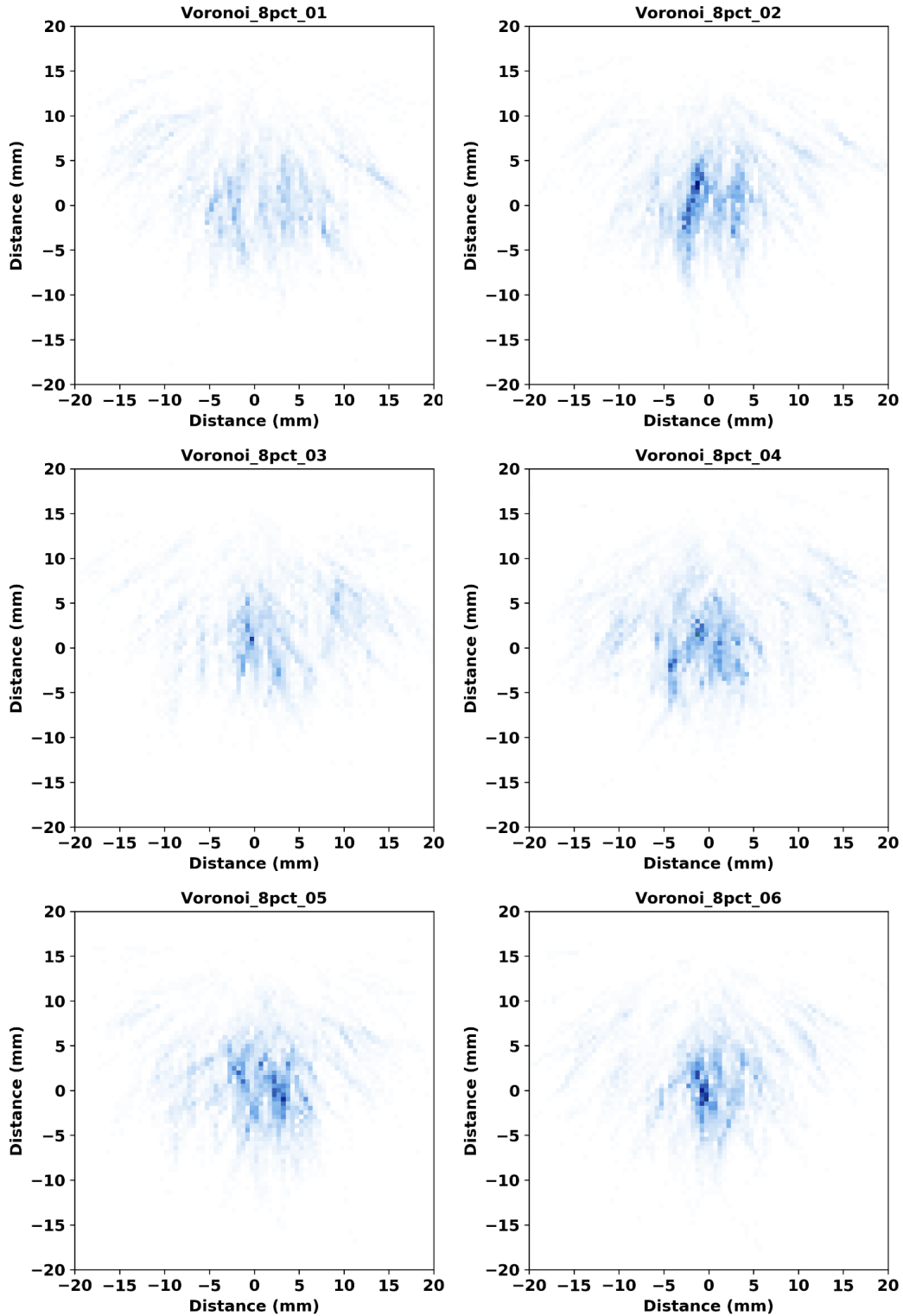


Figure 7.24. Voronoi simulation Results for  $\Delta V = 8\%$ . This figure is normalized to simulation 06 in Figure 7.22. A 1 MHz PA probe at  $45^\circ$  was used with the focal spot in the plane of the simulation.

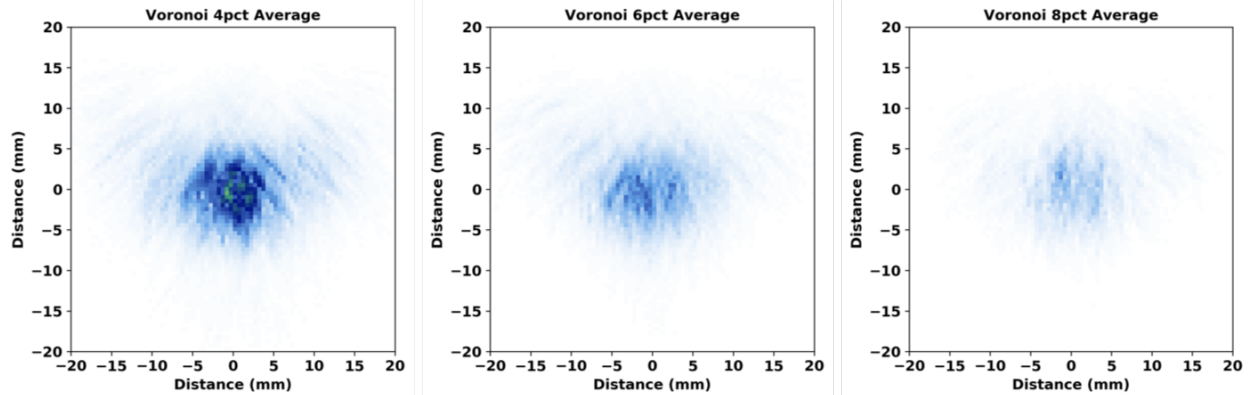


Figure 7.25. Average results of the three Voronoi  $\Delta V$  tests. This figure is normalized to simulation 06 in Figure 7.22.

Using the image similarity metrics, the Voronoi results were compared to the isotropic case (Table 7.3) and to the average case (Table 7.4). It is important to determine whether the Voronoi model can be used as a reasonable substitute for realistic grains. Here, results are compared to the AAD-3 model test case (see Tables 7.1 and 7.2). For both models, similarity metrics are characterized by a low SD and no strong outliers, indicating that the randomness in the beam scatter caused by the grains resulted in no individual simulations that stand out as being most (or least) similar to each group's average. In other words, the use of ten different sets of Euler angles in the AAD-3 simulations resulted in enough scatter that all simulations appear to have about the same degree of randomness, and the same can be inferred from the Voronoi simulations. Therefore, PNNL concludes that the Voronoi geometry provides a comparable level of beam scatter to the AAD-3 geometry.

Table 7.3. Similarity metrics of Voronoi simulations compared to the Isotropic case.

Run	SSIM	MSE	Correlation Coefficient
Voronoi_4pct_01	0.198	91.7	0.823
Voronoi_4pct_02	0.269	91.9	0.834
Voronoi_4pct_03	0.249	82.1	0.864
Voronoi_4pct_04	0.227	85.3	0.823
Voronoi_4pct_05	0.240	75.4	0.877
Voronoi_4pct_06	0.265	74.0	0.848
Average:	0.241	83.4	0.845
SD:	0.026	7.7	0.022
Voronoi_6pct_01	0.235	131	0.602
Voronoi_6pct_02	0.263	112	0.807
Voronoi_6pct_03	0.251	118	0.823
Voronoi_6pct_04	0.265	105	0.822
Voronoi_6pct_05	0.257	113	0.692
Voronoi_6pct_06	0.241	104	0.838
Average:	0.252	114	0.764
SD:	0.012	9.8	0.096
Voronoi_8pct_01	0.213	144	0.619
Voronoi_8pct_02	0.213	130	0.765
Voronoi_8pct_03	0.213	141	0.682
Voronoi_8pct_04	0.208	131	0.768
Voronoi_8pct_05	0.225	131	0.765
Voronoi_8pct_06	0.210	132	0.781
Average:	0.214	135	0.730
SD:	0.006	6.2	0.065

Table 7.4. Similarity metrics of Voronoi simulations compared to the average cases.

Run	SSIM	MSE	Correlation Coefficient
Voronoi_4pct_01	0.500	2.61	0.898
Voronoi_4pct_02	0.499	2.56	0.900
Voronoi_4pct_03	0.479	2.87	0.905
Voronoi_4pct_04	0.519	3.48	0.887
Voronoi_4pct_05	0.497	3.87	0.897
Voronoi_4pct_06	0.490	4.80	0.895
Average:	0.497	3.36	0.897
SD:	0.013	0.87	0.006
Voronoi_6pct_01	0.445	1.86	0.753
Voronoi_6pct_02	0.486	1.33	0.875
Voronoi_6pct_03	0.469	1.19	0.854
Voronoi_6pct_04	0.473	1.99	0.866
Voronoi_6pct_05	0.488	2.70	0.808
Voronoi_6pct_06	0.495	1.79	0.884
Average:	0.476	1.81	0.840
SD:	0.018	0.54	0.050
Voronoi_8pct_01	0.494	0.504	0.722
Voronoi_8pct_02	0.555	0.576	0.873
Voronoi_8pct_03	0.545	0.377	0.806
Voronoi_8pct_04	0.534	0.557	0.841
Voronoi_8pct_05	0.549	0.575	0.854
Voronoi_8pct_06	0.535	0.499	0.852
Average:	0.535	0.515	0.825
SD:	0.022	0.075	0.055

Table 7.5 summarizes the results of the image similarity metrics of AAD-3 and the Voronoi cases compared to the isotropic case. Results show that AAD-3 and the  $\Delta V = 8\%$  simulations are overall comparably different from the isotropic case. This means that they share about the same level of differences from the test case, but this does not necessarily mean that they are the same as each other. It should be pointed out that the AAD-3 simulations had missing pixels that were not calculated by CIVA, probably due to a low accuracy factor. This may have had some effect on the similarity metrics, but it is not likely to change the results significantly. Even so, it can be concluded that using Voronoi regions for simulations with a moderate  $\Delta V$  of about 6%–8% should provide a good surrogate for AAD-3 and potentially for general coarse-grained equiaxed CASS structures. It is important to note that the appropriate  $\Delta V$  may depend on the geometry being modeled as well as the method used to compare simulations to experimental data. For example, EPRI (2018) concluded that a  $\Delta V$  of  $\pm 3\%$  best represented their data.

Table 7.5. Image similarity metrics comparing Voronoi and AAD-3 simulations to the isotropic case.

	$\Delta V=4\%$	$\Delta V=6\%$	$\Delta V=8\%$	AAD-3
SSIM	0.241	0.252	0.213	0.242
MSE	83.4	113.6	135.0	132.7
Corrcoff	0.845	0.764	0.730	0.713
Mean signal	1.66	0.99	0.50	0.60

Interestingly, the beam scatter patterns in the Voronoi simulations appear more symmetric about the vertical axis than those of the AAD-3 simulations, implying that more beam redirection occurs with the AAD-3 specimen model. This is highlighted in Figure 7.26, which shows a representative beam map from each set of simulations; the black lines divide the images into quadrants and were added to help guide the eye. Most of the beam in the AAD-3 simulation appears to be concentrated in the right quadrants, whereas the beam in the Voronoi simulation is well centered and the low-intensity scattered signal along the periphery is more symmetric. A “center of mass” (COM) comparison was done to evaluate the degree of off-center beam redirection in the two scenarios. The COM was found by calculating the average position of all the pixels weighted by the pixel signal intensity values in each image. Figure 7.26 shows the COM indicated by red dots. The average  $\pm$  SD COM (x, y) coordinates of the group of AAD-3 simulations were  $(0.4 \pm 1.2, 0.7 \pm 0.8)$  and were  $(0.7 \pm 0.7, 1.1 \pm 0.4)$  for the Voronoi 6% simulations. The higher SD of the AAD-3 simulations suggests that the COM positions varied more than those of the Voronoi simulations. However, the difference in the average COM position was not statistically significant between the two model scenarios. Furthermore, the COM of the realistic grain simulations was within a SD of the true center, at (0, 0). Therefore, although there appeared to be more beam redirection in the realistic AAD-3 model than in the Voronoi model, the differences were not statistically significant.

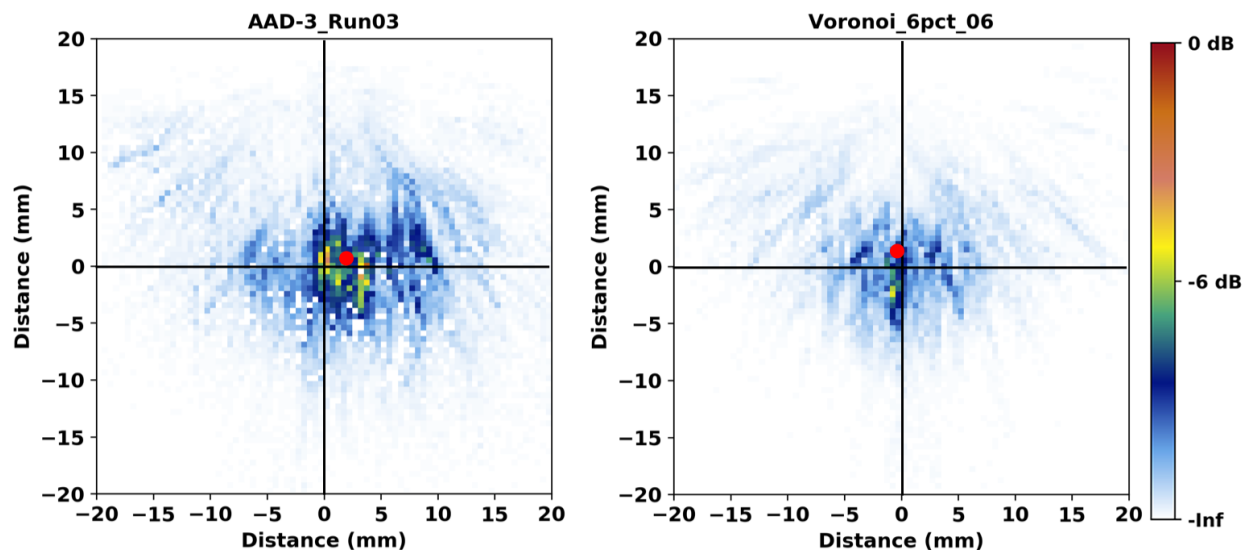


Figure 7.26. Center of mass comparison of two coarse-grained simulations. Left: AAD-3 Run 03. Right: Voronoi 6% Run 06. The red dots indicate the COM.

Results suggest that a high number of grains essentially reduces the issue of scatter in coarse-grained materials to a diffusion, or random-walk,<sup>(a)</sup> problem. With just two grains, as shown in Figure 7.16, the beam redirection was high, and the center of the resulting sound beam was deviated far from the intended location. However, the higher the number of grains—in other words, the more opportunities for the beam to “diffuse”—the higher the probability that the center of the beam will end up at the intended location while at the same time the beam becomes more spread out. Therefore, on average, when the Voronoi simulations include a sufficient number of regions or grains, results appear to largely mimic the properties of the realistic grain simulations. This may not hold true when the real specimen contains a few large grains that would have a disproportionate effect on the propagating sound as compared to many small grains of the same volume (Wan et al. 2017). One example of a specimen with a few disproportionately large grains is shown in Figure 7-20 of Jacob et al. (2019); this figure is reproduced below (see Figure 7.27). The high heterogeneity in the grain structure would be expected to have a significant and unforeseeable effect on the sound propagation. Such grain structures are not generally duplicated by random Voronoi geometries.



Figure 7.27. A polished and etched circumferential section of a CASS specimen. This figure illustrates that a large variety of grain sizes can exist in the same section.

#### 7.2.4 Accuracy Factor

To address the issue of missing pixels in the AAD-3 simulations, PNNL ran an AAD-3 simulation and a Voronoi simulation using the variation feature of CIVA to adjust the accuracy factor. Recall, the variation feature allows the user to run a parametric study by varying one or more parameters in a single CIVA simulation file. The accuracy factor values chosen were 1, 2, 4, 8, 16, 32, and 64 (note that the 64 value did not run for AAD-3 due to a user error). Figures 7.28 and 7.29 show the resulting images. It is clear with the AAD-3 simulations that increasing the accuracy factor indeed eliminates the blank or uncalculated pixels. The Voronoi simulations show a similar result, but it is less obvious because there were few uncalculated pixels in the first place. Increasing the accuracy factor also dramatically increases simulation time, so it is important to determine the minimum accuracy needed to achieve good results; this was done using the image similarity metrics.

(a) See [https://en.wikipedia.org/wiki/Random\\_walk](https://en.wikipedia.org/wiki/Random_walk) for more information about random walk.

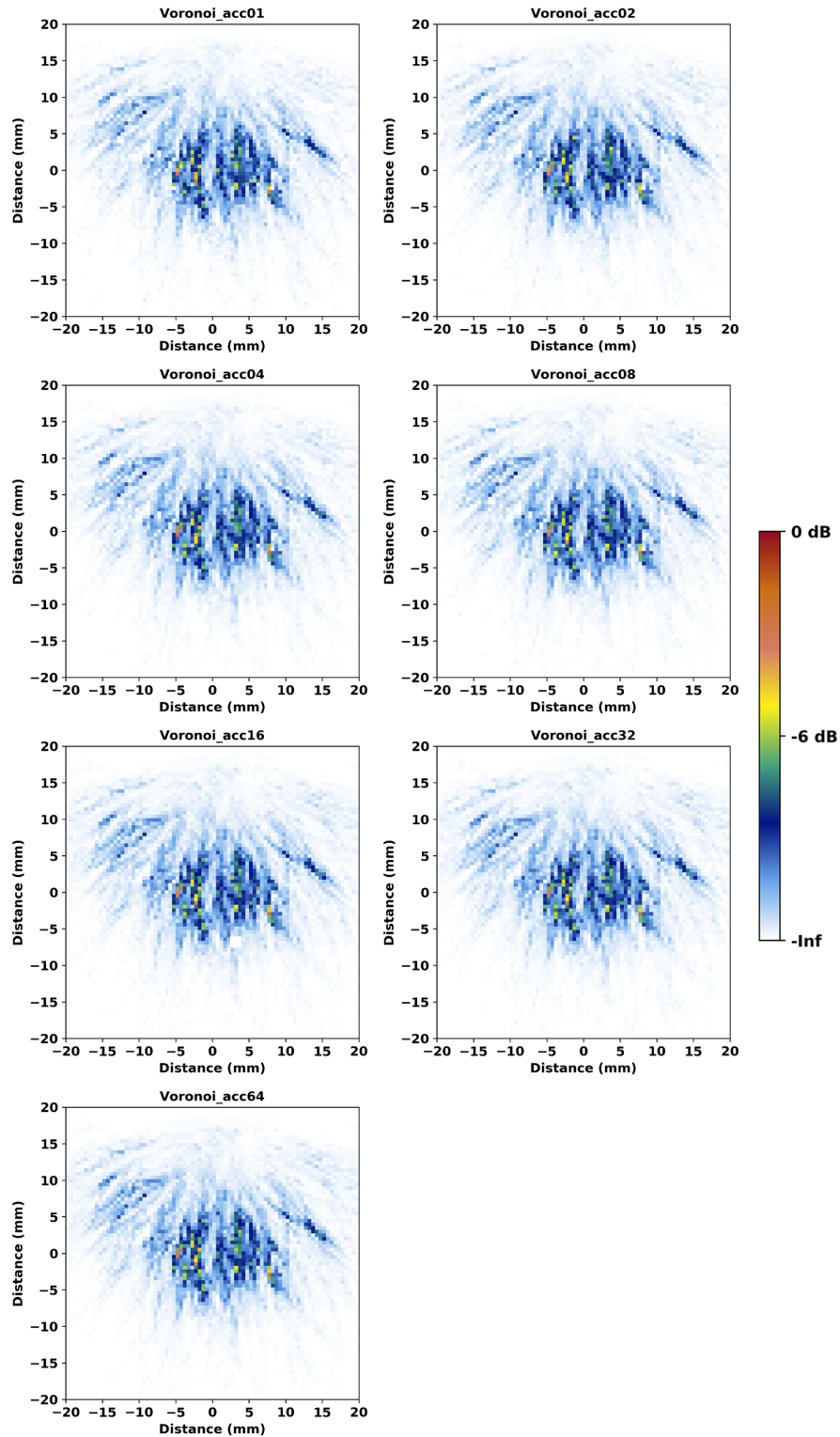


Figure 7.28. Beam simulations using a Voronoi model with increasing accuracy factor. The last two digits of the top label of each panel is the accuracy factor. A 1 MHz PA probe at 45° was used with the focal spot in the plane of the simulation.

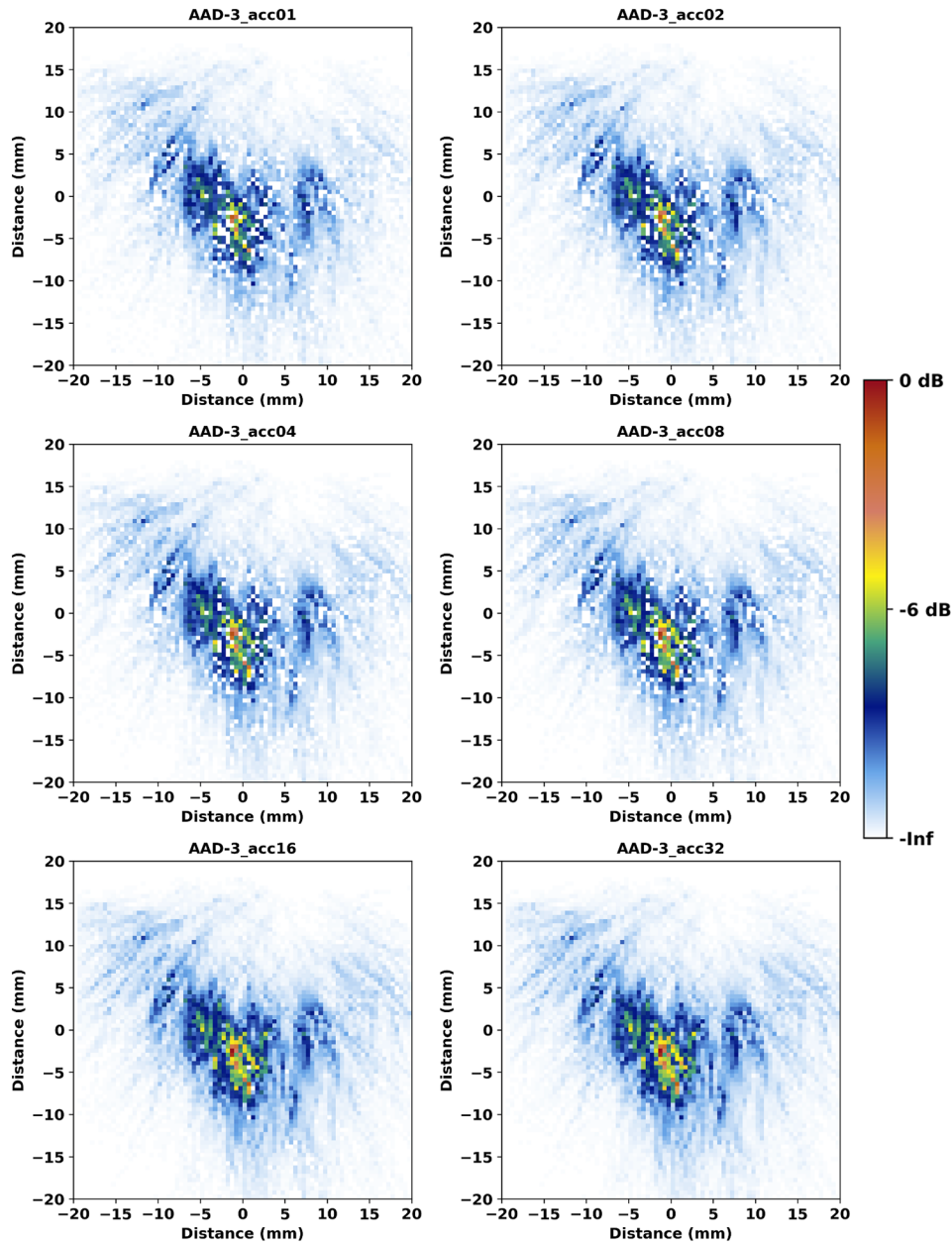


Figure 7.29. Beam simulations using the AAD-3 model with increasing accuracy factor. The last two digits of the top label of each panel is the accuracy factor. A 1 MHz PA probe at  $45^\circ$  was used with the focal spot in the plane of the simulation.

For each simulation set (i.e., AAD-3 or Voronoi), the highest accuracy factor result was used as the benchmark image, and the images were compared to that benchmark. That is, the AAD-3 accuracy=32 image and Voronoi accuracy=64 image were used as the respective benchmarks. Plots of the similarity metrics versus the accuracy factor are shown in Figure 7.30. Both the AAD-3 and Voronoi simulation sets show that the image similarity metrics approach their optimal values when the accuracy factor reaches about 16, indicating that an accuracy factor of about 16 is the lowest value that can be used to optimize these simulations. For the Voronoi model, a much lower accuracy factor may be acceptable because the similarity metrics were not strongly affected by the accuracy factor to start with. That is, an accuracy of 1 or 2 may be

adequate for the Voronoi-based models. Consistent with this, EPRI (2018) concluded from qualitative observation that an accuracy factor of 3 was appropriate for simulations with Voronoi models. Using Voronoi models as a substitute for realistic grain models is a significant time savings, and being able to do so with a low accuracy factor would realize an even greater time savings over realistic grains. Note that the required accuracy factor may be frequency-dependent (EPRI 2018); PNNL has not yet investigated this.

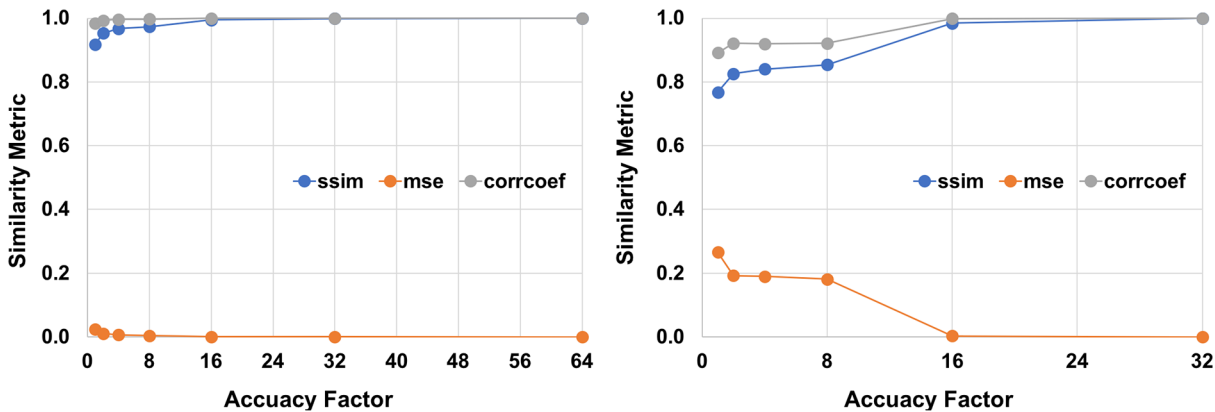


Figure 7.30. Image similarity metrics as a function of accuracy factor for Voronoi regions (*left*) and AAD-3 (*right*). Ideal values of ssim, mse, and corrcoeff (p) are 1, 0, and 1, respectively.

### 7.2.5 Comparison with Experiment

An effort was made to compare the simulated results with experimental results. Previously-acquired experimental sound field mapping data that matched the simulation conditions were used for comparison (Crawford et al. 2014). Because the signal intensities are totally different in simulations compared to experiment, the images need to be normalized to a control image of the same total gain. In this case, the ideal, or isotropic, condition for each case was used as the control image. This was done by integrating the signal in each image (the mean images were used from both the AAD-3 and Voronoi simulations) and taking the ratio of coarse-beam map to the isotropic case. For example, the ratio was taken of total signal measured in Figure 7.25 or Figure 7.14 to that in Figure 7.10. For the empirical data, the WSS image was used as the control case. Figure 7.31 illustrates the empirical data used. The top row shows the beam map through AAD-3 self-normalized (*left*) and normalized (*right*) to the WSS case, which is shown in the bottom row.

Table 7.6 shows the results of the calculated ratios. The fractional signal intensities for the 6% Voronoi case was closest to the experimental value, even when a noise level of ~10% was assumed for the experimental data. Results suggest that Voronoi models with a  $\Delta V$  range of between 6%–8% are likely a good representation of the total signal intensity that might be observed empirically. It is important to remember that this analysis represents only one experimental case and one realistic grain model. It is also important to remember that the null values in many of the pixels of the AAD-3 simulations dragged down the overall AAD-3 average. Ideally, the fractional integrated beam signal for each individual simulation would be calculated and then the average taken. Even so, this analysis should be taken as an example of one approach that can be used to quantitatively compare experimental and simulation results.

Table 7.6. Fractional integrated beam of simulations compared to experiment.

Scenario	Fractional Signal
Average of 4% Voronoi simulations	0.43
Average of 6% Voronoi simulations	0.25
Average of 8% Voronoi simulations	0.13
Average of AAD-3 simulations	0.15
Experimental data from AAD-3	0.24
Experimental data, assuming ~10% noise	0.22

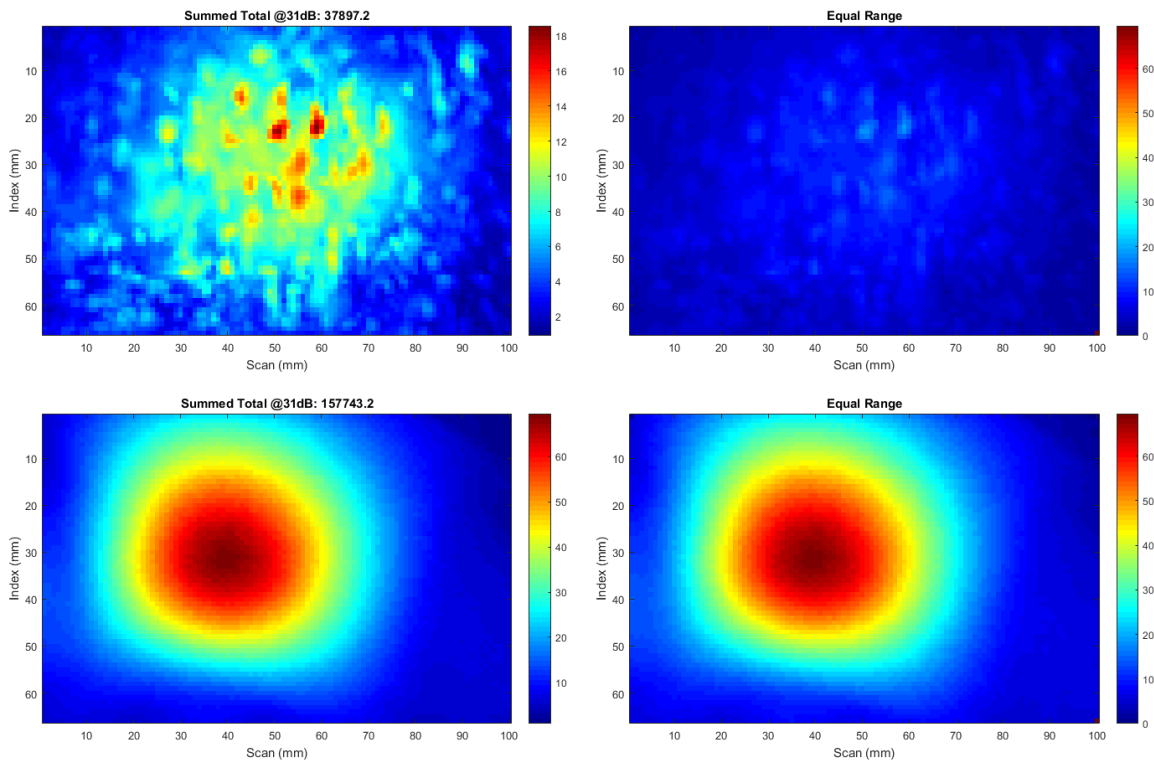


Figure 7.31. Empirical beam map data from AAD-3. Top row: Beam map, self-normalized (left) and normalized (right) to the WSS case (bottom row).

### 7.3 Summary

In this section, it was shown that realistic coarse-grained models can be faithfully replicated from actual specimens for import into CIVA. Beam simulations using these models produced results that are qualitatively consistent with those observed empirically, showing attributes of beam attenuation, redirection, and scatter. However, such models are expensive and time-consuming to generate, and they tax the capabilities of CIVA.

As an alternative to realistic specimen models, CIVA users can generate coarse-grained models from Voronoi regions. Beam simulations using the Voronoi models were qualitatively and quantitatively similar to simulations using the realistic models. Furthermore, the Voronoi model parameter  $\Delta V$  was tuned to optimize the simulation results to best match the realistic grain

simulations. PNNL concludes that the Voronoi model can be used as a reasonable substitute for realistic grain models, at least in the coarse-grained equiaxed case studied.

Table 7.7 summarizes the results and observations of the Voronoi and realistic AAD-3 grain simulations.

**Table 7.7. Comparison of realistic grains and Voronoi regions in beam simulations.**

<b>Realistic Grains</b>	<b>Voronoi Regions</b>
Grains are 2D, extruded in the third dimension	Grains are 3D, but can be “extruded” with high aspect ratios
Large variation in grain sizes	Grain sizes are much more uniform
Intricate and complex grain shapes, including islands, peninsulas, and concavities	Grain shapes essentially limited to convex polyhedra
Can define Euler angles to each grain	Euler angles are not user-defined
Can define elastic constants to each grain	Elastic constants are not user-defined
Sound velocity can be assigned to each grain	Sound velocity is defined for the specimen and can vary for each region within a percentage of a nominal value (e.g., 5900 m/s $\pm$ 10%)
CIVA can take tens of minutes to render complex geometries	Regions are calculated and rendered in seconds to minutes
Difficult to generate new geometries, requires additional polished and etched sections, and difficult to import geometries that CIVA can validate	CIVA instantly generates new random Voronoi regions, and CIVA can create elongated (columnar) regions or geometries with spatially varying region sizes
Beam simulations take ~45 minutes	Beam simulations finish in 5–7 minutes
Simulation results show many missing pixels in random locations when a low accuracy factor is used	Very few missing pixels with a low accuracy factor
Image centroid position has more variation, but is still consistent with the Voronoi centroid position	Image centroid location has less variation, indicative of less beam redirection
The resulting beam maps appear to be less symmetric, potentially indicating more beam scatter and redirection	The beam maps appear to be substantially symmetric, potentially a result of the absence of large grains
Completed simulation files take tens of minutes to open	Files open immediately

Overall, results suggest that the CIVA-generated Voronoi regions are a good representation of realistic CASS conditions for the coarse-grained example that PNNL investigated. PNNL plans to evaluate different grain geometries, such as B-519C (columnar CASS sample described above). Nevertheless, PNNL expects that this assumption will hold true in most cases, as long as there is a large enough number of grains to assure conditions for random scattering.

## 8.0 Summary of Findings

PNNL's research on modeling and simulation is striving to answer the question, "under what conditions do simulations provide useful predictions of flaw detection?" More specifically, the answers to the following four questions are sought: Can modeling currently be used to predict flaw responses

- in ferritic steel,
- in wrought austenitic steel,
- through austenitic steel welds, and
- in cast austenitic steel?

With respect to the first two questions, simulations of ultrasonic beams and flaw responses in homogeneous materials, such as ferritic and wrought austenitic steels, previous work has been conducted by multiple research groups (EPRI 2015; Dib et al. 2017; EPRI 2017; Holmer et al. 2017; Foucher et al. 2018). Results have shown that simulations predict both sound beams and flaw responses with good accuracy. Simple materials do not pose any unique challenges to models, and other effects, such as mode-converted signals and beam reflections, become more important. Therefore, PNNL did not investigate these scenarios in this study.

As shown in this TLR, two keys are necessary to answer the remaining questions. (1) Robust models are required that are built on sound mathematical framework and use appropriate approximations, including the user-supplied input parameters and specimen descriptions. As has been shown in this report, the specimen descriptions are extremely important and cannot be overlooked or oversimplified. (2) Empirical studies are required in order to validate the models by testing simulated scenarios. Without laboratory-based true-state information, the predictive qualities of models can never be assessed. It is therefore vital to obtain and use laboratory-based true-state information to verify and validate the predictive qualities of models.

Results of beam and flaw response simulations in anisotropic materials have been mixed. A significant issue is that the specimen models in most cases were vastly simplified, thereby reducing the realism of the simulation to the point that the results are not useful. Therefore, this report fills the gaps by laying the critical groundwork necessary to obtain the answers to the latter two questions. In particular, more realistic austenitic weld and CASS specimen models were developed, and beam simulation results were compared to empirical beam maps in order to determine the quality of the specimen models. By developing relevant specimen models, the ability to simulate realistic flaw responses in complex materials can now be investigated in a meaningful way.

This TLR outlined the process of developing the fundamental building blocks needed for the aforementioned keys. For the first key, one of the most critical user-supplied model inputs was the specimen information, including the geometry and granular structure. This report explored the process of developing models of austenitic welds as well as the practical and predictive limits of using such models in beam and flaw-response simulations. This report also described the development of cast austenitic stainless-steel models. The level of necessary realism in specimen models was examined, and the limitations of the modeling software were probed. For the second key, empirical beam mapping and flaw response activities are undertaken using the

same specimens and probes that were modeled in order to provide validation for the simulations and to guide follow-on simulation studies.

## 8.1 Metrics

*Multiple quantitative metrics may be necessary to adequately capture and compare different facets of simulations.*

Quantitative metrics are important for comparing simulation results to one another and to empirical results. Such metrics facilitate objective decision-making by allowing analysts to avoid judgment calls on issues such as what simulation best represents a nominal case or what the minimum acceptable accuracy factor is. There may not be a single metric that adequately describes all aspects of an image or that is useful for all situations. Thus, multiple metrics may be necessary to capture different facets of simulations. Several useful metrics were described in Section 2.0 of this report. For comparing echo responses, the area under the peak in an A-scan or B-scan was calculated as a fraction of the total sound energy to compute the fraction of energy that was received by the probe from a flaw. This method of normalization allows for comparison of flaw response amplitudes across different simulations and experimental outcomes when a calibration signal is not available. For comparing images of beam maps, PNNL tested three image similarity metrics: structural similarity (SSIM), mean square error (MSE), and Pearson correlation coefficient ( $\rho$ ). Each of these metrics is sensitive to different aspects or characteristics of the image, so using them together gives a fuller picture of beam simulation similarity. These metrics are not exclusive; additional or novel metrics can be developed and tested for simulation evaluation, as well.

## 8.2 CIVA Usability

*Results show that CIVA can adequately represent complex geometries and conditions such as those observed in CASS components. However, simulation results should not be assumed to be accurate reflections of reality. Selection of inappropriate software options or poor specimen descriptions, for example, can dramatically affect the results. Trial-and-error may be needed to determine the correct model parameters, and results should be benchmarked against empirical data.*

After testing many of the features of the CIVA UT module and running multiple varied simulations, PNNL determined that CIVA is a powerful and versatile tool for ultrasonic modeling, but it should be used with care. PNNL staff found the training materials offered by EXTENDE to be helpful in overcoming a steep learning curve. Also, communication with EXTENDE support staff is critical whenever questions arise about CIVA settings or features. Most importantly—and applicable when using any modeling software—the user should not assume that simulation results are accurate reflections of reality. Simple errors in input values or the selection of an inappropriate option can dramatically affect results. In particular, users should not assume that the default settings are appropriate for a typical scenario. For example, PNNL illustrated in Section 3.0 that using the default specular specimen interaction model instead of the Kirchhoff model for specimens with ID topography gave distinctly different results. The user should test CIVA parameters and settings in order to become familiar with them and their effects before relying on the results for decision-making. Ideally, results should be benchmarked against empirical data to the extent possible. Ultimately, trial-and-error may be needed to determine the correct model parameters, particularly in cases where simulations are being compared against

experimental tests. For example, the attenuation parameter can be adjusted until the sound penetration depth matches that of an empirical beam map.

When using CIVA metamodels, PNNL recommends using realistic values and value ranges for variation parameters, preferably based on empirical measurements. If empirical measurements are not available, one should run multiple metamodels to explore how different variable ranges affect outcomes. PNNL's results showed that seemingly inconsequential changes to a single input variable range can dramatically impact the metamodel results. When evaluating metamodel results, it is important to verify that the justifications for variable ranges and probability laws for each range are given.

Beam simulations are expected to be particularly useful in helping to develop coverage estimates, assuming that appropriate specimen models and model parameters are used. Beam simulations may also be useful for predicting flaw responses in certain scenarios, such as those with coverage limitations or when flaw response simulations are time-prohibitive. Before relying on beam simulations as a surrogate for flaw response simulations, it is important to understand the limitations imposed by parameters such as grain structures, attenuation, or probe position. For example, PNNL showed in Sections 5.0 and 6.0 that beam coverage in an isotropic material does not necessarily translate to flaw insonification through an austenitic or dissimilar metal weld. Also, failure to include appropriate attenuation may cause a significant over- or under-estimation of beam coverage. PNNL also showed that the flaw response through an austenitic weld model can be significantly affected by the flaw position because of beam scatter and redirection through the weld. The exclusive use of beam simulations to predict coverage *and* flaw response is attractive because of potential significant time savings, but this approach should be taken with care.

Reflectors can be defined in CIVA using the built-in flaw definitions or by drawing a flaw in the CIVA CAD tool. PNNL noted, however, that if several flaws are defined in a single specimen, it can result in significant lag in CIVA's response to changing or inputting parameters. If it is desired to include a flaw in a beam simulation, the flaw must be included as part of the specimen definition; the CIVA flaw definitions are not available in beam simulations. PNNL included flaws in both beam and flaw response simulations in Sections 5.0 and 6.0 by adding the flaw topography to the weld specimen CAD drawings. For backwall surface-breaking reflectors, it is important to remember to define the flaw interfaces as "backwall" so that CIVA can validate the geometry and correctly calculate the interaction with the sound beam. In this report, PNNL used both a simple notch geometry and a more complex branching geometry for reflectors. The simulated signal response from the complex flaw through isotropic material was compared to that of an empirical scan, and significant differences were noted.

### 8.3 Coarse-grained Models

*To minimize the computational demands of coarse-grained models, PNNL recommends starting with the lowest level of complexity and gradually adding complexity depending on what the situation warrants. Overly realistic weld models are difficult to produce and computationally expensive to use in simulations. The use of appropriate models will be practical for the end-user by minimizing both the required technical proficiency with CIVA and simulation times. Different grain structures and probe frequencies will result in different beam patterns, suggesting that simulation results of different grain structures will not be interchangeable.*

The Ogilvy weld model provides a mathematical replication of typical austenitic weld grain structures and has therefore been commonly used for modeling and simulation activities.

However, the model assumes a gradual change in crystalline orientation, so it does not produce scatter in beam simulations. Using the Ogilvy model, PNNL showed in Section 5.0 that the choice of stiffness matrix elements has a significant impact on the beam simulations, so it is important to determine the correct matrix elements or to establish a nominal case based on various simulation outcomes. PNNL used image similarity metrics to illustrate a method of determining a nominal case.

Realistic weld models provide a good representation of beam scatter if the model grains are small enough. However, realistic weld models are difficult to produce and are computationally expensive to use in simulations. One issue to consider is the level of detail needed for the models. Results in Section 5.0 of this report suggest that the 256-pixel ( $\sim 0.4\lambda$ ) geometry with seven sets of Euler angles produced scatter comparable to the 128-pixel ( $\sim 0.2\lambda$ ), 3-bin geometry, where  $\lambda$  is the wavelength. CIVA struggled with the 128-pixel, 7-bin geometry, and the 64-pixel geometries would not even load, so it was not worth pursuing those levels of model detail at this stage. Therefore, it was determined that the 256-pixel, 7-bin geometry was a suitable austenitic weld model that provided a good balance between usability and realism. The grain structures in real welds are spatially varying, so it should be noted that a realistic weld model represents a single scenario—one probe position on one weld. Different “positions” on a specimen can be replicated by, for example, using multiple sets of Euler angles within the same grain geometry (as was done in this report), or by altering the geometry. A variety of geometries is useful for determining an average or typical weld microstructure.

When setting up a coarse-grained model, whether an austenitic weld, a DMW, or a CASS microstructure, one should include only the necessary level of computational detail. Important items to consider are: beam simulation versus flaw simulations, the strength and type of attenuation, the type of material symmetry and the stiffness matrix elements, the number of specimen bounces, whether to include interface interactions, whether to include (and the number of) mode conversions, the size of the computation zone, the number of dimensions to scan (i.e., a 1D A-scan, a 2D B-scan, or a 3D C-scan), and the inclusion of noise. PNNL recommends starting with the lowest level of complexity and gradually adding complexity in a ranked or hierarchical manner, depending on what the situation warrants. By doing so, the use of models will be practical for the end-user by minimizing the required technical proficiency with CIVA and minimizing the simulation times. Minimizing these two attributes will help reduce simulation costs and help encourage the appropriate use of modeling by industry to inform beam coverage and signal responses in relief requests.

Furthermore, it is critical to compare simulation results to empirical measurements, such as those described in Section 4.0, whenever possible. Ideally, these measurements are made in-house, but data found in the literature may also prove useful. Without “ground truth” data there is no way of evaluating the realism or accuracy of the simulations. Empirical measurements should be used to adjust model parameters in a careful and informed manner.

In the austenitic weld beam simulations described in Section 5.0, for example, PNNL initially included a simple model geometry (Ogilvy) with no attenuation, no mode conversions, no specimen bounces, an accuracy factor of 1, a simple TRL probe, and other basic settings. When it was determined that the simulation results did not provide beam scatter patterns that are present in empirical beam maps, the Ogilvy model was replaced by geometrical structural detail. Several different iterations of geometries were tested to find the minimum acceptable level of detail that can be used. Comparison with empirical beam maps showed better agreement, but it was next observed that beam attenuation needed to be added to the model. Also, it was determined that 2D computation zones should be used in place of 3D computation

zones to significantly decrease the simulation time. In one test, interface interactions were added to a flaw response model but then removed when it was ascertained that they did not add appreciable value to the simulation results.

Another important parameter is the accuracy factor, which essentially determines the mesh resolution that CIVA uses for computations. The minimum accuracy factor that provides useful results should be used, because simulation times increase rapidly with increased accuracy factor. EXTENDE has emphasized to PNNL the importance of conducting parametric studies to determine the accuracy factor needed for quality simulation results, especially when using Voronoi regions. PNNL's results show that EXTENDE is correct, but such studies may not always be possible or practical due to time constraints because simulations with high accuracy factors can have very long computation times. PNNL showed that the accuracy factor was important for eliminating uncalculated pixels for complex, user-defined geometries but appears to be much less important for Voronoi regions. In particular, in Section 7.0 PNNL used the image similarity metrics to show that the Voronoi model tested required an accuracy factor of 1 or 2 to agree well with the ideal case whereas the CASS model required an accuracy factor of 16. However, increasing the accuracy factor does not always solve the problem of uncomputed pixels. During testing, PNNL encountered a situation where beam simulation results had many missing pixels when testing an austenitic weld model with 256 pixels and 5 bins (similar to those shown in Section 5.0). Based on the advice from EXTENDE, the accuracy factor was incrementally increased (as high as 50) to mitigate the problem; however, no changes were noted in the quantity or positions of the missing pixels. This indicated that there was an issue with the computation and not the meshing accuracy for that particular model. (Interestingly, changing the number of bins to 3 or 7 resolved the problem.) Thus, there may be unforeseen situations when increasing the accuracy factor to any practical level does not improve simulation outcomes, and such situations can only be determined empirically.

PNNL found that realistic CASS models can be difficult for CIVA to run because of the large number of regions and interfaces. Fortunately, quantitative comparisons in Section 7.0 suggest that the coarse-grained equiaxed CASS structure that PNNL tested is well approximated by Voronoi regions in beam simulations. PNNL also determined that a velocity range  $\Delta V$  of 6%–8% provided scatter comparable to that of the ten Euler angles used in the AAD-3 CASS model. Voronoi regions cannot duplicate high degrees of grain heterogeneity that may occur in CASS materials, but this may not be important if the number of regions is high enough to sufficiently randomize the scatter pattern. PNNL has not yet tested other CASS microstructures, although a columnar model based on Specimen B519-C has been developed.

It has been shown that different grain structures and probe frequencies will result in different beam patterns, suggesting that simulation results of different grain structures will not be interchangeable. The implication is that, unless the grain structure of the specimen being modeled is known, the models may not be representative, no matter the skill of the modeler or what CIVA settings are used. It is not likely that the grain structure of components in the nuclear fleet will be known. In cases where an unknown degree of variability exists, such as in the grain structure of a weldment or CASS material, PNNL recommends running multiple simulations with different model settings and/or specimen scenarios in order to establish best-case, worst-case, and nominal scenarios. Various specimen geometries should be tested, such as different grain structures and assignments of Euler angles. For complex geometries, PNNL showed the choice of Euler angles can have a dramatic effect on the simulation outcomes. In addition, results in Section 6.0 showed that modeling the sound beam through a weld with grains that are too large can result in unrealistic beam scattering patterns. Additional variables to consider include specimen isotropy and stiffness matrix elements, whether to simulate interface interactions, the

number of beam skips to include, and whether to simulate mode conversions. Ultimately, it is important to balance model complexity with simulation time; models that take too long to execute and do not meet time constraints and deadlines are not practical. Therefore, forethought should be given to what the desired outcomes are and what aspects of a scenario must be included and what aspects can be ignored or eliminated.

## 8.4 Evaluating Simulations – A Potential Thought Process

Ultimately, this work will result in the development of a Regulatory Guide to provide guidance and best practices for using modeling and simulations for ultrasonic examinations of NPP applications. Simulations may be presented in reports or relief requests as, for example, justification to support claims of limited inspection coverage. The results of PNNL's work to date has shown that, when presented with a model, one should consider several important questions when evaluating model accuracy, inspection coverage, or flaw response, including:

- Did the models use sufficiently realistic geometries and parameters, such as grain structure, attenuation, interface interactions, and an appropriate number of beam skips?
- Did the models consider multiple scenarios, such as different grain structures, levels of attenuation, probe positions, probe frequencies, etc.?
- Were sources of uncertainty identified, both in model input parameters and simulation outcomes?
- Were sources of parameter values identified? Parameter values may include the type of material isotropy, Euler angles, sound velocity, etc. Sources of parameter values may include direct measurements, published reports/literature, and measurements on mockups that are known to be representative.
- Were relevant model parameters defined and justified?
- Were the results quantified? For example, was the fraction of inspection volume coverage at the –20 dB level (or level determined to be relevant) calculated for the different scenarios? Was the sound intensity on the specimen backwall calculated to identify any potential coverage gaps?
- Are the actual simulation results shown or are they just sketched or described?

## 9.0 References

- Anderson MT, AA Diaz, AD Cinson, SL Crawford, SE Cumblidge, SR Doctor, KM Denslow and S Ahmed. 2011. *An Assessment of Ultrasonic Techniques for Far-Side Examinations of Austenitic Stainless Steel Piping Welds*. NUREG/CR-7113, PNNL-19353. Washington, D.C.: U.S. Nuclear Regulatory Commission. ADAMS Accession No. ML12011A130.
- Bannouf S, D Elbaz, B Chassignole, N Leymarie and P Recolin. 2014. "Validation of Simulation Tools for Ultrasonic Inspection of Austenitic Welds in the Framework of the MOSAICS Project." In *Proceedings of 11th European Conference on Non-Destructive Testing (ECNDT 2014)*. October 6-10, 2014, Prague, Czech Republic. NDT.net. Available at <https://www.ndt.net/search/docs.php3?showForm=off&id=16607>.
- Britton T, J Jiang, Y Guo, A Vilalta-Clemente, D Wallis, L Hansen, A Winkelmann and A Wilkinson. 2016. "Tutorial: Crystal Orientations and EBSD—Or Which Way Is Up?" *Materials Characterization* 117:113-126. DOI: <http://dx.doi.org/10.1016/j.matchar.2016.04.008>.
- Bunge H-J. 2013. *Texture Analysis in Materials Science: Mathematical Methods*, Philadelphia, PA: Elsevier. ISBN 1483278395.
- Carpentier C, C Nageswaran and YY Tse. 2010. "Evaluation of a New Approach for the Inspection of Austenitic Dissimilar Welds Using Ultrasonic Phased Array Techniques." In *10th European Conference on Non-Destructive Testing (ECNDT 2010)*, pp. 442-444. June 7-11, 2010, Moscow. NDT.net. Available at <https://www.ndt.net/search/docs.php3?id=9055>.
- Chassignole B, R El Guerjouma, M-A Ploix and T Fouquet. 2010. "Ultrasonic and Structural Characterization of Anisotropic Austenitic Stainless Steel Welds: Towards a Higher Reliability in Ultrasonic Non-Destructive Testing." *NDT&E International* 43(4):273-282. DOI: <http://dx.doi.org/10.1016/j.ndteint.2009.12.005>.
- Chassignole B, D Villard, M Dubuget, J-C Baboux and RE Guerjouma. 2000. "Characterization of Austenitic Stainless Steel Welds for Ultrasonic NDT." *AIP Conference Proceedings* 509(1):1325-1332. DOI: <http://dx.doi.org/10.1063/1.1307835>.
- Chatillon S, S Robert, P Brédif, P Calmon, G Daniel and F Cartier. 2015. "Results of the 2014 UT Modeling Benchmark Obtained with Models Implemented in CIVA: Solution of the FMC-TFM Ultrasonic Benchmark Problem Using CIVA." In *41st Annual Review of Progress in Quantitative Nondestructive Evaluation: Volume 34*, pp. 1847-1855. July 20-25, 2014, Boise, ID. DOI: 10.1063/1.4914810. Melville, NY: AIP Publishing.
- Chen Y, Z Luo, Q Zhou, L Zou and L Lin. 2015. "Modeling of Ultrasonic Propagation in Heavy-Walled Centrifugally Cast Austenitic Stainless Steel Based on EBSD Analysis." *Ultrasonics* 59:31-39. DOI: <http://dx.doi.org/10.1016/j.ultras.2015.01.009>.
- Cinquin M, L Le Ber, S Lonne and S Mahaut. 2007. "Results of 2006 UT Modeling Benchmark Obtained with CIVA at CEA: Beam Modeling and Flaw Signal Prediction." In *Review of Progress in Quantitative Nondestructive Evaluation, Vol. 26B*, pp. 1870-1877. July 30-August 4, 2006, Portland, OR. DOI: 10.1063/1.2718191. Melville, NY: AIP Publishing.

Crawford SL, MS Prowant, AD Cinson, MR Larche, AA Diaz and MT Anderson. 2014. *Phased Array Ultrasonic Sound Field Mapping in Cast Austenitic Stainless Steel*. PNNL-23393. Richland, WA: Pacific Northwest National Laboratory. ADAMS Accession No. ML14155A165.

Cumblidge SE. 2018. "Coverage-Based Relief Requests." Presented at *NRC/Industry NDE Technical Exchange Meeting*, January 16-18, 2018, Rockville, MD. ADAMS Accession No. ML18012A715. Available at <https://www.nrc.gov/docs/ML1801/ML18012A715.pdf>.

Dewey BR, L Adler, RT King and KV Cook. 1977. "Measurements of Anisotropic Elastic Constants of Type 308 Stainless-Steel Electroslag Welds." *Experimental Mechanics* 17(11):420-426. DOI: <http://dx.doi.org/10.1007/bf02324239>.

Diaz AA, SR Doctor, BP Hildebrand, FA Simonen, GJ Schuster, ES Andersen, GP McDonald and RD Hasse. 1998. *Evaluation of Ultrasonic Inspection Techniques for Coarse Grained Materials*. NUREG/CR-6594, PNNL-11171. Washington, D.C.: U.S. Nuclear Regulatory Commission. ADAMS Accession No. ML14071A001.

Dib G, SL Crawford, RE Jacob, MS Prowant and AA Diaz. 2017. *Validation of Ultrasonic Nondestructive Examination (NDE) Computational Models - Phase 1*. PNNL-26336. Richland, WA: Pacific Northwest National Laboratory. ADAMS Accession No. ML17082A190.

Dib G, M Larche, AA Diaz, SL Crawford, MS Prowant and MT Anderson. 2016. "Experimental Validation of Ultrasonic NDE Simulation Software." In *42nd Annual Review of Progress in Quantitative Nondestructive Evaluation: Incorporating the 6th European-American Workshop on Reliability of NDE, Volume 35*, p. 170004. July 26-31, 2015, Minneapolis, MN. DOI: 10.1063/1.4940627. Melville, NY: AIP Publishing.

Dib G, MR Larche, MS Prowant, RE Jacob, P Ramuhalli and AA Diaz. 2018a. *Ultrasound Modeling and Simulation: Status Update*. PNNL-28362. Richland, WA: Pacific Northwest National Laboratory. ADAMS Accession No. ML19010A072.

Dib G, S Sexton, M Prowant, S Crawford and A Diaz. 2018b. "On the Usage of Ultrasound Computational Models for Decision Making Under Ambiguity." In *44th Annual Review of Progress in Quantitative Nondestructive Evaluation, Volume 37*, p. 110001. July 16-21, 2017, Provo, UT. DOI: 10.1063/1.5031580. Melville, NY: AIP Publishing.

Dorval V, F Jenson, G Corneloup and J Moysan. 2009. "Simulation of Structural Noise and Attenuation Occurring in Ultrasonic NDT of Polycrystalline Materials." In *Ultrasonic Wave Propagation in Non Homogeneous Media*, pp. 365-375. eds: A Leger and M Deschamps. Berlin, Heidelberg: Springer. DOI: 10.1007/978-3-540-89105-5\_32.

EPRI. 2015. *Program on Technology Innovation: Benchmarking of Ultrasonic Simulation Software*. EPRI 3002004439. Palo Alto, CA: Electric Power Research Institute.

EPRI. 2017. *Evaluation of Ultrasonic Simulation Software: Summary of Recent Results Quantitative Ultrasonic Beam Profiles of Conventional Single-Element Probes*. EPRI 3002010408. Palo Alto, CA: Electric Power Research Institute.

EPRI. 2018. *Ultrasonic Modeling and Simulation of Cast Austenitic Stainless Steel*. 3002013160. Palo Alto, CA: Electric Power Research Institute.

- EPRI. 2019. *Evaluation of Ultrasonic Simulation Software: Summary of Recent Results—Ultrasonic Weld Simulations*. 3002015980. Palo Alto, CA: Electric Power Research Institute. Available at <https://www.epri.com/#/pages/product/3002015980/>.
- Fan Z, AF Mark, MJS Lowe and PJ Withers. 2015. "Nonintrusive Estimation of Anisotropic Stiffness Maps of Heterogeneous Steel Welds for the Improvement of Ultrasonic Array Inspection." *IEEE Transactions on Ultrasonics, Ferroelectrics, and Frequency Control* 62(8):1530-1543. DOI: <http://dx.doi.org/10.1109/TUFFC.2015.007018>.
- Foucher F, R Fernandez, S Leberre and P Calmon. 2018. "New Tools in CIVA for Model Assisted Probability of Detection (MAPOD) to Support NDE Reliability Studies." In *NDE of Aerospace Materials & Structures 2018*, pp. 32-43. June 5-6, 2018, Bridgeton, MO. ASNT. ISBN 1571174559.
- Gardahaut A, K Jezzine and D Cassereau. 2012. "Modelling Tools for Ultrasonic Inspection of Bimetallic Welds." In *Acoustics 2012*. 2012-04-23, Nantes, France. Available at <https://hal.archives-ouvertes.fr/hal-00811043>.
- Gardahaut A, H Lourme, F Jenson, S Lin and M Nagai. 2014. "Ultrasonic Wave Propagation in Dissimilar Metal Welds—Application of a Ray-Based Model and Comparison with Experimental Results." In *Proceedings of 11th European Conference on Non-destructive Testing (ECNDT 2014)*, pp. 302-311. October 6-10, 2014, Prague, Czech Republic. European Federation for Non-Destructive Testing. Available at [https://www.ndt.net/events/ECNDT2014/app/content/Paper/119\\_Gardahaut.pdf](https://www.ndt.net/events/ECNDT2014/app/content/Paper/119_Gardahaut.pdf).
- Ghoshal G and JA Turner. 2009. "Numerical Model of Longitudinal Wave Scattering in Polycrystals." *IEEE Transactions on Ultrasonics, Ferroelectrics, and Frequency Control* 56(7):1419-1428. DOI: <http://dx.doi.org/10.1109/TUFFC.2009.1197>.
- Ginzel E. 2018. "Modelling Probe Wedge and Pipe Geometry as Critical Parameters in Pipe Girth Weld Ultrasonic Inspections Using Civa Simulation Software." *NDT.net Journal*.
- Gueudre C, J Mailhe, MA Ploix, G Corneloup and B Chassignole. 2019. "Influence of the Uncertainty of Elastic Constants on the Modelling of Ultrasound Propagation Through Multi-Pass Austenitic Welds. Impact on Non-Destructive Testing." *International Journal of Pressure Vessels and Piping* 171:125-136. DOI: <http://dx.doi.org/10.1016/j.ijpvp.2019.02.011>.
- Holmer G, W Daniels and T Zettervall. 2017. *Evaluation of the Simulation Software CIVA for Qualification Purpose*. 2017:29. Stockholm, Sweden: Swedish Radiation Safety Authority. Available at <https://www.stralsakerhetsmyndigheten.se/contentassets/6942c0e6c7ca474f81e5533750853914/201729-evaluation-of-the-simulation-software-civa-for-qualification-purpose>.
- Hopkins D, M Datuin, J Aldrin, M Warchol, L Warchol and D Forsyth. 2018. *44th Annual Review of Progress in Quantitative Nondestructive Evaluation, Volume 37*, p. 140003. July 16-21, 2017, Provo, UT. eds: DE Chimenti and LJ Bond. AIP Publishing, Vol. 1949.
- Humphreys F. 2001. "Review Grain and Subgrain Characterisation by Electron Backscatter Diffraction." *Journal of Materials Science* 36(16):3833-3854. DOI: <http://dx.doi.org/10.1023/A:1017973432592>.

- Hwang Y-I, J Park, H-J Kim, S-J Song, Y-S Cho and S-S Kang. 2019. "Performance Comparison of Ultrasonic Focusing Techniques for Phased Array Ultrasonic Inspection of Dissimilar Metal Welds." *International Journal of Precision Engineering and Manufacturing* 20(4):525-534. DOI: <http://dx.doi.org/10.1007%2Fs12541-019-00085-1>.
- Jacob RE, BG Amidan, J Soelberg and KR Minard. 2010. "In Vivo MRI of Altered Proton Signal Intensity and T2 Relaxation in a Bleomycin Model of Pulmonary Inflammation and Fibrosis." *Journal of Magnetic Resonance Imaging* 31(5):1091-1099. DOI: <http://dx.doi.org/10.1002/jmri.22166>.
- Jacob RE, SL Crawford, TL Moran, MR Larche, MS Prowant, AA Diaz and CA Nove. 2019. *NDE Reliability Issues for the Examination of CASS Components*. NUREG/CR-7263; PNNL-28840. Washington, D.C.: U.S. Nuclear Regulatory Commission. ADAMS Accession No. ML19255J814.
- Jenson F, T Fortuna and L Doudet. 2009. "Modeling of Ultrasonic Propagation in a Coarse Grain Structure." *AIP Conference Proceedings* 1096(1):1201-1208. DOI: <http://dx.doi.org/10.1063/1.3114091>.
- Jüngert A, S Dugan, T Homann, S Mitzscherling, J Prager, S Pudovikov and T Schwender. 2018. "Advanced Ultrasonic Techniques for Nondestructive Testing of Austenitic and Dissimilar Welds in Nuclear Facilities."
- Juva A and J Lenkkeri. 1980. "The Effect of Anisotropy on the Propagation of Ultrasonic Waves in Austenitic Stainless Steel." In *Proceedings of the Specialists' Meeting on Reliability of the Ultrasonic Inspection of Austenitic Materials*, pp. 2-24. May 29-30, 1980, Brussels, Belgium. Nuclear Energy Agency of the OECD, France. Available at [https://inis.iaea.org/search/search.aspx?orig\\_q=RN:42022193](https://inis.iaea.org/search/search.aspx?orig_q=RN:42022193).
- Kim H-H, H-J Kim, S-J Song, K-C Kim and Y-B Kim. 2016. "Simulation Based Investigation of Focusing Phased Array Ultrasound in Dissimilar Metal Welds." *Nuclear Engineering and Technology* 48(1):228-235. DOI: <http://dx.doi.org/10.1016/j.net.2015.10.011>.
- Liu Q and H Wirdelius. 2007. "A 2D Model of Ultrasonic Wave Propagation in an Anisotropic Weld." *NDT&E International* 40(3):229-238. DOI: <http://dx.doi.org/10.1016/j.ndteint.2006.10.004>.
- Mahaut S, S Chatillon, N Leymarie, F Jenson and P Calmon. 2007. "Simulation Tools for Predicting Non Destructive Testing of Heterogeneous and Anisotropic Structures." In *The International Congress of Ultrasonics*. April 9-13, 2007, Vienna. Paper #1652.
- Mark A, Z Fan, F Azough, M Lowe and P Withers. 2014. "Investigation of the elastic/crystallographic anisotropy of welds for improved ultrasonic inspections." *Materials Characterization* 98:47-53.
- Murthy R, NM Bilgutay and J Saniie. 1989. "Application of Bandpass Filtering in Ultrasonic Non-Destructive Testing." In *Review of Progress in Quantitative Nondestructive Evaluation: Volume 8, Part A and B*, pp. 759-767. eds: DO Thompson and DE Chimenti. Boston, MA: Springer US. DOI: 10.1007/978-1-4613-0817-1\_95.

- Nageswaran C, C Carpentier and Y Tse. 2009. "Microstructural Quantification, Modelling and Array Ultrasonics to Improve the Inspection of Austenitic Welds." *Insight: Non-Destructive Testing* 51(12):660-666. DOI: <http://dx.doi.org/10.1784/insi.2009.51.12.660>.
- Nakahata K, H Sugahara, M Barth, B Köhler and F Schubert. 2016. "Three Dimensional Image-Based Simulation of Ultrasonic Wave Propagation in Polycrystalline Metal Using Phase-Field Modeling." *Ultrasonics* 67:18-29. DOI: <http://dx.doi.org/10.1016/j.ultras.2015.12.013>.
- Nowers O, DJ Duxbury and BW Drinkwater. 2016. "Ultrasonic Array Imaging Through an Anisotropic Austenitic Steel Weld Using an Efficient Ray-Tracing Algorithm." *NDT & E International* 79:98-108. DOI: <http://dx.doi.org/10.1016/j.ndteint.2015.12.009>.
- Ogi H, K Sato, T Asada and M Hirao. 2002. "Complete Mode Identification for Resonance Ultrasound Spectroscopy." *The Journal of the Acoustical Society of America* 112(6):2553-2557. DOI: <http://dx.doi.org/10.1121/1.1512700>.
- Ogilvy JA. 1985. "Computerized Ultrasonic Ray Tracing in Austenitic Steel." *NDT International* 18(2):67-77. DOI: [http://dx.doi.org/10.1016/0308-9126\(85\)90100-2](http://dx.doi.org/10.1016/0308-9126(85)90100-2).
- Papadakis EP. 1964. "From Micrograph to Grain-Size Distribution with Ultrasonic Applications." *Journal of Applied Physics* 35(5):1586-1594. DOI: <http://dx.doi.org/10.1063/1.1713671>.
- Ploix M-A, P Guy, R Elguerjouma, J Moysan, G Corneloup and B Chassignole. 2006. "Attenuation Assessment for NDT of Austenitic Stainless Steel Welds." In *9th European Conference on NDT (ECNDT)*. September 25-29, 2006, Berlin. Available at <https://www.ndt.net/article/ecndt2006/doc/Tu.2.2.1.pdf>.
- PNNL. 2013a. *Technical Letter Report, Evaluation of Alternative to 10 CFR 50.55a(g)(6)(ii)(F)(4) for Limitations to Volumetric Examinations of Dissimilar Metal Welds, Florida Power & Light, St. Lucie Power Plant Unit 1 – Docket Number 50-335*. Richland, WA: Pacific Northwest National Laboratory. ADAMS Accession No. ML14149A195.
- PNNL. 2013b. *Technical Letter Report, Evaluation of Licensee's Alternative to 10 CFR 50.55A(G)(6)(II)(F) for Limitations to Volumetric Examinations of Dissimilar Metal Welds, Constellation Energy, Calvert Cliffs Nuclear Power Plant – Docket Number 50-318*. Richland, WA: Pacific Northwest National Laboratory. ADAMS Accession No. ML13113A233.
- PNNL. 2013c. *Technical Letter Report, Evaluation of Licensee's Alternative to 10 CFR 50.55a(g)(6)(ii)(F) for Limitations to Volumetric Examinations of Dissimilar Metal Welds, Entergy Operations, Inc., Arkansas Nuclear One, Unit 2 – Docket Number 50-368*. Richland, WA: Pacific Northwest National Laboratory. ADAMS Accession No. ML13113A218.
- Ribay G, X Artusi, F Jenson, C Reece and P-E Lhuillier. 2016. "Model-Based POD Study of Manual Ultrasound Inspection and Sensitivity Analysis Using Metamodel." In *42nd Annual Review of Progress in Quantitative Nondestructive Evaluation: Incorporating the 6th European-American Workshop on Reliability of NDE*, p. 200006. July 26-31, 2015, Minneapolis, MN. DOI: 10.1063/1.4940650. AIP Publishing, Vol. 1706.
- Ribay G, S Mahaut, G Cattiaux and T Sollier. 2017. "Assessment of the Reliability of Phased Array NDT of Coarse Grain Component Based on Simulation." In *7th European-American*

*Workshop on Reliability NDE (Reliability 2017)*. September 4-7, 2017, Potsdam, Germany. NDT.net. Available at <https://www.ndt.net/search/docs.php3?id=21788>.

Sakamoto K, T Furukawa, I Komura, Y Kamiyama and T Mihara. 2012. "Study on the Ultrasound Propagation in Cast Austenitic Stainless Steel." *E-Journal of Advanced Maintenance* 4(1). Available at [http://www.jsm.or.jp/ejam/Vol.4No.1/AA/AA37/EJAM\\_CASS\\_Paper\\_sakamoto\\_Final\\_0419\\_.pdf](http://www.jsm.or.jp/ejam/Vol.4No.1/AA/AA37/EJAM_CASS_Paper_sakamoto_Final_0419_.pdf).

Sakamoto K, T Mihara, T Furukawa and Y Kamiyama. 2013. "Visualization of Ultrasonic Wave in Cast Austenitic Stainless Steel Piping." In *9th International Conference on NDE in Relation to Structural Integrity for Nuclear and Pressurized Components (JRC-NDE 2012)*, pp. 912-919. May 22-24, 2012, Seattle, WA. NDT.net. Available at <https://www.ndt.net/article/jrc-nde2012/papers/141.pdf>.

Schneider CA, WS Rasband and KW Eliceiri. 2012. "NIH Image to ImageJ: 25 Years of Image Analysis." *Nature Methods* 9(7):671-675. DOI: <http://dx.doi.org/10.1038/nmeth.2089>.

Schwartz AJ, M Kumar, BL Adams and DP Field, Eds. 2000. *Electron Backscatter Diffraction in Materials Science*. Boston, MA: Springer. ISBN 030646487X. DOI: 10.1007/978-0-387-88136-2.

Seldis T and C Pecorari. 2000. "Scattering-Induced Attenuation of an Ultrasonic Beam in Austenitic Steel." *The Journal of the Acoustical Society of America* 108(2):580-587. DOI: <http://dx.doi.org/10.1121/1.429589>.

Shivaprasad S, A Pandala, C Krishnamurthy and K Balasubramaniam. 2018. "Wave Localized Finite-Difference-Time-Domain Modelling of Scattering of Elastic Waves Within a Polycrystalline Material." *The Journal of the Acoustical Society of America* 144(6):3313-3326. DOI: <http://dx.doi.org/10.1121/1.5082298>.

Sy K, P Bredif, E Iakovleva, O Roy and D Lesselier. 2018. "Development of the Specular Echoes Estimator to Predict Relevant Modes for Total Focusing Method Imaging." *NDT & E International* 99:134-140. DOI: <http://dx.doi.org/10.1016/j.ndteint.2018.07.005>.

Szavai S, Z Bezi, J Dudra and I Mehesz. 2016. "Modelling of Phased Array Ultrasonic Inspection of a Steam Generator Dissimilar Metal Weld." *Procedia Structural Integrity* 2:1015-1022. DOI: <http://dx.doi.org/10.1016/j.prostr.2016.06.130>.

Tabatabaeipour SM and F Honarvar. 2010. "A Comparative Evaluation of Ultrasonic Testing of AISI 316L Welds Made by Shielded Metal Arc Welding and Gas Tungsten Arc Welding Processes." *Journal of Materials Processing Technology* 210(8):1043-1050. DOI: <http://dx.doi.org/10.1016/j.jmatprotec.2010.02.013>.

Temple JAG. 1988. "Modelling the Propagation and Scattering of Elastic Waves in Inhomogeneous Anisotropic Media." *Journal of Physics D: Applied Physics* 21:859-874. DOI: <http://dx.doi.org/10.1088/0022-3727/21/6/003>.

Van Pamel A, P Huthwaite, CR Brett and MJS Lowe. 2016. "Numerical Simulations of Ultrasonic Array Imaging of Highly Scattering Materials." *NDT & E International* 81:9-19. DOI: <http://dx.doi.org/10.1016/j.ndteint.2016.02.004>.

Vijayendra MK and AE Neumann. 1992. "Reflection and Transmission Energy Coefficients at the Interface Between Austenitic Base and Weld Metal." *Journal of Physics D: Applied Physics* 25(10):1504-1512. DOI: <http://dx.doi.org/10.1088/0022-3727/25/10/017>.

Wan T, T Naoe, T Wakui, M Futakawa, H Obayashi and T Sasa. 2017. "Effects of Grain Size on Ultrasonic Attenuation in Type 316L Stainless Steel." *Materials* 10(7):753. DOI: <http://dx.doi.org/10.3390/ma10070753>.

Wang, Z, AC Bovik, HR Sheikh and EP Simoncelli. 2004. "Image Quality Assessment: From Error Visibility to Structural Similarity." *IEEE Transactions on Image Processing* 13(4):600-612. DOI: <http://dx.doi.org/10.1109/TIP.2003.819861>.

Wirdelius H and G Persson. 2012. "Simulation Based Validation of the Detection Capacity of an Ultrasonic Inspection Procedure." *International Journal of Fatigue* 41:23-29. DOI: <http://dx.doi.org/10.1016/j.ijfatigue.2011.09.002>.

Zhou H, Z Han, D Du and Y Chen. 2018. "A Combined Marching and Minimizing Ray-Tracing Algorithm Developed for Ultrasonic Array Imaging of Austenitic Welds." *NDT & E International* 95:45-56. DOI: <http://dx.doi.org/10.1016/j.ndteint.2018.01.008>.

## Appendix A – Workflows

### A.1 A-scan Comparisons

#### A.1.1 Purpose

A-scan comparisons provide a method of quantitatively comparing the relative strength of echo responses in simulated or experimental A-scans. Such comparisons are important when a calibration signal was not acquired or is not available because it allows A-scan echoes from different scenarios to be directly compared.

#### A.1.2 Context

A-scan comparisons of echo responses were made with simulated A-scans to compare the echo response in flaw-response simulations with different material properties (Section 5.2).

#### A.1.3 Workflow (Section 2.2)

1. Acquire and rectify A-scan data of an echo response. Create an envelope of the rectified A-scan.
2. Identify the envelope peaks of interest based on a height threshold. This may require trial-and-error to select the desired peaks without including neighboring peaks.
3. Fit a Gaussian curve to each peak. This should be an excellent approximation for well-behaved echoes.
4. Integrate the Gaussian curve to find a peak's area. The normalized energy is calculated by dividing that peak area by the area under the envelope of the entire signal response.

### A.2 Similarity Metrics

#### A.2.1 Purpose

Similarity metrics provide a method to quantitatively compare beam simulation results. This is important because it allows for comparisons to be made objectively, thus better allowing for accurate assessments of simulation results.

#### A.2.2 Context

Similarity metrics were used to compare through-weld beam simulation results to one another (Sections 5.2 and 5.3), to compare beam simulations through coarse-grained materials to simulations through Voronoi models (Sections 7.2.2 and 7.2.3), and to determine the ideal accuracy factor value (Section 7.2.4).

#### A.2.3 Workflow (Section 2.4)

1. Images to be compared should be the same size (i.e., the same number of pixels in each dimension).
2. Select an image to be the standard, or the image that the others will be compared to. For example, in Section 5.3.2 one standard used was the isotropic beam (Figure 5.15), and in Section 7.2.4, the standard was the simulation with the highest accuracy factor.

3. Using a software tool such as Python or MATLAB, compute the similarity metrics. In this report, structural similarity (SSIM), mean-square-error (MSE), and the Pearson correlation coefficient ( $\rho$ ) were used.
4. The similarity metrics can be used to determine which simulation output was, for example, the most or least similar to the standard. Results can be used to determine an ideal accuracy factor or to select a geometry model for follow-on simulations.

## A.3 Quadtree Decomposition

### A.3.1 Purpose

Quadtree decomposition is a method of downsampling an image to a predetermined resolution. This is important because it allows for a rapid and objective method of preparing CIVA-capable models of high-resolution specimen images.

### A.3.2 Context

Images acquired from EBSD scans of a weld were downsampled to different resolutions using quadtree decomposition so that the effects of different grain size could be studied on the same weld geometry (Sections 5.3.2 and 5.4). The grains measured by EBSD were far too small for use in creating a model geometry, so this method essentially takes the average of the Euler angles of neighboring grains and combines them into one larger “grain”.

### A.3.3 Workflow (Section 5.3.1)

1. Evaluate the desired level of resolution of grain sizes for a simulation. Higher resolution will result in smaller grains and longer simulation times. Larger grains will result in reduced model realism but shorter simulation times.
2. Use the desired resolution to determine the minimum quad size for the decomposition (a quad is used as a surrogate for a grain). For example, a 256-pixel quad will be a square that is composed of  $256 \times 256$  of the original pixels. For this work, the original EBSD pixels were  $4 \mu\text{m} \times 4 \mu\text{m}$ , so a 256-pixel decomposition resulted in quads that were about  $1 \text{ mm} \times 1 \text{ mm}$ . 128-pixel and 64-pixel decompositions were also used. Note that because this method uses quads, the resulting quad sizes will always be powers of 2 (i.e.,  $256 = 2^8$ ,  $128 = 2^7$ ,  $64 = 2^6$ , etc.).
3. Start the decomposition by dividing the image into four squares, or quads (Figure 5.10).
4. Measure the mean and standard deviation of the values in each quad. The values will depend on the type of data conveyed in the image and may, for example, be based on Euler angles or color intensity.
5. If the standard deviation exceeds a pre-determined threshold, then the quad is divided into four daughter quads. The threshold may, for example, be based on the standard deviation divided by the mean.
6. Repeat Steps 4 and 5 until the threshold condition has been met or until the quad reaches the minimum desired resolution (Figure 5.12).

## A.4 Building and Executing an Empirical Weld Model

### A.4.1 Purpose

Empirical data are used to convert true-state EBSD information into weld models for CIVA. This is important for being able to evaluate beam simulations and flaw-response simulations through realistic austenitic welds.

### A.4.2 Context

EBSD data of grain sizes and orientations were collected on an austenitic weld and then converted to a model geometry for use in CIVA (Section 5.3.1).

### A.4.3 Workflow (Section 5.3.1)

1. Acquire EBSD data and IPF images.
2. Using a quadtree decomposition (see Section A.3.3), downsample the images to the desired resolution to create a model weld geometry for simulations. Each region of the model represents a grain with a unique crystalline orientation.
3. If desired, reduce the complexity of the weld geometry further by combining regions that have similar crystalline orientations. This can be done by assigning each region to a group, or bin (Figure 5.12).
4. Using a software tool such as MATLAB, define the boundaries of each region of the binned image, and save the line coordinates as a .dxf file that can be opened into the CAD editor in CIVA. The .dxf file should contain the proper line assignments for CIVA, such as backwall, frontwall, etc.
5. Open the .dxf file in CIVA, verify that the geometry is valid, and save the geometry from CIVA as an .xml file.
6. Load the .xml into MATLAB and assign Euler angles to each region. It is important to follow the CIVA-designated sequencing of each region so that CIVA will make the correct assignments when it opens the .xml file. Open the .xml file in CIVA and verify that the region sequencing is correct.
7. At this point, the rest of the CIVA simulation inputs can be entered. This includes the geometry extrusion factor, which gives the two-dimensional geometry some depth so that a UT probe can be placed on it. If a PA probe is being modeled, be sure to compute the PA laws with the probe off of the weld (see Section 3.3). Also, it is important to set an appropriate accuracy factor (see Section 7.2.4).
8. To investigate a range of simulation outcomes, multiple weld models can be generated from the same geometry by randomizing the Euler angle assignments or by changing the number of bins (cf. Figure 5.17).
9. Analysis can be performed to investigate the simulation outcomes. In this report, similarity metrics (see Appendix A.2.3) were used to determine what weld models produced results most similar to the isotropic case and to the average case (cf. Tables 5.3 and 5.4).

## A.5 Building and Executing a CASS Model

### A.5.1 Purpose

Empirical data are used to convert true-state CASS grain structures into realistic coarse-grain models for CIVA. This is important for being able to evaluate beam simulations and flaw-response simulations through coarse-grained materials.

### A.5.2 Context

Photographs highlighting the grain structures of CASS materials were collected and converted to a coarse-grained model for use in CIVA (Section 7.2).

### A.5.3 Workflow (Section 7.2.1):

1. Acquire photographs of a polished and etched CASS specimen with a light source at different angles.
2. Using the step-by-step procedure outlined in Section 7.2.1, generate a skeleton image of the grain boundaries (see Figures 7.3 and 7.4).
3. Using a software tool such as MATLAB, apply the line reduction algorithm to the skeleton to reduce the number of line segments (Figure 7.5).
4. Save the CASS model as a .dxf file that can be opened into the CAD editor in CIVA. The .dxf file should contain the proper line assignments for CIVA, such as backwall, frontwall, etc.
5. Open the .dxf file in CIVA, verify that the geometry is valid, and save the geometry from CIVA as an .xml file.
6. Load the .xml into MATLAB and assign Euler angles to each region. Because actual Euler angles were not found with EBSD, angles can be assigned randomly or taken from the literature. The CASS model is now ready for CIVA.
7. After loading the model into CIVA, the rest of the CIVA simulation inputs can be entered. This includes the geometry extrusion factor, which gives the two-dimensional geometry some depth so that a UT probe can be placed on it. If a PA probe is being modeled, be sure to compute the PA laws with the probe on an isotropic material (see Section 3.3). Also, it is important to set an appropriate accuracy factor (see Section 7.2.4).
8. To investigate a range of simulation outcomes, multiple CASS models can be generated from the same geometry by randomizing the Euler angle assignments (cf. Figure 7.12).
9. Analysis can be performed to investigate the simulation outcomes. In this report, similarity metrics (see Appendix A.2.3) were used to determine what weld models produced results most similar to the isotropic case and to the average case (cf. Tables 7.1 and 7.2).

## Appendix B – B-scan Similarity Metric

To illustrate the method and check its effectiveness, an image with two peaks with known areas was generated as a test image. Figure B.1 shows the two test peaks. The known area of Peak 1 is 377 pixels and Peak 2 is 251 pixels. A constant background of 0.1 was added as a noise surrogate. The total integral (peaks plus background), representing the total received energy, is 3628 pixels. For this example, Peak 2 was selected for integration.

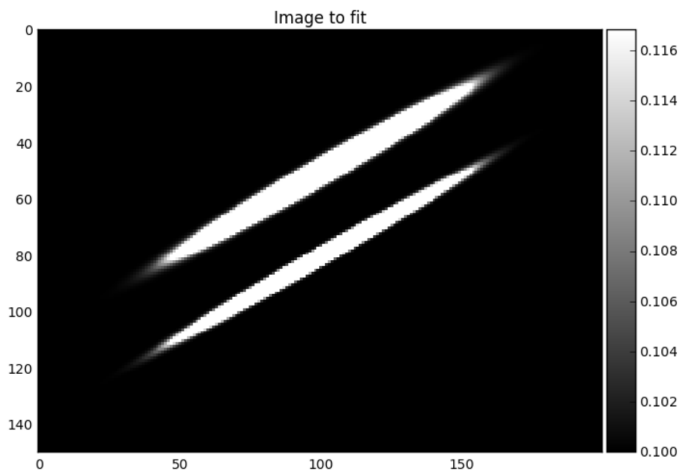


Figure B.1. Synthetic B-scan with test peaks for integration.

The first integration gives a total of 3628 pixels (which agrees with the known value) and a Peak 2 integral of 245 pixels, a bit lower than the known value; Figure B.2 shows the initial fit region. From this fit, a mask image was generated to isolate the peak from the rest of the image. The mask is shown in blue in Figure B.3. With the peak isolated, the second fit was performed, as shown in Figure B.4. The result is 251 pixels, which agrees with the known value.

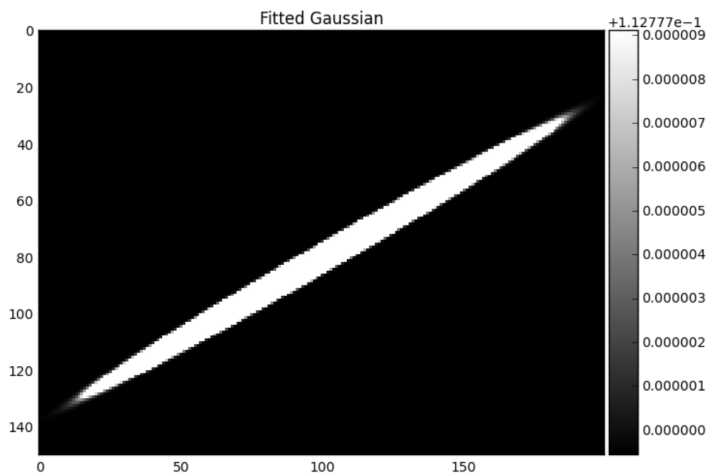


Figure B.2. Region isolated for the initial Gaussian fit.

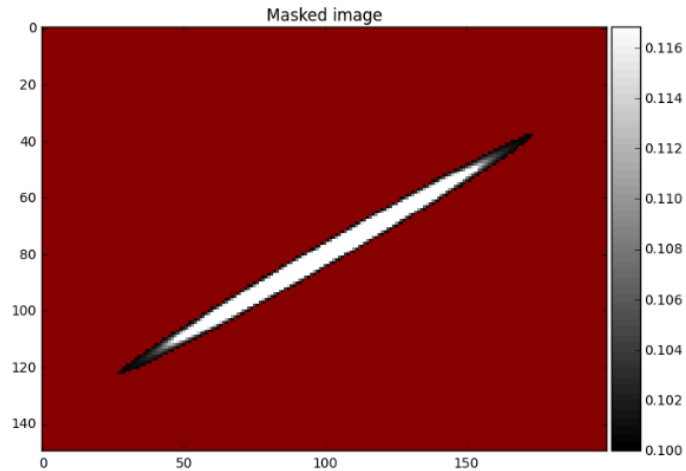


Figure B.3. Mask from the initial Gaussian fit.

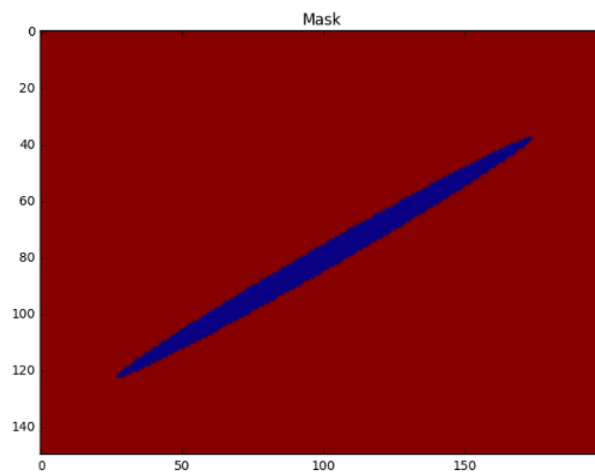


Figure B.4. The result of applying the mask in Figure B.3 to Figure B.2.

This approach was applied to CIVA-simulated data of a B-scan, the model comprising a flaw on the far side of an Ogilvy weld with a weld root present. Figure B.5(a) shows the peaks from the flaw and weld root (the horizontal stripes are a CIVA artifact). The endpoints of the red line represent the two user-identified points along the length of the peak (Step 1 above). The initial Gaussian fit identified the total integral to be 790 pixels and the peak integral to be 136 pixels. After applying the mask and the second Gaussian fit, the peak integral was 152 pixels; the integrated region is shown in red in Figure B.5(b). The metric of interest, the fraction of peak energy to total received energy, was 0.192.

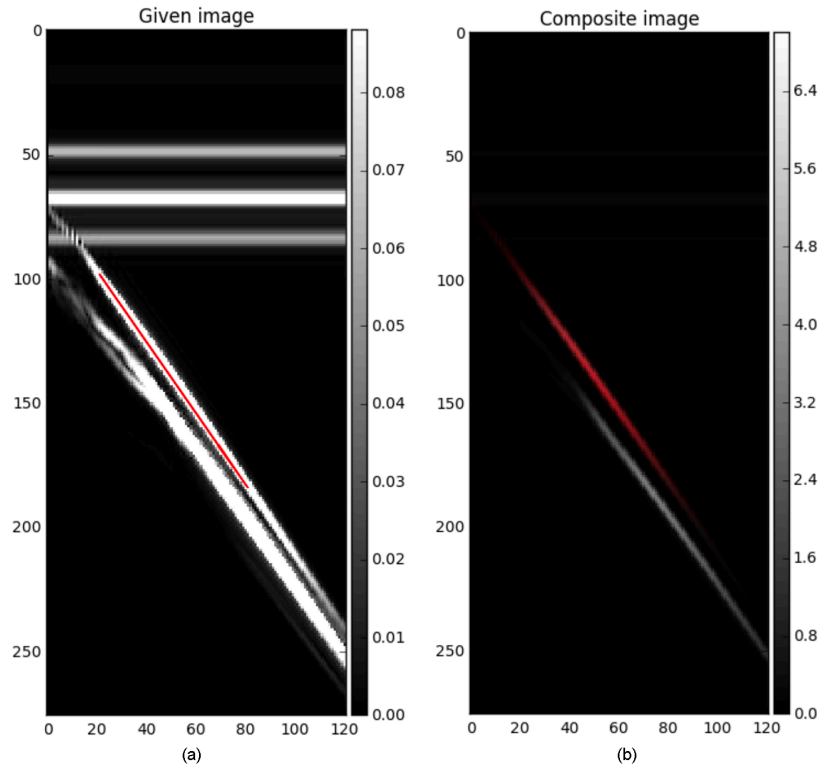


Figure B.5. (a) B-scan from a CIVA simulation. (b) The region included in the final Gaussian fit is shown in red.

The method was also tested on experimental data acquired with UltraVision. A single B-scan slice of a 3D image was selected and exported. Figure B.6(a) shows the signal response that was identified for measurement. Figure B.6(b) shows the region that was ultimately included in the calculation. The total integral of this image was  $5.93 \times 10^7$  and the integral of the peak was  $7.20 \times 10^6$ , resulting in a ratio of 0.121. Clearly, the absolute integrals of the UltraVision data and the CIVA results cannot be directly compared, because they are orders of magnitude different. However, the ratios of the peak area to total area can be directly compared. (Note that, in these examples, the simulation and empirical data represent different specimens, so direct comparisons are not relevant; data shown are for illustrative purposes only.) A correction to the total received energy could be done by subtracting the electronic noise in the system, if it is a relevant systematic offset. To measure the electronic noise floor, a raster scan was acquired on a specimen with a phased-array probe but with the transmit probe turned off. A second scan of a fine-grained carbon steel (CS) material was run with the transmit probe turned on. The noise was measured in the “quietest” region of the specimen scan. The mean noise in the no-transmit scan was 1.1% full screen height (FSH) while the noise in the region of the actual scan was about 6.3% FSH. So, the electronic noise accounted for approximately 20% of the total noise in a fine-grained material. This percentage would be much lower for scans of coarse-grained materials and austenitic welds. For purposes of comparing future simulation results with scan results, this experiment shows that the measured level of electronic noise will not be a significant source of systematic error at the level of precision anticipated being necessary.

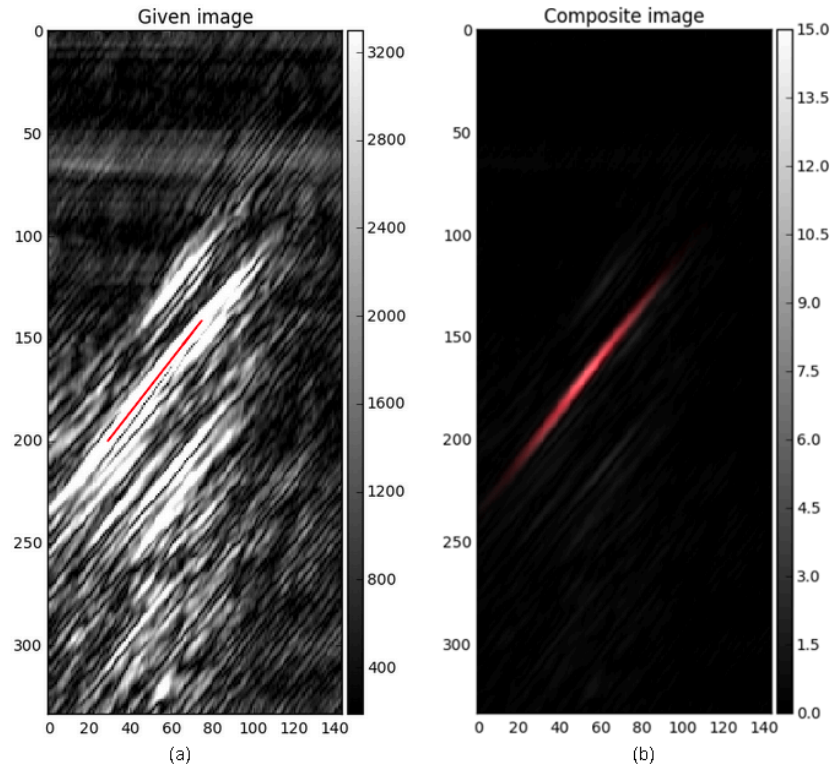


Figure B.6. (a) Empirical B-scan from a specimen scan using UltraVision. (b) The region included in the final Gaussian fit is shown in red.

## Appendix C – CIVA Tips

Summary of advice from EXTENDE and other items about CIVA 2017. This summary may be particularly useful for the novice user. Items are presented in no particular order.

- Use “Full Incident Beam” unless the backwall surface provides a flat or mirror-like reflection.
- It is recommended to perform convergence tests to determine the optimal value of the accuracy parameter. For flaw response simulations, this can be done with a single A-scan to save time. The Variation feature can be used, or simulations can be run independently.
- Use “Advanced Definition” instead of “Half-skip” or other settings to be able to control other options, especially the geometry diffraction model (Specular or Kirchhoff).
- When including attenuation in the simulation, define the attenuation properties of each region of the specimen independently in the Specimen tab. Also, be sure to select the Attenuation option in the Simulation tab. If the Attenuation option is not selected, attenuation will be not included in the simulation, even if attenuation properties are defined for the specimen.
- Check that the sound velocities are correctly defined in the probe definition. They should also be defined in the Specimen tab. Defining them in one location does not change the definition in the other location.
- The Kirchhoff approximation is well suited to calculate geometry echoes instead of Specular. Use Specular if the backwall is flat and the reflection is expected to be mirror-like.
- Minimize the size of the sensitivity zone to reduce computation time. The sensitivity zone is mandatory with the Kirchhoff model and should include any backwall or interfaces that will be included in the simulation. If many simulations will be performed, a convergence test may be warranted to determine the minimum size of the sensitivity zone. Keep in mind, however, that it may take less time to just run the simulations with a large sensitivity zone than it will to run both a convergence test and simulations.
- The Ogilvy model of weld microstructure is active for the entire weld volume, so reduce the specimen extrusion to save computation time. Maintain a small margin on either side of the length of the flaw.
- Defining a rectangular notch can reduce computation time over other flaw geometries because it reduces meshing. Flaws are re-meshed every time an option is changed or a tab is selected. Multiple non-rectangular flaws present in one specimen can slow CIVA down considerably. Remove any flaws outside the computation zone to reduce the latency. One approach is to minimize the number of flaws present while changing parameters to reduce latency, then add the flaws back just before running the simulation.
- Up to five modes can be returned in Simulation Setting Options, and the computation time is the same as if fewer nodes are selected.
- Minimize the number of interactions to only those necessary. Adding interactions, especially interface interactions in specimens with multiple regions, can dramatically increase simulation times.
- Use a manual gate to avoid simulating low-amplitude echoes that appear at a long time of flight to reduce computation time.

- For flaw response simulations, change probe (or field) accuracy and defect accuracy together. The field accuracy is linked to how the probe is meshed by CIVA while the defect accuracy is linked to how the defect is meshed.
- To switch from a Variation setup to a standard setup, return to the CIVA desktop, choose Inspection Simulation, and use the current configuration.
- To normalize different beam simulations to the one with the highest value, right click on the results with the highest amplitude and select “new reference.” For the other results, choose Reference to R0 (or R1, etc.). The results of the references are not saved.
- Use Batch Mode to keep track of computation times. The batch mode window displays the simulation time and stays open after the simulations are complete. CIVA can continue to be used to set up simulations or analyze data while batch mode is running, but additional simulations cannot be run while simulations are being run in batch mode. The main CIVA window can also be closed without interrupting batch mode simulations.
- If mode conversions are not enabled, the echoes from conversion from one mode to another will not be simulated. However, for L mode only or T mode only, the simulation will still account for the possible loss in energy (or transmission coefficient) when the beam encounters an interface.
- In certain cases with a beam simulation, such as when only a transmit probe is being modeled, post-processing must be used to display the beam. When the file first opens it shows the beam in Transmission/Reception, which is blank because of the lack of a beam in reception. Use post-processing to select Transmit Only to show the desired results.
- There is a bug that prevents reconstruction and display of the True B-scan of the beam through an Ogilvy weld or other complicated grain structures, such as our austenitic weld models, for probe locations that place the beam exit point over the weld region. This did not appear to be a problem for less complex specimens, such as the DMW model.
- The probe phase cannot be negative. It must be between 0 and 360.
- In 2D CAD, intersections of four or more line segments can prevent the drawing from being accepted by CIVA if the lines are not drawn in a specific order. In general, such intersections should be avoided. (*Note: this problem was fixed in CIVA 2020.*)
- CIVA’s method of region ordering for 2D CAD is very complicated and not reproducible. (*Note: the method was greatly simplified in CIVA 2020.*)
- In CIVA UT, it is possible to load your own color palette from the "Palette/Gain" toolbox. This can only be done in Inspection Simulation, but the pallet will be available in Beam Computation also. The file should contain the palette name, colors for different values from 0 to 1, and a color for saturated values. Colors are given in RGB color space. FAQ-0015 on the online CIVA HelpDesk has more information about how to do this.
- Holes may appear in a beam computation if some of the points of the beam computation zone are exactly on the borders of the volumes of the specimen. Moving the probe slightly may resolve the problem. Increasing the accuracy factor may or may not also resolve the problem.
- Regarding FAQ B:9 on the online CIVA HelpDesk, “Different Export Options”: A “sequence” refers to a group of elements in a PA probe being fired. For electronic scanning, it refers to the active subset of elements, for example 1–8, 2–9, etc. A “shot” refers to a specific delay

law. For multiple focusing options such as a sectorial scan, it would refer to a specific angle. “Position” refers to the physical location of the probe on the part.

- When exporting a beam simulation image as a text file, results are exported in units of both dB and pts in the same file. There is no option for selecting one or the other. When reading the text files into a program for analysis, be sure to select the correct data columns.
- There is no method of exporting a 3D block of data as one file. For 3D simulations, data must be exported slice by slice and reassembled into 3D off-line.
- When importing an.xml file with, for example, a probe or specimen definition, the file name is not shown anywhere in CIVA. When working with multiple files, be sure to make a note of which file was opened.
- Regarding FAQ B:15 on the online CIVA HelpDesk, “Displaying HF Mode for B-scans in a Beam Computation”: HF mode refers to the positive and negative half-cycles displayed from the A-scan, as compared to a rectified signal, which displays absolute values.
- For beam simulations, an “A-scan” is displayed. The beam A-scan refers to a 1D image displaying amplitude vs. time for a specific slice of the sound beam. Be aware that it is not a conventional A-scan in the sense of an echo or flaw response.
- Use a 2D rectangular computation zone instead of a 3D zone for beam simulations in complex geometries. 3D zones are very computationally expensive, and simulations may not even finish in some cases (although this is unpredictable).
- In “Storage options” for beam simulations, the “max beam only” approach makes the “save” operation much quicker with smaller results files. This does not allow the user to post-process the beam afterwards. If the probe is dual-element, the beam is automatically post-processed by default in T/R mode. Moreover, if the probes are single-element, there will be no need to post-process the beam with various focal laws.
- When using Voronoi regions, sometimes they are displayed and sometimes they are not—there seems to be a bug. Changing the opacity may help, but not always.
- Grain orientations (Euler angles) cannot be defined in Voronoi regions, only an average velocity and a velocity variation range.
- 64-bit CIVA is defaulted to be limited to only 2 Gb of memory. To increase available memory, modify the preferences in the set\_mem.bat file located in C:\CIVA\_2017\bin.
- To change the Delta V value in Voronoi definitions, click the velocity distribution reset button. Simply changing the value in the dialog box is not adequate.
- The color palette of a video cannot be changed once the video is produced. To generate a video with a different color palette, change the beam view from Max to A(t) (third blue icon on the tool bar on the top of the CIVA window) before generating the video. When the video is created from the A(t) view, the color palette of the video should match the color palette of the beam.
- The option “Activate Internal Conversions” refers to displaying mode conversion as the sound travels from one material to another through interfaces. Note that after checking this option the maximum number of conversions in transmission should be 1 or greater.
- Question: “When a probe radiates different beams, such as side lobes or anisotropy, the finite element box takes into account only the first one. Check the orientation to ensure the arrival of the desired beam first.” Does this apply to when both longitudinal and shear waves

are present from the same beam; for example, an L45 or mode conversion off the backwall?  
 Answer: If L and T waves options are selected, both are accounted for in the incident beam.  
 However, the computation zone must be big enough to contain both incident beams.

- CIVA-generated flaws cannot be included in beam simulations. In order to include a flaw in a beam simulation, it must be drawn into the specimen using the 2D CAD tool.
- Additional tips are available from EXTENDE at <http://www.extende.com/civa-tips>.

Information on transmitted and received beams, as quoted directly from EXTENDE:

*Beam in transmission is the calculation of the wave propagation generated by the transmitting transducer, the pulser.*

*Beam in reception is the mapping of the sensitivity of the receiving transducer, calculated as the beam received by the receiving transducer considering the different points of the computation zone as the transmitters. Of course, in Pulse-Echo, the pulser and the receiver are the same transducer.*

*The transmission (or reception) beam is the convolution between the input signal and the impulse response. It is equivalent to the mapping of the beam measured by a small receiver probe (like a needle probe) in the computation zone. For example, an equivalent measurement setup would be a transmission configuration with a probe emitting at a single position, and a needle probe scanning the opposite surface to measure the beam after a given propagation distance.*

*The transmission/reception beam is the convolution product of both components of the field that gives the whole mapping of the transducer sensitivity for one transducer position. Because this is a product (not a classical product but a "smart" product), the amplitude in T/R is much higher than the amplitude in T or R. It is equivalent to the mapping of the beam reflected back to the transducer by a set of small spherical reflectors in the computation zone, actually quite close to a defect response but considering an elementary reflector and not a "real" defect for the beam/defect interaction. If the defect is very small compared to the wavelength, then this is similar. For example, an equivalent measurement setup would be a pulse echo configuration measuring the response of a small target (steel ball) in a water tank for different probe positions.*

*Comparing the absolute amplitude of a beam in transmission and beam in transmission/reception does not really make sense (but you can consider that transmission/reception is a kind of product of 2 beams) but considering the one or the other will affect the focal spot size and can also affect the beam shape.*

*The 6dB focal spot size given by probe manufacturers corresponds to the focal spot size in transmission/reception (generally close to the focal spot size in transmission but at -3dB).*

CIVA RGB color scale, for import to MATLAB, Python, etc.

```
<entry red="76" green="76" blue="0" alpha="255" value="0.0"/>
<entry red="96" green="96" blue="0" alpha="255" value="0.019569471624266144"/>
<entry red="174" green="174" blue="0" alpha="255" value="0.13894324853228962"/>
```

```
<entry red="178" green="171" blue="0" alpha="255" value="0.15851272015655576"/>
<entry red="178" green="41" blue="0" alpha="255" value="0.36007827788649704"/>
<entry red="178" green="14" blue="0" alpha="255" value="0.3796477495107632"/>
<entry red="186" green="0" blue="8" alpha="255" value="0.39921722113502933"/>
<entry red="191" green="0" blue="59" alpha="255" value="0.4187866927592955"/>
<entry red="191" green="0" blue="118" alpha="255" value="0.44422700587084146"/>
<entry red="191" green="0" blue="122" alpha="255" value="0.4481409001956947"/>
<entry red="191" green="0" blue="182" alpha="255" value="0.4794520547945205"/>
<entry red="199" green="16" blue="192" alpha="255" value="0.49902152641878667"/>
<entry red="212" green="10" blue="200" alpha="255" value="0.5185909980430529"/>
<entry red="223" green="1" blue="218" alpha="255" value="0.5362035225048923"/>
<entry red="237" green="0" blue="238" alpha="255" value="0.5596868884540117"/>
<entry red="250" green="0" blue="250" alpha="255" value="0.5792563600782779"/>
<entry red="247" green="0" blue="255" alpha="255" value="0.598825831702544"/>
<entry red="234" green="0" blue="255" alpha="255" value="0.6183953033268101"/>
<entry red="203" green="0" blue="255" alpha="255" value="0.6771037181996086"/>
<entry red="186" green="0" blue="255" alpha="255" value="0.6986301369863014"/>
<entry red="136" green="0" blue="255" alpha="255" value="0.776908023483366"/>
<entry red="112" green="0" blue="255" alpha="255" value="0.8003913894324853"/>
<entry red="88" green="0" blue="255" alpha="255" value="0.8199608610567515"/>
<entry red="31" green="0" blue="255" alpha="255" value="0.8395303326810176"/>
<entry red="0" green="31" blue="255" alpha="255" value="0.8590998043052838"/>
<entry red="0" green="74" blue="255" alpha="255" value="0.8786692759295499"/>
<entry red="0" green="102" blue="255" alpha="255" value="0.898238747553816"/>
<entry red="0" green="169" blue="255" alpha="255" value="0.9393346379647749"/>
<entry red="0" green="189" blue="255" alpha="255" value="0.9549902152641878"/>
<entry red="0" green="228" blue="255" alpha="255" value="0.9784735812133072"/>
<entry red="0" green="255" blue="255" alpha="255" value="1.0"/>
```

## Appendix D – Transformation of Bunge Euler Angles to CIVA Rotation Angles

The Bunge convention Euler angles  $\varphi_1$ ,  $\phi$ ,  $\varphi_2$  represent rotation (in the crystal reference frame) about the Z axis, the new X axis, then about the new Z axis, respectively. In order to transform this rotation into an equivalent rotation in a fixed reference frame, the new angles X, Y, and Z need to be computed.

First, calculate the rotation matrix R:

$$R = \begin{bmatrix} c1c3 - c2s1s3 & -c1s3 - c2c3s1 & s1s2 \\ c3s1 + c1c2s3 & c1c2c3 - s1s3 & -c1s2 \\ s2s3 & c3s2 & c2 \end{bmatrix} = \begin{bmatrix} R11 & R12 & R13 \\ R21 & R22 & R23 \\ R31 & R32 & R33 \end{bmatrix}$$

where:  $c1 = \cos(\varphi_1)$   
 $c2 = \cos(\phi)$   
 $c3 = \cos(\varphi_2)$   
 $s1 = \sin(\varphi_1)$   
 $s2 = \sin(\phi)$   
 $s3 = \sin(\varphi_2)$

Next, calculate the new angles X, Y, and Z in the fixed reference frame. Three special cases must be considered, and multiple solutions may exist: the set (X, Y, Z) and the set (X1, Y1, Z1). The two sets result in identical rotations and are interchangeable. Note that angles are in radians.

If  $R31 \neq \pm 1$ :

$$\begin{aligned} Y &= -\text{asin}(R31) \\ Y1 &= \pi - Y \\ X &= \text{atan2}(R32/\cos(Y), R33/\cos(Y)) \\ X1 &= \text{atan2}(R32/\cos(Y1), R33/\cos(Y1)) \\ Z &= \text{atan2}(R21/\cos(Y), R11/\cos(Y)) \\ Z2 &= \text{atan2}(R21/\cos(Y2), R11/\cos(Y2)) \end{aligned}$$

If  $R31 = -1$

$$\begin{aligned} X &= \text{atan2}(R12, R13) \\ Y &= \pi/2 \\ Z &= 0 \end{aligned}$$

If  $R31 = +1$

$$\begin{aligned} X &= \text{atan2}(-R12, -R13) \\ Y &= -\pi/2 \\ Z &= 0 \end{aligned}$$

The function  $\text{asin}(x)$  is the arcsine, and  $\text{atan2}(x,y)$  is the arctangent of  $x/y$  such that the resulting angle is in the correct quadrant.

Below is Python code that can be used for the angle conversion.

```

# Python code for converting from Bunge Euler angles to fixed reference frame
import numpy as np

# Bunge Euler angles converted to radians
phi1=np.radians(90) #z
psi2=np.radians(0) #x'
phi3=np.radians(0) #z''

# Definition of trig functions
c1,s1=np.cos(phi1),np.sin(phi1)
c2,s2=np.cos(psi2),np.sin(psi2)
c3,s3=np.cos(phi3),np.sin(phi3)

# Definition of rotation matrix elements
R11,R12,R13=c1*c3-c2*s1*s3,-c1*s3-c2*c3*s1,s1*s2
R21,R22,R23=c3*s1+c1*c2*s3,c1*c2*c3-s1*s3,-c1*s2
R31,R32,R33=s2*s3,c3*s2,c2

#Rotation matrix
R=np.array(((R11,R12,R13),(R21,R22,R23),(R31,R32,R33)))

# Print R
print np.around(R,decimals=4)

# Calculate angles in fixed reference frame.
if R31 == 1.0:
    Z=0
    Y=np.radians(-90)
    X=np.arctan2(-R12,-R13)
elif R31 == -1.0:
    Z=0
    Y=np.radians(90)
    X=np.arctan2(R12,R13)
else:
    Y=-np.arcsin(R31)
    Y2=np.pi-Y
    X=np.arctan2(R32/np.cos(Y),R33/np.cos(Y))
    X2=np.arctan2(R32/np.cos(Y2),R33/np.cos(Y2))
    Z=np.arctan2(R21/np.cos(Y),R11/np.cos(Y))
    Z2=np.arctan2(R21/np.cos(Y2),R11/np.cos(Y2))

# Print results converted to degrees
print np.around((np.degrees(X),np.degrees(Y),np.degrees(Z)),decimals=4)
print np.around((np.degrees(X2),np.degrees(Y2),np.degrees(Z2)),decimals=4)

```

## Appendix E – Grain Modeling

### E.1 Gardahaut et al. (2014)

**Approach:** Polished, etched, and photographed DMW cross section. Used stiffness matrix values from the literature (citation was given, reference not found). Used attenuation values and their angular dependence from the same reference. Modeling in CIVA. Used stiffness matrix values for Inconel 182 instead of Inconel 600. Applied Ogilvy model with  $D=6.14$ ,  $T=1$ ,  $\alpha=12.5$ ,  $\eta=1$ .

**Stiffness Matrix coefficients:** Stiffness matrix coefficients for Inconel 182. Measured.

C11	C22	C33	C23	C13	C12	C44	C55	C66	$\rho$
255.8	255.8	236	135.4	137.9	130.5	111.4	111.9	81.4	8260

### E.2 Tabatabaeipour and Honarvar (2010)

**Approach:** Ultrasonic testing of AISI 316L SS welds by shielded metal arc welding (SMAW) and gas tungsten arc welding (GTAW). TofD and velocity measurements.

**Stiffness Matrix coefficients:** Measured. AISI 316L SS. Base metal is approximately cubic.

Material	C11	C22	C33	C23	C13	C12	C44	C55	C66	$\rho$
316L	265.5	265.5	265.5	112.9	110.2	121.8	79.5	76.5	77.9	7968
SMAW	258.5	225.1	208.9	112.9	131.8	178.7	115.3	101.1	74.2	7745
GTAW	278.6	254.9	247.2	112.1	148.1	173.7	106.5	73.9	74.3	8021

### E.3 Szávai et al. (2016)

**Approach:** Modeling to capture microstructure evolution. CIVA used to model PA UT. Created 11 homogeneous regions in the weld and assigned velocities. Used elastic constants by Tabatabaeipour and Honarvar (2010). Used attenuation of 0.09 dB/mm for isotropic austenitic and weld metals at 2.25 MHz.

**Stiffness Matrix coefficients:** Same as Tabatabaeipour.

### E.4 Liu and Wirdelius (2007)

**Approach:** Theoretical model of a weld using a mesh. Elastic coefficients taken from an unavailable reference. Assumed Inconel weld material.

**Stiffness Matrix coefficients:** Inconel 182, transversely isotropic.

C11	C22	C33	C23	C13	C12	C44	C55	C66	$\rho$
259	259	245	139	139	115	102	102	72	8300

### E.5 Sakamoto et al. (2012)

**Approach:** Measured velocity, attenuation, and noise in static cast SS and centrifugally cast SS with columnar grains. Calculated stiffness matrix from velocity measurements. Attenuation on different test blocks was columnar: 0.117, 0.118, equiaxed: 0.076, and 0.073 dB/mm (compared to SS304 base metal 0.04 dB/mm).

**Stiffness Matrix coefficients:** CASS JIS G5121 SCS14A (CF8M, 316C) parent material. Transversely isotropic.

C11	C22	C33	C23	C13	C12	C44	C55	C66	$\rho$
265.8	265.8	215.0	128.5	128.5	114.0	117.1	117.1	75.9	7900

### E.6 Seldis and Pecorari (2000)

**Approach:** Measured and modeled beam attenuation in bulk cast austenitic samples.

**Stiffness Matrix coefficients:** CASS 18/10 parent material, theoretical values verified by experiment. Hexagonal symmetry (transversely isotropic).

C11	C22	C33	C23	C13	C12	C44	C55	C66	$\rho$
257.5	257.5	220.1	150.5	150.5	103.9	118.7	118.7	76.8	7880

### E.7 Ploix et al. (2006)

**Approach:** Measured attenuation for different angles of grain orientation. Austenitic SS welds, AISI 316L steel. No stiffness matrix coefficients.

### E.8 Chen et al. (2015)

**Approach:** Used EBSD to characterize grain structures in CASS parent material. This paper gives the equations needed to calculate the stiffness matrices for each grain based on the Euler angle. Also describes the resolution or grain size needed is 1/10 the wavelength. Used cubic symmetry.

Euler angles ranges:  $\varphi_1=0^\circ-360^\circ$ ;  $\Phi=0^\circ-45^\circ$ ;  $\varphi_2=0^\circ-90^\circ$

**Stiffness Matrix coefficients:** Centrifugally cast SS Z3CN20-09 M material, cubic symmetry.

C11	C22	C33	C23	C13	C12	C44	C55	C66	$\rho$
265.8					114.0	117.1			7890

## E.9 Nageswaran et al. (2009)

**Approach:** EBSD of austenitic weld at 40  $\mu\text{m}$  resolution. Determined ten dominant orientation angles. Cubic stiffness coefficients taken from Juva and Lenkkeri (1980). Used CIVA for modeling. Weld map from EBSD was processed using “a digitizer” to generate a CAD image to import into CIVA. This did a good job of outlining and preserving the grain boundaries, but did not describe how it was done. 2 MHz PA. Did not use the whole weld, just one section of the EBSD scan. An in-depth discussion of adapted focal laws. Also talks about the 1/10 wavelength limit.

Euler angles ranges:  $\varphi_1=0^\circ-360^\circ$  (nothing between  $30^\circ-320^\circ$ );  $\Phi=-27.5^\circ-27.5^\circ$ ;  $\varphi_2=0^\circ-360^\circ$

**Stiffness Matrix coefficients:** Austenitic weld metal, DMW. Does not say what kind of metal. Measured. Cubic symmetry.

C11	C22	C33	C23	C13	C12	C44	C55	C66	$\rho$
203.6					133.5	129.8			

## E.10 Bannouf et al. (2014)

**Approach:** CIVA simulation of austenitic welds characterized by photographs. Results compared with experiment. 2.25 MHz. Also provided attenuation values with angular dependence.

**Stiffness Matrix coefficients:** 316L SS austenitic welds. Orthotropic symmetry.

Material	C11	C22	C33	C23	C13	C12	C44	C55	C66	$\rho$
Set 1	247	247	218	148	148	110	110	110	80	
Set 2	250	255	230	137	127	112	102	123	60	

**Attenuation Values:** 316L austenitic welds at 2.25 MHz.

Angle	0	15	30	45	60	75	90
Atten (dB/mm)	0.037	0.036	0.048	0.075	0.115	0.168	0.235

## E.11 Vijayendra and Neumann (1992)

**Approach:** Sound propagation models to predict reflection and transmission coefficients between austenitic base metal and welds. Material properties of X6CrNi 1811 are calculated.

**Stiffness Matrix coefficients:** Austenitic SS X6 CrNi 18-11 (304H), monotropic.

C11	C22	C33	C23	C13	C12	C44	C55	C66	$\rho$
241.1	241.1	240.1	138.0	138.0	96.9	112.3	112.3	72.1	7820

### E.12 Dewey et al. (1977)

**Approach:** Measured sound velocity and static tensile testing in a 308 electroslag weld in different directions. Sectioned the weld in three different directions.

**Stiffness Matrix coefficients:** 308 SS, orthotropic.

C11	C22	C33	C23	C13	C12	C44	C55	C66	$\rho$
262	262	229	160	160	148	82	82	57	

### E.13 Temple (1988)

**Approach:** Modeled and measured sound velocity in 308 SS.

**Stiffness Matrix coefficients:** 308 SS, transversely isotropic.

C11	C22	C33	C23	C13	C12	C44	C55	C66	$\rho$
263	263	216	145	145	98	129	129	82.5	8010

### E.14 Fan et al. (2015)

**Approach:** Used modeling and experiment to examine propagation of L and T waves in welds. Used the MINA model to approximate the weld grains structure. Calculated the stiffness matrix from EBSD. Shows ray model simulations and experimental results. Uses the same elastic constant for all grains, but changes grain orientation.

**Stiffness Matrix coefficients:** 308 SS, transversely isotropic.

material	C11	C22	C33	C23	C13	C12	C44	C55	C66	$\rho$
Anisotropic weld	245	245	227	121	121	104	105	105	74.5	8010
Isotropic parent	283	283	283	121	121	121	80.7	80.7	80.7	7900

### E.15 Chassignole et al. (2000)

**Approach:** 316L Welds, used micrographs to visualize structure in two types of welds (same types of welds as Tabatabaeipour et al). Calculated stiffness matrix based on theory, literature, and x-ray diffraction measurements. Performed modeling on a weld with 12 homogeneous domains of different rotation angles.

**Stiffness Matrix coefficients:** 316L SS, orthotropic symmetry.

C11	C22	C33	C23	C13	C12	C44	C55	C66	$\rho$
234	238	216	126	130	98	102	109	73	

## E.16 Chassignole et al. (2010)

**Approach:** Austenitic SS welds, 316L. Two different welds, grain structures mostly vertical. Measured stiffness matrix values by ultrasonics. Did 2D finite element modeling with ATHENA. Divided the weld region into squares with mean grain orientations in each square. Comparisons of modeling to experiment.

**Stiffness Matrix coefficients:** 316L stainless steel, orthotropic symmetry.

Weld	C11	C22	C33	C23	C13	C12	C44	C55	C66	$\rho$
A	234	240	220	126	130	98	99	110	95	
B	237	247	210	134	132	84	122	125	70	

## E.17 Jenson et al. (2009)

**Approach:** CEA. Used CIVA to generate Voroni cells and assign random velocity fluctuations. Modeled scatter and backwall echo, compared to experiment. Did an amplitude vs. grain size sensitivity study.

## Appendix F – Modeling Computer Specifications

The specifications of the computer used by PNNL for modeling and simulation work:

- Dual Intel Xeon Gold 6146 3.2 GHz, 4.2 GHz Turbo, 12C, 10.46 GT/s 3 UPI, 24.75 M Cache (165W) DDR4-2666
- Windows 10 Pro for Workstations
- NVIDIA NVS 310, 1 GB, 2 DP (2 DP to DVI adapters) (7X20T)
- 128 GB (8×16 GB) 2666 MHz DDR4 RDIMM ECC
- Intel vPro Technology Enabled
- MegaRAID SAS 9460-16i 12 GB/s PCIe SATA/SAS HW RAID controller (4 GB cache)
- Four 2.5-inch 1 TB SATA Class 20 Solid State Drives
- NVIDIA TITAN Xp Graphics Card, 1.42 GHz Core – 1.58 GHz Boost Clock – 12 GB GDDR5X

The following figure shows the EXTENDE-recommended hardware and software requirements.



## HARDWARE & SOFTWARE REQUIREMENTS

### *Minimal configuration\*:*

- 64 bits OS == Windows 7 / Windows 8 / Windows 8.1 / Windows 10
- Dual core
- Ram : Minimum  $\geq$  8Go, Recommended  $\geq$  16Go
- Hard Disk  $\geq$  250 Gb
- Graphic Resolution == 1280 x 1024 or 1920 x 1080
- DVD ROM
- USB port for Hardware dongle (Software key is proposed by default)

*\*Windows XP and 32 bits OS are no longer supported (Windows XP is not supported any more by Microsoft).*

### *Optimized configuration\*\*:*

- 64 bits OS == Windows 7 / Windows 8 / Windows 8.1 / Windows 10
- Hexa / Octo core
- Ram  $\geq$  24 Gb
- Hard Disk  $\geq$  500 Gb (with CIVA installed on SSD system disk 256 Gb):
  - o All disks (data and system) on SSD for CIVA UT Analysis
- Graphic Resolution == 1920 x 1200
  - o Dedicated graphic card if computer is a laptop
- DVD ROM
- USB port for Hardware dongle (Software key is proposed by default)
- GPU Graphic Processor (useful for CIVA CT only) with compute capability version  $\geq$  2.x

([http://en.wikipedia.org/wiki/CUDA#Supported\\_GPUs](http://en.wikipedia.org/wiki/CUDA#Supported_GPUs))

For instance == GTX1080 Ti or Quadro P4000

*\*\* An efficient use of CIVA CT requires this optimal configuration*

From:

[http://www.extende.com/files/extende/download\\_files/CIVA\\_2017\\_Software\\_Data\\_Sheet\\_EN.pdf](http://www.extende.com/files/extende/download_files/CIVA_2017_Software_Data_Sheet_EN.pdf)

# Pacific Northwest National Laboratory

902 Battelle Boulevard  
P.O. Box 999  
Richland, WA 99354  
1-888-375-PNNL (7665)  
[www.pnnl.gov](http://www.pnnl.gov)